Investigation of the effects of colloidal suspension properties on spatially resolved diffuse reflectance

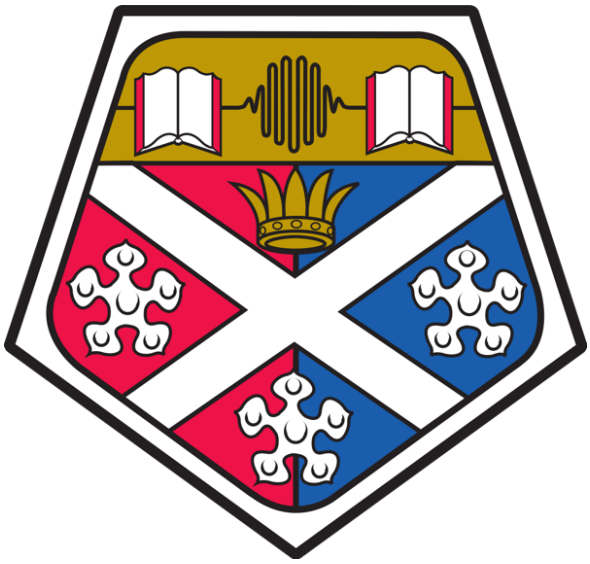

Daria Stoliarskaia

Department of Chemical and Process Engineering
University of Strathclyde

This dissertation is submitted for the degree of
Doctor of Philosophy

November 2019

DECLARATION

This thesis is the result of the author's original research. It has been composed by the author and has not been previously submitted for examination which has led to the award of a degree.' 'The copyright of this thesis belongs to the author under the terms of the United Kingdom Copyright Acts as qualified by University of Strathclyde Regulation 3.50. Due acknowledgement must always be made of the use of any material contained in, or derived from, this thesis.

Signed:

Date:

Daria Stoliarskaia
November 2019

ACKNOWLEDGEMENTS

I would like to express my deepest gratitude to my supervisor, Dr Yi-chieh Chen for her consistent guidance, expertise and countless hours she was willing to spend to help me. Her vision of this project and continuous support helped me to grow during the span of this project and fulfil the research proposal. I am equally thankful to Dr Leo Lue for his consistent consular, generation of new ideas and open-door policy. My appreciation extends to the AMT group in Pfizer Inc., specifically to Polina Kishinevskaya, Dr Jun Huang and Dr Mojgan Moshgbar for introducing me to process analytical technology and for supporting the project directly. I would like to thank Nicolau Dehanov, Carla Ferreira and Kelly Thomson for their consultation and willingness to help during this research.

However, when I'm thinking of my PhD research experience, I cannot argue with words of Fyodor Dostoyevsky, who wrote: "But man is a fickle creature and, like a chess-player, is interested in the process of attaining his goal rather than the goal itself". Therefore, I would like to thank my friends who made this experience a fantastic journey. I am fortunate to have Martin, Maria, Joao and Daria as my friends, thank you for being there for me. Same goes to Vladimir, whos patience, support and love played an important role. *Ogromnoye spasibo* to Andrew, Scott, Ruben, Alexandra, Neret, Georgia, the 'outlaw' GURSS, David and many more. I wish I could acknowledge all the moments we shared, but I am grateful for every event and festival, grateful to Andrew for sharing the roof with me for over 3 years, Carla for (Da)rla, and to Robert for sincere appreciation of my Matlab knowledge and the best creativity with nicknames. And special thank you goes to Paul, Carlota, Fiona and Sarahjane for being generous human beings.

Lastly, I can't find the right words to describe how indebted I am to my family, especially my mom Zhanna and sister Mariia, for their unconditional support, unquestionable belief in me and all the patience.

ABSTRACT

Many quality attributes of pharmaceutical suspensions are directly influenced by the physical properties of constituting particles. The influence has not been explored fully as the chemical characteristics (composition/concentration) are of primary concern. Particle size distribution provides with detailed characteristics of the material population, however, it is a challenging parameter to monitor during the process, due to limitations of the available analytical techniques.

In this thesis, a methodology which analyses particle size distribution and concentration using the optical scattering properties extracted from a novel spatially and angularly resolved diffuse reflectance measurement (SAR-DRM) is proposed. This approach incorporates Mie theory and particle size distribution function, followed by Farrell's diffuse approximation to model specified reflectance signal. The developed methodology does not require a calibration model and was used to investigate three main objectives. Firstly, the sensitivity of the simulated SAR-DRM to the mode radius, distribution width and concentration of solids variations is explored. An inversion algorithm for the measured SAR-DRM is proposed and studied on polystyrene suspensions sample sets. Lastly, the methodology is then expanded to incorporate the particle shape parameter in the form of aspect ratio. To my knowledge, this study is a unique attempt to directly invert SAR-DRM to obtain the particle size distribution and concentration parameters from modelled and experimental measurements as well as the first study of particle shape effect on SAR-DRM.

The simultaneous inversion of all three parameters of interest produced results comparable with reference measurements. The study provides a set of method limitations that when considered allow the optimal estimation of the parameters of interest. The results produced by the methodology developed and presented throughout this thesis suggest the great potential of using the methodology as a calibration-free tool for robust and reliable in-process analysis of pharmaceutical suspensions.

CONTENTS

LIST OF FIGURES

NOMENCLATURE

Roman Symbols

m	Complex refractive index	—
$\bar{R}$	Mean radius	nm
C	Particles concentration (weight percent)	$\%wt$
d	Dipole spacing	μm
g	Asymmetry parameter	—
k	Wave number	$1/nm$
N	Number of dipoles	—
n_m	Real part of the refractive index of the surrounding medium	—
N_p	Number of particles per unit volume	$1/mm^3$
n_p	Real part of the refractive index of the particle	—
R_H	Hydrodynamic radius	nm
$R_{d(S-R)}$	Spatially resolved diffuse reflectance	—
$R_{d(tot)}$	Total diffuse reflectance	—
x	Size parameter	—
Mode[R]	Mode radius of the particle size distribution	nm
R	Normalised reflected intensity	—

RC	Relative change	%
RMSE	Root mean square error	—
S-R	Source-to-receiver	mm
tmfp	Transport mean free path	mm

Greek Symbols

α	Scattering albedo	—
χ^2	Chi-squared error	—
δ	Relative error	%
λ	Wavelength	nm
λ_m	Wavelength in the surrounding medium	nm
$\mu_a(x)$	Bulk absorption coefficient	mm^{-1}
$\mu_s'(x)$	Reduced scattering coefficient	mm^{-1}
$\mu_s(x)$	Bulk scattering coefficient	mm^{-1}
$\mu_{a,m}$	Bulk absorption coefficient of the surrounding medium	mm^{-1}
$\mu_{eff}(x)$	Effective attenuation coefficient	mm^{-1}
$p(\theta,x)$	Phase function	—
ρ_m	Density of the medium	g/cm^3
ρ_p	Density of the particle	g/cm^3
σ	Distribution width of lognormal distribution	—
$\sigma_a(x)$	Absorption cross-section of the particle	mm^2
$\sigma_s(x)$	Scattering cross-section of the particle	mm^2

Other/Acronyms

AD	Adding-doubling
AR	Aspect ratio
CNC	Cellulose Nanocrystals
DA	Diffuse approximation
DDA	Discrete Dipole Approximation
DLS	Dynamic light scattering
DRS	Diffuse reflectance spectroscopy
ER	Equivalent radius
FDA	Food and Drug Administration
IS	Integrating sphere
LD	Laser diffraction
NIR	Near-infrared
NTA	Nanoparticle tracking analysis
PAT	Process Analytical Technology
PDF	Probability density function
PSD	Particle size distribution
RPM	Rotations per minute
RTE	Radiative transfer equation
SLS	Static light scattering
SAR-DRM	Spatially and angularly resolved diffuse reflectance measurement
SRDR	Spatially resolved diffuse reflectance
UV-vis	Ultra-violet-visible

CHAPTER 1

INTRODUCTION

The pharmaceutical industry, driven by Process Analytical Technology (PAT) and Quality by Design(QbD), is focusing on efficiency improvement, often through monitoring of critical parameters of particulate substances. Process analytical technology (PAT) has been a term of increasing importance, and the focus of PAT can be defined as the process of building up the quality of the product by placing greater emphasis on in-process instead of end-product testing and release [1]. The ultimate goal of PAT development and application is to decrease the production time, stages and cost, increase the efficiency and batch to batch consistency, improve process understanding, and provide with rapid feedback about process properties[2]. The product-by-process manufacturing is generally relying on knowledge of the physical and chemical properties of the product. Polymers and crystals engineering fields are great examples of the manufacturing process where the quality of the final product depends greatly on the reaction process [3].

To support PAT agenda across different areas, there are not enough reliable methods that can provide accurate information about physical and chemical properties of the product and their variations during the process. Optical spectroscopy is a relatively simple and effective way to identify variations in the size of particles and its distribution, as they result in changes in optical (scattering, absorption, transmission) properties. It is a reliable and fast method, equally suitable for off-line, and in-line analysis. Optical techniques usually have limited applicability to turbid media analysis, although spatially resolved diffuse reflectance (SRDR) has a known potential to overcome it due to source-to-receiver(S-R) separations range [4]. Most of the studies to-date that involve analysis of optical spectra utilise multivariate statistical modelling due to the complexity of the spectra parameters separation, especially light scattering effect [5]. Despite being a widely

recognised tool to solve real-life problems of different complexity, chemometrics method has its significant limitations. The underlying multivariate analysis often requires building a calibration model, that consists of a well-designed dataset. The quality and accuracy of the multivariate analysis performance depend greatly on such dataset, making this approach, ultimately, not the most robust. Compex spectral signal can be also described and decoupled into material properties via underlying physical theories and their approximations, which would eliminate the need in the calibration model. The focus of this work was shifted towards such an approach, which required the development of the multistage methodology for calculation of SRDR, based on available theories. Apart from proposing calibration-free approach, solving the SRDR spectra analytically allowed to conduct a comprehensive study on physical (particle size distribution, aspect ratio) and chemical (concentration) properties effect of this type of spectroscopy signal. By performing spectra modelling, this study provides significant insight into particle-light interaction behaviour within turbid media, especially in the context of particle size distribution effect on SRDR, which has not been reported previously. Furthermore, the ability of diffuse reflectance spectra to overcome the limitations related to concentration unveils the opportunity to examine physical properties of the particles without dilution, covering an important gap between currently known capabilities of most of the analytical techniques and possible implementation of the calibration-free tool into process monitoring.

1.1 Motivation background

1.1.1 Physical and chemical properties of pharmaceutical suspensions

A pharmaceutical suspension as a pharmaceutical dosage forms has multiple advantages, like the effective dispensing of hydrophobic drugs, avoidance of the use of co-solvents, resistance to degradation of drugs due to hydrolysis and, for oral administration - easy swallowing for young or elderly patients [6]. In an ideal suspension formulation, insoluble particles should be uniformly dispersed. However, during the storage, the solid particles in suspensions can separate from the liquid media and sediment. In a well-formulated suspension, particles should re-disperse uniformly in the continuous phase upon moderate shaking, regardless of the amount of sedimentation.

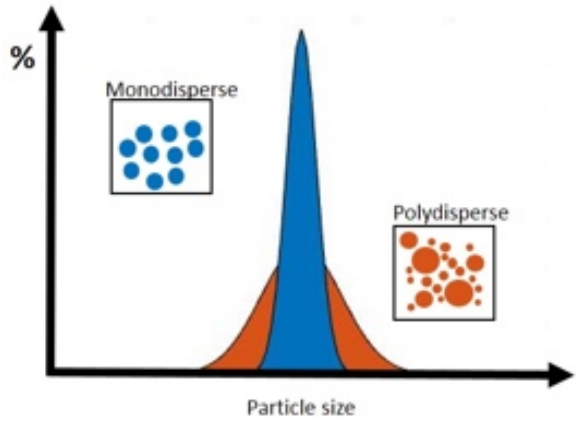

Figure 1.1.1 A graphical illustration of monodisperse and polydisperse system of particles [7]

The particle size can be represented by less or more detailed parameters, however, for simplicity, the usual approach is to monitor a single parameter, like the average size. This allows estimating the sedimentation rate, solubility and dissolution velocity, which are also vital quality attributes of the formulation. The rate of sedimentation for a monodisperse system of perfectly spherical particles that do not interact with each other is defined by the Stokes equation, which relates it to viscosity and size of the particle. In reality, the particle size of suspensions is rarely uniform. Particulate suspensions tend to have particles of different sizes. The distribution of sizes can be either narrow (almost all particles are of the same size) or wide (Figure 1.1.1). Maintaining narrow particle size distribution is an ultimate goal for suspensions manufacturing because it permits a better understanding and consistency of the particles sedimentation and dissolution behaviour.

When comparing monodisperse and polydisperse suspensions from an example in Figure 1.1.1, the polydisperse suspension would naturally contain a higher number of fine and coarse particles, assuming that both suspensions are of the same particle volume fraction. Increase of fine particles counts leads to a significant increase of particle surface area, a vital parameter of drug release. The challenges of the polydispersity are not limited to the presence of fine particles. Large particles and/or agglomerates in a polydisperse system can lead to problems, such as needle clogging for injected suspensions. The viscosity of the suspension highly depends on the fraction of both, fine and coarse particles in the suspensions. Depending on the fraction of each particle size group, viscosity can get lower or higher as a result of colloidal interactions that increase or decrease shear stress [8–10]. Considering the possibility of an impact on the product quality, neither of

the variations is preferable. Since particle size distribution has a direct link to quality attributes, implementation of particle size distribution measurement into the suspension manufacturing process would provide valuable information about quality attributes, and consequently product quality [11].

Another simplifying assumption in particles characterisation is the approximation of the particles to spheres. For processes like crystallisation where crystal is gradually growing or Ostwald ripening occur during the process, knowing the variation of the dimensions of the particles in time is crucial. Besides, irregularities in the particle surface usually lead to higher viscosity, mainly due to one of two common reasons. Firstly, the deflection of solvent flow lines around particles is stronger than for spheres. Secondly, the increase in surface area increases the probability of particle-particle interactions, which are stronger for high particle concentrations and high shear rates [12].

The concentration of the particles is ultimately an important parameter of the end product as it is tied with the amount of active ingredient that is carried by it. Implementation of the concentration monitoring during the product-by-process making can assist some of the specific processes. When the pharmaceutical suspension is a result of the polymerisation reaction, the concentration of the end product also indicates the conversion degree of monomer into the polymer during the polymerisation process. In this case, being able to monitor the conversion rate is crucial for efficiency, implying the preference of providing the parameter during the reaction process.

The solid content in suspensions typically ranges, depending on the use of the suspension, between 0.5% and 40% of volume [13]. Diluted suspensions do not exhibit the significant relationship between volume fraction and quality of the product, whereas when the volume fraction increases, forces, like particle-particle interactions, become significant and therefore may contribute to quality parameters. For example, these interactions hinder the freedom of movement of the particles, which is resulting in increased viscosity by affecting fluid flow around embedded particles. Hence, monitoring of the concentration variation ideally should be covering not only diluted but also highly concentrated suspensions.

1.1.2 Process spectroscopy as process analytical technology (PAT) tool

A vast number of techniques exist that are capable of measuring the physical properties of the particles, like particle size distribution and shape. Most popular techniques can be grouped by the measuring principles, such as light-based (optical microscopy, electron microscopy, dynamic light scattering, laser diffraction, etc.), sound-based (ultrasound extinction) or separation-based (sieve analysis, sedimentation). One of the objectives of the PAT agenda is to optimise, reduce and, ultimately, eliminate destructive analysis. Light-based technologies have advanced greatly due to non-destructive principle of analysis (interaction of the light with the material), variety of the methods available and existing additional knowledge base from other fields [14–16].

Product-by-process manufacturings are widely employing spectroscopic methods. UV-vis, NIR and Raman have been extensively studied for monitoring monomer conversion, whereas the UV-vis and NIR spectroscopy for mean particle size monitoring. NIR is a relatively inexpensive type of spectroscopy, besides, according to a study published by Ambrogi *et al* [17] on comparing Raman and NIR for monitoring an emulsion polymerisation, NIR spectroscopy has proved to be a reliable tool for monitoring monomer conversion and particle size simultaneously, giving it a wide possibility to its application and developments as a process spectroscopy tool. However, despite its potential, implementation of the spectroscopy into process monitoring still constrained by significant challenges, related to re-distribution of light after light-particle interaction, that leads to non-linear light scattering. It is especially significant when the concentration of particles is high, increasing the probability of light re-radiation. Modification of traditional spectroscopy measurement setup is one of the most promising courses of action to tackle this limitation. Diffuse reflectance measurement (DRM) is a measurement setup that uses either an integrating sphere for total diffuse reflectance measurement or a fibre optic probe placed inside the analysed suspension to collect the signal, typically in the UV-vis-NIR wavelength range.

1.2 Motivation and Objectives

The principal goal for this project is to develop a physics-based method that provides physical and chemical characteristics of turbid suspensions from spatially and angularly

resolved diffuse reflectance measurement (SAR-DRM). Proposed methodology expected to provide robust, calibration-free non-destructive measurements of parameters of interest (particle size distribution and concentration) with the potential of consideration of the aspect ratio of the particles.

To fulfil the above-mentioned goal, acquiring the knowledge about the sensitivity of diffuse reflectance to each of parameters of interest, examining the effect of measurements design on signal sensitivity to the parameter of interest and establishing the forward and inversion algorithm for parameters of interest estimation can be named the main vectors of this project. They were investigated through the project by exploring the objectives below.

Forward calculation of the SAR-DRM for polystyrene suspensions:

- Combination of available theories to describe the bulk optical properties and diffuse reflectance of a concentrated polydisperse system to provide a forward model for total and spatially resolved diffuse reflectance simulation, followed by the investigation of the measurement configuration influence on spectra sensitivity to the parameters of interest.

- Evaluating the degree of effect of particle size distribution on its own and in combination with a concentration on the simulated diffuse reflectance measurements, what is the specifics of each of the parameter's effect and the wavelength range it appears at.

Inversion of the SAR-DRM for polystyrene suspensions:

- Investigation for the optimal objective function that indicates the best fit of simulated to measured multi-wavelengths SAR-DRM.

- Development of the inversion routine for estimation of the particle size distribution, concentration individually or simultaneously and implementation of it onto feasibility polystyrene sample sets.

- Establishment of limitations of the method application, regarding the particle radii range, distribution width and concentration, that are observed from the diffuse reflectance signal inversion.

Investigation of the aspect ratio effect of SAR-DRM

- Examination of the particle shape parameter (aspect ratio) influence on simulated SAR-DRM for reflective material (polystyrene) and moderately reflective material (cellulose nanocrystals suspensions).

- Conducting the simulational and experimental case study of cellulose nanocrystals suspensions to overview the sensitivity of the SAR-DRM to the aspect ratio of the commercially available cellulose nanocrystals suspensions.

1.3 THESIS STRUCTURE

The thesis is organised in eight main chapters. The first and current chapter summarises the background motivation and the research aims and objectives and provides an overview of the thesis structure.

The second chapter consists of a literature review on the parameters of interest for process monitoring and a detailed discussion about light-based methodologies and their applicability to monitor turbid suspensions. Chapter 3 covers the theoretical background and the formulae of the forward computation of the bulk optical properties for the polydisperse system, followed by diffuse reflectance calculation routine for two different measurement setups.

To clarify the sensitivity of each of the suggested types of the diffuse reflectance measurements, Chapter 4 presents the model of a UV-vis-NIR spectral behaviour from the hypothetical polystyrene particles suspension of various mode radii, distribution width and concentrations of solids. It studies each of these parameters of interest and the combined effect of the diffuse reflectance measurement configuration.

The findings from Chapter 4 are used to shape an experimental methodology, described in Chapter 5. The chapter consists of three sections: description of sample sets, experimental procedure and signal process routine, and computational routine for signal inversion.

Chapter 6 presents the result of the validation of the inversion method as well as results of its application to a monodisperse (Sample set 1) and a polydisperse (Sample set 2) sample sets. Examination of these sample sets unveils the overall information about the sensitivity of the SAR-DRM measurements to the parameters of interest. Since these sample sets were prepared to study the exact parameters of interest combination, Chapter 7 expands the study with a complex sample set analysis. It begins with inversion and analysis of Sample set 3, which is prepared as the result of the polymerisation reaction, affected by process parameters. The chapter concludes with a case study on the possible effect of particle shape on SAR-DRM in the form of aspect ratio. Precisely, this section of

Chapter 7 discusses the aspect ratio effect appearance on modelled SRDR for polystyrene and nanocrystalline cellulose systems. The chapter is concluded with an analysis of diffuse reflectance spectra collected from cellulose nanocrystals and its sensitivity to particle shape parameter.

Chapter 8 concludes the thesis with major observations made during the project, followed by considerations for potential directions for future work.

CHAPTER 2

INTRODUCTION TO PARTICLE SIZE MEASUREMENT

2.1 PHYSICAL AND CHEMICAL PROPERTIES OF THE SUSPENDED PARTICLES

Suspended particles may be characterised by their size, shape and quantity. In pharmaceutical and many other industries, unaccounted variation in these properties may affect the quality of the end product. Therefore, control of particle properties throughout the process is declared as a preferable analysis framework to ensure the needed quality of the product.

Development of the methodology for characterisation of the particles within pharmaceutical suspensions can be identified as one of the main aims for this project. This research is focusing on properties like concentration and distribution of particle sizes. The latter is difficult to define clearly as the exact definition will vary with selected methodologies for particle properties analysis. Each of the measuring techniques assesses some selected measurable parameter. Hence, before discussing available methods for particle size characterisation and the challenges associated, the desirable measurands should be defined distinctly.

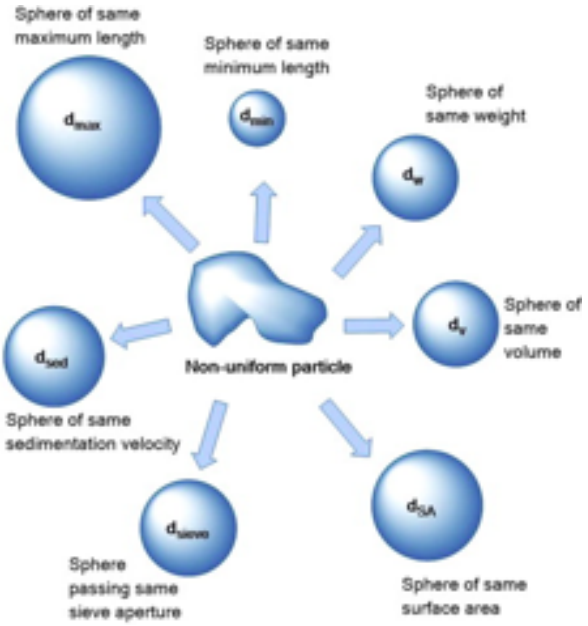

Figure 2.1.1 Illustration of various alternative equivalent diameter [20]

2.1.1 EQUIVALENT RADIUS

Particle radius is a fairly obvious parameter to consider for size representation. However, it can be used as such only for homogeneous perfect spheres. Measuring instruments for particulate suspensions are built based on a variety of measurement principles, such as sedimentation, conductivity changes, optical diffraction or scattering, translatory or rotary diffusion, to mention a few [18]. The relevant theoretical expression exists for each type of measurements for estimation of some one-dimensional property of the particle (e.g. weight, volume, settling rate, projected area, minimum sieve aperture through which the particle will fall). If the analysed particle differs from the sphere, the radius measurements that are delivered by each of the methods will differ as well. There is no consistent result among different particle measurement techniques as each of them relies on some specific property of the particle [19].

To account for variations in particle shape, the particle radius is commonly re-defined by the equivalent radius (ER) which represents the hypothetical sphere that has the same measured property as the actual particle in the analysed suspension. Figure 2.1.1 demonstrates various possibilities of defining ER. This definition clarifies some of the ambiguity of particle size characterisation. The exact value of the ER would then depend on the measuring principle used. Based on that, the variations between the equivalent

radius of the homogeneous particles are not large when the shape of the particles is close to the spherical. Deviation from spherical shape would cause a larger difference between different ER as each of measured physical phenomena has a dependence upon different particle dimensions. Obtaining ER from different techniques knowing that the results are not comparable is not necessarily unappealing because the differences between different ER may help the particle shape identification [21]. Yet, for highly non-spherical particles, such an approach is generally combined with measurements of particle shape parameters, like length, aspect ratio, perimeter and others. Therefore, up to date, the particle physical properties analysis is a continuous search for providing the adequate number of measured parameters what would illustrate the particles e as close to the realistic image of them as possible. Implementation of the ER as the particle size parameter allows to simplify the analysis; however, it also generalises the particle size information.

In realities of industrial agenda, the possibility to characterise material with a minimum necessary number of techniques is desirable for optimal analysis time. Ultimately, the introduction of the ER allows the use of fewer parameters to describe the changes in the particle sufficiently. On the other hand, this raises a question regarding the feasibility of relying on a single parameter like ER when the analysis is conducted on particles population. Indeed, the availability of the many characterisation parameters is beneficial for system understanding and consequently would help to provide a quality of the product needed. At the same time, attempt to gain a too detailed description of physical properties would imply the growing number of techniques needed to be involved. This concludes the need to identify the minimum number of parameters and techniques needed to characterise particle accurate enough on a case-by-case basis. Besides, limitation of monitored parameters to an absolute minimum without liberating the quality of the end product is a necessary simplification of the actual terms to accelerate the process analysis speed. Such an approach is generally in favour by regulatory bodies, such as the FDA, which control strategies and specifications revolve around a single particle size and the accepted tolerances on the selected parameter [22], where possible. At the same time, the concerns regarding the variability of the sizes within a single batch kept the discussion open for more details particle size characterisation parameters, like particle size distribution.

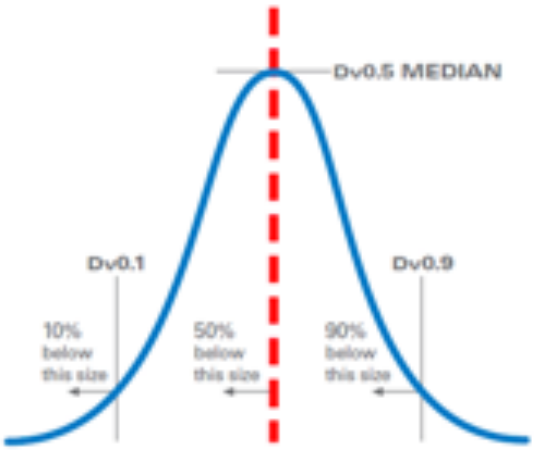

Figure 2.1.2 Illustration of D_{10}, D_{50} and D_{90} on a normal distribution example [24]

2.1.2 Distribution of particle sizes

This section will overview the validity of the assumption to a single size of particles collection. In reality, the particulate system normally shows some variation in their size, since there are always deviations during their generation(synthesis or another route of production). The deviation of sizes defines the polydispersity of the suspension. Occasionally, the differences between these size indicators are minor, and all particles within the system have nearly the same size, indicating that the distribution of sizes is narrow or monodisperse. According to the National Institute of Standards and Technology, the particles are called monodisperse if at least 90% lies within 5% of the average size [23]. Outside such boundaries, the material would have a significant number of fine and large particles in the population and would be named polydisperse.

It is a common practice to represent particle size population by two popular forms: cumulative (undersize) distribution curve or a frequency distribution curve. Particle size distributions mostly represented in mathematical form by probability density functions (PDF), or by the integration of the PDF, cumulative distribution functions (CDF). The probability density function is a straightforward and illustrative way to characterise the population of particles in the system according to the measured equivalent radius.

The basic characteristics of the PDF are frequently described by a few parameters that indicate a "predominant size" and the width of the distribution. The predominant size commonly defined by mode or mean. Mode corresponds to a peak of the distribution curve, and the mean size is indicating the average of the population. During the particle

size analysis, instead of reporting a single predominant size, a widely used solution is to report a few values also to indicate the width of the distribution. Such values are known as D_{10}, D_{50} and D_{90} and illustrated in Figure 2.1.2. D_{50} indicates where half of the total particles population is residing. In a similar manner, D_{10} and D_{90} are describing the point of distribution where 10 % and 90 % of the population lies respectively. By monitoring these three parameters together, it is possible to state if there are significant changes in the particle size population, which can indicate the presence of agglomeration or extremely fine particles. Description of high polydispersity can be challenging with only a few indicators as the presence of a large number of agglomerates and fine particles may be overlooked with such an approach. To balance the necessity to have full information about particle sizes in the system and also comply with the regulatory documentation, the focus of many-particle sizing techniques was shifted towards a description of the particle size population by a continuous function.

There is multiple continuous PDF available that can be applied to characterise particle size distribution. Namely, normal distribution, lognormal, gamma and Weibull are the most often applied in this context. The function form of the size distribution of particles depends on how the particles were formed. In practical applications, the exact PDF shape of the suspension is unknown, but the idea of the expected shape of the probability density distributions could be approximated based on some general knowledge about the particles generations during the process. Lognormal distribution has a form of a skewed normal distribution and describes the presence of large particles, which occur during milling processes and various polymerisation reactions, although the latter often characterised more precisely with multimodal distribution[25, 26]. According to previous studies, the particle size variations in suspension polymerisations exhibit similarities with liquid-liquid dispersions with high viscosity dispersed phase [27]. Many investigators have studied drop size distributions in liquid-liquid dispersion and have reported that the volume drop size distribution can be represented by a normal, lognormal, or gamma distribution [28–31, 21, 32]. The lognormal distribution is often used as a default model for the analysis of particle size distribution data, and the following research will be considering this PDF as a starting point for discussion [33].

For instance, a number of weighted distribution illustrate the system by assuming that the constituent particles are weighted equally irrespective of its size. Number weighted distribution is a convenient form that can be re-converted into other distributions forms,

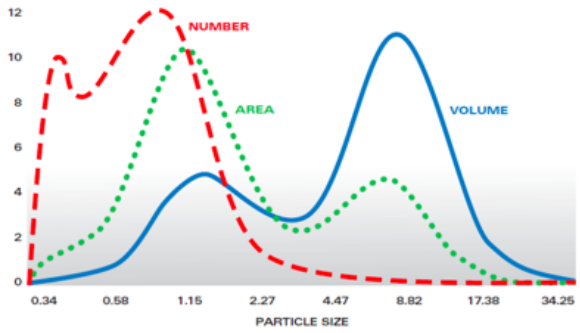

Figure 2.1.3 Particle size distribution based on number, volume and surface area of particles [24]

but it is specifically useful in foreign particle detection, for example, or in the analysis of the system where particle by particle resolution is required. Another common form of illustration of particle population is the mentioned volume or mass distribution which can be either measured directly or derived from number distribution. In such a case, each particle in the distribution is weighted with respect to the volume of that particle or mass. Figure 2.1.3 shows how knowing about volume distribution changes the perspective regarding material properties. This is often extremely useful from a commercial perspective as the distribution represents the composition of the sample in terms of its volume/mass, and therefore its potential value.

Generally, the distribution of sizes indicates the variations in ER; therefore, it is vital to choose such methodology that benefits the accuracy of the material population representation. Once the physical properties of the collection of particles are measured, a specified model generates a representation of a particle size distribution. Depending on the type of measurements, there is a variation in the provided ER and its distribution. The following section will give an overview of the commonly used particle size distribution analytical techniques and their capabilities to provide additional parameters of interest like shape factors or concentration of solids. Based on the review, the major limitation will be shortlisted to evaluate the needs of the current process analytical technologies market.

2.2 Overview of Standard Optical Technologies

Light-based methods for measuring particles physical properties have become the preferred particle sizing technique in a wide range of industries [34]. It attributes to the

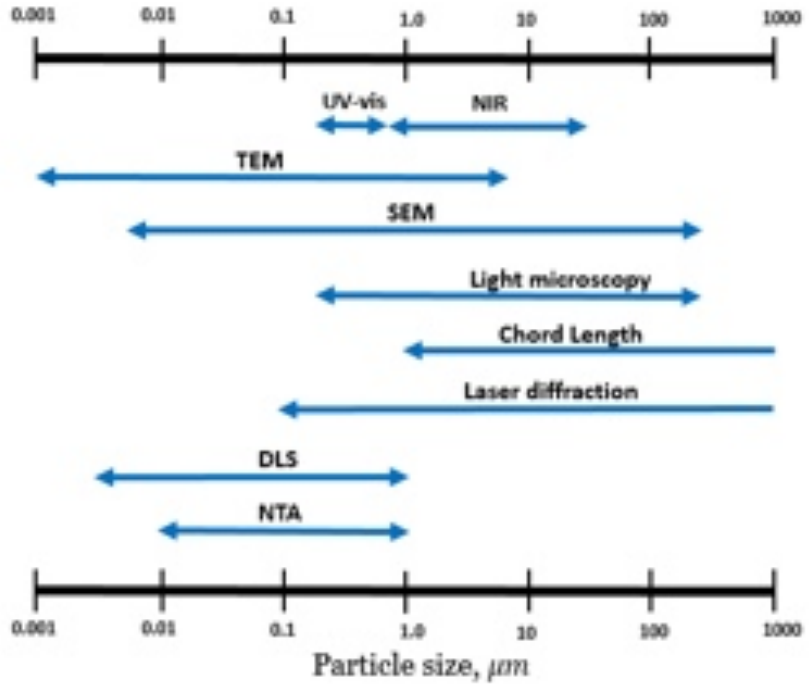

Figure 2.2.1 Typical measurement ranges of selection of PSD light-based techniques [35]

interaction of the light with objects, resulting in the visible appearances of them, which implies the major reason behind such variety of microscopy techniques.

Nowadays, there is a various number of light-based techniques that can perform particle size measurements. Figure 2.2.1 outlines some of the most used light-based methods in comparison with particle size range covered. Currently, there is no unified method that would be applicable for broad size range, i.e. from nm to μm range. Apart from the particle size, these techniques vary in the other parameters they may determine during the analysis and the analysis procedure itself. In the following sections, the general operating principles of common particle analysis techniques will be described and discussed. Process analytical technologies initiative has seriously changed the direction of measurements from a sampling-based analysis towards an embedded form of monitoring of material parameters during the process. Some of the renowned and widely used techniques will be described in details, highlighting the assets and liabilities of each of the methods.

2.2.1 MICROSCOPIC-BASED IMAGING

Microscopy can be used as an ultimate method of particle size and shape analysis since it is the only method where individual particles are observed and measured [36, 37]. Optical microscope often referred to as the "light optical microscope", as it employes visible light and a system of lenses to magnify images of particles. There general usage of visible light in the microscopy is also why the method generally applies to particles of the size above 0.8 μm [38].

As was mentioned previously, each technique measures some property of the material, deriving the equivalent radius from it. The optical microscopy is no exclusion, the image of a particle seen in a microscope is a two-dimensional projected area, and from this image, an estimate of particle dimensions must be made. This stage involves comparing the projected area of a particle with the areas of reference circles, or graticules, of known sizes and routine repetition of the method for particles that appeared in the collected image. The relative number of particles is determined in each of a series of size classes. These combined represent the size distribution by number, which can be later converted into distribution by volume and by weight for homogeneous systems. The total number of particles in the derived distribution would reflect the concentration of the sample captured by frame exclusively, and therefore information about the actual concentration would need to be determined via other, more appropriate for the application methods.

The estimation of particle size distribution from the processing of generated images was expanded towards smaller sizes (down to 1 nm) using electron microscopy. One of the most widely applicable methods is scanning electron microscopy (SEM) which produces images of a sample by scanning it with a focused beam of electrons and the transmission electron microscopy (TEM) which as the name suggests, uses the transmitted electrons. Figure 2.2.2 schematically shows the differences between these methods and overview of the methods setups. The methodology requires the execution of a quite elaborated sample preparation procedure, which directly affects the efficiency of the analysis, which is a significant limitation [40].

Sample preparation, however, is not the only nuisance of the traditional image-based particle analysis. Due to the nature of the analysis, which is based on the individual frame processing, the image analysis is time-consuming. Semi-automatic and automatic image processing systems have been developed which speed up analyses and reduce the tedium of manual methods [37]. The modern image analysis enables rapid processing of the

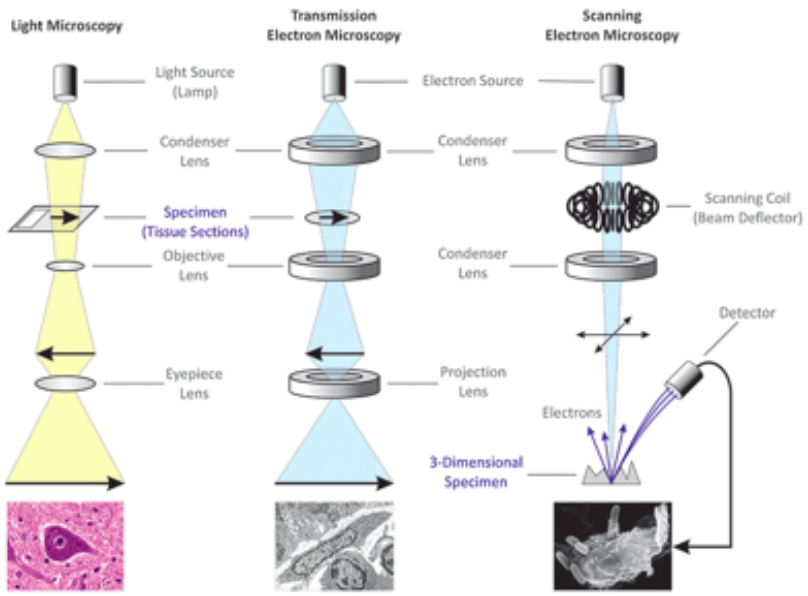

Figure 2.2.2 Illustration of light microscopy (a), transmission electron microscopy (b) and scanning electron microscopy (c) measuring principle [39]

image and therefore quick availability of information regarding the for particles; however, to employ these developments, many images must be captured during the analysis. The development of charge-coupled device (CCD) camera-based methods has made possible the rapid sizing of particles as well as a determination of their shape features.

2.2.2 Dynamic light scaterring

Implementation of light - material interaction properties are not limited to images generation, but also correlate with other properties of the particles. One of the well-known events that occur in particle suspensions is Brownian motion which is the random thermal-initiated fluctuations of a particle position in a fluid. The Brownian motion causes the relocation of particles (also referred to as a walk), followed by more fluctuations of particles in the fluid [41]. An illustration of a typical measuring setup can be seen in Figure 2.2.3.

Such motion of particles depends on their size, temperature, and solvent viscosity [42]. Dynamic light scattering (DLS), also known as photon correlation spectroscopy or quasi-elastic light scattering, is a technique that measures the Brownian motion of particles in solution by recording intensity fluctuations of laser light scattering. When the movement of particles over time is monitored, information on the size of particles

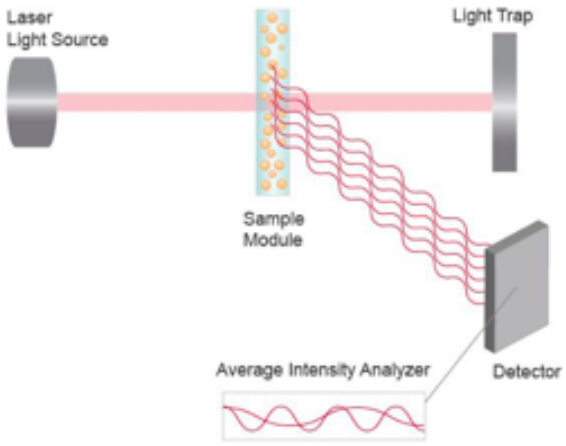

Figure 2.2.3 Dynamic Light Scattering (DLS) diagram [46]

can be estimated, as large particles diffuse slowly. The relation between the speed of the movement of the particles (D) in the medium of known temperature (T) and viscosity (η) and the hydrodynamic radius (R_H) is given by the following Stokes-Einstein equation [43]:

$$D = \frac{k_b T}{6\pi\eta R_H} \tag{2.2.1}$$

The Stokes-Einstein equation is applicable with assumption to no other forces aside from Brownian motion that affect the movement of the particles in the system. Increase of the particle size, which naturally leads to the sedimentation occurrence, disrupts random movement pattern, therefore the upper size limit of the DLS is generally assigned in respect to this factor. Since fine particles do not scatter a great amount of light, it could lead to an insufficient measurement signal. The maintenance of high signal-to-noise ratio defines lower size limit [44]. The particle size in the equation considers particle size as the hydrodynamic radius, which is defined as the radius of the equivalent sphere that diffuses at the same rate as the particle studied. While this parameter doesn't relate to the shape of the particle, however, there are theoretical developments available that allow deriving the axial ratio for simple, ellipsoidal-like particle [45].

Signal interpretation is often carried out using a correlator which processes incoming signal data in real-time. The measured autocorrelation function indicates the intensity-weighted sum of the decays caused by each particle in the system, determining the distribution of sizes in the measured sample [47]. The intensity-weighted distribution can be converted to volume-weighted distribution that represents the relative proportion of

multiple sizes in a particular sample based on their volume or size, by taking advantage of the Mie theory [48]. The light scattering theories, particularly Mie theory, are a fundamental part of this project and will be thoroughly described in the following Chapter 3.

For the successful performance of DLS measurements, several conditions should be satisfied. First of all, the concentration of the material used in the analysis has natural limitations due to the methodology of the DLS technique. The lowest possible concentration depends first of all on the quality of the scattered light intensity as the samples with low solids content being too dilute for general DLS measurements setup. The measurement detects the scattering from several particles as they diffuse, but if the concentration is so low that the number of particles in the detection volume becomes sensitive to particles migrating in and out of the detection volume, then the detected scattering will vary due to the number of particles as well as their diffusive nature. [49]. The highest concentration is dictated by the assumption that the light is scattered once before hitting the detector, not allowing the analysis of the concentrated sample. Another consideration of the Brownian motion-based methodology is the elimination of other forces that might affect particles movement. For example, measurements of large particles or suspensions under mixing would be contaminated with gravity and centrifugal forces, respectively.

The estimation of particle size distribution from Brownian motion is an example of an ill-posed problem due to the possibility of multiple solutions and high variability of the estimated results with the presence of measurement noise [50]. Several algorithms are available for estimation of the PSD from the DLS signal, [51–53], showing a high standard performance of straightforward single-peaked relatively monodisperse distributions of a homogeneous system, yet struggle to deliver reliable results from complex materials analysis[54]. Increase of the distribution width results in the presence of the particles of larger size, which tends to predominate the DLS signal, affecting the autocorrelation function [50].

The search for a more reliable source of information about particles population has lead to the developments that replaced the detector with a camera, hence utilising the leverage of imaging-based method and Brownian motion method in tandem. Nanoparticle tracking analysis (NTA) introduced in 2006, is a system for sizing particles in size range up to a micron. This technique combines laser light scattering microscopy with a CCD camera, which enables the visualisation and recording of particles moving in a solution.

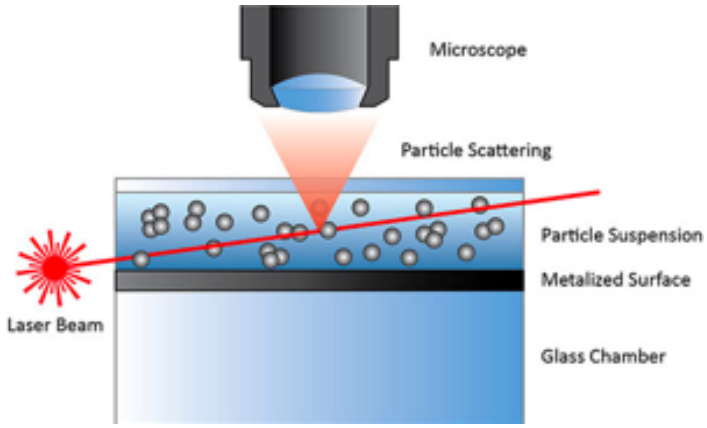

Figure 2.2.4 Nanoparticle tracking analysis (NTA) diagram [55]

The NTA software identifies and tracks the Brownian motion of the individual particles and inverts the dynamic movement into the hydrodynamic radius, as the DLS technique described above. Information from the camera tracking the exact number of the scatterers in the provided samples, which then can be used to derive a number-weighted particle size distribution and relative concentration of the sample. Due to track of the individual particles, this analysis is not biased by the presence of large particles and agglomerates, compared to DLS [56]. Similarly to DLS, the principles and current design requirements of NTA do not permit the implementation of the technique for the process for monitoring purposes.

2.2.3 Laser diffraction

It can be concluded from the previous section that relying on Brownian motion constrains the scope of the method to certain concentration range and most importantly, to motionless suspensions. The limitations do not affect the characteristics of the method performance, however, may be considered as a difficulty while implementing PAT into the manufacturing. A general overview of the possible scenarios of light-particle interaction outcome can be seen in Figure 2.2.5. Deviation from dynamic light scattering towards other scattered light properties has to lead to the exploration of possibilities of static light scattering (SLS). Laser diffraction (LD) is a common version of SLS and also grounds on the alliance between particle size and the laser beam. However, it employs the angle and intensity of scattered light rather than Brownian motion information.

Figure 2.2.5 Illustration of light-particle interaction events

A typical LD setup is presented in Figure 2.2.6. During the analysis of particles suspended in medium, the dispersed particles are radiated by the monochromatic beam of light, producing the light re-radiated opposite to the light source. The distribution of the re-radiated light is forming a specific rings-shaped image, known as the Airy pattern. The main idea of the method orbits the fact that the light is diffracted at different angles, depending on the particle size, resulting in different Airy patterns. Light scatters more intensely and at smaller angles for large particles and this property was used by a number of analytical methods to retract particle size information. Two different theories can be used for the analysis of laser diffraction raw data, namely Fraunhofer and Mie. Unlike dynamic light scattering methodology, light diffraction behaviour can be fully described by these analytical solutions of these theories. The analysis results in the estimation of the percentage of particles in a certain size class, forming a particle size distribution. These methods are conditional as the quality of their performance depends on parameters at which the light has been collected. The application of the laser diffraction method is generally considered for analysis of highly diluted samples to avoid errors from multiple scattering, which occurs when the radiation undergoes more than one scattering event before reaching the detectors. A valid diffraction pattern typically requires the particulate concentration in about 0.001 - 1% v/v range. The analysis inverts the diffraction pattern, typically using the Fraunhofer theory, and typically results in a volume-weighted PSD [58, 59, 40]. For analysis of particle shape, a method for determining shape information by sensing the cross-correlation in the azimuthal diffraction pattern over short periods has been proposed by Heffelset *et al.* [60]. It uses a wedge-type detector in the measurement

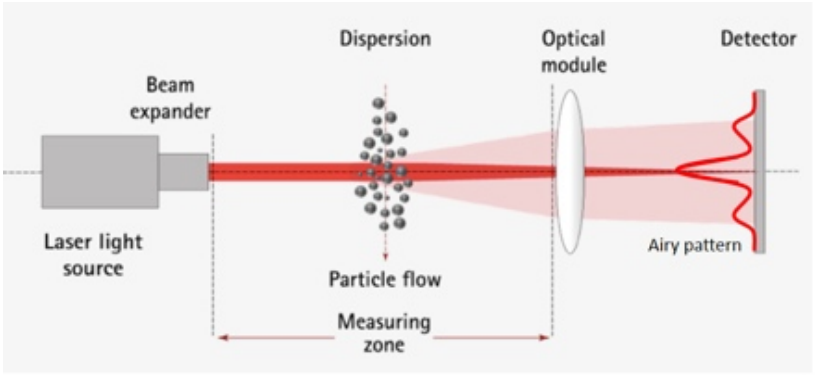

Figure 2.2.6 Laser diffraction diagram [57]

system and by correlating the signals over the azimuthal angle to estimate particle shape [61].

Laser diffraction provides a measurement averaged over time, hence can be applied to stirred suspensions, increasing the possibility to be applied in-line. Nevertheless, there is a number of factors that are constraining this method from this. First of all, only the scattered light that reaches the detector elements can be interpreted for physical information about particles, therefore with the wrong choice or positioning of the lens, scattered light at large or small angles may be lost. Apart from that, the concentration limitation, named above, should be treated with great caution as if the concentration exceeding the limit, it starts interfering with methodology limitations. Lastly, like many other particle characterisation methods, one of the biggest challenges for laser diffraction methods is to obtain a representative sample out of an analysed product.

2.2.4 Optical spectroscopy

Monochromatic bean implies that all of the light produced by the light source is of a single wavelength, such as a laser. Apart from being characterised by a single wavelength, the major difference between laser light and light generated by sources like white light is that laser is directional and coherent. When a monochromatic beam of light encounters the suspension of particles, the light begins interacting with particles within the solution, causing various measurable changes to the pre-existing equilibrium. The exact light interaction event depends on the multiple parameters, however, the major factors would be the wavelength of the incident light and the optical properties of the material

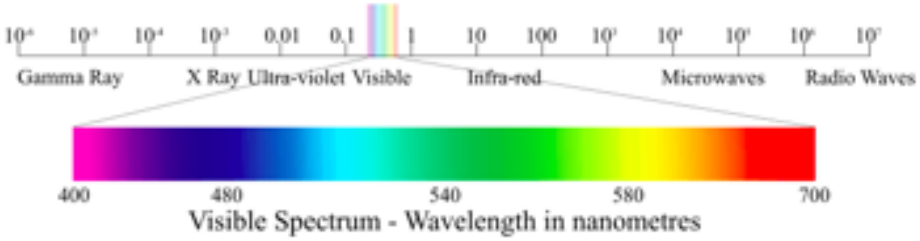

Figure 2.2.7 Electromagnetic spectrum [63]

[62]. Expanding the measurements with a number of wavelengths allows measuring wavelength-dependent properties of light-particle interaction.

The electromagnetic spectrum consists of a wide wavelength range, presented in Figure 2.2.7. There are many spectroscopic techniques available, covering the electromagnetic spectrum and widely applied in the pharmaceutical industry, from X-ray to infrared (IR). The spectrum gives valuable information about the chemical structure and the intensity is related to the concentration and physical properties of the particles. The analytical information then can be measured, such as transmittance, absorbance or reflectance of energy. One of the widely applied ranges in the process monitor and analytical science, in general, are ultraviolet-visible (UV-vis) and near-infrared (NIR) spectroscopy, which for convenience will be referred hereafter as UV-vis-NIR spectroscopy based on the wavelength those techniques provide.

The typical spectroscopy instrument operates by shining a beam of light on a sample and measuring the intensity of light reaching a detector in a range of wavelength. Generally, the light of a certain wavelength and energy is illuminated on the sample, where, depending on the properties of the material, a fraction of the incident light is absorbed. At a particular wavelength or number of them, there may be the absorption of that radiation which specific to analysed material and may not occur at neighbouring wavelength. Absorption of radiation may be recorded in a reflection mode also, resulting in the spectrum that represents the amount of light absorbed and scattered by particles as a function of wavelength.

Interaction of the light with particles suspended in a solution is generally described by two major events: absorption and scattering. Absorption of light indicated the process of capturing a photon's energy and following transformation of it into internal energy of the particle. The rest of the light that interacts with the suspension is diverged or scattered. Interaction of light with a particle can be classified into four different types: specular

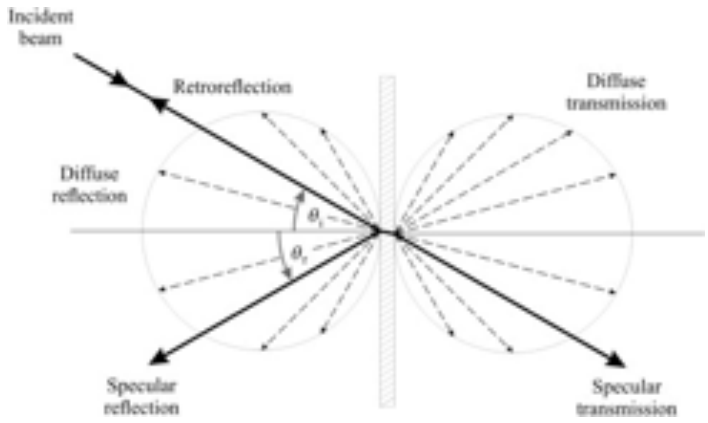

Figure 2.2.8 Diffuse and specular reflectance and transmittance [64]

reflection, diffuse reflection, specular transmittance and diffuse transmittance (Figure 2.2.8). The term "specular" usually associated with reflection from smooth, polished surfaces or with the light passing through the sample with the low refractive index. The term "diffuse" is associated with the reflection from rough surfaces or after undergoing multidirectional scattering. The way of setup and geometry to collect diffusely scattered light defines the type of measurement. When incident radiation passes through a turbid material, some of the light will scatter into forwarding directions. This fraction of scattered light is referred to as diffuse transmittance. The fraction of light that is scattered into the direction opposite to incident light defined as diffuse reflectance.

The distribution of light intensity between different light-particle interaction events can be theoretically described by different methods. They vary from methodologies that simplify light-matter behaviour to single or no scattering, like Beer-Lambert law (BLL) [65] to complex development for multiple scatterings, like radiative transfer theory (RTT) [66]. Either of them relates the measured spectroscopic observable to optical properties, widely known and absorption and scattering coefficients in the unit of inverted length. Generally characterised by Mie theory, these parameters mostly employed under single scattering event consideration. They are combining multiple parameters that affect light scattering behaviour. Bulk optical properties can be obtained, for example, from turbid materials via frequency-domain photon migration measurements [67–69], or from diffuse reflectance and transmittance measurement from integrating-sphere based measurements [70] and double-integrating sphere setup [71]. The details regarding the exact correlation between the parameters of interest and bulk optical properties are described in Chapter 3.

The application of spectroscopy as a PAT tool range in difficulty from simple tasks, such as determining moisture content to broad and complex challenges, such as full characterization of hydrocarbon composition and properties in refinery process streams [72]. Effect of various parameters and their combination on spectroscopy and the potential of analytically invert it was previously studied on a number of materials and types of spectroscopy, especially metal nanoparticles. Goh *et al.* investigated the effect of particle size on the UV absorption of zinc oxide nanoparticles [73]. As was noted by [74], some researchers like Prathna *et al.* [75], Talu *et al.* [76] predicted the particle size from UV-vis spectra using Mie theory and investigated the mechanism of nanoparticles formation during the synthesis process. Similar research aiming to estimate particle size was conducted on diffuse reflectance signal [77]. Particle size estimation was also considered in the form of size distribution and was investigated on diffuse reflectance for metal nanoparticles [78–80]. These studies were carried out by analytical inversion of spectra in UV-vis-NIR range, to provide with particle size, its distribution and solids content for non-turbid samples.

However, analytical inversion is not the only way to study the relationship between the spectral signal and the needed parameters. One of the approaches to undertake is to apply chemometric analysis on spectra signal to estimate parameters of interest. For example, Rosse *et al.* [81] developed a multivariate regression model for determining the mineral composition of soil using diffuse reflectance spectroscopy (DRS). In the pharmaceutical industry application, the approach was also employed for parameters of interest estimation, like for particle size estimation of lactose monohydrate [82] or size and shape of chitosan nanoparticles [83]. The application of the chemometrics of NIR spectra signal in the context of process monitor of particle size was considered for processes like wet granulation [84] or precipitated silica reaction [85].

The multivariate analysis has a number of beneficial properties, in comparison with spectra theories. In order to develop a multivariate regression model, the pre-knowledge of material parameters, like the refractive index is not needed; besides, the theories are generally based on a number of approximations that complicate the solution and applicability of them to non-homogeneous systems. However, implementation of chemometric-based models requires calibration and validation of the developed models [82, 83]. Hence, to develop a robust method for inversion of parameters of interest from the spectroscopy signal, the research should focus on the determination of the preferable type of spectroscopy

measurements and thorough understanding of limitations arising from the analytical solutions to the spectra in order to use one.

2.2.5 DEVELOPMENTS FOR EXISTING TECHNIQUES

Naturally, the concentration limitation has lead many researchers towards finding a possible solution. The most straightforward approach is the optimisation of the existing techniques to improve the quality of particles properties estimation. Examples of the laser-based standard techniques modifications are presented below.

DYNAMIC LIGHT SCATTERING For a 90^0 detection angle DLS instrument, in order to perform measurements with minimum contamination of such by multiple scattering, the concentration of solution must be low. The required concentration level can be achieved by dilution of the analyte sample as many times as needed to mitigate multiple scattering events. One of simplest optical configuration that allows measurements of samples at higher concentration is backscatter detection [86]. The utilisation of larger angle for diluted sample to increase the analysed volume and non-invasive backscatter (NIBS) system to collect a large portion of the reflected light for concentrated systems allow maintaining the concentration limitation boundaries wide enough for many materials [87]. When detected at a large angle, laser beam propagates through a certain fraction of the sample which results in the scattered light passing through a shorter path length of the sample. As a consequence, for such setup, multiple scattering is reduced allowing measurements to be taken for samples of much higher concentrations [88].

Dynamic light scattering technique can also be implemented in a cross-correlation design, which allows the suppression of the multiple scattering effects. For instance, Segr$\tilde{e}$ and Van Megen introduced the design and operation methodology of two colour DLS technique (available commercially as ALV -GmbH, Langen, Germany) [89]. The instrument utilises the cross-correlating scattered light using two lasers with 488 and 514.5 nm wavelength. In this light collection geometry, only singly scattered light contributes to the time-dependent part of the measured intensity cross-correlation function, thus allowing straightforward interpretation of the data. Introduction of a second laser beam has also been developed in a different design. The original two colours DLS projected the incident and scattered beams all lie in the same plane. Another approach, a three-dimensional dynamic light scattering uses the third dimension emitting the light beams

onto the sample from positions different from the average scattering plane, and detectors at scattering angle would be similarly placed at the corresponding positions [90].

Despite providing the possibility of measuring scattered light in concentrated suspensions, the above-mentioned DLS methods involve optical set-ups that are complex to such degree that does not allow in-line measurements implementation. As In contrast, fibre-optic-quasi-elastic light scattering (FOQELS) [91] or fibre optic dynamic light scattering (FODLS) [92] methods use an immersion probe with a simple and robust optical setup and are therefore suited for in-line applications. Both techniques are fibre-coupled and collect the backscattered light for particle size determination. With small penetration depths, concentrated dispersion with high solid content up to 40 wt% can be measured [91, 93]. Nevertheless, the low penetration depth of such techniques and the need in the non-disturbed environment is limiting the applications of DLS.

LASER DIFFRACTION Unlike dynamic light scattering, other methods like laser diffraction appear to deliver most of the particle size distribution without constrains to undisturbed media. Since low concentration is needed to produce a clear Airy pattern, the methodology is expected to be limited to a specific concentration. In order to apply laser diffraction to turbid samples, Hamidi and Swithenbank [94] resolved the problem of multiple scattering using the beam extinction intensity. The latter is generally defined as the fraction of light that due to interaction with body or particle, has been scattered out of the beam path; this event can be accounted for via set of correction equations. Felton *et al.* [95] determined the extinction level to be greater than 50% for multiple scattering effects to become significant. It should be indicated, that the conventional laser diffraction measurements are conducted at less than 50% extinctions, meaning that the majority of commercial instruments do not consider the impact of multiple scattering.

One of the ways to account of multiple scattering in laser diffraction is by considering orders for the discrete annular detectors of the sizing instrument [96]. In this assumption, a single scattering event equates to order one. Consequently, multiple scattering orders are defined by the number of single scattering events undergone by a photon before it reaches the detectors. Holve and Harvill have also worked on solving the multiple scattering problem using this theory, developing a successful correction of the scattering data down to light transmissions of 5% [97]. The problem of multiple scattering continues to be a concern to researchers who are interested in measuring highly concentrated medium and expanding measured properties of the particles.

2.3 PROCESS SPECTROSCOPY TECHNIQUES

Section 2.2 highlighted the method that is widely applied for the determination of particles physical and/or chemical properties. The limiting factors of further development of the standard particle characterisation methods may be summarised down to a few major conclusions.

Mainly, the fundamental principles of these techniques are restricted to dilute suspensions or certain size range. Furthermore, some of them require a specific design for taking measurements and/or extensive samples preparations or calibrations for the specially developed models. Constraining the analysis to such limits prevents the standard techniques from the in-line application. This section will review the key aspects of the parameters of interest limitations in more details, followed by the developments that were introduced on standard techniques to overcome these limitations as well as a brief overview of the developed techniques.

2.3.1 LIMITING FACTORS FOR IN-LINE APPLICATION

As can be concluded from the overview presented above, the majority of the process spectroscopy techniques are based on simplistic assumptions that incident light from the source is scattered by each particle independently. In other words, the light has been scattered only once and this scattered light is detected. This assumption is generally described as single scattering. In order to ensure independent scattering, the typical mutual distances need to be greater than 20 times the radii of the particles [98]. Consequently, low sample concentration is necessary to ensure independent scattering.

The occurrence of multiple scattering is a common attribute of a concentrated solution, however, there will always be some small fraction of multiple-scattered light in most of the suspensions since the single scattering is difficult to achieve in the real-life suspensions analysis. Re-radiation of the scattered light to another particle breaks the assumptions that are made at the background theories and therefore affects the accuracy of the estimated physical properties of the suspensions. Hence, accounting on re-radiation of the scattered light to neighbour particles should be considered by background theories of signal processing for reliable results.

Lastly, good practice requires representative sampling. When sampling and dilution are performed, the particle size or particle size distribution might be adversely influenced.

There is a number of standardised operations available in order to ensure the best result after necessary sampling [99, 100]. However, the modernisation of the analysis that is promoted by PAT agenda is aiming to measure materials in their original state, by non-destructive method, without the need for sampling or diluting them. Considering the standard methodologies overview presented above, most promising techniques that are accordant to PAT agenda are light scattering based. They are non-destructive in their core principle, available in the monochromatic or polychromatic arrangement and have needed flexibility in setup design.

Tackling the multiple scattering influence on methodologies performance would be critical for applying the method as a PAT tool. This project focuses on theoretical considerations regarding the multiple scattering region for a PAT spectroscopy technique. The complexity of this research question appears in the form of nonlinear behaviour of concentration increment effect and involvement of other factors. Its main challenge can be summarised as the study of the parameters of interest effect in the multiple scattering region and distinguishing the associated limitations.

The potential solutions include measurements, design improvement and evolution of existing theoretical assumptions in order to ensure the possibility of embedded analysis of turbid materials. There are multiple studies that propose alternative measurement setups, which will be reviewed in the following section.

2.3.2 Implementation of existing techniques for process monitoring via design changes

Expanding the concentration limitation set by the originally developed methodologies is a vital step in the development of analytical techniques. The overview of the presented solutions is demonstrating the variability of possible approaches. However, the popular measurement designs intend the sample collection and are generally suitable for laboratory analysis as bench-top units. Driven by the constant demand from the market to provide with a robust technique capable of monitoring the multiple material parameters, some instruments have been designed specifically for on/at/in-line measurements in drugs production processes including suspensions. The following sections focus on the few most popular designs and their background methods, concluding the specific choice of methodology that will be considered further in this research.

Laser-based techniques

Imaging techniques For most of the methods that lie under microscopy definition, the main obstacles for any further evolution are concerning the need for sampling and certain concentration to provide with a reliable representation of sample population during the process [38]. One of the most advanced developments in the area of image-based analysis allows collecting 2D images of the particulates during the process. Namely, Particle Vision and Measurement (PVM) and Pixact Crystallisation monitoring (PCM) techniques were developed in a probe-based apparatus to allow implementation into the process. The general measurements setup consists of an immersive probe that utilises video-based microscope to record the optical response of particles, generating the 2D images of the particles as viewed from the probe window. The information regarding particle size, distribution and morphology can then be extracted indirectly by image processing algorithms [101]. However, the nature of the particle size estimation, similar to standard microscopy, indicates the relatively high limit of the minimum particle size used as well as suggests that the quality of the images directly affect the quality of the estimated physical properties.

Dynamic light scattering Applying DLS measurements during the process is challenging, since particles are often moved by the process stream or by agitation. Accurate particle sizing using DLS necessitates resting particles in the sample. As one of the ways to resolve this limitation, a probe head design is introduced, which enables at-line monitoring of particle sizes in undiluted stirred fluids using dynamic light scattering [102]. The novel probe head separates a small sample volume of 0.65 ml from the bulk liquid utilizing an impeller. In this sample volume, particle sizing is performed using a commercially available fibre-optical backscatter probe. Despite the innovative approach of DLS measurements application, such design does not eliminate the sampling procedure from the analysis but automate it.

Laser diffraction An investigation into the capabilities of at- and in-line laser diffraction analysis for improved process monitoring and control has been produced by Heng *et al.* [103]. The study utilised a commercial system (Incitec, Malvern) to analyse highly concentrated solutions. However, as the method is based on Mie theory and applicable to transmittance as low as 5%, according to the manufacturer, it could be assumed that the

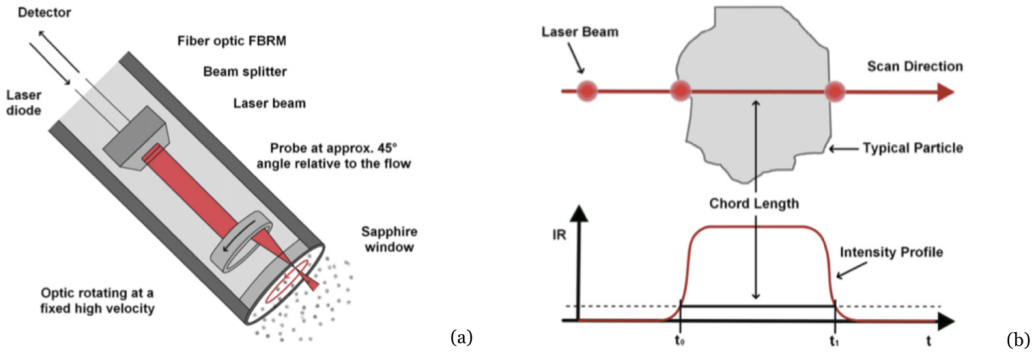

Figure 2.3.1 Focused beam reflectance measurement probe diagram: (a) design of the technique, (b) measuring principle of a particle chord length using the FBRM technique [106]

methodology is similar to what was described by Hirleman [96]. The tandem of such design and methodology provides with possibility of measuring particles properties during various processes while avoiding the classical concentration limitations. The design of the measurement set up, though, is quite unique and hence costly compared to alternative offline techniques.

Several designs and design adjustments for in-situ laser diffraction instruments were designed in past years [104, 105]. These are fast, free from sample collection methods that were successfully used for characterisation of the size distribution of material with a low concentration of the particles. Hence, the availability of in-situ measurements has mitigated uncertainties introduced by sample handling, however, its application range falls in standard concentration requirements for lasers diffraction.

CHORD LENGTH DISTRIBUTION One of the widely used alternative approaches is based on the measurement of the chord length distribution (CLD). The core of the underlying measurement is based on the estimation of measurement of the distance between two opposite ages of the particle, a chord. Despite being previously used as an offline method, the wide implementation of the methodology in the various industries has started with the development of the focused laser beam measurements (FBRM) system. It is in principle based on time-resolved measurement of scattering intensity when the light is passing through the particle in the studied sample. The probe-based method works on the principle of light backscattering. A laser is emitted from a source inside the probe, whereas the source is rotated around the probe axis such that the laser traces a cylindrical surface

at high speed (Figure 2.3.1). When the revolving laser encounters, it gets returned to be collected by a detector, placed in the probe tip. Each of these reflections is treated as one count of particle detection, and the chord length is calculated by multiplication of the duration of reflection event by the known scan speed of the laser. Over the course of the period of time, reflections that correspond to multiple particles are recorded, and the results are an exhibit by the number of counts in different particle chord length, hence forming a chord length distribution. The applicability for such technique is broad; it has been studied among different materials used in the pharmaceutical industry, and it is especially popular in the monitoring of crystallisation processes [107, 108].

This measurement can be indirectly related to various parameters of the system, and a lot of work has been done to extract parameters like particle size distribution, encrypted in the measured data. The CLD measurements, despite being related to the particle size distribution, does not exhibit the direct linkage to the latter and needs to be inverted. Usual approaches include gathering standardised datasets, like Li *et al.* empirical methodology, based on a transformation matrix of CLD measurements for pre-known particle sizes [109]. Gathering standardised dataset is time-consuming, cumbersome and simply is not always possible [110]. Besides, the CLD result obtained by FBRM is complex, depending not only on the PSD but also on particle optical properties and shape [111].

One of the major disadvantages of the chord length measurements is the tendency of the probe to become fouled with small particles. Total counts of chord lengths have been found to change linearly and then nonlinearly with solids concentration as solids concentration varies from low to high. This is due to a larger particle being more likely to be detected than a smaller one and therefore generates more counts [112]. Increment of concentration of particles of small size generates the signal based on inserted of the measured data. Along with the indirect nature of the PSD information, these observations raise the question regarding the availability of advanced and less uncertain measurement principle.

Reflectance and transmittance UV-vis-NIR spectroscopy

Implementation of theories like Mie for connection of particle properties with the scattered light is not limited to analysis of the directionality of the scattered light. In fact, the intensity of the light averaged across scattered directions contains the equivalent degree of information about particle size and can be express through the optical properties. This

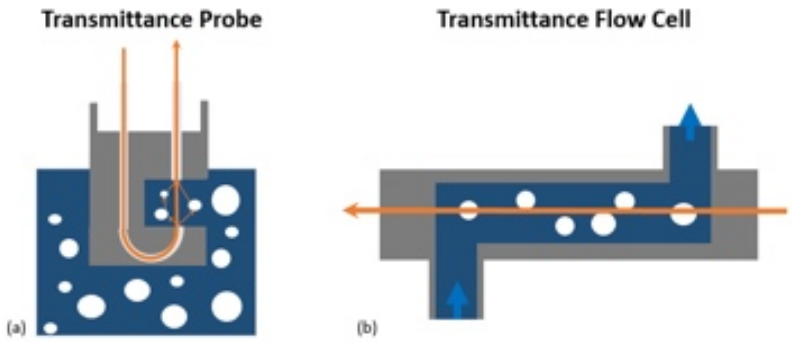

Figure 2.3.2 Schematic of basic inline transmission measurement design: (a) transmittance probe, (b) transmittance flow cell [113]

is the underlying concept used in UV-vis-NIR spectroscopic-based methodology. The short integration time in the millisecond-range, high sensitivity results and relatively low cost makes the multiwavelength spectroscopy approach a compelling tool for process monitor application. The outstanding properties of the process multiwavelength spectroscopy over other reviewed techniques have been already briefly covered when the conventional spectroscopy of materials was discussed. Ability to provide with spectra across a wide range of wavelength at a relatively low cost of the components, flexibility in measuring configurations and non-destructive nature of the analysis has naturally led to design modifications to provide with process monitoring equipment. Different types of optic instrument are available on the market; they can be generally classified by the type of measurement collected. Below presented two main classifications of the diffuse spectroscopy setups and the required background theories.

TRANSMITTANCE MEASUREMENTS The goal to implement the spectroscopy instrument into the process has lead to a few prominent design adjustments, most popular out of which being flow cells and transmission insertion probe [113]. Flow cells may be plumbed directly into a process, but are more often used for on-line measurement where the by-pass loop is used to flow some of the samples through the device and return to the main stream. The setup typically exhibits the sample gap, that may vary between setups from 1 mm up to several centimetres, in between two opposing lenses, forming the flow path of the Z-like configuration, as shown in Figure 2.3.2(b).

Alternatively, to plumb cell design, transmittance measurements can be collected via a probe-based instrument, inserted in the particulate suspension. (Figure 2.3.2(a)). These

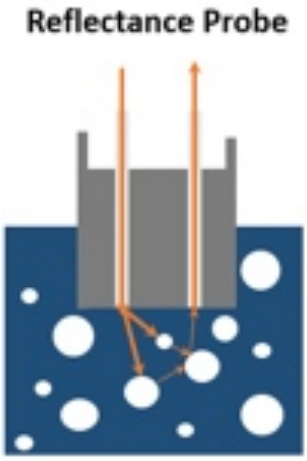

Figure 2.3.3 Schematic of basic inline reflectance measurement design [113]

probes may be inserted through a port in a pipe or vessel. For the analysis, the probe tip must be immersed in the suspension. Transmittance probe work by sending a beam of light into a sample gap where it is collected by the receiving fibre on the opposite end of the gap. [113].

Collection of the transmitted light remains the most applied configuration up today. It is generally justified by the straightforward Beer-Lambert law. For transmittance measurement, however, the presence of the receiver of the light on the opposite side of the light source leading to discussion regarding the feasibility of the usage of such instrument in highly turbid systems [114]. Depending on the size of the particles, there is a point when the concentration reaches such value when the intensity of the transmitted signal would decrease with concentration od solids increase. This constraint also typically found in the classic, bench-top transmission spectroscopy.

REFLECTANCE MEASUREMENTS Diffuse reflectance spectroscopy is a non-invasive optical technique that is widely used for biomedical application, and one of the principal methods used to interrogate solid samples, especially powders in pharmaceutical industry [115]. Perhaps one of the greatest benefits of diffuse reflectance, which contributed to its rising popularity is that it is ideally amenable to automation, requires less complex design arrangements and is applied to the semi-infinite turbid medium. [116].

To explain the latter, it should be stated that the quality of the estimation of material properties highly depends not only on methodology but also on the quality of the sig-

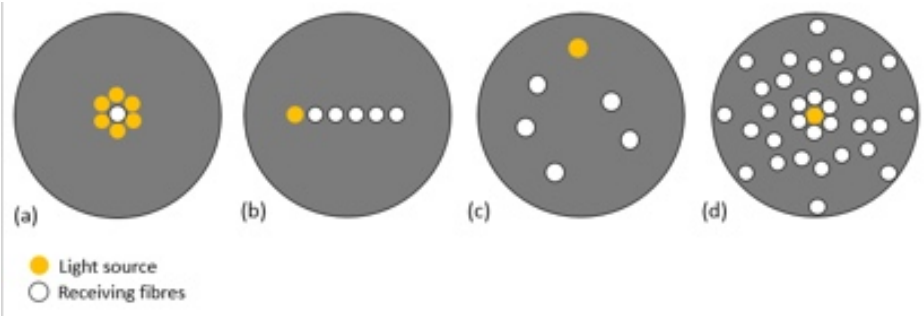

Figure 2.3.4 Selected examples of spatially resolved diffuse reflectance probe fibres configurations: [4, 117, 117, 118]

nal. Analysis of the concentrated particulate suspensions makes diffuse transmittance measurements more complicated than diffuse reflectance measurements due to the low transmitted intensity of the signal received, which can lead to poor signal to noise ratio. Despite the possibilities to have an analytical solution of either type of spectra, implementation of diffuse reflectance spectroscopy can be more beneficial to accommodate a wide concentration range. Hence, diffuse reflectance measurements on turbid samples are of practical interest to this research.

There are some variations in the actual design between different suppliers, and the overall operating principle can be seen in Figure 2.3.3. Each of the probes consists of the incident and receiving fibre bundle, to deliver illumination and direct the collected light to a spectrometer. There are multiple variations between fibres layout; the general setup incorporates several illumination fibres in a ring around a central detection fibre (Figure 2.3.4 (a)).

For material analysis, the probe is immersed in the sample of the particulate suspension, however, additional protection layer of glass/quartz may be incorporated as well because it is not catalytically inert concerning the reaction mixture or does not withstand its corrosive influence. In that case, diffuse reflectance must be ascertained that the shielding does not falsify the signal, e.g. by specular reflection on the glass [113]. However, once the suitable way of probe protection is selected, it is generally easy to implement probe-based tool into desired processes, making diffuse reflectance probe-based techniques attractive for various areas and applications.

There are variations in the design, which allow different types of measurements collection. For example, the incident fibre may be placed to illuminate a light at an angle different to normal to the probe tip surface [119]. The receiving fibres can be placed at dif-

ferent distances to the source: the arrangement is known as spatially resolved [117, 118, 4], or even combine a few features in one instrument to regulate the path length [120].

With the source-to-receiver (S-R) separation, the collection of diffuse reflectance measurement at several distances allows differentiating measurements which travelled shorter distances through a sample as well as the light that propagated through the sample for longer distances. In the case of multilayer thick samples, the spectral signal collected by fibre close to the light source would obtain the information gathered from the layer closest to the surface. Consequently, the light collected further from the light source contains the cumulative information of multiple layers of the material, including those that are lying at larger depth. This property was broadly used in the biomedical applications of diffuse reflectance. The spatially resolved diffuse reflectance has been a subject of many studies as a diagnostic tool for medical applications, alongside with time-resolved and frequency domain techniques [121–124]. Spatially resolved spectroscopy among those named is one of the most affordable and flexible, therefore the concept then gradually transitioned into food and agricultural fields, where it was applied for optical properties studies to determine the ripeness stages studies [125], meat freshness [126], sugar content prediction in vegetables [127] and many more [128].

The same principle can be applied to the analysis of the other turbid materials to retrieve properties like particle size, shape and concentration. At the moment, there is a limited number of studies available that study the effect of physical properties of the particles, like particle size, distribution and morphology on such spectra, either via multivariate analysis or analytical solutions. The primary examples can be summarised from work of Naglič *et al.* [129] for determination of bulk optical properties from SRDR via inverse Monte Carlo and Scheibelhofer *et al.* [130] via various methods applications for powders analysis. Limited research has been reported because spatially resolved techniques are still not well developed and not widely available for implementation as PAT in the pharmaceutical sector. Spatially and angularly resolved diffuse reflectance measurement (SAR-DRM) tool is a novel technique that was already applied on suspended polystyrene particles analysis by Chen *et al.* [120] via partial least squares (PLS) model application on spectra. This research opens up a possibility to expand their methodology for SAR-DRM analysis from data-driven approach onto the calibration-free method. With the right choice of the background theories, particle physical and chemical properties

can be estimated without the need in the calibration dataset, resulting in a more robust method.

2.4 CONCLUSIONS

The review in the chapter above aimed to distinguish the challenges and limitations of the current particle sizing techniques with respect to process analytical technology agenda. To achieve this aim, the particle size as a parameter of measurement was discussed, standard methodologies and the common examples of the measurement designs were presented. A large number of techniques require sampling, slowing down the analysis process and waisting the material. Light-scattering techniques, on the other hand, are of non-destructive nature and have the potential to be implemented directly into the process with instrument design adjustments. However, the background theories pose additional limitations as some of the methodologies are strictly limited to certain conditions, like still media or low concentration of particles.

Diffuse reflectance spectroscopy is one of the most promising approaches for in-line analysis of turbid media because of its measurement design which benefits from concentrated materials, unlike transmittance-based measurements. One of the most rapidly developing type of diffuse reflectance is spatially resolved diffuse reflectance, however, there are not many studies reported the physical properties effect on this type of spectroscopy. It offers the measurements from deeper layers of the samples, which is expected to assist the analysis of concentrated materials. Due to the complexity of the diffuse reflectance spectral signal, it is often analysed via multivariate data analysis techniques, which would rely heavily on the quality of the calibration dataset. This review concluded that the focus of the study will be placed on spatially resolved diffuse reflectance potential for the estimation of the parameters of interest from turbid suspensions and the development of the inversion algorithm based on available analytical solutions to SRDR spectra. Development of methodology steps, their validation and thorough investigation of the interrelation between diffuse reflectance design and parameters of interest effect of spectra are the essential steps of the project. The next Chapter 3 will focus on an overview of the theoretical background behind the methodology proposed, followed by Chapter 4 that will cover aspects of the exact methodology of the forward calculation and discuss the practicability of involving S-R distance parameter into suspensions analysis.

CHAPTER 3

THEORETICAL MODELS DESCRIPTION OF LIGHT SCATTERING BY AN OBSTACLE

Diffuse reflectance signal consists of light scattering events generated by many particles in the solution. The event of light interaction with a system of particles can be defined in three essential steps. The first step is to describe the interaction of the light by a single particle, which is assumed to be isolated and be of a defined size and shape. The second step is to explain the expansion of the solution for a single particle with a number of particles within one system. This step combines the individual contribution of each light-particle interaction event to account for the total bulk optical properties. Extension of the simplified result of the second step towards accurate, multiple scattering-based solutions is executed in the third and final step of the forward calculation. This chapter describes in details the theories for all these steps to give an insight into principles of optical properties of particles systems as well as indicates the limitations and theoretical adjustments of the measuring setups.

3.1 SCATTERING BY SINGLE PARTICLE

3.1.1 SPHERICAL OBSTACLE

Interaction of the light with a single particle has been studied for over 150 years, and since then it was almost perfected for spheroidal particle shape. Bohren and Huffman reviewed it in 1983 in details [131], with significant milestones highlighted as follows.

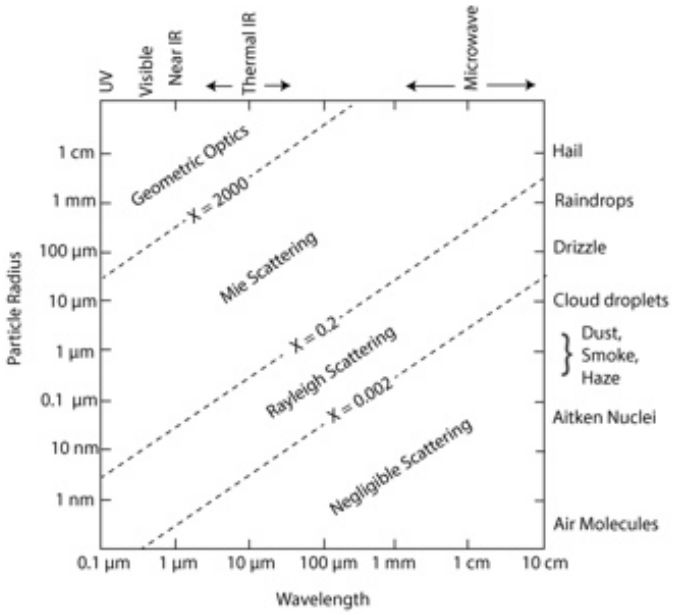

Figure 3.1.1 A diagram of scattering regime as a function of radiation wavelength and particle radius [132].

Scattering by a single homogeneous sphere became a question of study in 1869 with Tyndall's initiative [133], which were followed by two separate studies. The first is published by Lord Rayleigh [134], where he relaxed size conditions and dielectric constraints, and derived the expression for light scattering by the relatively small particle. The second piece of work was built on Rayleigh's results to waive size limitation. In 1908, the general solution of Maxwell's equations for the sphere of arbitrary size was obtained by Gustav Mie on gold nanoparticles in aqueous suspensions [135]. It is one of the most studied and widely applied solutions in the light scattering field, however, due to the necessity to incorporate the refractive index of the particle and medium, it was simplified and gained popularity as Fraunhofer theory. [136]. Hence, the interactions between particle and light are traditionally classified by two major categories or regimes: Rayleigh scattering and Mie scattering. The classification is based on the size parameter x, also known as the ratio of particle radius to the wavelength of the light in the surrounding medium, λ_m:

$$x = \frac{2\pi R}{\lambda_m} \tag{3.1.1}$$

This parameter is commonly used to identify the actual limitations of each regime. The boundaries of the regimes are illustrated in Figure 3.1.1. Depending on the wavelength used, the scattering encounters limitations of the Rayleigh regime at a size of a few nanometres. With the radius of a scatterer below that, the particle exhibits the Rayleigh scattering characteristics regardless of shape [137]. Mie scattering, on the contrary, covers larger particle size ranges which are relevant to many chemical industries. Unlike Rayleigh's approach, the theory is limited to spherical and some highly symmetrical shapes (spheroid, infinite cylinder).

As was already reviewed in Chapter 2, the theory forms the basis of many laser-based particle characterisation techniques. When the material and fundamental characteristics are unknown, the choice for optical properties computation theory is considered in favour of Fraunhofer theory, however, as was previously examined, lack of material specification in Fraunhofer results in over-reporting of scattering extinction especially for nano-sized particles [138]. Hence, in this project, Mie theory is employed for characterisation of single, spherical and homogeneous particle.

Aside from particle size, Mie scattering theory incorporates multiple parameters to describe the redistribution of the light caused by particle scattering. The theory assumes that a particle with a complex refractive index, m, is embedded in a non-absorbing medium with a refractive index n_m and illuminated by an incident plane wave at a wavelength λ. The latest represents the wavelength unaffected by surrounded medium, which is a wavelength in vacuum. To account for the medium, λ can be modified into aforementioned term $\lambda_m = \frac{\lambda}{n_m}$.

Refractive index is a dimensionless measure that describes the ration of the velocity of light when it passes through material to the velocity of light in a vacuum with indication to what part of the light is refracted (real) and attenuated (imaginary). The complex refractive index combines real part of the refractive index of the particle n_p and imaginary part ik_p. To make it relative to the ambient medium, this term should be adjusted with the real part of the refractive index of the surrounding medium n_m, which in total can be expressed as $m = \frac{n_p + ik_p}{n_m}$. This term is wavelength dependent, making the following light scattering terms dependent on wavelength also.

Once all the parameters above are defined, the changes in the electromagnetic fields of the light-particle interaction can be calculated. However, in practice, the rates at which energy from the incoming light is scattered and absorbed are of more interest than the

propagation of the electromagnetic fields after light-particle interaction. According to Bohren and Huffman [131], the extinction cross-section ($\sigma_e(x)$) is a measure of a total re-radiated light ($Q_e(x)$) that has been distributed by scatterer of a defined geometrical cross-sectional area. This measure combines scattering and absorption cross-section ($\sigma_s(x)$ and $\sigma_a(x)$ respectively) parameters into a single term yet they may be derived separately. Its mathematical expression is given by:

$$\sigma_e(x) = Q_e(x,\lambda)\pi R^2 = \frac{2}{x^2}\sum_{n=1}^{\infty}(2n+1)Re(a_n+b_n) \tag{3.1.2}$$

$$\sigma_s(x) = Q_s(x,\lambda)\pi R^2 = \frac{2}{x^2}\sum_{n=1}^{\infty}(2n+1)(|a_n|^2+|b_n|^2) \tag{3.1.3}$$

where a_n and b_n are Mie coefficients, which represent the amplitudes of the scattered field from the Bessel functions. Based on energy conservation law, the absorption cross-section, $\sigma_a(x)$, of a particle can be defined as a difference between extinction and scattering cross-sections. The detailed mathematical formulation is given in Bohren and Huffman [131].

The shape of the scattering pattern in space is expressed by phase function, $p(\theta,x)$:

$$p(\theta,x) = \frac{2\pi}{x^2(\sigma_a(x)+\sigma_s(x))}[|S_1(\theta,x)|^2+|S_2(\theta,x)|^2]; \qquad g = \int_{4\pi} p(\theta)cos\theta d\Omega \tag{3.1.4}$$

where θ is the scattering angle, $S_1(\theta,x)$ and $S_2(\theta,x)$ are known as the scattering amplitudes which correspond to the vertical and horizontal polarisation of the scattered light. The scattering amplitudes are defined in Mie theory by angular dependent functions $\tau_n(\theta)$ and $\pi_n(\theta)$, which determine the angular dependence of the electromagnetic field. These amplitudes form an essential analytical background to understanding the way light propagates after scattering. If the particle grows, the light is dominantly scattered in the forward direction $\tau_n(\theta)$ and $\pi_n(\theta)$. An illustration of this can be found in Figure 3.1.2.

A particle of the size much smaller than the wavelength scatters light equally in the forward and backward directions, whereas a larger particle exhibit distinctive forward scattering. Extensive knowledge of the angular dependence of the scattered light is necessary for techniques like laser diffraction. The predominant direction of the scattered light can also be characterised by the averaged cosine of the scattered angle or anisotropy factor (also known as asymmetry parameter), g, as expressed in Equation 3.1.4. Along with

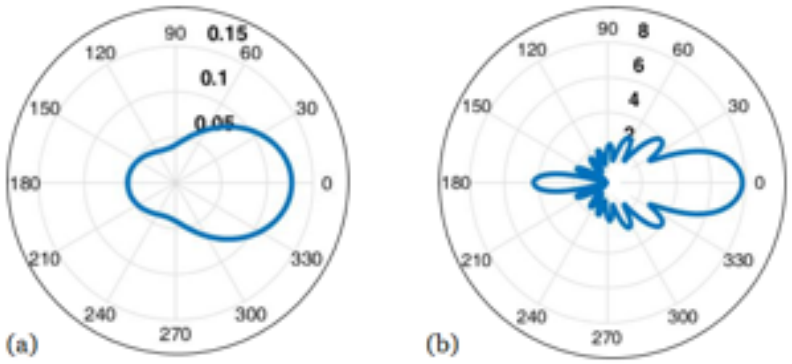

Figure 3.1.2 Angular distribution of the scattered light $p(\theta, x)$ by polystyrene particle with (a) x=0.5 and (b) x = 10

cross-section values, they are the critical parameters needed to describe the light-sphere interaction.

3.1.2 Arbitrary shaped obstacle

The biggest constraint of the Mie theory is its restriction to spherical particles, as in reality, the majority of the materials used in the pharmaceutical industry consist of non-spherical particles. Non-spherical particles scatter light in a way different from spheres, however, due to the complexity of such a scattering event, the solution is normally approximated. A rough approximation for describing light scattering and absorption by non-spherical particles is to replace the term of particle radius with the radius of the equivalent sphere, either by the surface area or volume. Chylek and Ramaswamy [139] showed that for non-spherical particles with particle size parameters x<0.6 using a sphere with the equivalent surface area yields a better approximation to the extinction cross-section of the non-spherical particle than the volume-equivalent sphere, and the opposite is found for larger particles. The work generally concludes that an approximation of non-spherical particles to equivalent sphere radius has to be taken with caution as a further increase of the particle dimensions decreases the accuracy of optical properties representation from the solution for exact shape by up to 40% [139]. As mentioned before, the Rayleigh scattering regime does not require taking particle shape into account. However, despite the possibility of describing scattering by non-spherical particle, the size limitation does not allow to apply the method to the majority of size parameters below 0.6. Thus, more advanced

methods to describe light scattering by arbitrary-shaped particle should be included in the consideration.

Electrodynamic models that expand the theory beyond Mie have been developed for particles of non-spherical shape. Analytical solutions of Maxwell's equations are available for light scattering by only a few simple shapes like spheroids and infinite cylinders. [140–143] Most of the solutions address the problem of light scattering by such particles via expanding the incident, scattered, and internal fields in vector spheroidal or cylindrical harmonics respectively, similarly to the approach taken by Mie theory for spheres. However, the spheroidal harmonics do not represent a complete set of orthogonal functions as the spherical harmonics do. Therefore, these solutions are considered complex and usually applied when the approximation to the equivalent sphere is unsatisfactory. For the method to be applied to analyse measurements from PAT tools, factors, such as computational time are important to consider.

To improve the computational efficiency and to extend the types of shapes to be calculated, a number of numerical models for arbitrarily shaped particles have been developed, like discrete dipole approximation (DDA) [144] and the T-matrix method of extended boundary condition [145]. These methods are the best evolved and the most commonly used; T-matrix is claimed to be the fastest out of the two [146]. Yurkin and Kahnert [147] presented a study where they compared both methods performance and accuracy, suggesting that T-matrix shows a higher relative error, compared to DDA.

Discrete dipole approximation describes the interaction of a molecule of the particle with the incident and re-radiation wave from the other excited molecules of the particle. The re-radiation by the molecule is coupled to the radiation of all other molecules. This concept was introduced by Langbein to calculate van der Waals attraction between molecules; hence it does not assume dipole-dipole coupling.[148] A similar method was developed later, which divides the scattering particle into spherical sub-regions placed within a lattice. Those sub-regions are small enough to be considered as radiating dipoles. The method referred above was described by Purcell and Pennypacker [149] and later reviewed by Draine and Flatau who implemented the calculation in C++ code (DDSCAT). A detailed description of the DDA can be found in [144], a summary is presented in the following paragraph.

The DDA considers the particle consist of a collection of dipoles, N, with polarisability α_j. Each of dipoles interacts with a fraction(E_j^{inc}) of the plane wave of the incident light

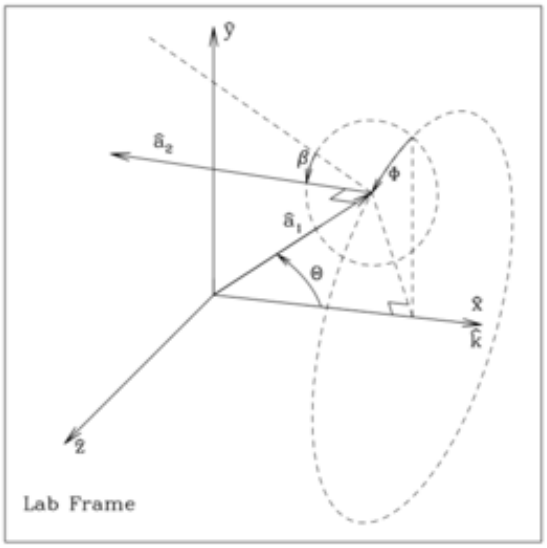

Figure 3.1.3 Definition of particle orientation used in DDSCAT calculation [144]

(E_0). As a result of interaction, the local dipole field E_j can be estimated and converted to more common terms, like scattering and absorption cross sections:

$$\sigma_s(x) = \sigma_e(x) - \sigma_a(x) = \frac{4\pi k}{|E_0|^2} \sum_{j=1}^{N} Im[(E_j^{inc}) \cdot \alpha_j E_j] - \sigma_a(x) \tag{3.1.5}$$

where

$$\sigma_a(x) = \frac{4\pi k}{|E_0|^2} \sum_{j=1}^{N} Im[(E_j \alpha_j E_j^*) - \frac{2}{3} k^3 |\alpha_j E_j^2|] \tag{3.1.6}$$

where k is a wavenumber of the incident light and defined as $k = \frac{2\pi}{\lambda}$. This approach is hardly limited to any specific shape. For convenience, the DDSCAT algorithm provides easy access to different lattice frames, which correspond to different particle shapes.

Introduction of particle shape into calculation also introduces particle orientation parameter. The rotation of the studied particle can be considered within three different planes,Θ, Φ and β, which are illustrated in Figure 3.1.3. These planes, refereed as Euler angles, are placed within the Cartesian axes, where particles are located in the origin of them. The current study uses an isotropic assumption (i.e. the particles are randomly oriented). In order to satisfy such an assumption, the optical properties shall be averaged uniformly over all orientations.

In order to successfully perform optical properties simulation using DDSCAT, there are a few limitations that should be considered. Firstly, the distance between dipoles,

d, should be very small, compare to the wavelength. Hence, there is a specific criterion, set as $|m|kd < 1$, that will abort the simulation when exceeded. Too fine dipole spacing would run against practical considerations of central processing unit (CPU) performance and standard computer memory capacities which limit the number of dipoles potentially employed. For best computational speed without affecting result accuracy, it is advised to keep N below 10^6 at the same time. Therefore, it is obvious that the DDA is not suitable for huge size parameter x, or particles of very large values complex refractive index m. Same as the Mie theory, the primary utility of the DDA is for scattering by dielectric targets with sizes comparable to the wavelength.

3.2 BULK OPTICAL PROPERTIES

Formulas above describe the optical properties for single-particle only, either of spherical or arbitrary shape. In practice, a particle system can rarely be described by the behaviour of a single particle. Hence the bulk optical properties are of more interest for study on suspensions.

The most studied system in those consisting of particles with identical chemical, optical and physical properties. If one considers a beam of light propagating in a suspension with $N_p(R)$ number of spheres per unit volume, where each of them will have a scattering cross-section, the bulk optical properties can be calculated using the defined volume fraction of the suspended solids and a surrounding medium. For the suspended solids, the number of particles per solids volume fraction can be defined as:

$$N_p(R) = \frac{\rho_m}{(\rho_m + \rho_p/C - \rho_p)\ 4/3\ \pi R^3} \tag{3.2.1}$$

where ρ_m is the density of the medium, ρ_p is the density of the particle, and C is the weight fraction of the particles. The product of the scattering and absorption cross-section and number density are called scattering and absorption coefficients, respectively. The formulae of these parameters expressed as follow:

$$\mu_s(x) = \sigma_s(x) N_p(R) \qquad\qquad \mu_a(x) = \sigma_a(x) N_p(R) \tag{3.2.2}$$

The above-mentioned parameters can be used to describe a single scattering system, i.e., the system where particles are located far enough from each other to prevent light re-radiation. An average distance that light travels between scattering events is called transport mean free path (tmfp). In other words, tmfp corresponds to the distance after which the propagation direction of an incoming wave or particle gets randomised [150]:

$$tmpf = \frac{1}{\mu_a(x) + \mu_s'(x)} \tag{3.2.3}$$

Asymmetry parameter, g, represents the average cosine of the scattered angle of a particle with specific intrinsic properties, such as size, shape as well as the refractive index. Therefore when such properties are constant for the system of particles, this parameter will remain unchanged. The two scattering parameters, $\mu_s(x)$ and g can be incorporated into another parameter called reduced scattering coefficient which describes light propagation per random walk:

$$\mu_s'(x) = (1-g)\mu_s(x) \tag{3.2.4}$$

Another difference in comparison with a single particle model is that the bulk optical properties usually considered as properties of the system of scattering bodies that are embedded in the medium. Water, for instance, is generally considered as a homogeneous medium and is well known for its light absorption properties. During propagation through water, light is highly attenuated by absorption in the NIR regime of the spectrum. So far, absorption and scattering of the surrounding medium were absent, however, must be incorporated into the model for the system of particles. For a known volume, the bulk absorption coefficient of the medium can be expressed as follows [131]:

$$\mu_{a,m} = \frac{4\pi\ ik_m\ (1-C)}{\lambda} \tag{3.2.5}$$

where $ik_m(\lambda)$ is the imaginary part of the refractive index of water and C is a concentration of material in specified volume. The electromagnetic scattering by particles immersed in an infinite absorbing medium though was considered previously and recently developed into a computational tool [151], however approximation to finite volume is comprehensible yet accurate for medium like water with well defined absorption spectra

region. The total bulk absorption coefficient, $\mu_a(x)$ of the system can be then expressed as:

$$\mu_a(x) = \mu_a(x) + \mu_{a,m} \tag{3.2.6}$$

3.3 DIFFUSE REFLECTANCE

The methods described above consider only particles are located far enough from each other in the suspension to let the scattering event occur just once. This assumption is no longer correct once volume fraction of particles increases, resulting in multiple scattering. This term was already mentioned in Section 2.2.3 as a definition of one of the limitations for light scattering techniques. Re-radiation of the light results in scattering events within the system, which are not accounted for by above-mentioned theories, and which are inevitably happening in highly scattering or concentrated systems. Therefore, the presence of the multiple scattering re-defines the properties of the measurements. The exact choice of measurements setup is dictated by the needed applications, however, as discussed in Chapter 2, diffuse reflectance spectroscopy is a promising design for turbid media analysis due to stronger signal collected. Total diffuse reflectance and the spatially resolved diffuse reflectance are two types of the diffuse reflectance that are widely employed for this purpose. To describe those analytically with respect to multiple scattering, radiative transport equation (RTE) and diffuse approximation (DA) were selected for this research. The following section describes the theory for these two solutions, defining main differences between methods.

3.3.1 TOTAL DIFFUSE REFLECTANCE

The propagation of the light in a turbid media can be expressed by the radiative transfer equation. A beam of light loses energy through absorption and scattering away from the main traveling direction. In that case, the reflectance is formed by gaining energy from fraction of light reflected and re-radiated by particles usually after some number of times. RTE incorporates the optical properties of the single scattering system into describing multiple scattering process. The formula for the steady-state radiative transfer equation is given by Patterson *et al* [152]:

$$\hat{s}\cdot\nabla I(r,\hat{s}) = -\mu_a(R,\lambda)I(r,\hat{s}) - \mu_s(R,\lambda)I(r,\hat{s}) + \frac{\mu_s(R,\lambda)}{4\pi}\int d\hat{s}' P(\hat{s},\hat{s}')I(r,\hat{s}) + S(r,\hat{s}) \quad (3.3.1)$$

where r is the position of the particle from the source and s is the direction of the particle. The terms of the equation indicate the convection of photons on the left-hand side. The equation illustrates the effect of absorption (first term) and scattering (second term) in all possible directions, described by included phase function and concluded with a light source term.

To provide the RTE with an exact solution, there are a number of mathematical models available, such as the principle of invariance [153], discrete-ordinates [154] and the adding-doubling method [155]. The principle of invariance is efficient for thin layer materials, becoming complex and extensive to solve with an increase of layer width. The discrete-ordinates approaches RTE by discretising the latest into a number of first-order differential equations. Aside from relatively inefficient computational efficiency, the method becomes ill-conditioned for highly anisotropic cases. Generally, the computational inefficiency is shortcomings of other solutions of RTE, for instance, Monte Carlo, leading to consideration of more efficient theories [156].

The adding-doubling (AD) method is another numerical solution and, unlike the discrete-ordinates approach, provides an accurate solution to the systems of any anisotropy, and computationally efficient for multi-layered media. This method is applied in this project as a solution for the total diffuse reflectance. To estimate the total diffuse reflection term, AD method refers to a system with two identical layers (or slabs) which interact with incident light of known intensity and direction. The illustration of such a system is given in Figure 3.3.1 and the formulae expression of it can be seen below:

$$R_{d(tot)} = \int_0^1 \int_0^1 R(\mu_0,\mu) 2\mu_0 d\mu_0 2\mu d\mu \quad (3.3.2)$$

where $R(\mu_0,\mu)$ is a matrix operator that defines the reflected radiance in the μ direction by a slab, considering the conically incident light directed to μ_0.

3.3.2 Spatially resolved diffuse reflectance (SRDR)

Collection of the total diffuse reflectance signal is not the only option available for consideration. With optical fibre measurement setups, a wide range of possible irradiation

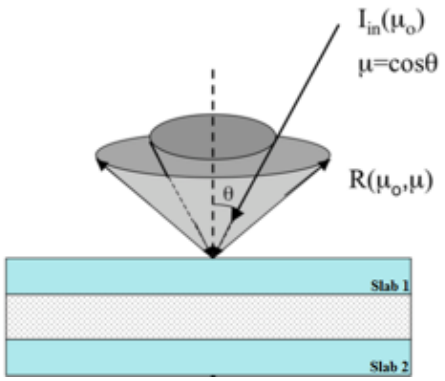

Figure 3.3.1 Schematic diagram illustrating the incident radiance and the total diffuse reflectance [157]

geometries becomes available. From biomedical applications, the light-emitting and receiving fibres can be placed in the different arrangements to improve the tissues analysis strategies [152], as reviewed in Section 2.3.2. This study utilises the optical fibre designs in analysing particle information from the suspensions. In particular, this project will focus on probe design from Thennadil *et al* [158], which involved spatially resolved receive fibres as well as multiple light sources, placed at different angles. The latest is not a question of study in this project; hence, the discussion of the theoretical and measurement approach will be focused on the specificity of spatially resolved diffuse reflectance measurements.

The schematic setup in Figure 3.3.2 summarises the geometry of the spatially resolved spectroscopy system design. With the application of the instrument to suspensions analysis, collection of the diffuse reflectance at further source-to receiver allows obtaining the signal that travelled further in the sample, presumably interacting with a larger number of scatterers. However, the intensity of the light is fading while propagating through the medium and so fades the reflectance collected at further S-R distances.

To model the above mentioned diffuse reflectance setup, a diffuse approximation of radiative transport theory, which expands the intensity term through spherical harmonics, is considered as the best approach [159]. It is a flexible and computationally efficient way to describe diffuse reflectance, however, it is limited to systems where the reduced scattering coefficient dominates over the absorption coefficient [160].

Diffuse approximation with respect to radial dependence of the reflected light can be solved by a few approaches. Reynolds *et al* [161] and Groenhuis *et al* [162] initially attempted to express the radial variation of diffuse reflectance, followed by the number of other developments, most popular among which are Farrell *et al* [163], Paterson *et al*

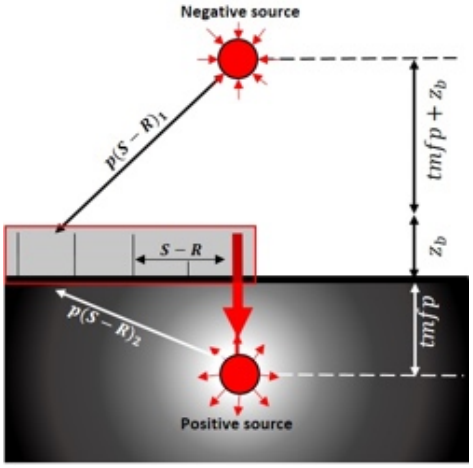

Figure 3.3.2 Schematic image of the diffuse reflectance model for normal light incidence[119]

[121], Marquez *et al* [164]. Farrell's method was widely applied in the biomedical field and previously employed in the current research group studies, hence is applied for the analysis in current work.

This method based on the assumption that scattering is isotropically distributed, meaning that any direction of scattering after light interacts with the particle is probable. The criteria of such assumption satisfaction can be conveniently described by using an isotropic point source placed at a depth of single transport mean free path (tmfp), which was defined by Equation 3.2.3.

With normal incidence of light, the boundary conditions are satisfied by placing a negative source at the equal distance from the extrapolated boundary as point source, as seen in Figure 3.3.2. The formulae expression of the radially dependent diffuse reflectance is presented below:

$$R_{d(S-R)} = \frac{\alpha(x)}{4\pi}\left[\frac{tmfp\ (1+\mu_{eff}(x)p_1(S-R))e^{(-\mu_{eff}(x)\ p_1(S-R))}}{p_1(S-R)^3} + \frac{(tmfp\ +2z_b)(1+\mu_{eff}(x)\ p_2(S-R))e^{(-\mu_{eff}(x)p_2(S-R))}}{p_2(S-R)^3}\right] \quad (3.3.3)$$

where $p_1(S-R)$ and $p_2(S-R)$ are the radial distances, depended on source-to-receiver distance, z_b is the parameter that unites internal reflection at boundary layers with dif-

fusion coefficient. Aside from tmfp, particles bulk optical coefficients are also supplied through the albedo, $\alpha(x)$, and effective attenuation coefficient, $\mu_{eff}(x)$, as:

$$\alpha(x) = \frac{\mu_s'(x)}{\mu_a(x) + \mu_s'(x)}; \qquad \mu_{eff}(x) = 3\mu_a(x)(\mu_a(x) + \mu_s'(x)) \tag{3.3.4}$$

The equations shown above illustrate the major steps of the diffuse reflectance calculation. Selected model, expressed in Equation 3.3.3 provides a relation between bulk optical properties of particles embedded in medium, signal collection distances and the diffuse reflectance signal. Bulk optical properties depend on particle size, shape and volume fraction, consequently affecting the diffuse reflectance. Gaining further understanding of the type of changes that the above-mentioned parameters of interest cause to the reflectance signal in the context of different S-R distances will be objectives of the next chapter. Additionally, the details related to the incorporation of the polydispersity into the bulk optical properties computation are discussed in the next chapter also, followed by the results of the forward simulation for the hypothetical particulate system.

CHAPTER 4

SIMULATION OF REFLECTANCE SIGNAL FOR SYSTEMS OF SPHERICAL PARTICLES WITH THE DISTRIBUTION OF SIZES

The analysis of simulated reflectance signal is a vital step before signal measurement and analysis as it allows to estimate the values of material properties that, in theory, affect the spectra at a significant extent. Knowing the sensitivity of diffuse reflectance to parameters of interest needed to initiate the discussion about the feasibility of parameters of interest inversion. This chapter focuses primarily on the quantitative evaluation of the effects of parameters of interest (mode radius of the particles, the distribution width and concentration of solids) on bulk optical properties on different types of diffuse reflectance. Furthermore, it investigates the potential of using total or spatially resolved diffuse reflectance (SRDR) to estimate parameters of interest. The benefit of the spatially resolved diffuse reflectance over total diffuse reflectance measurement on analysis of turbid systems has been studied by modelling and measurements for biomedical diagnosis [165–167]. The increased dimensionality of the spatially resolved measurement enriches the information captured for the determination of tissue's optical properties with the $S-R$ distances, which may be optimised to reduce noise and target specific depths for specific tissue applications. However, to our knowledge, there is no systematic comparison of the performance between diffuse reflectance and the spatially resolved diffuse reflectance in the context of particle size distribution and concentration influence. The study involved

modelling both total and spatially resolved reflectance to compare the sensitivity of the methods to parameters of interest and their applicability.

The chapter is organised into three parts. It starts with a description of the methods which were developed to model bulk optical properties for the polydisperse system, total diffuse and spatially resolved diffuse reflectance signal. It follows by validation of the developed algorithm. The rest of the chapter analyses the results from the modelling performance. They were studied to evaluate the effect of physical and chemical properties, potential limitations and transferability of the effects from bulk optical properties to the reflected spectral signal.

4.1 DEVELOPMENT OF THE METHODOLOGY FOR CALCULATING OPTICAL PROPERTIES OF POLYDISPERSE SYSTEM

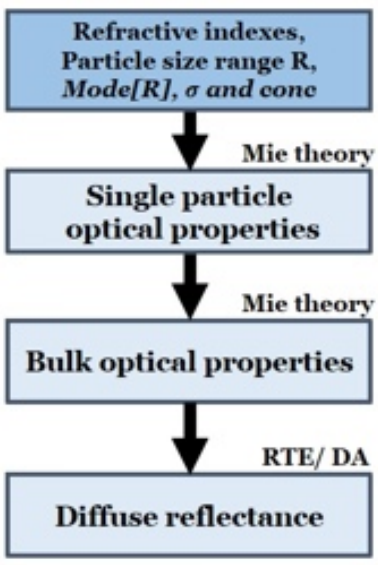

Figure 4.1.1 Flow chart of diffuse reflectance computation routine

The forward calculation routine for light scattering behaviour is desirable to model the dependence of spectral response for both, the particulate suspensions properties and measuring setup parameters. With the ability to conduct such modelling, the inversion process can be initiated to obtain parameters of interest. An algorithm to calculate the diffuse reflectance based on physical and chemical properties has been selected, consisting of three major stages, illustrated by the flowchart in Figure 4.1.1. The first stage is the calculation of optical properties for a single particle, extensively covered by Mie theory. The second stage transits to bulk optical properties, which also described by traditional Mie theory for monodisperse system and has been extended with distribution width also. These stages are essential as this calculation ties together material properties (particle size distribution, concentration, refractive index) and particles

bulk optical properties, which describe the scattering of an electromagnetic plane wave. The computed bulk optical properties were then applied to the Radiative Transport Equation (RTE) and its Diffuse Approximation (DA) in the last stage of the forward calculation to obtain the total and spatially resolved reflectance, respectively. The steps for computing the bulk optical properties and reflectance spectra are described in detail below.

4.1.1 EXTENDED BULK OPTICAL PROPERTIES FOR POLYDISPERSED SYSTEM

The most common method for describing the scattering, absorption and angular distribution of light is the Mie theory, which is presented in Chapter 3. The discussion of Section 3.2 indicates that the optical properties can be approximated from one particle to a monodisperse collection of them and the limitation to the non-absorbing medium can be tackled for mediums like water by calculating absorption for a given volume fraction of the medium. In the case when sufficient difference in particle size is present, the bulk optical properties must account for the contribution of particles of different sizes. Implementation of particle size distribution to Mie theory parameters was considered and derived before [168–171], however, the general interest was focused mostly on angularly dependent parameters of scattered light and the studies on optical properties did not provide great details regarding the effect of the distribution width itself and its combination with other parameters of the particulate system. The closest agenda was addressed by Aernouts *et al.* [171], who focused on the development of the inversion methodology for particle size distribution from the bulk optical properties, which was later utilised by Postelmans *et al.* [172] in the resent work on milk fat globules. These studies are based on the relatively low concentration range to ensure the independent or single scattering regime, which is necessary for the measurement setup employed. In the approach proposed below, we aim to provide an algorithm that allows evaluation of the proportional contribution of particles to the bulk optical properties for a range of wavelength with following computation of the diffuse reflectance to account on multiple scattering. Such development lifts the limitation to a low concentration of particles, hence expanding overall method applicability.

Optical properties, like scattering and absorption cross-section as well asymmetry parameter, are dependent on particle radius and therefore shall be combined with particle size distribution for calculating bulk optical properties of a polydispersed distribution. Equations for the scattering and absorption cross-section (Equation 3.1.3), can be ex-

tended directly with integration over particles sizes, resulting in the distribution averaged cross-section for scattering and absorption as follow [170]:

$$\sigma_s = \int_{R_{min}}^{R_{max}} Q_s(R)\, \pi R^2\, f(R) dR; \qquad \sigma_a = \int_{R_{min}}^{R_{max}} Q_a(R)\, \pi R^2\, f(R) dR \tag{4.1.1}$$

To calculate the bulk optical properties, a total number of particles in the system should be accounted for. The probability density function, $f(R)$, is used as a normalised number density function and is defined as a normalised number of particles per unit volume at each radius R. The normalised distribution function means that, when the integral of the function is equal to 1, the total number of particles per unit volume is one [173]. Therefore, the optical properties above correspond to ensemble-averaged optical properties. Accounting on the number of particles, N_p, the bulk optical properties can be calculated.

Bulk optical properties for the polydispersed system can be obtained similarly to those for a monodisperse system [174]. However, the involvement of distribution function requires revisions of equations valid for the monodispersed system, specifically, the total number of particles should now account for particles of all sizes. Despite several studies available which incorporated particle size distribution into the Mie theory, almost all of them omit the derivation of the total number of particles per unit volume in respect to particle size distribution (PSD) [175, 173, 176, 177, 170].

Despite being a straightforward term, it is a forward calculation stage, that should be thoroughly understood in the context of its relationship with PSD. Since the inclusion of Mie theory also includes integration over particles size distribution, the number of particles per unit volume described first, to avoid any following confusions. This may create confusion regarding the implementation of such variable into Mie theory. To avoid the confusion and clarify the vital for this research calculation procedure, the following section presents the derivation of the total number of particles per volume for a polydisperse system.

Total number of particles per unit volume is defined from mass fraction, C, which is expressed as follows [174]:

$$C = \frac{V_p\ \rho_p}{V_w \rho_w + V_p \rho_p} = \frac{V_p\ \rho_p}{(V_{tot} - V_p)\rho_w + V_p \rho_p} \tag{4.1.2}$$

where, V_p and V_w are the volume of particles and volume of water, respectively, and V_{tot} is total volume of the suspension, assuming the suspension is an ideal solution. Density of particles and waver expressed as ρ_p and ρ_w respectively. By rearranging the Equation 4.1.2, the volume fraction of the particles, $\frac{V_p}{V_{tot}}$, can be derived as follows:

$$C\ V_{tot}\ \rho_w = V_p \rho_p + C\ V_p \rho_w - C\ V_p \rho_p \tag{4.1.3}$$

$$V_p = \frac{C\ V_{tot}\ \rho_w}{\rho_p + C\rho_w - C\rho_p} \tag{4.1.4}$$

$$\frac{V_p}{V_{tot}} = \frac{\rho_w}{\rho_w + \rho_p / C - \rho_p} \tag{4.1.5}$$

The volume fraction of particles can be then converted into the number of particles per volume, N_p. This require to normalise the Equation 4.1.5 by the volume of the single particle, which, in the case of a single sphere, is $\frac{4}{3}\pi R^3$. Hence, the equation for monodisperse system is:

$$N_p = \frac{\rho_w}{(\rho_w + \rho_p / C - \rho_p)\ 4/3\ \pi R^3} \tag{4.1.6}$$

For a polydisperse particle system, Equation 4.1.6 is revised as:

$$N_p = \frac{\rho_w}{(\rho_w + \rho_p / C - \rho_p) 4/3\ \pi\ \int_{R_{min}}^{R_{max}} R^3\ f(R) dR} \tag{4.1.7}$$

Hence, bulk scattering and absorption coefficients can then be derived from combining Equation 4.1.1 and Equation 4.1.7 [177]:

$$\mu_{s,a} = N_p\ \sigma_{s,a} = \int_{R_{min}}^{R_{max}} Q_{s,a}(R)\ \pi R^2\ N_p\ f(R) dR \tag{4.1.8}$$

where s and a denote scattering or absorption, respectively. The anisotropy factor expressed in Equation 4.1.9 is the final form as it is independent of the number of scatterers. To describe the polydisperse system, the asymmetry parameter is estimated for particles of all sizes and then normalised, which is expressed as follows:

$$g = \frac{\int_{R_{min}}^{R_{max}} g(R) N_p \, \sigma_s(R) \, f(R) dR}{\int_{R_{min}}^{R_{max}} N_p \, \sigma_s \, (R) \, f(R) dR} \tag{4.1.9}$$

4.1.2 Materials and methodology

Materials selection To examine the light scattering behaviour, the example of colloidal suspension had to be chosen. Preferably, the study needed to focus on the suspension of nearly perfect smooth spherical nanoparticles that exhibit highly scattering properties and almost negligible absorption, and also can be synthesised in significant amounts and relatively high concentrations, to evaluate the effect of the latter. Polystyrene suspensions were selected to match the above-mentioned criteria and will be used in the current and majority of the following studies in this thesis.

There are several parameters that needed to be provided before performing a forward calculation. First of all, the material properties had to be ascertained. This stage requires the density of the particles (polystyrene), of the surrounding medium (water) and their refractive indexes (RI). The density of polystyrene was set to 1.06 g/mL [178]. RI values for water in the UV-vis-NIR range (450 - 1850 nm) were taken as the values reported by Hale and Querry [179]; the refractive index of polystyrene was provided by Sultanova et al. [180]. The forward calculation below was computed for a range of parameters of interest of the polystyrene particles. The limits of the studied range have been defined as follows.

Particle size distribution parameters Analysis of polydisperse suspensions requires to consider the distribution of different size groups. The presence of polydispersity can be described with a discretised range or continuous function. As discussed in Chapter 2, during the polymerisation reaction, the size of the particles formed is influenced by a number of factors. Based on previous studies, log-normal probability density function, $f(R)$, was chosen as the most prominent way of describing the particle size population of the studied polystyrene suspensions:

$$f(R) = \frac{1}{R\,\sigma\,\sqrt{2\pi}} e^{-\frac{(\ln R - \bar{R})^2}{2(\sigma)^2}} \tag{4.1.10}$$

where σ stands for the log standard deviation of the distribution, R is a value of the radius in a range between 0 and infinity and $\bar{R}$ is the mean size of the particle population. Although mathematically the chosen distribution form may extend to infinity, the truncation of integration to some specified maximum value (R_{max}) is recommended [181]. With a choice of R_{max} that is large enough to converge the bulk optical properties computation to desired numerical accuracy, the computation time can be significantly reduced. Same is applicable to determine the lower limit of R, termed as R_{min}. If the above mentioned is satisfied, the truncated particle size distribution becomes an equivalent of the distribution with original limits.

Mode radius of the system was considered in the context of the Mie particle size parameter x. This parameter is defined as a ratio of particle radius to wavelength. Theoretically, Mie theory does not have the upper size limit, however, with the increase of particle size, the forward scattering also increases, forming a difraction peak, which complicates the interpretation of the scattering coefficient due to its large contribution to it. Generally, the particle size parameter that corresponds to the Mie regime of light scattering lies between 0.1 and $x \sim 1$, where it expects to have the peak of scattering efficiency before forming strong scattering peak [131]. By reverting Equation 3.1.1 for the largest wavelength used in the study (1850 nm) and assuming the largest x to be lower than 3, the minimum and maximum values of mode radius were roughly estimated to 25 nm and 650 nm respectively to cover Mie scattering regime.

Once the predominant particle size is placed, the following step is a consideration of the particle size distribution inclusion. The distribution width parameter, σ, was used in the following study in the range from ultra-narrow (0.05) to ultra-wide (1.5). To perform the integration with a guaranteed convergence, *a priori* sufficient minimum and the maximum value of R are required. Maximum radius value, R_{max} was derived to be 15 μm based on defined maximum mode radius and distribution width in such way so it leads to convergence, i. e. satisfy the following: $\int_{R_{min}}^{R_{max}} f(R)dR = 1$. The lowest radius boundary, R_{min}, was assumed to have a value as small as 1 nm. These limits were used to set a linearly spaced range with a step size of 2 nm. Despite the apparent low efficiency of the selected approach, the purpose of such wide boundaries is to illustrate the sensitivity

of the optical properties and diffuse reflectance, hence, is a sufficient solution for the objective. The above-mentioned parameters are valid for most of the studies in this project, if not mentioned otherwise.

DIFFUSE REFLECTANCE SIMULATION PARAMETERS The majority of the parameters needed for the diffuse reflectance calculation are set during the calculation of the optical properties; the rest of them correspond to the experimental setup. The total diffuse reflectance of polystyrene particles was modelled for 1 mm thick quartz cuvette with the refractive index of the quartz being 1.5. Spatially resolved diffuse reflectance were computed with setup for the Spatially and Angularly Resolved Diffuse Reflectance Measurement (SAR-DRM) system, developed by Chen *et al* [158], where the system provides four-light source-to-receiver(S-R) distances: 0.3, 0.6, 0.9 and 1.2 mm, which were included as S-R distances for simulation. SAR-DRM has the capability of emitting light at 0^0, 30^0 and 45^0 to the probe surface. However the study below will focus exclusively on normal (0^0) light emittance, and therefore, the simulated signal will be referred to as spatially resolved diffuse reflectance (SRDR). Some of the parameters were eliminated, as the relative refractive index of the sample-air interface due to the probe being immersed into the sample.

COMPUTING ENVIRONMENT The formulae above summarise the changes that have been made to original Mie theory to include particle size distribution. The equations above were then implemented into Matlab subroutines for computing. The two stages routine, written in Matlab that combines the above-mentioned calculation parameters with the forward calculation of diffuse reflectance methodology. The latter includes Mie-based extended bulk optical properties algorithm, merged with either total or spatially resolved diffuse reflectance.

This study uses Matzler's Mie code implemented in Matlab [182]. The method uses built-in functions (including half-odd order Bessel functions of the first and second kind, $J_{L+1/2}$ and $J_{L+1/2}$) to numerically solve for the optical parameters, μ_s, μ_a and g. This study expands Matzler's code to calculate the system of polydispersed particles in the manner described above to include particle size distribution in the study. The code developed is a functioning tool for computing bulk optical properties for a polydisperse particle system over the needed range of wavelength.

The second part of the developed algorithm is based on the simulation of diffuse reflectance signal of two different measurement designs. The main difference between

those in the light collection setup since spatially diffuse reflectance offers multiple source-to-receiver distances. To complete the reflectance simulation algorithm, the bulk optical properties were supplied into two models for diffuse reflectance computation. Total diffuse reflectance was obtained by using Adding-Doubling-based Matlab computational routine, developed by Thennadil & Chen [183]. The spatially resolved reflectance model is based on Farrell's diffuse approximation solution [163] and also implemented in Matlab 2018b by researches within the research group.

4.2 Validation of the developed forward calculation

4.2.1 Comparison of performance of extended bulk optical properties algorithm with classical Mie theory

The developed computational routines have to be validated to avoid misleading results and evaluate the degree of confidence in its predictions. The routine for Mie calculation, originally introduced by Matzler's as a solution for a single particle, includes the extension to account for the monodisperse collection of particles. In this research, this routine was expanded to incorporate a particle size distribution function. Since the distribution function is a statistical representation of the population of the particles, comparison of monodisperse bulk optical properties, computed for collection of particles of the same size with those, computed for a polydisperse system with narrow distribution width, may serve as a benchmark for model validation. Theoretically, the optical properties of the polydisperse system calculated from the extended algorithm should be identical to those for the monodisperse system if σ was set to zero.

For comparison, the original Matzler's routine was used to simulate the optical properties for a monodisperse system. The optical properties of a polydisperse system with a narrow distribution width were simulated using 0.002 for a distribution width in Equation 4.1.8 to avoid singularities. Simulations were performed in 450-1850 nm wavelength range for a range of mode radii between R_{min} and R_{max} with a step size of 1 nm. For both simulations, the concentration of the particles was set to 10 wt%.

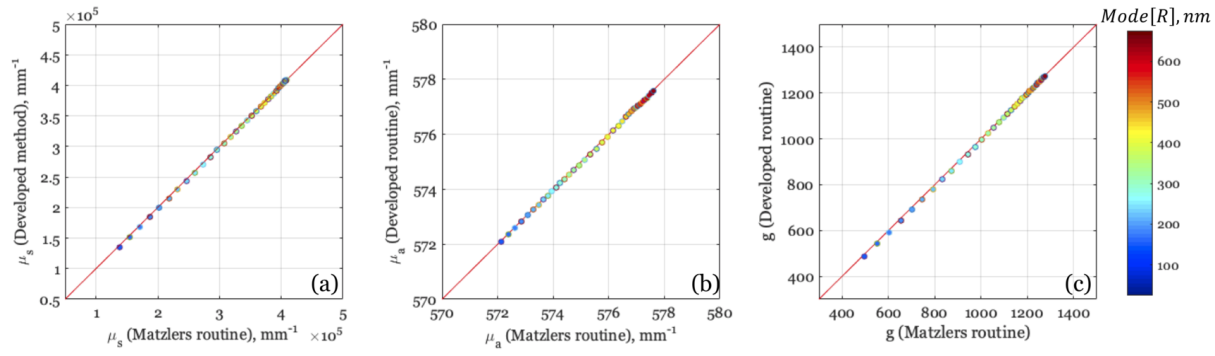

Figure 4.2.1 Comparison of bulk optical properties simulated via the original (Matzler's) and the developed computational routines: (a) bulk scattering coefficient, (b) bulk absorption coefficient, (c) asymmetry parameter

The results can be seen in Figure 4.2.1. They represented in the form of scatter plot, where each point corresponds to simulation for a given mode radius, specified by the colour bar. Since the validation is targeting to unveil the differences caused by distribution width only, the effect of wavelength shall remain constant, and therefore each simulation was summed over wavelength. The obtained scatter plot allows a visual comparison of the data, where any deviation between outputs from the two methods will manifest as a deviation from the diagonal line. All simulations show a strong, linear correlation between bulk optical properties for a monodisperse system and those for a polydisperse system with a narrow distribution width. For all of the optical properties calculated, there are no outliers in the simulated data. The difference between outputs from different routines does not exceed $\sim 10^{-5}$. The results agreed with the hypothesis, confirm the accuracy of the developed routine in one of the extreme cases for a polydisperse system.

4.2.2 Comparison of performance of extended bulk optical properties algorithm with literature results

Since the extension of bulk optical properties to the polydisperse system of particles has been available to the research community for a while, another route for routine validation can be a direct comparison of results with those available from the other researchers. Majority of such studies though were focusing on angular properties of scattered light, like phase function, which is not used in this form in current research [184, 185, 168, 186]. In addition, execution of such study involves pattern comparison, due to unavailability of raw data, leading to a degree of uncertainty. An alternative route to validate the developed

routine would be to use the routine developed by other researchers for their work. A small number of studies up to date attempted to implement the theory into an open-source computational code. To my knowledge, there are at least three open-source codes available that calculate optical properties by an ensemble of polydisperse particles. For example, Bond *et al*[187] have shared the Matlab code for optical properties computation for the lognormal particle size distribution of homogeneous or coated spheres. The other code, written in C and Fortran, was released by McGarragh [188] in 2012 and called *LMie*. Similarly to Bond's work, it computes optical properties for a polydisperse system of particles, however, the particles are strictly homogeneous. This code expands the distribution functions range to six different functions, implementing the mathematical derivation by Mishchenko *et al* [170] into a computational routine. The last published work is the Fortran code by Mishchenko [189] himself, who have implemented their previous work on electromagnetic scattering by particles embedded in the infinite absorbing medium in a Fortran-based computational tool for the calculation of far-field optical properties with a possibility to account for polydispersity. In this work, the code developed by Bond *et al* was used for validation of developed routine as the code is also Matlab based.

The following analysis investigates the bulk optical properties affected the most by the changes in the width of the distribution. The validation of the results was performed by comparing the bulk scattering coefficient and asymmetry parameter computed by the Bond's code and the routine developed in this research (Equations 4.1.9 and 4.1.8). A number of fixed input parameters was selected and both of the routines were executed accordingly. Since Bond's method returns the optical cross-sections of the light, not the bulk optical properties, the result from this code was then used in the Equation 4.1.8. The input parameters included particle size distribution (mode radius and σ), wavelength range and corresponding refractive index for the particles and the medium. For both simulations, mode radius was assigned as 250 nm, the distribution width was submitted as a range between 0.002 and 1 with the interval 0.05. Wavelength range and the corresponding material properties were chosen the same as described in the previous section. The interval wavelength range was also identical.

The results of the comparison are presented in Figure 4.2.2 for the bulk scattering coefficient (in (a)) and asymmetry parameter (in (b)). The scatter plot compares the results of simulations between the methods summed over the wavelength range. The colour of the markers indicates the corresponding distribution width. The simulated results

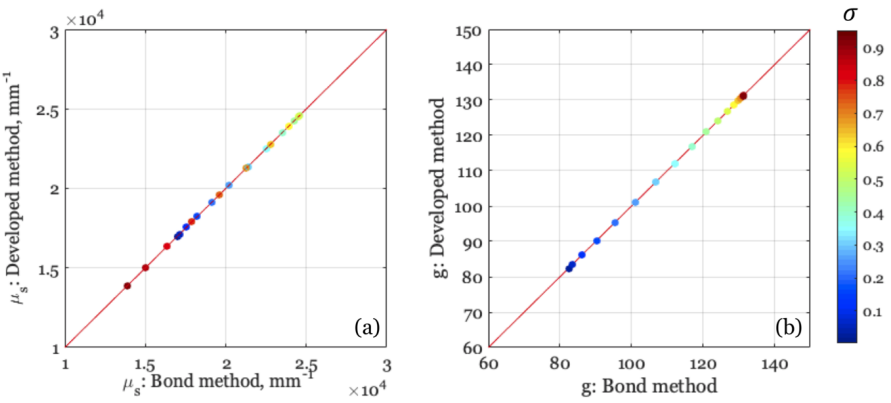

Figure 4.2.2 Comparison of optical properties simulated by Bond's and the developed routine: (a) bulk scattering coefficient, μ_s, (b) asymmetry parameter,g

from both methods are close to identical as the difference in values below 10^{-7} for both parameters analysed. These results set a degree of confidence in the routine developed and therefore, the following results of simulations are considered as accurate estimations of the bulk optical properties.

4.3 Investigation of sensitivity for different types of diffuse reflectance to parameters of interest via computational modelling

As stated at the beginning of the chapter, conducting the comparison analysis on simulated total and spatially resolved diffuse reflectance is a vital step for this research to gain understanding on the potential of each type of spectra. The study in this section has a significant impact on the following work as, depending on the degree and appearance of each property and their combination, the inversion approach may be considered accordingly. The previous study [120] suggested that the main effect of concentration can be seen by the changes of the magnitude of optical properties dependent on a number of particles, whereas particle size effect appears in the form of the spectra peak shifts over wavelength, therefore there is a degree of prior knowledge about some of the parameters of interest. At this point, there is no knowledge of the influence of size distribution and its cumulative effect with mode radius and concentration on diffuse reflectance for the

selected material. Therefore, the study below has prioritised the distribution width effect on analysing the simulated spectra.

The following study is organised in three main sections. First of all, the effect of PSD on the bulk scattering coefficient (μ_s), absorption coefficient (μ_a) and asymmetry parameter (g) was studied, followed by those on the total and diffuse reflectance. The analysis was focused primarily on observation of the effect of particle size distribution parameters (mode and width) on bulk optical properties and at what degree the effect becomes noticeable in diffuse reflectance. The effect is also evaluated in the context of its wavelength dependence and source-to-receiver distances dependence for spatially resolved diffuse reflectance. Lastly, the combined effects were studied on SRDR to depict potential interference with each other.

4.3.1 Influence of parameters of interest on bulk optical properties

Effect of mode radius on bulk optical properties

It is common knowledge in the spectroscopy field that particle size has a strong effect on measurable optical properties [131]. The following study is conducted for analysis of the particle size effect appearance on the bulk optical properties of polystyrene suspensions.

The study was conducted with an assumption to monodisperse suspensions for mode radii range explained in Section 4.1.2, however for clarity, the illustrations below focus on the range from 50 to 500 nm in radius. The concentration of them was set to 10 $wt\%$. The calculated bulk optical properties can be seen in Figure 4.3.1.

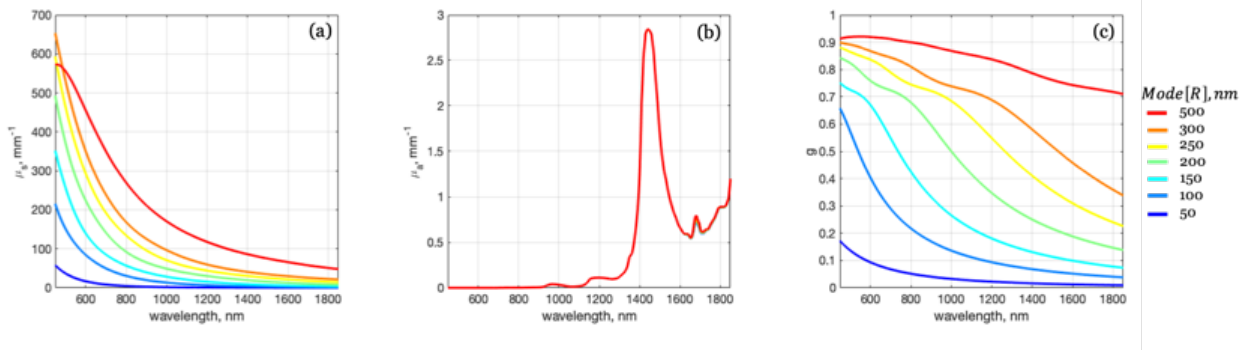

Figure 4.3.1 Bulk optical properties computed for monodispersed systems: (a) scattering coefficient μ_s, (b) absorption coefficient μ_a, (c) asymmetry parameter g with concentration of 10wt %.

With an increase of particle radius, the bulk scattering coefficient is increased nonlinearly (Figure 4.3.1 (a)), and the increment is not evenly distributed across the wavelength range. The particle size effect is more prominent between 450-1000 nm. The effect of increasing particle size on an increment of the increased bulk scattering coefficient is straightforwardly justified because large particles have significantly larger scattering cross-section.

The bulk absorption coefficient in Figure 4.3.1 (b) is not affected by mode radius changes since the volume fraction of the particles remains unchanged. The asymmetry parameter, on the other hand, exhibits strong responsiveness to the changes in particle size. The effect is wavelength dependent; with the increment of particle size, the features are observed to shift toward longer wavelength. Simultaneously, the effect appears in changes in magnitude as well, which arises from the increased forward scattering peak that is averaged into the g parameter (Figure 3.1.2). The response of bulk optical properties to particle size, observed in Figure 4.3.1 is similar across different concentrations [183]. Therefore, the study above confirms that the particle size of polystyrene beads has a strong effect on the bulk scattering coefficient and asymmetry parameter, which was recognised previously [131, 169]. However, the results above are necessary for analysis in the context of other parameters of interest.

Effect of distribution width on bulk optical properties

Computation of the bulk optical properties is a first stage of the routine, therefore the general idea of distribution width effect can be observed from the analysis of them.

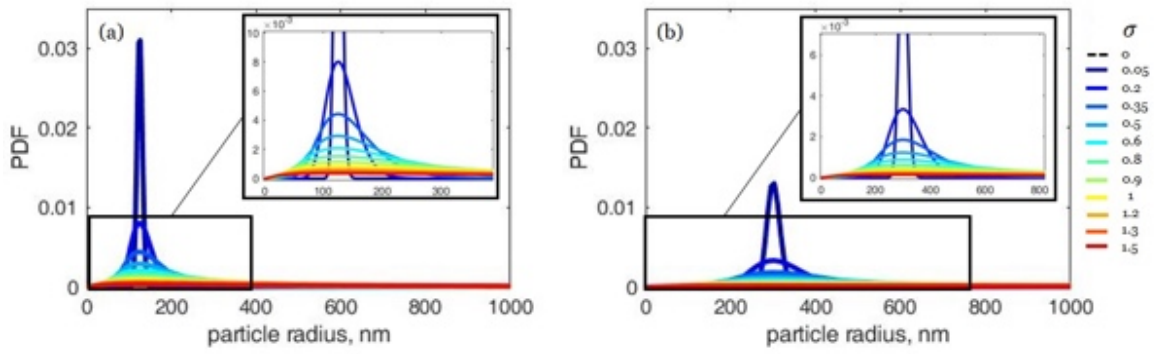

Figure 4.3.2 Probability density function for particulate system with mode radius (a) 125nm and (b) 300nm. Colour corresponds to distribution width, σ

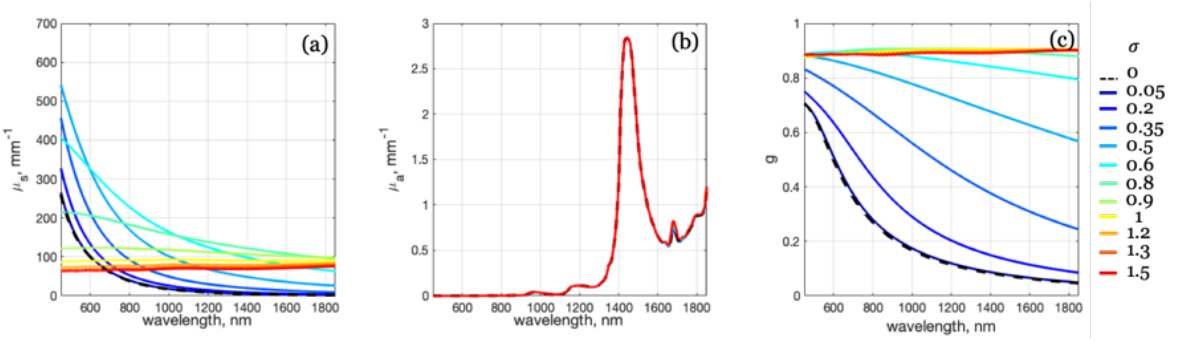

Figure 4.3.3 Bulk optical properties computed for mono(dashed line) and polydisperse(solid lines) systems: (a) Scattering coefficient μ_s, (b) absorption coefficient μ_a, (c) asymmetry parameter g for collection of particles with mode radius 125 nm and concentration of 10wt %. Colour corresponds to different distribution width, σ.

The effect of distribution width was investigated in a range specified in Section 4.1.2. The selected range extensively illustrate narrow and ultra-large distribution width (Figure 4.3.2) of lognormal probability density function (PDF).

In order to illustrate the distribution width effect appearance in full, results for two particulate systems with different mode radii, 125 and 300 nm are discussed below. An illustration of bulk optical properties can be seen in Figure 4.3.3. There are three sets of plots corresponding to μ_s, μ_a, and g, respectively. Polystyrene has weak absorbing properties with an absorption peak at around 1680 nm. Changes in distribution width do not affect the bulk absorption coefficient, μ_a, since the volume fraction was kept the same. However, the bulk scattering coefficient and asymmetry parameter are greatly affected by particle size distribution. Hence, most of the further analysis in this section is focused on these optical properties.

The chosen material exhibits strong scattering properties, which is reflected in μ_s. As was anticipated from results in Section 4.2.1, while using a relatively low σ parameter (close to 0) in the bulk optical properties simulation, scattering coefficient properties did not differ from those for a monodisperse system of particles. With a gradual broadening of the distribution, μ_s mainly decreases with the addition of distribution function into the analysis. Yet, this decrement is not linear across the wavelength range. Inclusion of the distribution parameter causes more prominent changes in 450-1000 nm wavelength range, although the further broadening sees the scattering coefficient in the NIR region affected. It should be noted that the increase of particle size distribution width does increase the bulk scattering coefficient yet only for σ under 0.5. After this value, the μ_s decreases as was

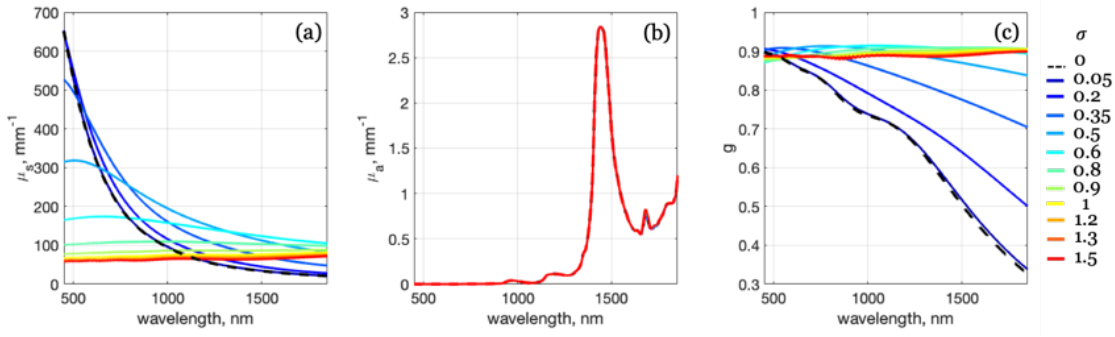

Figure 4.3.4 Bulk optical properties computed for mono(dashed line) and polydisperse(solid lines) systems: (a) Scattering coefficient μ_s, (b) absorption coefficient μ_a, (c) asymmetry parameter g for collection of particles with mode radius 300 nm and concentration of 10wt %. Colour corresponds to distribution width, σ.

mentioned. This tendency continues strongly until σ reaches 0.85, and after this value, the sensitivity of the bulk scattering coefficient to distribution width drops significantly and the scattering coefficient values becoming very similar across the wavelength studied. Increase of distribution width includes large particles into a simulation, which in its turn obliterate the scattering features that can be seen at smaller distribution width [169].

Another effect of large particles present in the particulate system is the occurrence of strong forward scattering. It can be seen in Figure 4.3.3(c), that forward scattering starts to dominate the asymmetry parameter while the distribution width is increasing. Hence, g is constantly increasing with the increase in size distribution. The increase is not uniform across wavelength and has a larger magnitude at 750-1850 nm wavelength. Similarly to what was observed on the scattering coefficient, at σ larger than 0.85, the asymmetry parameter does not change with changes of σ and wavelength any longer.

The observations for the particulate system with mode radius 125 nm are similar, but not identical to the system with mode radius 300 nm. Figure 4.3.4 illustrates the same bulk optical properties computed for different mode radius and the same distribution width range. In this system, the bulk scattering coefficient mostly decreases with the increase of distribution width, after the latter exceeds 0.3. The asymmetry parameter for the monodisperse system has different appearance over the wavelength range from the one for 125 nm, exhibiting two distinguishable peaks at 750 and 1100 nm. The effect of the distribution width on the asymmetry parameter is similar to the one observed previously.

Summarising the observation from simulated spectra for both mode radii, incorporating the particle size distribution caused a distinct change in the scattering coefficient

and asymmetry parameter for σ values above 0.1. The exact value of σ which starts to affect the bulk optical properties is difficult to retrieve given that none of the studied optical properties increases strictly proportionally with the distribution width. The largest relative difference between monodisperse and the polydisperse systems is observed at the asymmetry parameter, where the strongest influence of distribution width was located in the NIR range. On the other hand, the bulk scattering coefficient is affected the most at UV-vis wavelength range, at the lower extent in NIR range in relative units, compared to the asymmetry parameter. Moreover, the presented simulations correspond to fixed parameters (mode radius and concentration), and therefore the effective value of σ may vary with varying the fixed parameters. It is challenging to conclude what property is the most sensitive to the particle size distribution. The scale cannot be directly compared, which complicates the comparison of the effect's degree.

Effect of concentration on bulk optical properties

Another parameter of interest in this research is the concentration of solids. As can be concluded from the Equation 3.2.2, bulk optical properties are proportional to the concentration of particles in the system. The asymmetry parameter is a measure of average cosine of the scattering angle by a particle and does not involve the concentration (Equation 3.1.4) and therefore independent from its effect. Nevertheless, a study was presented to illustrate the effect and compare it with the effect of physical parameters, like mode radius or distribution width. An example of monodispersed polystyrene suspensions of different concentrations presented in Figure 4.3.5.

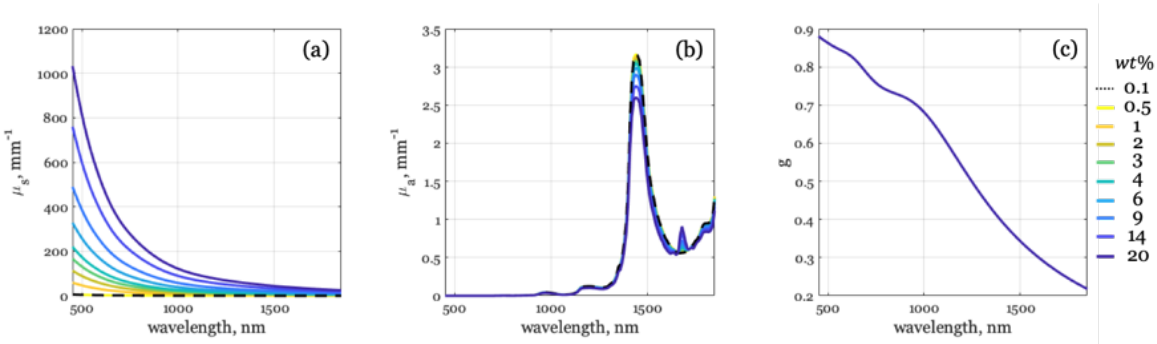

Figure 4.3.5 Bulk optical properties computed with assumption to monodispersed system: (a) Scattering coefficient μ_s, (b) absorption coefficient μ_a , (c) asymmetry parameter g with mode radius 250 nm. Colour corresponds to concentration.

The variations in the concentration of solids affect the scattering coefficient and absorption coefficient only. The latter has a more prominent response to changes in concentration than to changes in particle size distribution. The proportion of absorption between water and the solids is changing with the change of the concentration. The increase in concentration causes the growth of the polystyrene absorption peak and consequential reduction of water absorption peak.

Despite the fact that changes in the concentration affect the magnitude of the bulk scattering coefficient, this appearance of the effect is different to the effect of particle size that also results in the magnitude differences (Section 4.3.1). While analysis of bulk optical properties individually would indeed lead to analysis complication, in the method developed, bulk optical properties are supplied to the next stage of diffuse reflectance calculation in full. Despite the similarities of some of the parameters appearance on one of the optical properties, the simultaneous involvement of multiple bulk optical properties contributes towards to specificity of the effect. In this case, the particle size effect appears mostly at the bulk scattering coefficient and asymmetry parameter, whereas the absorption coefficient does not carry the effect due to constant volume fraction. On the other hand, the variations in the concentrations change the absorption coefficient as well as the bulk scattering coefficient, without affecting the asymmetry parameter, as it is independent of a number of scatters. The effect of both studied parameters have a strong wavelength dependence and appear differently at a different wavelength. Therefore, the analysis of a combination of bulk optical properties at multiple wavelengths may prevent misinterpretation of effects.

As was diffuse reflectance is affected by the cumulative effect of all bulk optical properties, the influence of parameters of interest at the diffuse reflectance and how it compares with those seen at bulk optical properties should be analysed further.

4.3.2 Influence of parameters of interest on diffuse reflectance

The following section summarises the results of the complete forward calculation and presents the analysis in two major aspects. First of all, the effect of particle size distribution and concentration on diffuse reflectance was evaluated to analyse the overall sensitivity of this type of measurements to parameters of interest. Secondly, the diffuse reflectance measurements can be conducted via a number of different instruments, and with the type of instrument, the diffuse reflectance signal may be subject to change, which consequently

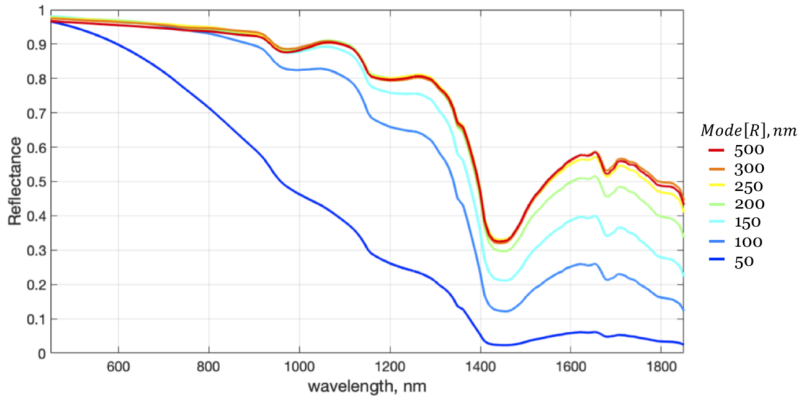

Figure 4.3.6 Total diffuse reflectance computed with assumption to a monodisperse system for collection of particles of concentration $10wt\%$. Colour corresponds to mode radius

results in the amount of information it provides about the studied system. To evaluate the preferences in the measurement design to benefit the quality of the parameters of interest inversion, the performance of diffuse reflectance in the context of parameters of interest effect were compared by supplying the bulk optical properties, computed in the previous section.

Effect of particle size on diffuse reflectance

The bulk optical properties, computed for the polystyrene systems of various particle sizes, are used to compute the total and spatially resolved diffuse reflectance. Total diffuse reflectance intensity increases with an increase of particle size, as seen in Figure 4.3.6. The magnitude of particle size effect reduces when particle radius approaches 200 nm, the spectra no longer responds to the size changes at when the radius exceeded 300nm. UV-vis region of wavelength is not as sensitive to particle size changes, as, in the NIR region, the differences in spectra caused by particle size are prominent and straightforward. If measurements of total diffuse reflectance are considered for estimation of particle size, the analysis should be truncated to NIR range.

Spatially resolved diffuse reflectance was computed for four different source-to-receiver distances, results for each of them are presented in Figure 4.3.7. With an increase of S-R distance, the intensity of the reflectance signal reduces. It is caused by the losses that light experiences after propagating through the sample. The SRDR at the closest S-R distance for the smallest particle radius (50 nm) exhibits a distinctive peak at 585 nm, which

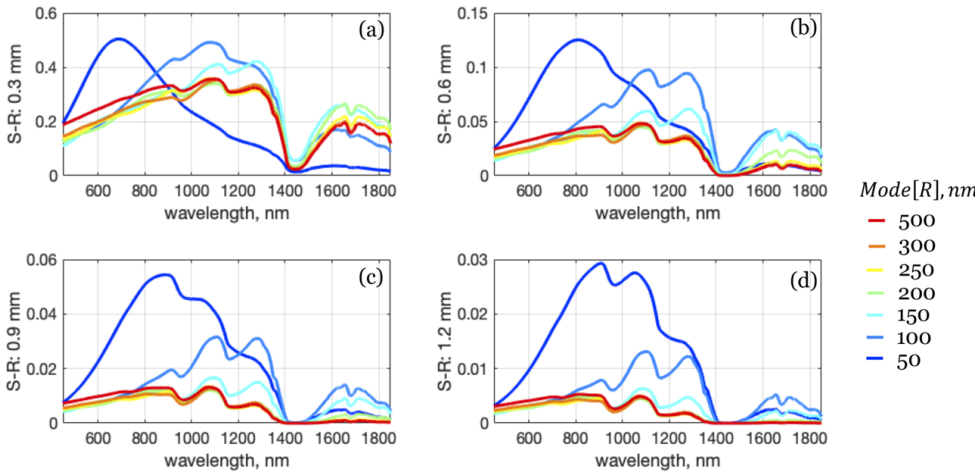

Figure 4.3.7 Spatially resolved diffuse reflectance computed with assumption to monodispersed system for collection of particles of concentration $10wt\%$. The signal collection distances are: (a) 0.3 mm, (b) 0.6 mm, (c) 0.9 mm, (d) 1.2 mm. Colour corresponds to mode radius

changes position towards to large wavelength with increase of particle radius. Between 450-1400, the difference between SRDR signals for the different radius is almost negligible and the spectra profiles are entangled, although for particle radius below 150 nm, the difference between signals is distinguishable. For particles with a radius larger than 300 nm, the difference between their SRDR spectra is relatively small, however divisible one from another. At other wavelengths, the magnitude between studied SRDR signals peaks between 1600-1850 nm.

The general response of SRDR to the particle size at current S-R is analogous to total diffuse reflectance, yet some of the spectra features, like absorption peak, appear differently. While total diffuse reflectance is sensitive to particle size in the form of magnitude change at specified wavelength range, spatially resolved diffuse reflectance is sensitive to particle size across the presented wavelength range and also exhibits strong spectra profile features at different $S-R$ distances. A significant degree of variation between signals is an essential condition for parameters inversion, which spatially resolved diffuse reflectance provides with. Total diffuse reflectance appears to be more sensitive to particle size changes than SRDR spectra at the NIR region, whereas the SRDR is more responsive to size changes at UV-vis range. Increasing S-R distance changes the appearance of the wavelength-specific features for a signal from each particle size group. The noticeable

difference in the SRDR spectra for particle radius below 200nm can potentially be utilised to separate the effect caused by a specific size group below 200nm.

One of the observations arises from the comparison of results from total and spatially resolved diffuse reflectance simulations. The total diffuse reflectance intensity increases with an increment of mode radius, however, the appearance of the effect on SRDR spectra decreases. This observation demonstrates the difference in the selected theories, precisely, the accuracy of them at different diffuse reflectance regions. The diffuse approximation does not model near -to-source diffuse reflectance accurately, it describes the reflectance signal for the light that travels longer than single transport mean free path. Considering the discussion by Lin *et al* [119] based on Monte Carlo simulations, it implies that the major share of the total reflected light corresponds to a region close to the light source. The simulation of total reflectance represents the sum of the diffuse reflectance and predominance of near diffuse reflectance contribution from areas near the incident light to the total signal leads to the inverse magnitude of the signal for analysed systems compare to spatially resolved diffuse reflectance simulation. The increase of the particle size that leads to more directional light scattering, which is resulting at the stronger intensity in the near to source region and the opposite at the light travelled further distances, as executed in SRDR. Large sizes may result in more specular reflection, therefore exceeding the capabilities of the diffuse approximation-based modelling.

Effect of distribution width on diffuse reflectance

Firstly, the analysis investigates the total diffuse reflectance, simulated for a polystyrene particulate suspensions a mode radius of 125 nm for a range of σ, using the optical properties shown in Section 4.3.1. From Figure 4.3.8, the diffuse reflectance signal for polydisperse system behaves differently at different values of distribution width. When the distribution width is below 0.4, the total diffuse reflectance signal increases in comparison with the monodisperse system, mainly at 1500-1850 nm wavelength, however, it is quite similar to monodisperse approximation when the width is below ~ 0.2. Further increment of the distribution width leads to a gradual decrease in signal intensity. This behaviour continues until the width reaches 1. The diffuse reflectance signal does not respond to changes in the distribution width any further for the width exceeds 1. When looking at the same analysis conducted for the system with a different mode radius (300 nm), the effect of distribution width changes the spectra systematically (Figure 4.3.9). Particularly,

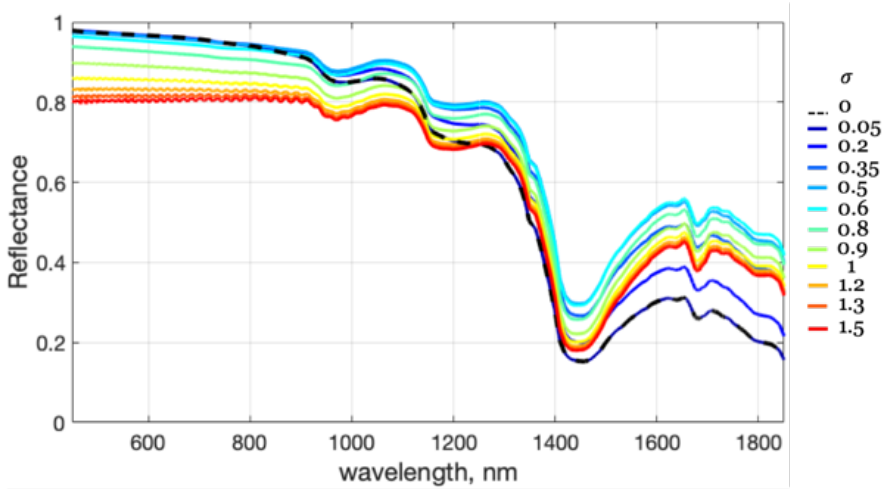

Figure 4.3.8 Total diffuse reflectance computed with assumption to mono (dashed line) and polydisperse (solid lines) system for collection of particles with mode radius 125 nm and concentration 10 wt%. Colour corresponds to distribution width, σ

with an increase of the σ, the diffuse reflectance signal decreases across the wavelength range studied. It also changes the sensitivity to the distribution width variations once it exceeds 1. The change of the particle size distribution width within chosen constrains changes the intensity of the total diffuse reflectance by approximately 0.2, compared with the monodispersed samples, with an average difference between different samples of 0.02.

Concluding the observations from the general analysis, with consideration to estimate the distribution width from diffuse reflectance, the effect of it on signal is not strong enough unless it becomes significantly broad for real-life suspensions (σ over 1). The relatively small difference observed on the total diffuse reflectance implies the possible issues to distinguish small changes in the σ.

The second part of the analysis focuses on another type of diffuse reflectance measurements. The spatially resolved diffuse reflectance is calculated for several signal collection distances. It presents the simulations for systems of two different mode radii.

The simulated signal for one of the systems with a mode radius of 125 nm is presented in Figure 4.3.10. With a closer look at SRDR for closest S-R distance (0.3 mm), increasing the distribution width up to 0.5 decreased the intensity of the spectra. The signal intensity begins to increase if the distribution width increased further. This trend is wavelength dependent and is valid 700-1850 nm range, whereas at a shorter wavelength, the intensity increase monotonically with the increase of the distribution width. When the σ is as large as 1, the spectra signal does not respond to any further changes, leading to a low

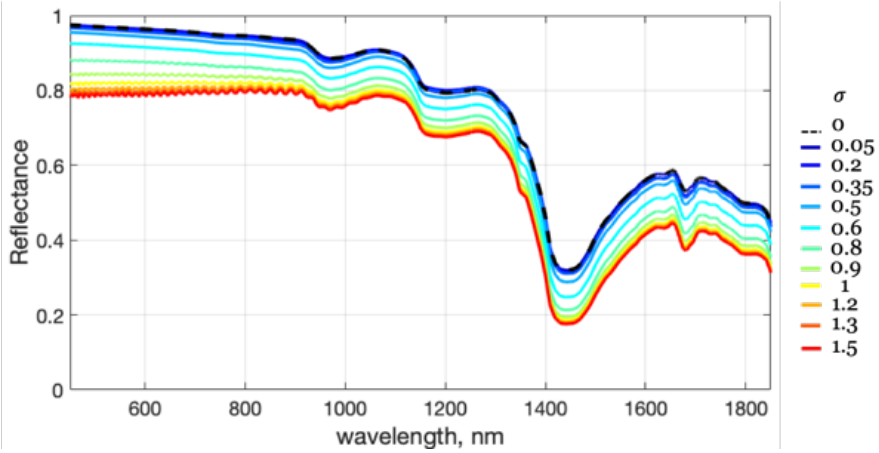

Figure 4.3.9 Total diffuse reflectance computed with assumption to mono(dashed line) and polydisperse(solid lines) system for collection of particles with mode radius 300 nm and concentration 10 wt%. Colour corresponds to distribution width, σ

possibility to distinguish the higher values of distribution width. A similar issue is found for σ below 0.2. Although there is a noticeable difference at some of the wavelength, the signal is more responsive to changes in the distribution width only at higher values of it. In general, the changes caused by the distribution width are not uniform across the wavelength range and are stronger between 450-1000 nm. In another example on a larger mode radius (Figure 4.3.11) for the same S-R distance, the increment of distribution width leads to an increase in diffuse reflectance intensity systematically across the wavelength range. The changes in spectra when σ is below 0.4 are negligible in comparison to the spectra for a monodisperse system. The intensity of the signal increases with an increase of σ up to 0.8, after which it does not change with distribution width any more. The observations on the spectra from the closest S-R fibre are similar to those from the total diffuse reflectance, disregarding the direction of changes, meaning that the similar values of σ cause the similar type and degree of effect on both types of spectra.

The increase in the S-R distance reduces the intensity of the signal, however, the effect of distribution width still can be seen clearly at the reflectance signal collected at further S-R distances for both examples presented. While light propagating further through the sample, it interacts with a larger fraction of particle population, hence, increasing S-R distance leads to more differentiable spectral changes between different σ as well as more prominent wavelength-dependent features. The effect of the same σ appears differently on different S-R distances, for example, the signal that corresponds to mode radius 300 nm and 0.4 σ is more distinguishable from monodisperse at 1.2 mm S-R distance than

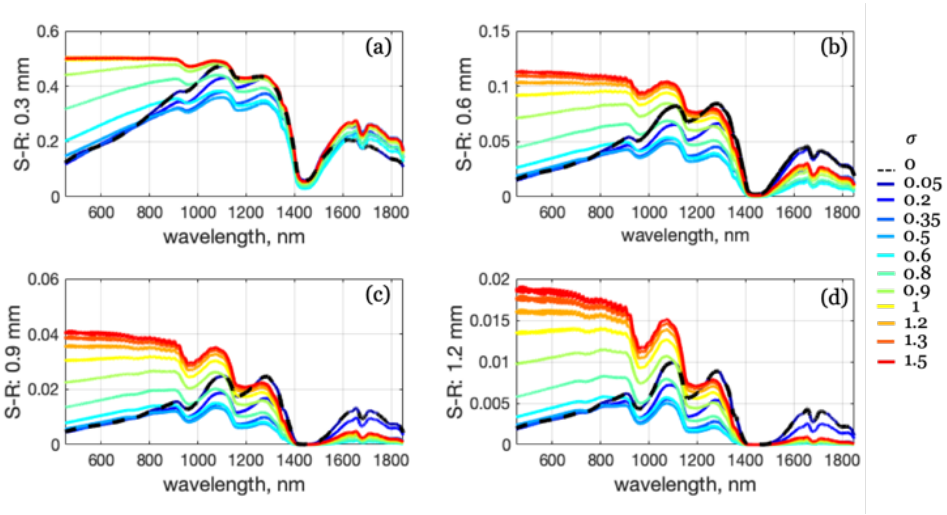

Figure 4.3.10 Spatially resolved diffuse reflectance computed with assumption to mono(dashed line) and polydisperse(solid lines) system for collection of particles with mode radius 125 nm and concentration $10 wt\%$. The signal collection distances are: (a) 0.3 mm, (b) 0.6 mm, (c) 0.9 mm, (d) 1.2 mm. Colour corresponds to distribution width, σ

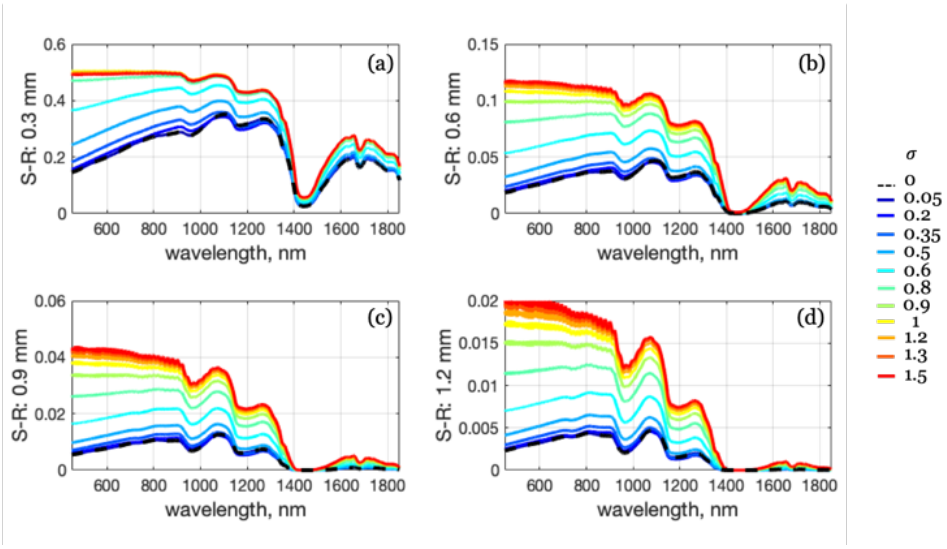

Figure 4.3.11 Spatially resolved diffuse reflectance computed with assumption to mono(dashed lines) and polydisperse(solid lines) system for collection of particles with mode radius 300 nm and concentration $10 wt\%$. The signal collection distances are: (a) 0.3 mm, (b) 0.6 mm, (c) 0.9 mm, (d) 1.2 mm. Colour corresponds to distribution width, σ

at 0.3 mm. It also better separate the spectra corresponding to the width as large as 1 or higher. Nevertheless, both figures show a higher sensitivity of the SRDR to the distribution width than total diffuse reflectance. Despite the higher intensity of the signal for the total diffuse reflectance, the difference in reflectance intensity caused by distribution width does not exceed 0.25 between the smallest and broadest distributions. On the other hand, SRDR spectra at 0.3 mm S-R distance returns signal of relatively high intensity with a difference of ~ 0.4. Moreover, the effect of distribution width is even more pronounced at longer S-R distance in relative units, suggesting a potential to invert PSD from measured SRDR spectra.

Finalising the comparison between two different types of diffuse reflectance, the influence of particle size distribution on the total diffuse reflectance was significant yet less prominent, compared to that on the spatially resolved diffuse reflectance. A more pronounced effect of distribution width on the signal was observed with increased source-to-detector distance. Hence, there is a relationship between the distance that light propagates through the turbid sample and the corresponding size distribution effect. The concept behind this is similar to well - studied light propagation behaviour in tissues [190]. A spectrum, which is captured by a receiving fibre placed close to the emitting fibre is affected by the top layer of tissue only due to low penetration of the beam and less interaction with the tissue, compare to those collected by fibres further away from the source. The collected light loses the intensity due to multiple scattering, however, light penetrates deeper into the tissues and record more of light-matter interactions. A schematic representation of this concept in the context of the PSD effect is depicted in Figure 4.3.14. Even though the signal strength is significantly lower if collected at a further S-R distance, the sensitivity of the signal to physical properties increases. This occurs due to more light-particles interaction and subsequential longer transport mean free path length of the light, which in case of a polydisperse system, allows gaining more information about particle size population.

Effect of concentration on diffuse reflectance

Analysis of bulk optical properties revealed the similarities between distribution width and concentration effect. Similarly to what was shown in the previous sections, the analysis was followed up by the study on the total and spatially resolved diffuse reflectance for the same conditions.

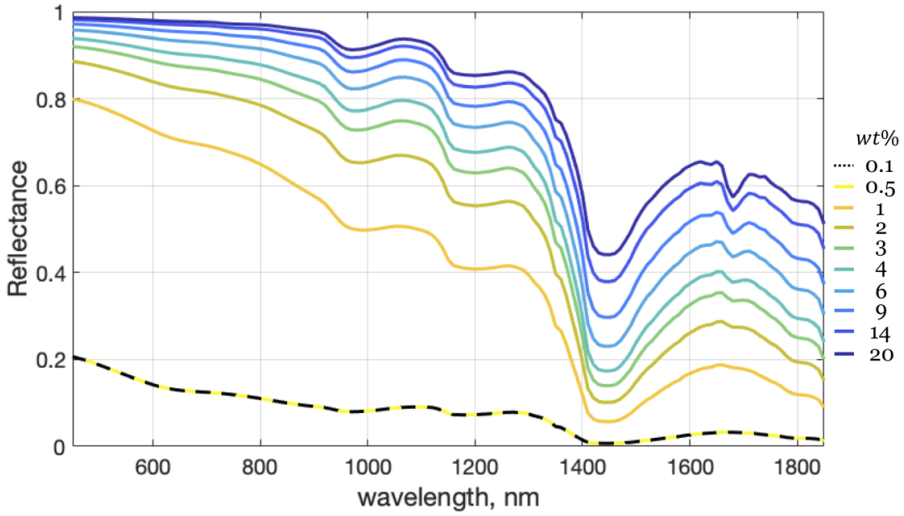

Figure 4.3.12 Total diffuse reflectance computed with assumption to low(dashed) and concentrated(solid) particulate system of monodisperse PSD with mode radius 250 nm.

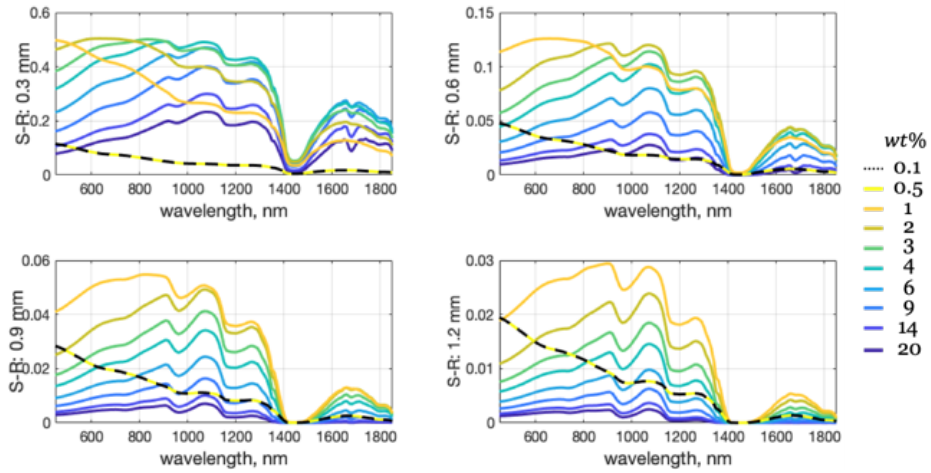

Figure 4.3.13 Spatially resolved diffuse reflectance computed with assumption to low(dashed) and concentrated(solid) particulate system of monodisperse PSD with mode radius 250 nm. The signal collection distances are: (a) 0.3 mm, (b) 0.6 mm, (c) 0.9 mm, (d) 1.2 mm

Figure 4.3.12 illustrates the changes in the total diffuse reflectance signal with changes in the concentration. The intensity constantly increases with an increase in concentration for the wavelength range. Once the concentration approaches 6 wt%, the magnitude of the increment significantly reduces, and, with a further increase of the concentration, the difference between the signals for 14-25 wt% becomes close to untraceable. The differences between different concentrations can be observed at multiple wavelengths, specifically around water absorption peak. At smaller wavelengths (450-1000 nm), differences can be distinguished for the concentration below 4 wt%. The trend shown by the total diffuse reflectance emphasises that the systematic changes in the reflected light can be related to the scattering coefficient, seen in Figure 4.3.5.

The simulated spatially resolved diffuse reflectance signal for the same conditions is present in Figure 4.3.13. At closest S-R distance, spectral intensity increases with the increase of the concentration until the latest reaches ~ 2 wt%. Increasing the concentration further leads to the decrease in the intensity of the diffuse reflectance signal, therefore reverting the signal change trend. The decrease varies at different concentration values, once the concentration approaches high values (~ $14 wt\%$), the difference between corresponding signals significantly reduced. At longer S-R distances, the relative difference between signals of different concentrations decreases with the increase of the concentration. However, the difference between signals at high concentration (>14 wt%) becomes smaller at longer S-R distances and almost negligible at 1.2 mm. Notably, the observations that were valid for low concentrations at 0.3 mm S-R distance lessen at longer S-R distances, meaning that at longer S-R distance, the trend becoming more systematic and if the concentration is above 1 wt%, the SRDR is systematically decreasing.

The results of simulations obtained in this section allow the comparison of the two different diffuse reflectance measurements. The concentration effect on the spatially resolved diffuse reflectance differs from those on the total diffuse reflectance. The opposite direction of the change in total and spatially resolved diffuse reflectance echoes the observations from the mode radius and size distribution effect.

Conclusions

The modelling results gave an overview of what kind of effect parameters of interest can have on bulk optical properties and diffuse reflectance. The latter was also compared in its two forms: total diffuse reflectance and spatially resolved diffuse reflectance. The

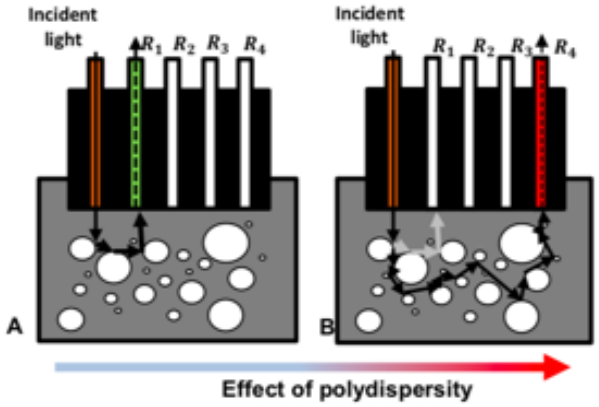

Figure 4.3.14 A schematic image of SRDR measurements taken for polydisperse particle system A: light collection at 0.3 mm; B: light collection at 1.2 mm

variations in physical properties of the particles (mode radius and distribution width) appear strongly on bulk scattering coefficient and asymmetry parameter. The concentration effect influences the bulk scattering coefficient, as well as the absorption coefficient. The bulk optical properties are supplied to the reflectance simulation together, therefore the effect appearance and degree of each effect transforms. One of the major observations is that, due to differences in the measurements types, the trend of parameters effect appears to be in the opposite direction, depending on the type of measurements. This illustrates the distribution of diffuse reflectance intensity, where most of the light n the modelled systems being scattered back at the distance that is not covered by SRDR simulation but summarised into a simulation of total diffuse reflectance. Although, this phenomenon can be illustrated partially from the general decrease of the light intensity with increase of S-R distance in SRDR. Notably, with an increase of the S-R distance, the difference between spectra of different samples increased, the differences were distinguishable at a wider range of each parameter of interest, than on the total diffuse reflectance.

However, despite the apparent beneficial influence of S-R distance increase on the strength of parameters of interest effect appearance on the SRDR, there are concerns regarding its feasibility raised. Since the SRDR intensity decreases with the increase of the S-R distance, the reflectance is not a straightforward way of expressing the relative effect of the parameters. The intensity of the SRDR spectra is lower than total diffuse reflectance which could be a concern regarding the possibility of distinguishing the parameters of interest effect from measured spectra, that is affected by mode radius, distribution width and concentration. The inversion of the parameters of interest, which was a part of the

current project, is generally executed via one of the objective functions, that measures the relative difference between simulated and measured signal. Implementation of the objective function would, therefore, affect the way how the difference between the effects of parameters of interest would be used and interpret in the analysis.

The diffuse approximation is based on the assumption of the isotropic scattering, hence each of the re-radiation events is random at the length of a single tmfp [191]. To satisfy such assumption, the diffuse reflectance signal should be accrued at a minimum of transport mean free path S-R distance. Hence, the potential limitation of the SRDR in its sensitivity to parameters of interest is directly related to which S-R distance is considered for analysis. The direct comparison of tmfp with available S-R distance would help to map the parameters combinations that result in the SRDR signal that lie too close or exceed the diffusion scattering theory limitations.

4.3.3 Study of the combination of parameters of interest on spatially resolved diffuse reflectance

The concerns raised as a result of the previous section study were attempted to be answered in the following section. The study below proposes an alternative view on parameters of interest effect on SRDR. Since the intensity of the light is lower than on total diffuse reflectance and also differs across S-R distances, the relative difference for SRDR was calculated for a combination of parameters of interest. The degree of the effect was then analysed in the context of parameters combinations to compare the degree of parameters of interest influence between S-R distances. The feasibility of inversion of the observed effect was then checked by analysing the tmfp for the same combination of parameters in order to find out the most feasible combination of S-R distances.

The section can be split into three parts. The first part illustrates the relationship between parameters of interest for the monodisperse system, precisely, mode radius and concentration of the solids in the context of the effect they have on SRDR and how it changes with the increase of concentration at different mode radius values. The second part moves the focus onto the SRDR spectra influenced by the combination of a variety of mode radii and different distribution width. Lastly, the effect of the distribution width on the SRDR signal across samples of different concentrations is analysed. Each of the above-mentioned three parts will be followed up by the analysis of SRDR sensitivity of the studied parameters with respect to the corresponding tmfp. There is a minimum value for

the S-R distance existing that can be modelled correctly for a specific set of parameters. This study aims to surface the tmfp at different combinations of the parameters of interest.

The effect of parameters of interest can be quantified by methods, like relative difference or relative change. In current study, it takes a form of a comparison between reference and the studied signal and was executed via formula below:

$$RC = \frac{1}{N_\lambda} \sum_{i=1}^{N_\lambda} \left(\frac{|R(\lambda_i) - R_{ref}(\lambda_i)|}{R_{ref}(\lambda_i)} \right) \cdot 100\% \tag{4.3.1}$$

where $R_{ref}(\lambda_i)$ is the SRDR signal simulated for the particulate reference system, defined in each study below individually, and $R(\lambda_i)$ refers to the simulated SRDR spectra for the conditions to compare. Depending on the properties studied, the condition can be a combination of multiple parameters. As the effect of parameters of interest exhibited strong wavelength dependence, the relative difference considered to be averaged over the selected wavelength range.

Mode radius and concentration

The relative difference caused by concentration changes across different mode radii has been studied first. Looking at the specificity of the effect of concentration in the context of mode radii relationship helps to understand the sensitivity of the SRDR to the classic monodisperse system, prior to escalating the study to the polydisperse system. Figure 4.3.15 presents the relative difference RC between reflectance for monodisperse polystyrene samples at different concentration of solids (R_i) and reference samples (R_{ref}) of very low concentration (0.1 $wt\%$) for particle size in the range between 25 and 650 nm (y-axis).

The changes in reflectance spectra associated with the changes of particle size are consistent to those seen in the literature [131]. They exhibit oscillations which decrease with the increase of the particle size and such pattern is observed across different concentrations at different extent. On the other hand, the variations in the relative difference with an increase of the concentration are of particular interest for this study. Starting from the closest S-R distance, the RC grows with an increase of the concentration up to 4 wt% and until it reaches a plateau of the RC values after 200 nm mode radius. With further increase in concentration, the difference starts to show a decrease. This observation

indicates the transition point between regimes, where the increasing number of particles consequently increases the number of simultaneous scattering events, decrease the tmfp length, consequently contributing to the near-to-source reflectance at the stronger extent. This causes the decrease of the intensity at very high concentration, resulting in the RC values comparable with diluted systems of particles, which is emphasised by pale yellow and white areas in the Figure 4.3.15(a)

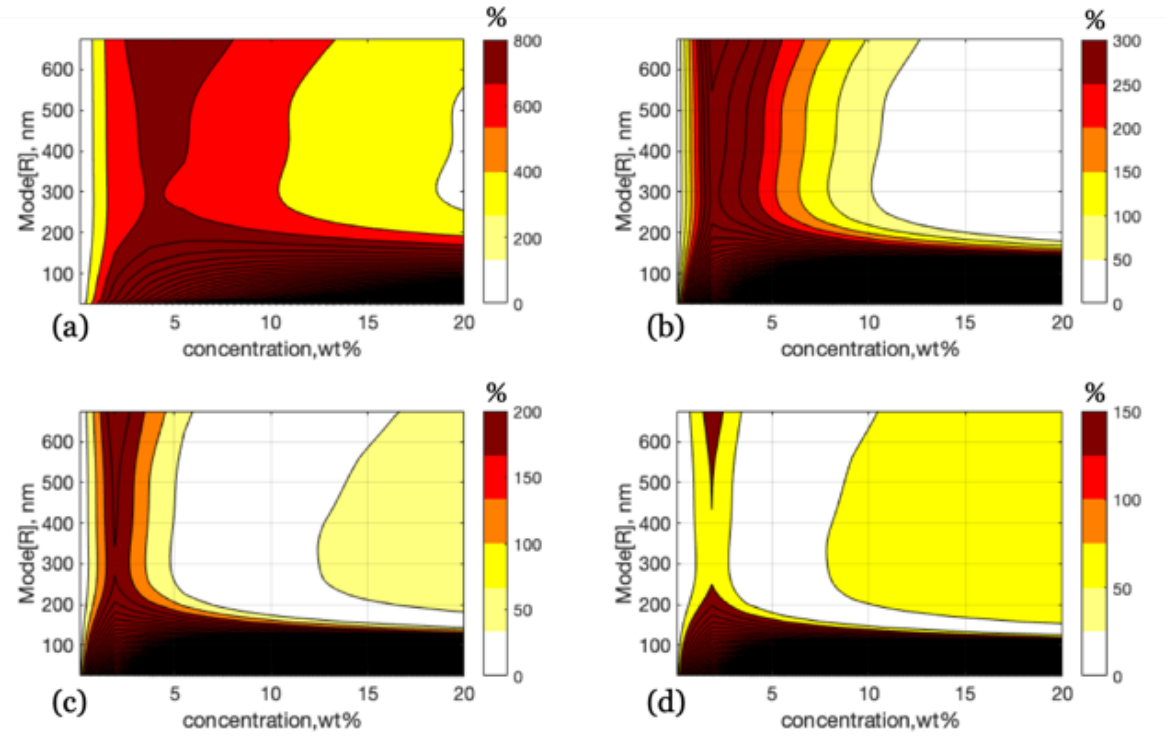

Figure 4.3.15 Relative change, RC between SRDR for monodisperse particulate systems with the low and high concentration of solids.The signal collection distances are: (a) 0.3 mm, (b) 0.6 mm, (c) 0.9 mm, (d) 1.2 mm

The values of the relative difference are the largest at the closest S-R distance compare to other collecting fibres. Apart from the decrease of RC values, with an increase of S-R distance, a number of distinctive changes happen to the diffuse reflectance. The relative change decreases with the S-R distance increase. Reduction in the relative change emphasises the reduce in the specifics of the concentration effect at longer S-R distances across a wider combination of mode radii than at closer S-R distance. The large size of the particles and high concentrations imply that the scattered light does not propagate far enough through the medium to be collected at further distances, resulting in the less

specific effect of above-mentioned parameters on SRDR. In fact, after 0.6 mm S-R distance, the concentration effect on RC drops so low that it reaches the plateau across the majority of the concentrations. Some areas of the plateau indicate the RC values equal to the ones that correspond to the reference SRDR.

Figure 4.3.15 indicates that there are combinations of mode radius and concentration which return the same or similar RC at difference concentration regimes: very low and very high. The variability of the RC between different parameters is also not large beyond ~ 4-10 wt%, depending on S-R collection distance. Therefore, in the context of inverting the parameters of interest, the example above indicates the possibility of local minima and therefore misprediction of the results. These observations raise concerns regarding the possibility of inversion of the correct values of parameters of interest. The possible solution for overcoming this issue can be a result of a combination of the approaches.

First of all, it is desirable to locate the most probable solution before initiating the inversion via solvers. If this can be successfully achieved, then by truncating the search to a moderate range of conditions, the search can be carried out accurately. It is important to note that such a strategy for inversion is only reliable if the most probable solution is located correctly, otherwise, the inversion might be artificially affected by a set of constraints. Lastly, including the SRDR measurement from different S-R distances may help to identify the differences between similar regions better. However, to proceed with this approach, it is vital to know if the signal from S-R distances covers at least single tmfp.

Despite the decreasing of concentration effect over S-R, the signal collected at those distances may help to overcome the limitations that have not been discovered yet, that is arising from the DA theory. Figure 4.3.16 illustrates the tmfp across the mode radii and concentrations analysed. Since the concentration of solids has a significant influence on bulk absorption coefficient, the tmfp is presented below for three wavelengths, instead of an average: for 550 nm (general appearance of the tmfp across UV-vis-NIR), 1440 nm (waver absorption peak) and 1680 nm (polystyrene absorption peak).

Most of the combinations of mode radius and concentration result in relatively short tmfp, under 0.3 mm. As mentioned, the increase of the particle size and concentration per unit volume decrease the tmfp, therefore the reduction of these parameters affect SRDR is expected. The same reasoning explains long tmfp at the area of fine particles and low concentrations. Variations in particle concentration have the most prominent effect on the wavelength of polystyrene absorption peak (Figure 4.3.16(c)), showing that if

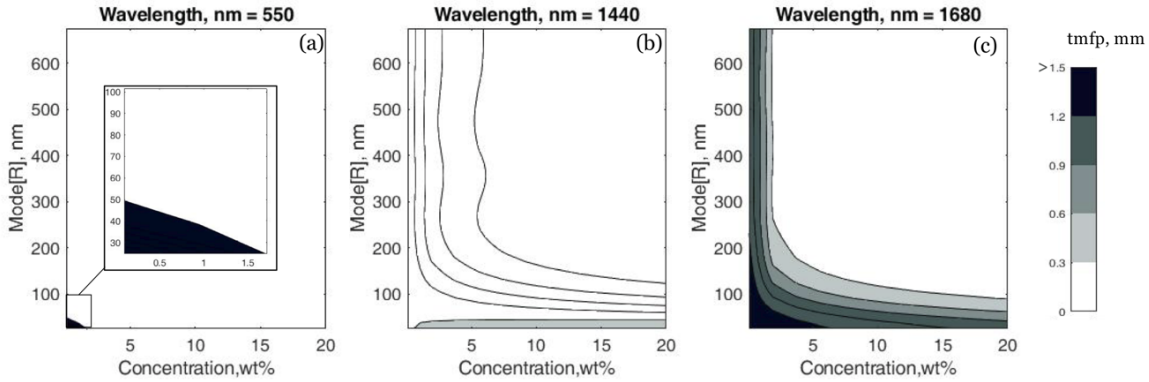

Figure 4.3.16 Transport mean free path corresponding to range of mode radii and concentrations at: (a) 550 nm, (b) 1440 nm and (c) 1680 nm wavelength

this wavelength range is included, the analysis of diffuse reflectance for majority of the concentrations and particle radii below 200 nm will be accurate only if large S-R distances are in use. Concluding this, exclusion of signal from closest S-R distances from the signal analysis can eliminate the need in excluding wavelength.

MODE RADIUS AND DISTRIBUTION WIDTH

Another studied combination was mode radius and distribution width. The comparisons of the effects caused by distribution width on systems with different mode radii have a special interest within this study. Both of the parameters presented are associated with physical properties of particles and the sensitivity of the SRDR measurements to each of them, particularly to distribution width, is the centre of the research interest in the project.

For this study, R_{ref} for Equation 4.3.1 was defined as monodisperse polystyrene system of particles with particle size between 25 and 650 nm. R_i incorporates the distribution width parameter to each of particle size condition, illustrating the relative difference between SRDR spectra for mono and polydisperse system. The results of the RC are presented in Figure 4.3.17

Each subgraph shows the effect of size distribution inclusion on SRDR. At the closest S-R distance, the influence of broadening the distribution width up to 0.5 exhibits the similar relative difference as varying mode radius in size range analysed. Broadening the distribution further results in the significant changes in RC, especially in the area of small particles. The relative difference for these parameters, however, decreases with

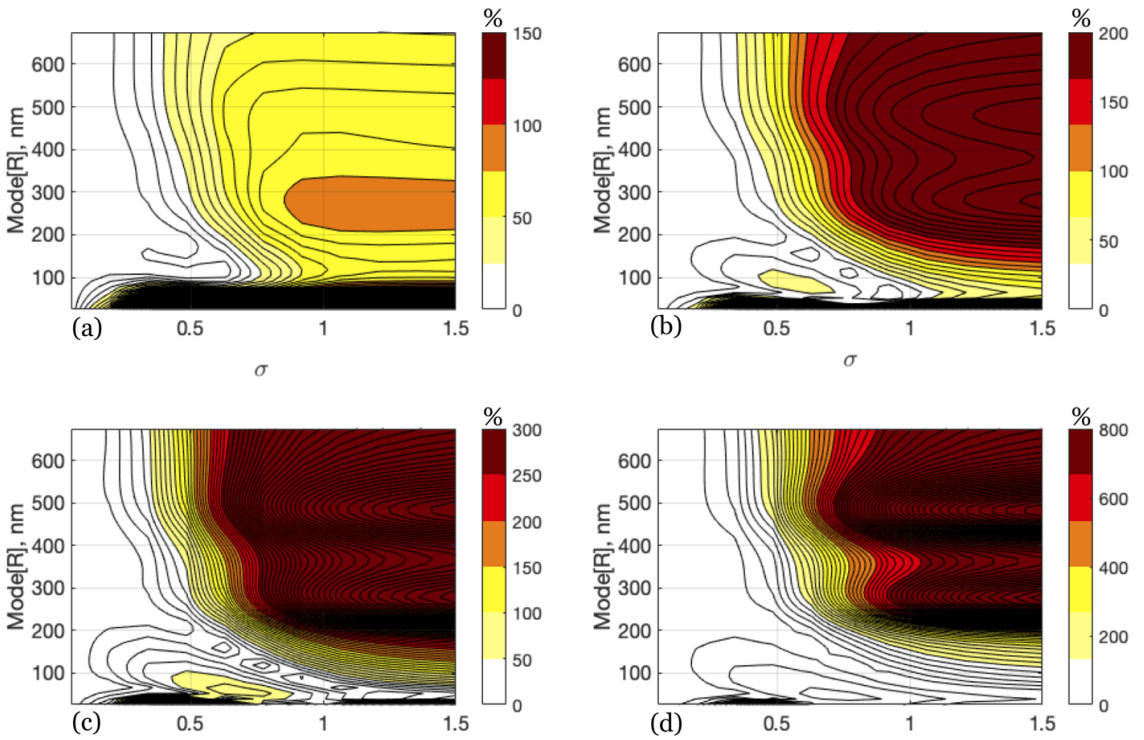

Figure 4.3.17 Relative change, RC, between SRDR signal for monodisperse and polydisperse particulate systems. The concentration constrained to 10wt%. The signal collection distances are: (a) 0.3 mm, (b) 0.6 mm, (c) 0.9 mm, (d) 1.2 mm

the increase of σ. For larger mode radii, the relative change values also becoming more prominent distribution width exceeds 0.5, yet with conditions close to the maximum mode radius and distribution width, the increased rate of RC suspends and remains rather unchanged across parameters neighbouring the limitations of the selected parameter.

At the second closest S-R distance, the relative change increase for the majority of conditions, compared to the closest distance. The variation in the relative difference across various combinations of mode and distribution width become more distinguishable. For mode radius between 200 and 300 nm and σ larger than 0.8, calculated relative change start forming a peak, increasing the RC compare to similar parameters by a few orders. This behaviour progresses with a further increase of S-R distance.

The effect of concentration observed can be discounted as the primary contribution of it is the change in relative difference magnitude. The effect of distribution width below 0.2 can be seen primarily in combination with fine mode radius (below 50-100nm, depending on S-R distance). The difference between combinations of larger mode radii and σ up to ~ 1 changes in the magnitude of the relative difference non-linearly, and appears at

the different degree at different S-R distances. At larger σ, the variations in RC remain similar across different mode radii, despite the large RC to the monodisperse reference systems. However, these variations are not even across different S-R distances, therefore, the simultaneous analysis of multiple S-R distances of SRDR may assist the parameters estimation quality.

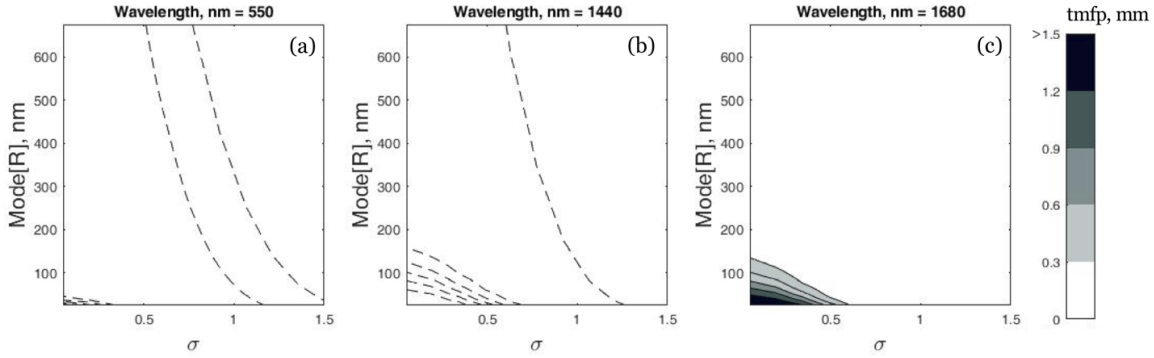

Figure 4.3.18 Transport mean free path corresponding to a range of σ and mode radii at: (a) 550 nm, (b) 1440 nm and (c) 1680 nm wavelength.

The relative changes across chosen parameters combinations can be significant for inversion of the parameters. In addition, the tmfp was calculated for the range of mode radii and σ parameters, identical to the one used earlier in the section. The summary of the results obtained averaged over wavelength can be found in Figure 4.3.18.

The majority of the combinations of mode radius and σ used to provide the signal that is reliable even if collected relatively close to the source (Figure 4.3.18). However, there is an area of values that lead to longer tmfp, which can be explicitly seen in polystyrene absorption peak 4.3.18(c). For this wavelength, the signal collected at 0.3 mm cannot be described by the diffuse approximation accurately. Most of this area can be represented by signal collected at further S-R distances, however, the systems of particles with radius 35 nm or lower and with σ up to 0.25 are having the tmfp longer than the SRDR fibres placements and therefore this signal cannot be simulated accurately within the current experiment. To overcome this limitation, the simplest solution is to manipulate the wavelength range used for analysis, selecting the range with minimum or no combination of parameters where tmfp exceeds the measurement configuration. Alternatively, as was mentioned in Section 4.3.3, the SRDR signal collected at closest S-R distance may not be used in the analysis to ensure the compliance with the diffuse approximation regime.

DISTRIBUTION WIDTH AND CONCENTRATION

The last combination of parameters to analyse is the concentration of particles and the distribution width. Previously, it was discovered that the effect of these parameters on SRDR is similar as it takes the form of the magnitude change between lines. Although the change of the magnitude from concentration variation is opposite to the changes caused by σ changes, the similarity between the effects might be an obstacle for parameters inversion. To gain a better understanding of the effects of interference, the analysis of simulated SRDR was conducted.

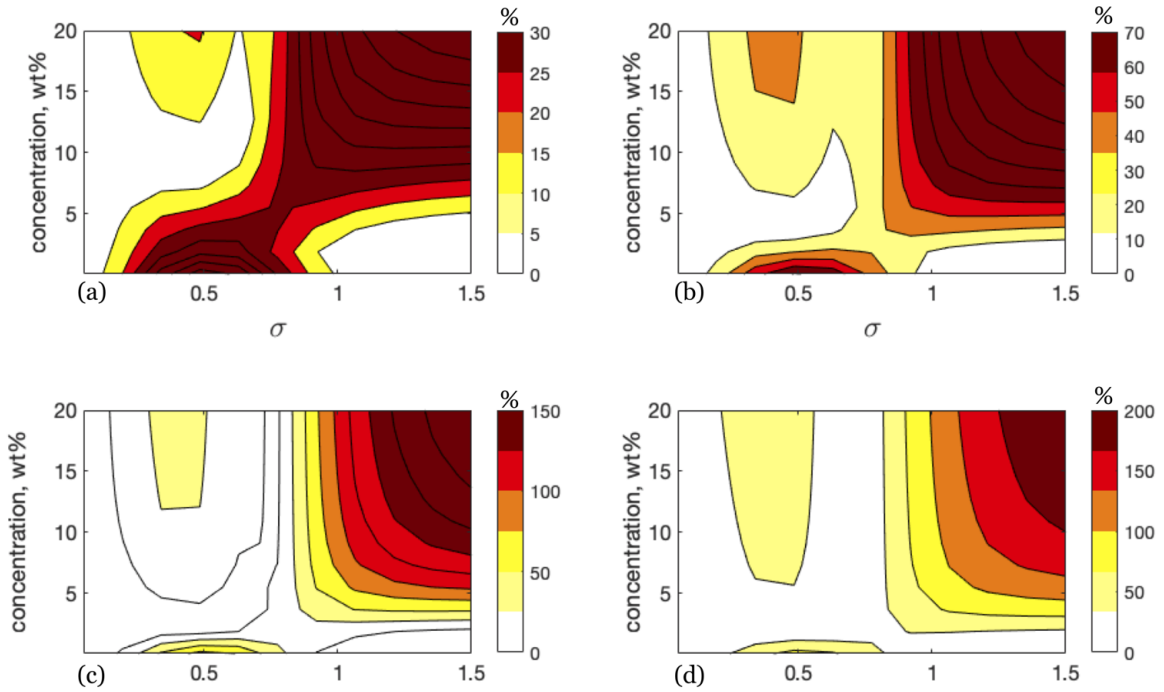

Figure 4.3.19 Relative change, RC, between SRDR signal for monodisperse and polydisperse particulate systems for range of concentration of solids. The mode radius constrained to 250 nm. The signal collection distances are: (a) 0.3 mm, (b) 0.6 mm, (c) 0.9 mm, (d) 1.2 mm

The reference reflectance in this analysis (R_{ref}) corresponds to monodisperse suspensions with a constant mode radius 250 nm, which was chosen as the parameter that illustrates the RC variations generally applicable to the most of the sizes in the selected range. As seen in Figure 4.3.19, the signal, corresponding to the closest S-R distance expresses a complicated pattern across σ. The effect of distribution broadening up to 0.1 is weak and not specific across concentrations. At larger σ, the relative difference increases, however not evenly for different concentrations. This effect leads to stronger

differences between different combinations of parameters, yet it also results in combinations where the relative difference drops to values comparable to the monodisperse system. Such response appears similarly at all of the S-R distances analysed. The number of combination of parameters at which RC is lower than 25% and the variation between neighbouring conditions is below 5% increases with the increase of S-R distances. At the same time, the relative difference for large concentrations and large σ increases drastically. The presence of small relative difference across multiple parameters combinations implies the possibility of the existence of such SRDR that would correspond to more than one combination of parameters of interest. These combinations are not the same but similar across different S-R distances, therefore this issue cannot be tackled by a reasoned combination of S-R distances for inversion. Some of those combinations are far apart and can lead to large over/underestimations.

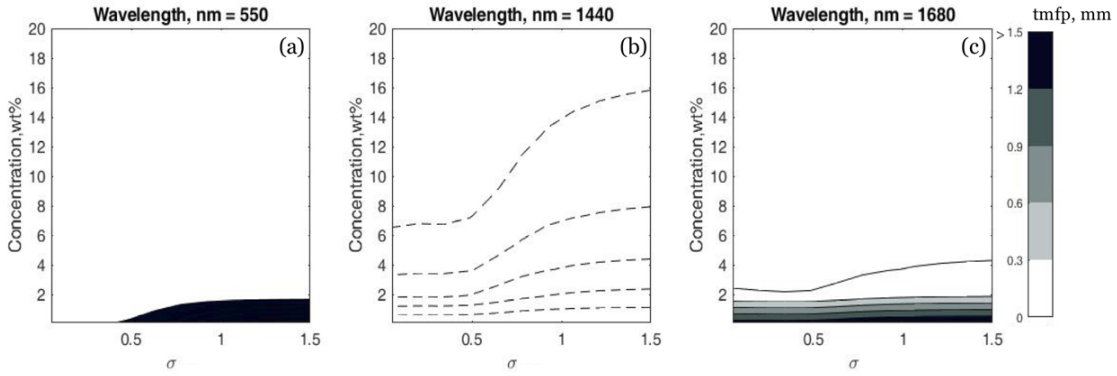

Figure 4.3.20 Transport mean free path corresponding to a range of σ and concentrations at: (a) 550 nm, (b) 1440 nm and (c) 1680 nm wavelength

One of the approaches to consider is to invert the parameters of interest in separate steps. Mode size and concentration, as parameters that cause the most significant change in the magnitude of the SRDR, can be inverted in tandem to pre-locate the most probable values, whereas σ may be inverted afterwards. Since the effect of σ is limited below 0.1 and above 1, the values outside this range can be excluded from the analysis. This solution route is applicable if discussed in the context of the inversion algorithm as the pre-location of the minima must not interfere with the global minima search. This suggestion will be discussed in more details in Chapter 5.

Another limitation that can be brought to the discussion is the applicability of the diffuse approximation within some concentration boundaries in the context of polydisperse

systems analysis. As illustrated in Figure 4.3.20, the transport mean free path of diluted samples (<2 wt%) exceeding the SRDR receiver distances and therefore the simulation would not be accurate. This example is valid for mode radius of 250 nm and all of the studied σ, however, other mode radii and wavelengths have shown a similar result. Similarly to the proposal in Section 4.3.3, isolation of specific wavelength or excluding the closest S-R distance maybe a potential solution. The main shortcoming of such approach is that it is not universal and would be applicable for polystyrene and studied wavelength range, however with similar research conducted on different materials, it could be possible to optimise the limitation establishment, which will be elaborated in future work discussion.

4.4 Conclusion

This chapter aimed to investigate the performance of the model developed for the forward calculation of SRDR, validate the chosen method and to specify the parameters and the constraints needed for successful estimation of the concentration and size distribution parameters of polystyrene colloid suspensions based on simulated results. As part of this study, there was a particular interest in studying the effect of source- to-receiver distances on the simulated reflectance signal for inverting the properties of the suspension.

To meet these aims, a systematic analysis investigated the influence of each of the considered variables, namely different mode radii, distribution width and concentrations onto different types of diffuse reflectance. The effects from the above-mentioned parameters were studied in combinations with each other and hence surfaced potential challenges. As a result of the experiment, three significant outcomes were gathered.

Total diffuse reflectance exhibited high sensitivity to the mode radius and concentration variations, lesser to the distribution width parameter. The sensitivity of the SRDR to the same parameters of interest is higher overall, exhibiting stronger wavelength dependence and response to the parameters of interest variation. However, the intensity of the signal is lower, especially at the longer S-R distances due to natural losses of the light during its propagation through the medium.

The beneficial impact of spatially resolved diffuse reflectance was investigated in more detail, focusing on the combinations of the parameters of interest. Collection of the spectra from the multiple S-R distances unveils changes in the spectra, that are specific to

the particular combination of the parameters of interest, indicating the potential for the inversion possibility.

The diffuse scattering regime limitations were identified if insufficient S-R distances for diffuse approximation were used for polystyrene suspensions of the selected range of the parameters of interest. The combination of concentration and distribution width has resulted in a wide area of similar solutions, which should also be considered during the inversion development and the inversion results justification. Multi-staged inversion with pre-location of the most probable solutions was proposed as a vector for inversion routine development.

CHAPTER 5

EXPERIMENTAL AND METHODOLOGY AND DESIGN

This chapter describes the types of equipment, methods and experimental design used in this work. First, a dataset from monodisperse polystyrene suspensions is investigated to validate the methodology developed. Then, a second dataset, from polydisperse polystyrene particles suspensions is studied. The study is followed by an analysis of another two sample sets, which consist of more challenging particle constituents, like non-spherical particles. Section 5.3 describes the SAR-DRM system, including the hardware set up and the data processing steps. Section 5.4 describes the method for inverting performance.

5.1 EXPERIMENTS

5.1.1 SAMPLE SET 1: MONODISPERSE POLYSTYRENE SUSPENSIONS

The dataset was compiled using a published dataset from polystyrene suspensions [120]. Seventeen polymerisation reactions were run with varying experimental parameters (surfactant and initiator amounts, reaction time and temperature) to prepare monodisperse polystyrene particle suspensions. Materials for the reactions were purchased from Sigma-Aldrich (United Kingdom). Resultant suspensions vary in mode radius Mode[R] between 50 - 250 nm. The 45 samples dataset was formed from the 17 original samples and their derivatives after four serial dilutions. A detailed description of this particular dataset is available in recent work provided by Chen et al. [120].

Table 5.1.1 Parameters of monodisperse polystyrene suspensions

Sample name	Mode[R], nm	Conc, wt%
1	80.75	12.97
2	102.5	13.04
3	190.75	10.54
4	223.75	10.68
5	177.75	12.63
6	69.75	12.66
7	96.75	12.75
8	107.5	9.37
9	127	12.36
10	188.75	12.67
11	160.5	12.87
12	69.75	7.68
13	188.75	7.64
14	102.5	6.26
15	223.75	5.13
16	96.75	6.12
17	188.75	6.10
18	190.75	4.03
19	223.75	4.03
20	69.75	4.79
21	96.75	4.74
22	107.5	3.57
23	127	4.70
24	188.75	4.78
25	160.5	4.87
26	80.75	3.93
27	190.75	3.14
28	223.75	3.21
29	103.5	3.78
30	177.75	3.80
31	96.75	3.78
32	107.5	2.85
33	127	3.73
34	188.75	3.79
35	160.5	3.86

The SAR-DRM were collected for all 45 suspensions, however, based on the quality of the spectra, a spectra sub-dataset of 35 suspensions was formed and used in this study. The sub dataset was selected in such a way that the original 17 reactions has at least one dilution present in the new dataset. Those samples are expected to have similar mode radius while differing only on the concentration of solids. The information about mode and concentration for the final 35 samples was provided in Table 5.1.1.

5.1.2 SAMPLE SET 2:POLYDISPERSE POLYSTYRENE SUSPENSIONS

One of the most important validation studies in this project would be an analysis of the degree of polydispersity effect on spectra measurements. The previous set of suspensions is ideal for method validation and sensitivities analysis for parameters of interest like predominant particle size (mode radius) and concentration of solids. Although those samples have some degree of polydispersity, it may not be sufficient to analyse the effect of size distribution and its interference with other physical properties. To conduct such an analysis, another set of samples that consist of polydisperse suspensions was created.

Table 5.1.2 Monodisperse polystyrene suspensions particle size and concentration used for creating polydisperse suspensions.

Sample name (SN)	Mode[R], nm	Conc, wt%
1	62.6	14.47
2	84.8	14.82
3	87.7	14.31
4	128.4	14.15
5	136.8	14.07
6	140.6	14.42
7	153.1	14.38
8	166.6	13.79
9	200.7	10.89
10	223.0	8.18
11	249.6	10.84

The sample set was prepared by mixing a set of monodisperse polystyrene suspensions of a different mode radius. The suspensions for the experiment were chosen from available

polystyrene suspensions synthesised similarly as the last sample set. Monodispersity of the suspensions was evaluated by the reference method, such as dynamic light scattering (DLS). Eleven polystyrene suspensions were used in the experiment with the mode radius ranges between 62.6 to 249.6 nm with an average interval of 20 nm. It creates a relatively uniform size grid for forming particle mixtures with various mode radius and distribution width. Particle radius and original concentrations are given in Table 5.1.2

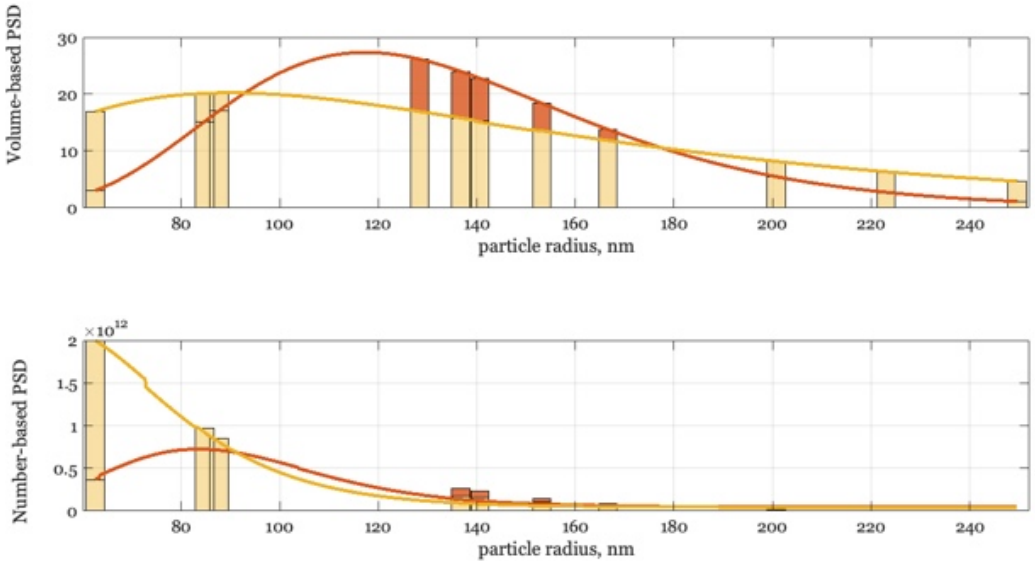

Figure 5.1.1 Calculated proportions of suspensions additions into the mixtures presented as (a) volume-based population, (b) number-based population

Table 5.1.3 Calculated proportions of suspensions additions into the mixtures presented as volume-based and number-based distribution

	Volume –based distribution		Number –based distribution	
	$\bar{R}$, nm	σ	$\bar{R}$, nm	σ
SN1	128.40	N/A	128.40	N/A
SN2	117.24	0.30	83.73	0.22
SN3	89.91	0.60	62.57	0.34

In such mixture, each suspension would correspond to a specific size population of a newly prepared mixture. The desired contribution proportion was pre-calculated based on volume-based lognormal distribution. The distribution of each mixture has the same mean radius, $\bar{R}$, whereas the distribution width controls the volumetric contribution of the

suspended particles to the mixture. Mean radius was assigned to 128.4nm, the distribution width was chosen to obtain two samples with distribution width broad enough to include all the sizes in (Table 5.1.2), while being different from each other to verify the sensitivity of the measurements. The parameters for describing the PSD of the mixtures are presented in Table 5.1.4.

Based on the pre-calculated volume-based proportions, two mixtures of the same mean radius but different distribution width were prepared. The full polydisperse sample set 2 consists of these two mixtures and one original monodisperse suspension of the same mean radius. The original suspension and mixtures had a concentration of polystyrene particles ~ 13 wt%. Each of the samples was further diluted into two concentrations, making a total of 9 samples in this sample set. These suspensions were diluted by deionised water to expand the sample set with suspensions of different particle concentrations for each suspension, approximately 6.5 wt% and 3.5 wt%. The details regarding the sample set concentration can be seen in Table 5.1.5.

The advantages of the chosen method over synthesis are:

- Rapid method to prepare a set of samples with different distribution width;

- Opportunity to control the distribution width of the end product with greater accuracy than directly synthesised by polymerisation reaction;

The main disadvantage of the chosen methodology would be the possibility of complicating samples with bi-modality of size distribution. However, mixing suspensions of similar particle size may blend the gaps between the sizes in enough extent to eliminate the bi-modality.

Table 5.1.4 Mode radius and distribution width of the lognormal distribution fitted to the DLS of polystyrene suspensions of the Sample set 2

Sample	Number-based distribution	
	Mode[R], nm	σ
SN1	106.44	0.28
SN2	101.67	0.38
SN3	84.03	0.45

Table 5.1.5 Concentration of solids in different dilutions of polydisperse polystyrene samples

Composition					
Original sample,wt%		1^{st} dilution,wt%		2^{nd} dilution,wt%	
Sample name	Conc,wt%	Sample name	Conc,wt%	Sample name	Conc,wt%
SN11	12.99	SN12	6.50	SN14	3.25
SN21	12.98	SN22	6.49	SN24	3.24
SN31	13	SN32	6.50	SN34	3.25

5.1.3 Complex sample sets

Sample set 3: Polydisperse polystyrene suspensions synthesised from polymerisation reactions

Another set of polystyrene suspensions, Sample set 3, with different levels of polydispersity was synthesised by a polymerisation reaction. Instead of mixing a set of pre-made suspensions, control of polydispersity can be achieved by synthesising the suspension using a modified addition procedure of the initiator. This is concluded from the fact that in a standard polymerisation process, the growing phase of the colloidal particle a monotonically decreasing function of time. In order to produce a monodisperse suspension, the initiator has to be added at the beginning of the reaction in order to start the reaction so that all polymer chain nucleate at the same time. The growing phase of the particle starts quickly after the nucleation phase, and particle grows uniformly. In this study, the experiment used gradual delivery of initiator to the reactor to polymerise the monomer at a different time and, therefore, lead to a non-uniform particle size distribution. In principle, the longer the initiator is supplied into the system, the broader the size distribution becomes. The link between the length of the nucleation stage and size distribution of the end product was studied previously [192]. The experimental procedure is designed based on the different procedures of adding the initiator. By varying the amount of each initiator part, when each part is added and its adding speed, the size distribution and total reaction time will be affected. By supplying the initiator gradually at the beginning of the reaction, the formation of the particles will be initiated and the gradual addition would allow the

Table 5.1.6 Composition and process parameters for the Sample set 3 of polystyrene suspensions

	Composition				Process parameters	
Sample	Monomer, ml	Surfactant, g	Initiator,g		Pump speed ml/min	TRT min
			syringe pump	at once		
SR1	200	1.48	0.09	1.71	0.4	132
SR2	200	1.48	0.54	1.26	0.4	163
SR3	200	1.67	0.9	0.9	0.52	143
SR4	200	1.67	1.26	0.54	0.52	161

forming particles to grow into a reasonably large size. Addition of the second part of the initiator, shortly after the supply of the initiator part via syringe pump finishes, will initiate the reaction with remaining monomer, forming a size distribution peak in the are of small sizes. Such an approach should form the distribution similar to lognormal.

The polymerisation reaction used in this study is the same to those described by Chen *et al* [120], except the procedure for adding the initiator. Apart from deionised water, the reaction requires monomer (styrene, 99%, Sigma-Aldrich), surfactant (sodium dodecyl sulfate, 98.5%, Sigma-Aldrich) and initiator (potassium persulfate, 99.0%, Sigma-Aldrich). The styrene polymerisation reactions were carried out in a 2L glass reactor with a heating jacket, an impeller and a thermometer. The initiator and surfactant were weighted in their powder form (quantities of which in grams can be found in Table 5.1.6) and then diluted in the aliquot of the deionised water. A 1L of deionised water was prepared in a volumetric flask. The 50 ml of water from the measured amount was taken for dissolving the initiator, the rest was mixed with surfactant. The heating jacket temperature was controlled by a thermostatic bath (Huber Compatible Controller, GmbH) connected to a temperature sensor. An overhead stirrer (Radleys RS37) was connected to the bladed impeller and operated at a constant mixing rate. A syringe pump was employed for adding the initiator to the monomer mixture at a controlled speed.

Using empirical knowledge about suspension polymerisation [120], the amount of the initiator used at different stages, the speed of initiator supply and the total reaction time (TRT) were estimated (Table 5.1.6). Some of the reaction parameters, like the temperature of the reaction and mixing rate, were kept constant across reactions as 70^0C and 200 rotations per minute (RPM) respectively.

The weighted initiator after being dissolved in the 50 ml of deionised water, was separated into two portions according to the recipe. The corresponding part of the

solution is placed in a 40 ml syringe. A PVC hose (1 cm in diameter) was connected to the syringe, and the other end was connected to a 0.1 ml pipette tip which enters the reactor, with each end tightly fixated. The syringe pump delivers the initiator solutions at the set speed, followed by the addition of the second part of the initiator.

Table 5.1.7 Mode radius and distribution width of the lognormal distribution fitted to the DLS of polystyrene suspensions of the Sample set 3

	Number–based distribution	
Sample	Mode[R], nm	σ
SR1	43.32	0.16
SR2	40.62	0.12
SR3	59.09	0.22
SR4	82.47	0.49

Increasing the amount of time for the gradual addition of the initiator subsequently led to an increase in the reaction time. Due to the time constrains for experiment performance, samples SR3 and SR4 were based on faster reactions. As can be seen from Table 5.1.6, these changes were reflected in the amount of surfactant, which differs from SR1 and SR2.

Suspensions obtained were used to make a sample set consisting of original suspensions and their dilutions. Table 5.1.8 provides information the particle size and composition in the sample set. The dilution protocol was identical to the one used for Sample set 2.

Table 5.1.8 Dilution table for the Sample set 3 of polystyrene suspensions

Original sample,%wt		1^{st} dilution,%wt		2^{nd} dilution,%wt		3^{rd} dilution,%wt		4^{th} dilution,%wt	
Sample	Conc,%wt	SN	Conc,%wt	SN	Conc,%wt	SN	Conc,%wt	SN	Conc,%wt
SR1	15.37	SR12	12.00	SR13	9.00	SR14	6.00	SR15	3.00
SR2	15.16	SR22	11.98	SR23	8.99	SR24	5.99	SR25	2.91
SR3	14.90	SR32	12.00	SR33	8.95	SR34	5.97	SR35	2.98
SR4	15.60	SR42	12.00	SR43	8.99	SR44	5.99	SR45	2.99

SAMPLE SET 4: CELLULOSE NANOCRYSTALS (CNC) AQUEOUS SUSPENSIONS

In the framework of the developed approach, the study aims to characterise the physical properties of the particle in full. This requires an understanding of the effects caused by

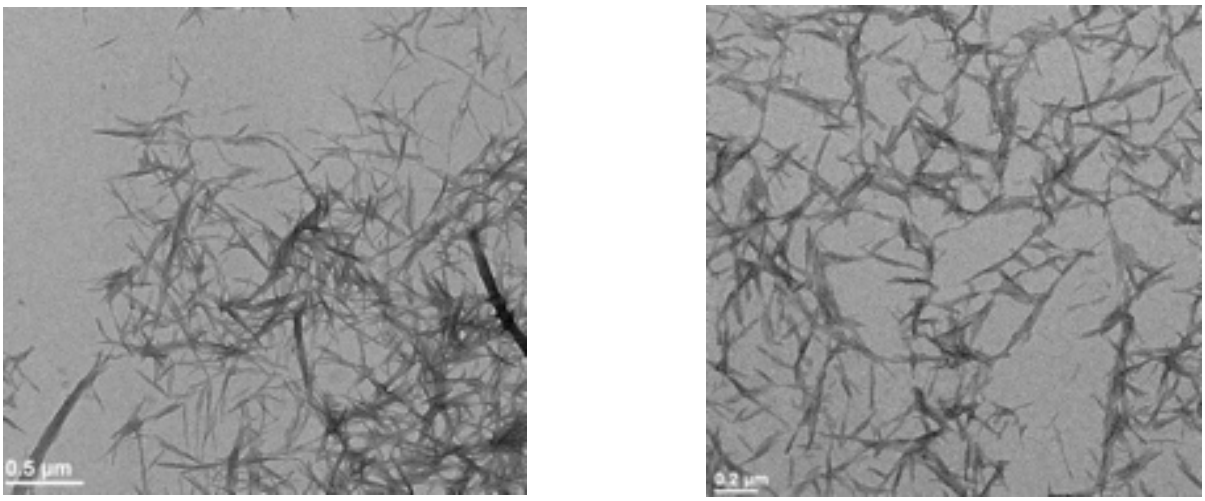

(a) (b)

Figure 5.1.2 Electron microscope image of cellulose nanocrystals (a): BG Natural; (b):BG Ultra. Image obtained using FEI Tecnai 12 BioTwin microscope at 120 kV [193]

the full aspects of physical properties. The inclusion of particle shape into analysis would be a rational step to undertake. Apart from modelling of the diffuse reflectance for the non-spherical particles, the project conducted a study on the spectra dataset measured from the suspension of the non-spherical particles.

The choice of the material for such a study was based on a few requirements. As discussed in Chapter 2, the size of the particles, when exceeding $x \sim 1$ forms a forward diffraction peak of the scattered light, which causes problems in the application of diffuse reflectance theories. Considering the size limitation arising from chosen theory, a nano-scale material which is highly non-spherical and available in the form of colloidal suspension is desired. Needle-like cellulose nanocrystals (Figure 5.1.2) are chosen due to its wide usage in biomedical, wastewater treatment, energy and electronics industrial sectors which results in their availability commercially.

The CNC suspensions studied are supplied by Blue Goose, Canada. Two types of the material were provided: BG Ultra, which contains 8 wt% CNC in aqueous gel with uniform nanocrystals, and BG Natural, a 7.4 wt% aqueous gel which has varied size and aspect ratio distribution from batch to batch. From the specification of the material, it is known that a typical crystal length in both samples is 100-150 nm and diameter 9-14 nm.

Above a certain concentration, approximately 3.5 wt%, CNCs can self-assemble into a nematic or chiral nematic liquid crystalline phase [194] which would divert light scattering behaviour from diffuse approximation. Liquid crystalline phase appears as gelation of

Table 5.1.9 Concentration of CNC samples from Sample set 4

Sample name	1st dilution, wt%	2nd dilution, wt%	3rd dilution, wt%
BG Ultra	3.08	1.56	1.29
BG Natural	6.55	3.64	1.76

the liquid suspension and, among other parameters, depends on particle size [195]. As characterised by the supplier, the samples available for analysis differ in crystals length distribution and therefore hydrodynamic particle size, which is illustrated in Figure 5.1.2. Therefore, original gels were diluted to the point at which the original get begins to liquefy. This concentration becomes the concentration corresponding to the 1st dilution, which is diluted two more times afterwards. The full list of samples dilutions is present in Table 5.1.9.

5.2 Reference measurements

The objective of the measurement is the determination of sample characteristics which are going to be inverted, i.e. mode radius, distribution width and concentration. The particle content analysis is conducted using a gravimetric approach and the PSD parameters are determined using dynamic light scattering-based methods, where the detailed description of procedures performed can be found below.

5.2.1 Gravimetry analysis

Particle concentrations of all suspensions were measured via gravimetric analysis, which is the standard technique used in the chemical industry. In this study, we used two different materials and therefore the methodology vary slightly.

For estimation of the monomer conversion, one millilitre of the suspension was removed from a sample by micropipette and placed in a weighted, dry, empty glass vial. Before that, the dry empty vial, then same vial filled with the sample was weighed and the weights recorded. Then, vials were placed in an oven at 65^0C for 24h to evaporate all present solvents. The actual concentration of solids was calculated based on the mass of suspension placed in the vial, the weights of the dry mass, densities of material and medium. It also discounts the weights of the other solid materials present in the suspension (surfactant and initiator).

Measurement of cellulose nanocrystals concentration in the suspensions was carried out using gravimetric analysis procedure described by [196]. It involved evaporating solvent of approximately a 1.5 g sample at 90^0 C in a ventilated oven. In 1h, after most of the solvent evaporated, the mass of the beaker was determined every hour until the residuals of moisture evaporated as well and the constant mass was achieved [196].

5.2.2 PARTICLE SIZE MEASUREMENTS

Dynamic light scattering (also known as photon correlation spectroscopy) is a very powerful tool traditionally used for studying the hydrodynamic radius of macromolecules. The mode particle radius, Mode[R], and distribution width, σ, were measured using dynamic light scattering (DLS) by ALV-MBH (ALV/CGS-3 Platform based Goniometer System). Particle size information for Sample set 1 was provided along with a sample set from the DLS measurements. All sample sets discussed here were analysed via DLS technique, however, Sample set 2 was also run through nanoparticle tracking analysis (NTA), Nanosight (Malvern). Since the latest was used exclusively on Sample set 2, reference mode radius and distribution width measurements, refereed through the thesis, are the result of DLS number density function measurements, that were fitted in OriginPro 2018 to log-normal distribution function using Non-linear curve fit tool.

DYNAMIC LIGHT SCATTERING

Dynamic light scattering requires the analysis to be conducted at particle concentration that produces a single light scattering event. Therefore, to avoid distortion due to particle-particle interaction, polystyrene suspensions were diluted by over 1000:1 proportion to create a just barely cloudy suspension.

Dynamic light scattering measurements by ALV-MBH were collected at room temperature from a glass vial containing a sample-filled cylindrical cuvette surrounded by toluene. The range of scattering angles measured by the detector was set to a very narrow value near 90^0. The viscosity of water was adjusted according to temperature fluctuations before every measurement. The collection time was set for 20 seconds with five runs per measurement. Three repetitions of measurements were made for each sample, the results of sample size analysis and size distribution were returned by the software supplied with the instrument.

NANOPARTICLE TRACKING ANALYSIS (NTA)

Similarly to DLS, highly diluted samples needed for best performance. Original samples were diluted down to 3000:1 to ensure that the number of particles in the frame does not exceed 200. The video frames were recorded for 60 seconds. NanoSight is supplied with a software which is operated with either automatic or manual settings for Camera Control. For consistency, automatic settings were used throughout the measurements, whereas the viscosity of water was set to the 0.0089 poise which corresponded to the average temperature in the room. The video frames collected are processed to return the distribution of particles sizes.

5.3 SPATIALLY AND ANGULARLY RESOLVED DIFFUSE REFLECTANCE MEASUREMENTS (SAR-DRM)

5.3.1 SAR-DRM INSTRUMENT SETUP

The setup of the SAR-DRM system includes a multi-fibre optical probe, a light source and UV-vis and NIR spectrometers in conjunction with a multiplexer [120]. An illustration of the SAR-DRM setup can be seen in Figure 5.3.1.

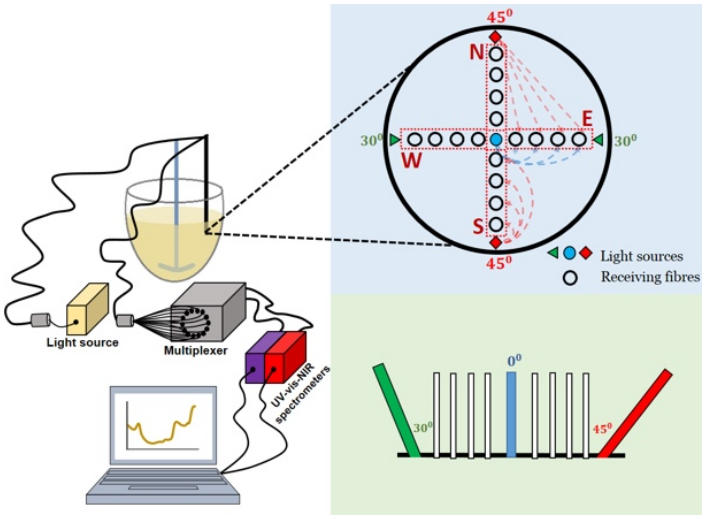

Figure 5.3.1 Schematic representation of SAR-DRM system

The SAR-DRM probe is a custom-built apparatus that uses 5 source and 16 receiving fibres to perform the diffuse reflectance measurements. The light source uses a 50W halogen lamp, powered at 12 V input voltage. The light source is connected to the light source fibres of the probe. The setup also includes a shutter for blocking the light from coupling into the source fibres.

All of the receiving and source fibres have a numerical aperture of 0.22 and a diameter of 200 μm. Fibres are placed to form a cross at the tip of the optical probe with a 0.3 mm distance between each other. The receiving fibres can be combined into branches based on their location regarding the centre of the probe: North(N), South (S), East(E), West(W). Light can be emitted at 3 different angles to the surface of the probe: 0^0, 30^0 and 45^0, whereas all collecting fibres are normal to the probe end. Each branch of the detecting fibres has an angular light source placed at the end of the branch. A normal incidence source is placed at the centre of the probe (Figure 5.3.1). Since the angular light sources are not employed in this study, the probe design offers a total of 16 combinations between source-to-receiver distances for the normally emitted light.

All detecting fibres are connected to an optical multiplexer (FOM-UVIR200-2 x 8, Avantes). Fibres are individually coupled by the multiplexer to spectrometers. The multiplexing is achieved by a stepping motor for switching the connection between detecting fibres and the spectrometers.

Spectra are collected by 2 spectrometers in UV- vis- short NIR (USB4000, Ocean Optics) and NIR (NIRQuest 2.2-512, Ocean Optics) spectral regions. The UV-vis- short NIR spectrometer covers a spectral range between 350 and 1000 nm with around 0.2 nm spectral interval (3648 data points). The NIR spectrometer measures spectra between 900 and 2100 nm with 4 - 5 nm spectral interval (512 data points). Typical measurement time per fibre for the UV-vis is 25 - 100 ms and 2 s for the NIR spectra.

The same workflow also had to be repeated for a 3" integrating sphere (IS). It is a hollow spherical cavity with walls that have non-absorbing and only diffusely reflective properties. SAR-DRM spectra from IS were used as the calibration for the SAR-DRM system as it provides signal intensity free from the effects of beam shape, incident direction, and incident position [197].

Both sets of measurements, sample and IS were taken with the incident light being on and off. Therefore, four sets of the signal were collected:

I_{on} - the signal detected from the sample with the light-emitting onto a sample,
I_{off} - the signal detected from the sample with no incident light,
B_{on} - the signal detected from the integrating sphere, and
B_{off} - the signal detected from the integrating sphere with no incident light

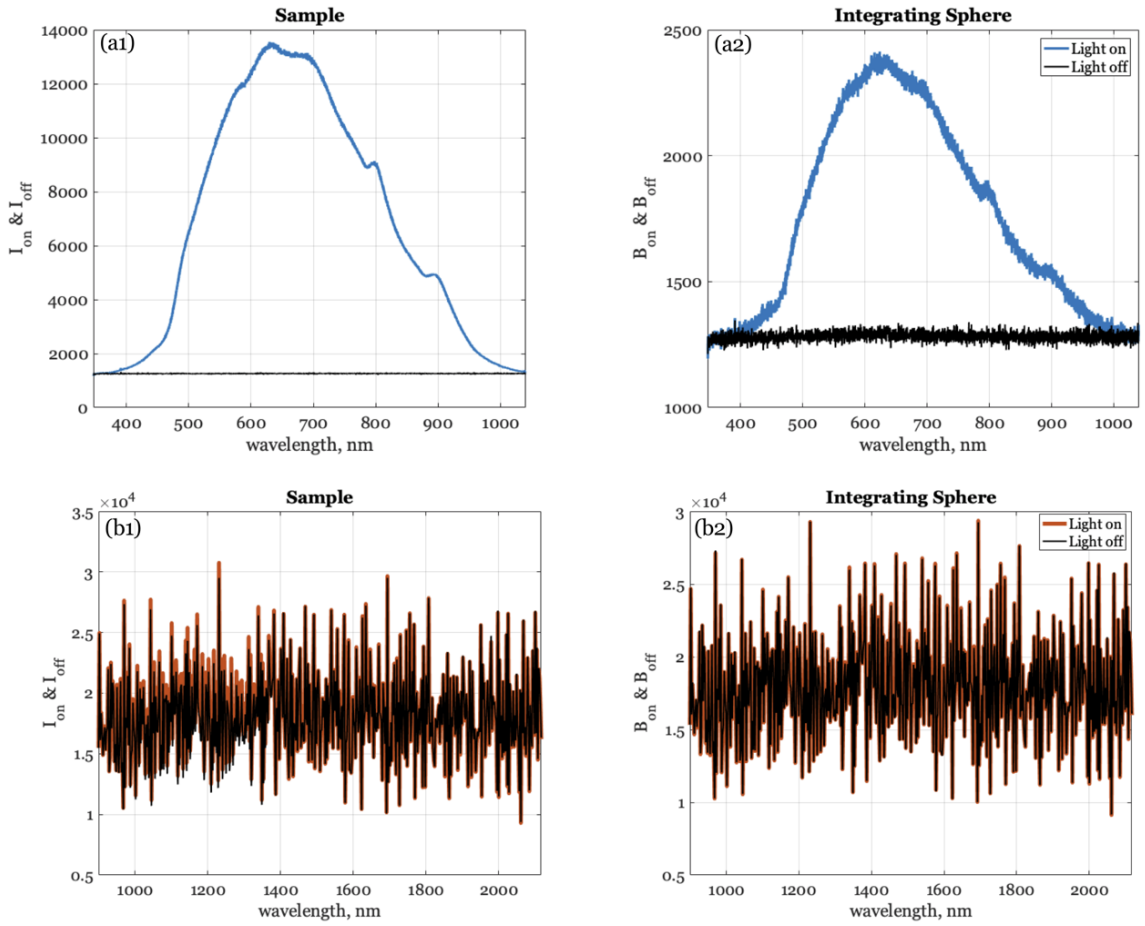

Figure 5.3.2 SAR-DRM spectra in (a) UV-vis-short NIR and (b) NIR regions. Colour corresponds to light being switched on or blocked from the sample.

The SAR-DRM system is controlled by a Matlab based software (developed in R2012b version) which command the moving of the multiplexer's stopping motor and the spectra acquisition.

5.3.2 SAR-DRM SIGNAL PROCESSING

Spectra collected by SAR-DRM cannot be used in analysis straight away, there is a number of steps undertaken beforehand. Apart from subtracting baseline measurements, the sample measurement must be filtered from the noise that appears during the signal collection. It is then followed by the last step in the form of calibrating the measured signal by using integrating sphere (IS) measurements, resulting in diffuse reflectance.

Typical example of SAR-DRM spectra from a polystyrene suspension and IS is presented in Figure 5.3.2 for UV-vis-short NIR and NIR signal. This example signal will be used throughout the chapter to illustrate the steps of signal processing. In the following sections, the original signal processing steps are described, the advantages and disadvantages are considered and modifications to the original processing method are proposed.

ORIGINAL METHOD OF SIGNAL TREATMENT

STEP 1: BACKGROUND SUBTRACTION Spectral signal collected needs to be corrected to remove baseline signal from the noise and dark current of the spectrometer. The intensity of the light collected from the sample (I_{diff}) and integrating sphere (B_{diff}) could be expressed as follows:

$$I_{diff} = I_{on} - I_{off} \qquad B_{diff} = B_{on} - B_{off} \tag{5.3.1}$$

Naturally, the intensity of the light collected with the light shutter up is lower than the spectra clollected from normal shining state (Figure 5.3.2 (a1)-(a2)). However, there are spectral regoinds in SAR-DRM, like NIR, where the noise and dark current are strongly appearing on the collected measurments (Figure 5.3.2 (b1)-(b2)). This leads to the event where the shape of the intensity pattern over wavelength region cannot be read without substraction at all, which states the importance of this spectra processing step for this spectromeneter in the SAR-DRM setup.

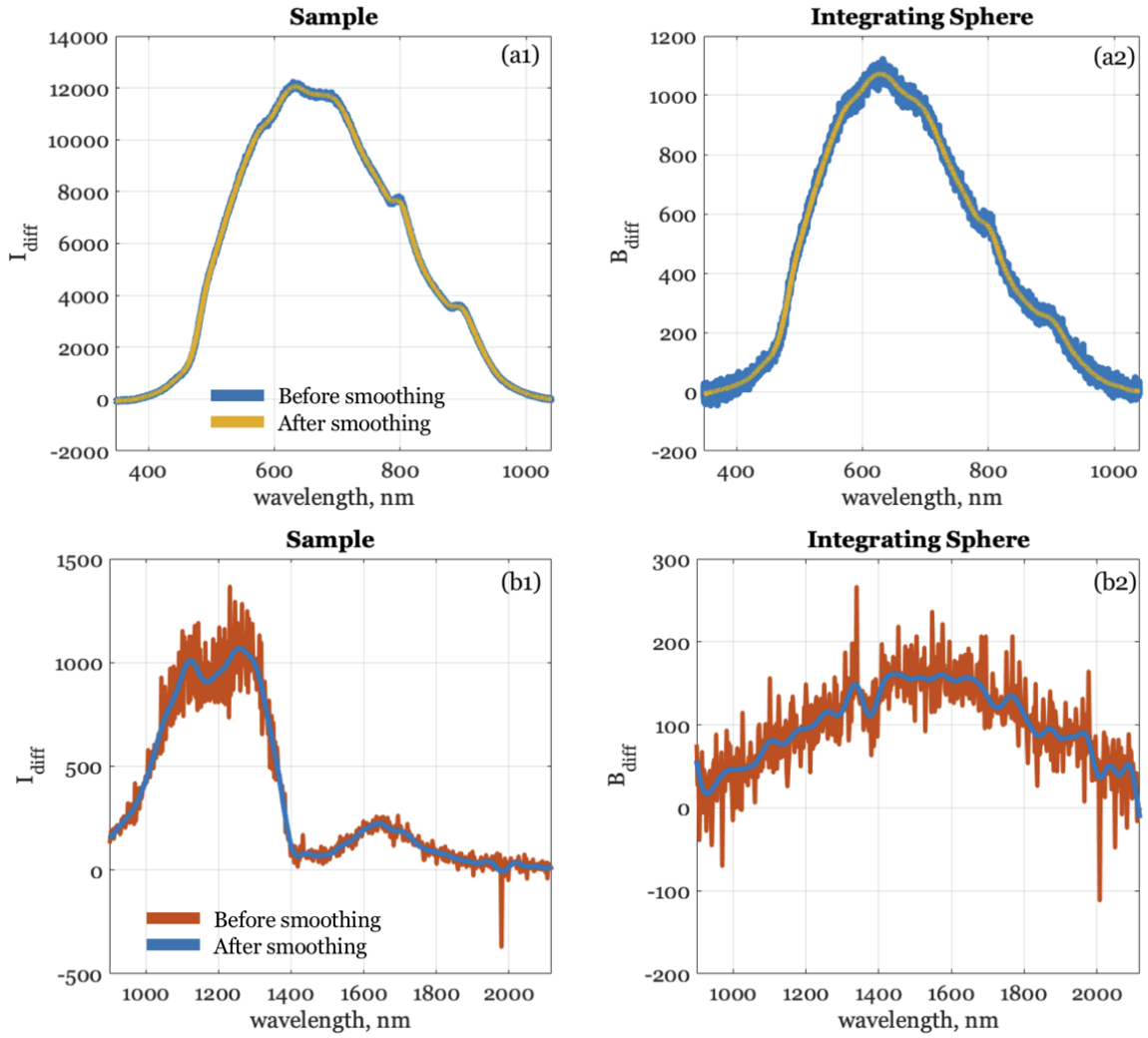

Figure 5.3.3 Before and after smoothing of $I_{diff}(1)$ and $B_{diff}(2)$ in (a) UV-vis-short NIR and (b) NIR spectral ranges

Current step accounts for the effect of the instrument noise, however, the signal-to-noise ratio at spectra from the integrating sphere is small to proceed with the analysis. The signal fluctuations have to be removed or smoothed before processing to the last part of the calculation.

STEP 2: SMOOTHING The level of fluctuations in the UV-vis signal is significantly lower than in the NIR signal. Meanwhile, the weak signal collected from the integrating sphere for both spectrometers leads to difficulty in finding a single smoothing method suitable for all spectrometers and types of measurements.

The original method in [120] suggests using a Savitzky - Golay filter for UV-vis-short NIR spectra. It is a least-square regression-based method with moving window averaging. Since the window can move within a flexibly defined span, the method performs well at both low and high signal frequency level. This method was implemented using the function *smooth* in Matlab Curve Fitting Toolbox. Previous analysis of UV-vis-short NIR signal intensity variations from a variety of samples suggests an optimal span for the moving average from 81 to 111 data pixels for a UV-vis-short NIR spectrum, which corresponds to 20-25 nm in wavelength. Those conditions were applied for all UV-vis-short NIR spectra after Step 1. The effect of the Savitzky - Golay filter for I_{diff} and B_{diff} can be seen in Figure 5.3.3 (a1) and (a2) respectively.

For smoothing NIR spectra, a Fourier transform-based method is suggested by [120]. It decomposes the original signal into frequency components. The underlying principle is to approximate the signal within the moving window by a constant, not by a polynomial of a higher order like in Savitsky- Golay. The algorithm for smoothing NIR spectral signal was developed based on the steps provided in OriginPro 8.6 (OriginLab, USA) for a parabolic low-pass filter. The function requires the assignment of the pass and stop frequencies, which were set to 0.04 and 1, respectively, for all NIR spectra. Pass frequency defines the value below which signal intensity will be kept unchanged after being filtered whereas a stop frequency is a value above which all values will be removed completely.

Despite the overall good performance of the original signal processing method, there are multiple cases where the spectra were not processed successfully. The signal variation across a number of samples was consistent enough for the chosen pass and stop frequencies, however, due to the large fluctuation between adjacent pixels, the performance on smoothing B_{diff} is not sufficient. Figure 5.3.3 (b2) shows the smoothed B_{diff} exhibits many small peaks. As the integrating sphere is known to be non-absorbing and the light source is expected to exhibit a smooth profile across the entire wavelength range, such peaks can be considered as artefacts, indicating the limitation of the smoothing method. Any further manipulations with a pass and stop frequencies can lead to loss of spectral pattern across wavelength. Lastly, the smoothed spectra are offset to zero by subtraction of the minimum value from the signal.

STEP 3: NORMALISATION AND TRUNCATION When light from an optical probe is introduced to an integrating sphere, the light is redistributed by the diffuse reflection of the internal wall of the sphere. Mathematically, the correction of the spectra signal by the

IS signal can be executed by dividing the I_{diff} signal to B_{diff} to obtain the normalised reflected intensity, R, as follow:

$$R = \frac{I_{diff}}{B_{diff}} \tag{5.3.2}$$

The results from this step using the smoothed spectra from Figure 6.1.2 in Equation 5.3.2 are shown in Figure 6.1.2. The diffuse reflectance of UV-vis-short NIR range consists of a "bell shape" pattern, similar to the one observed before at I_{diff}. The overall pattern is clear apart from a number of wavelengths in the beginning and the end of the instrument wavelength range. NIR signal shows a quite distinctive absorption peak related to light absorption by water. The beginning of the signal consisting of multiple indistinct peaks with a low chance of connecting them with the pattern specifics spotted in the raw signal (Figure 5.3.3 (b)). Suchlike occurrence in measurements requires clarification.

Analysis of the number of SAR-DRM datasets concluded a repeatable development disaccording signal peaks on R spectra. Those peaks, when appear, occur mostly at the same wavelength range among different datasets analysed, however not associated with exact wavelength value. The fluctuations of the signal collected from the integrating sphere, B_{diff}, matches with peaks later appearing in $R(\lambda)$ which imply the link with the phenomena. Since the signal is collected from the integrating sphere, that fluctuation cannot belong to any material reflection and therefore they are numerical artefacts. Further investigation concluded that the artefacts appear due to the division of low intensity of $I(\lambda)_{diff}$ to $B(\lambda)_{diff}$ (Equation 5.3.2) that also has extremely low values especially in pixels affected by artificial fluctuations.

The false spectra peaks were discovered in signals from both spectrometers, mostly in the NIR region. Combining the limitations shown in Step 2, they introduce uncertainties in the data which may lead to misinterpretation of the optical properties.

PROPOSED MODIFICATION OF SIGNAL PROCESSING METHOD

The focus of the following analysis was to provide a solution that avoids the loss of meaningful spectra in Step 2 and 3. Methods that are used for SAR-DRM spectra processing in [120], their operating principle and what could be improved are taken into consideration. The sections will suggest an alternative approach for signal processing in order to improve issues identified in Step 2 & 3 in Section5.3.2.

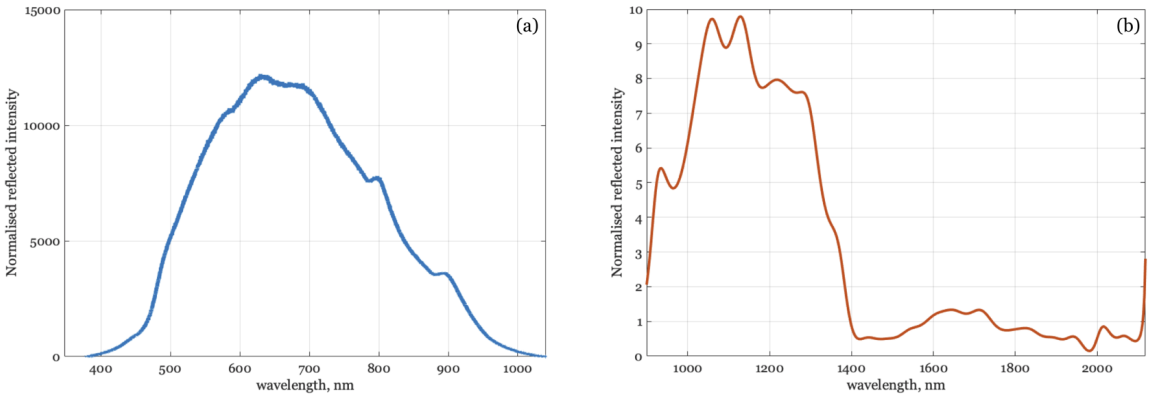

Figure 5.3.4 UV-vis-short NIR (a) and NIR (b) diffuse reflectance after normalising I_{diff} to B_{diff} following Step 2.

STEP 2*: IMPROVED SMOOTHING The first shortcoming of the original signal treatment method was the inability to consistently provide satisfactory smoothing. The reflectance signal collected by NIR spectrometer struggles the most from the chosen method. Disaccording peaks of the high intensity appear sporadically, not letting the averaging window methods take place as it would lead to the problem of under or overfitting the data.

To eliminate artefacts without affecting the overall spectral pattern, proximal optimisation for multidimensional total-variation regularisation was proposed as an alternative. This is a recently developed signal filtering method that involves the taut string method developed by Barbero *et al* [198]. The taut string method is classically used in statistical applications to obtain a sparse estimation for a density given by point measurements. A discrete formulation is employed to interpret the data as piecewise constant splines. Instead of moving the empirically defined window, proximal optimisation solves the task by graph trend filtering. This method is published by the same author as *proxTV* toolbox for Python 2.7. The method requires to define the proximity operator. In this study, the operator is fixed to 5000.

The proposed method was applied to I_{diff} and B_{diff} obtained after Step 1 in both spectral regions used. The output was then compared with the results from the original methods. The difference between the methods is most noticeable when analysing the signal from the integrating sphere. The example of raw and filtered NIR signal from the integrating sphere can be found in Figure 5.3.5. The processed signal using *proxTV* reveals a smooth pattern across the wavelengths similar to the outcomes using the original smoothing method. However, the degree of fluctuations has decreased drastically. Signal

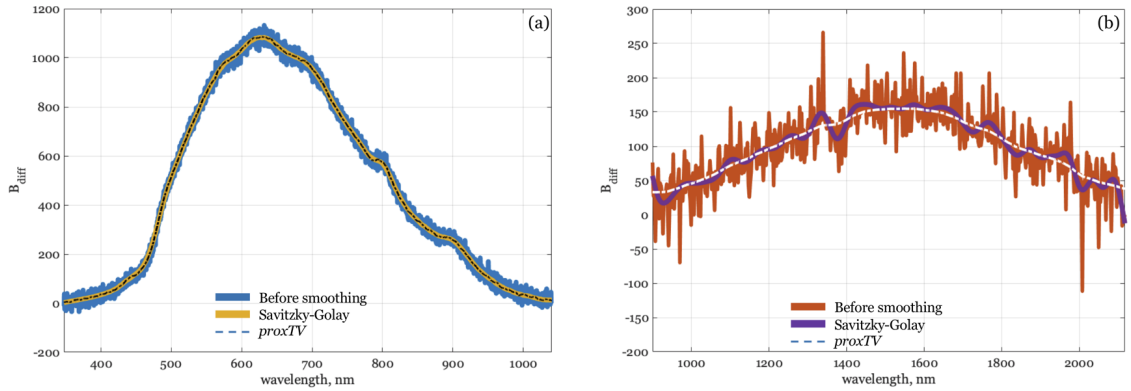

Figure 5.3.5 UV-vis-short NIR (a) and NIR (b) signal collected from integrating sphere B_{diff} in comparison with different smoothing methods performance.

collected from the sample has benefited from the new method too; the nuances of spectral response were picked up better by *proxTV*. Overall, a great improvement and consistency can be seen in the processed signal with an application of the new smoothing method. For consistency, the *proxTV* smoothing was applied to SAR-DRM for UV-vis-short NIR and NIR signal.

STEP 3*: IMPROVED NORMALISATION The elimination of issues in smoothing improves the overall pattern of SAR-DRM spectra and discard false spectra fluctuations. However, there is a number of outstanding peaks that appear due to the division of low values of light intensity (equation 5.3.2). This phenomenon occurs for the spectra collected from the longest source-to-receiver distance as the intensity is the weakest compared to the other distances. These artefacts appear occasionally at the smallest and largest wavelength on the studied regions. Truncation of spectra would cause loss of information while leaving it untreated would disturb the spectra. To tackle this problem, equation 5.3.2 was rearranged. Instead of normalising I_{diff} by B_{diff}, analysing directly the I_{diff} signal is suggested. In this case, the I_{diff} values would be the result of the signal processing routine.

5.4 Computational algorithm for estimating physical and chemical properties: Inversion of SAR-DRM spectra

The general procedure of the parameters of interest inversion can be metaphorically split into two main stages: inversion of the monodisperse system and following inversion of polydisperse system. Figure 5.4.1 shows the main steps of the proposed inversion algorithm. The first step is to pre-compute the optical properties for each of the particle sizes in the grid R for the selected material. This step is done once for selected parameters of inversion and described in more details in Section 5.4.2. Steps 2-4 return the estimated parameters of interest for the monodisperse system of particles. If the analysis conducted with assumption to the analysed monodisperse system, the inversion algorithm terminates at Step 4. For inversion of polydisperse system, the estimated mode radius and concentration from Step 4 are used as a starting point for the search in the following Step 5, resulting in three parameters of interest estimation: mode radius, concentration and distribution width. The sections below describe the inversion algorithm in more details.

5.4.1 Preparation of SAR-DRM for the inversion and the choice of the objective function

Normalisation of the SAR-DRM signal for inversion

Section 5.3.2 concluded the necessity of using I_{diff} for analysis instead of R to avoid the spectra artefacts. This raises the question regarding the signal comparison to simulation as the result that later appears in the form of the diffuse reflectance spectra R_{sim}.

To assess relative merits of measured and modelled spectra, there will be added an additional step to obtain I_{sim}, which can then be compared to I_{diff}. I_{sim} should be developed as follow:

$$I_{sim} = R_{sim} \cdot B_{diff} \tag{5.4.1}$$

The only remaining issue of the selected approach is the difference in signals scale. I_{diff} and B_{diff} have arbitrary units of light intensity, whereas diffuse reflectance $R(\lambda)_{sim}$, by definition ranges between 0 and 1 where 1 means that all the incident light is returned.

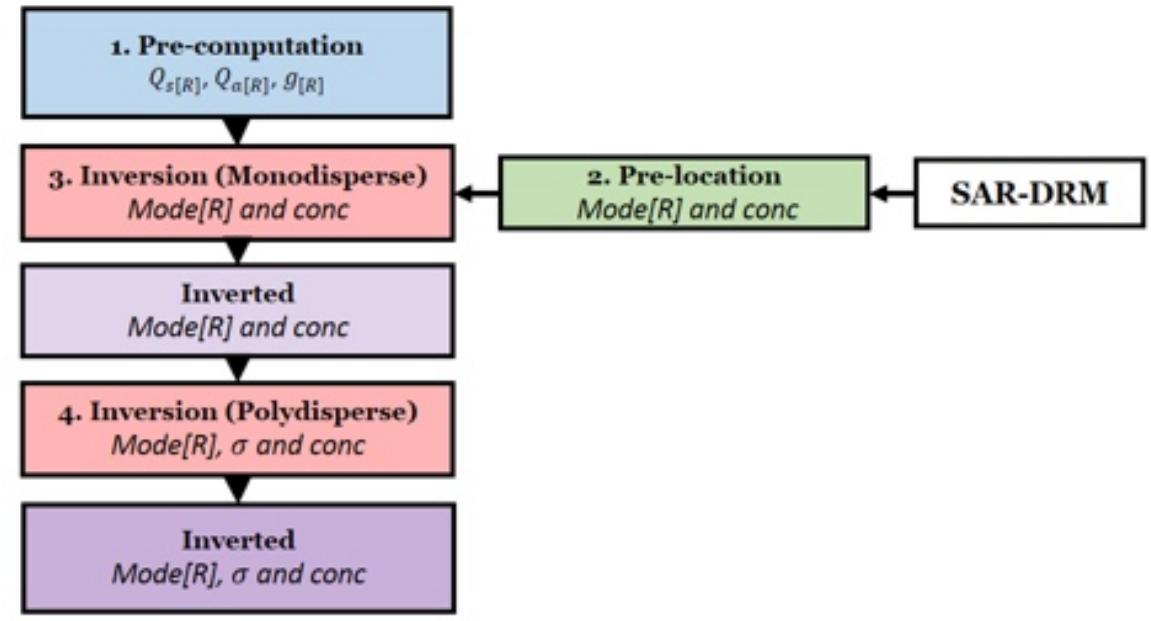

Figure 5.4.1 Flow chart of parameters of interest inversion algorithm

To overcome the scaling limitation, I_{sim} and I_{diff} were re-scaled by the maximum value of each of them, respectively. As a result of it, simulated and measured intensity would be within 0 and 1, where 0 is the lowest value, and 1 is the highest for each particular measurement.

$$I'_{diff} = \frac{I_{diff}}{max(I_{diff})} \qquad B'_{diff} = \frac{B_{diff}}{max(B_{diff})} \tag{5.4.2}$$

$$R'_{sim} = \frac{R_{sim}}{max(R_{sim})} \tag{5.4.3}$$

Therefore, Equation 5.4.1 with scaling correction will look as following:

$$I'_{sim} = \frac{R'_{sim}\, B'_{diff}}{max(R'_{sim} \cdot B'_{diff})} \tag{5.4.4}$$

The proposed solution does not include division of two types of SAR-DRM yet provides the measured and simulated reflectance values that can be compared against each other.

The evaluation of the similarities between simulated and measured signal traditionally established by various functions for a measure of the uncertainty.

OBJECTIVE FUNCTION

The common way to analyse a simulated solution in comparison with a measured signal is the selection of a function that indicates the degree of differences between values in a specific way. In the context of inversion problem solution, which is essentially a search for the original system parameters that affect the measured data, is it a quantitative method in which predictions I'_{sim} are compared with experimental data I'_{diff}. The choice of such method, commonly defined as an objective function, depends on the quality of agreement between modelled and experimental signal, which is usually interpreted as a proof that the chosen objective function is the one that delivers the reliable prediction [199].

The analysis is based on an objective function that measures the merit of the fit between theory and experiment, where the best fit corresponds to the lowest value returned by the function. The choice of the objective function is a biased process and solely depends on the application and specificity of the data it is applied to. Ultimately, the selected function should indicate true parameters of the system. In this research, we complied with the following criteria during the objective function selection:

- Compatibility of the good fit value to the same conclusion from visual evaluation of fitted and measured data

- Absence of multiple local minima

- Speed of convergence

The performance of two functions was mainly considered: chi-squared test, χ^2, and the relative error, δ. χ^2 is a method that calculates the squared difference between simulated and measured data values, divide it by the measured value and average over data points. In this study, the calculation is conducted between simulated I'_{sim} and measured I'_{diff}:

$$\chi^2 = \frac{1}{N_\lambda} \sum_{i=1}^{N_\lambda} \left(\frac{I'_{sim}(\lambda_i) - I'_{diff}(\lambda_i)}{I'_{diff}(\lambda_i)} \right)^2 \tag{5.4.5}$$

Relative error is calculated the similar way, however in this function, the change in measured and simulated signal is an absolute value divided by measured signal and multiplied by a 100:

$$\delta = \frac{1}{N_\lambda} \sum_{i=1}^{N_\lambda} \left(\frac{|I'_{sim}(\lambda_i) - I'_{diff}(\lambda_i)|}{I'_{diff}(\lambda_i)} \right) 100\% \tag{5.4.6}$$

The formulas above illustrate that the inversion of I'_{diff} is based on an analysis of average effect from all wavelength. It is justified by the need of normalisation of the objective function values over different spectrometers which return a different number of data pixels as well as requirements of the selected non-linear solver, which will be discussed further in the corresponding section.

After examination of each function performance, the decision was made in favour of relative error function usage. χ^2 assumes that uncertainty is proportional to the magnitude of the signal, besides the units of χ^2 are more difficult to interpret than percentage returned by relative error. As a result of the comparative analysis of both functions performed at the simulated signal example, presented in Chapter 6, the relative error method needed a similar amount of time to achieve successful conversion as χ^2, however, the prediction error was higher for the latest.

5.4.2 Step 1. Pre-computation of optical properties for a single particle in particle size population

As discussed in Chapter 4, the particle size grid R is linearly spaced in a wide radii range. Moreover, the optical properties are used in a broad wavelength range, which contributes to computational time. Such an approach is not efficient in the iterative process of searching for a global minima. In this study, Mie theory is used for computation of scattering (Q_s) and absorption (Q_a) efficiencies and asymmetry parameter (g) by a single particle of size. A concentration of particles in the system, as well as size distribution function, are only introduced afterwards at scattering and absorption cross-section computation. Detailed formulae of estimation of optical parameters can be found in Chapter 4. Having optical properties of a single particle known in prior would reduce the time needed for bulk optical properties calculation.

The first step of parameters estimation was designed to eliminate unnecessarily repeated computation of fundamental optical properties. Since the analysed material, particle size range and wavelength range used in the experiment are known, Q_s, Q_a and g can be pre-computed for every size in the size population and every wavelength in UV-vis- short NIR range, creating a matrix of optical properties values. These values are

independent of inversion parameters and therefore can be calculated for given material with known density and refractive indexes. Pre-computation allows to significantly reduce computational time without negative effect on algorithm robustness.

5.4.3 Step 2. Pre-location of the initial guess for parameters of interest

During the inverse problem optimisation, by starting the minima search from the most plausible solution, *a priori* the convergence is most likely to be achieved faster than from a random combination of the parameters of interest. The optimisation of model parameters is then made by the successive iteration of solving a set of standardized linear equations for corrections at each step. The later is executed by the implementation of nonlinear programming solver, described later in Section 5.4.4, whereas the initial guess close to the most plausible solution shall be defined individually for current research. Locating the initial guess obscurely might lead to mispredicting the parameters of interest by trapping the initial guess in the local minima. Presumably, with a satisfactory choice of the inversion procedure, the convergence must be achieved even with a random initial guess. A solution for more intelligent initial guess pre-location that is based on the objective function selected for the SAR-DRM inversion is proposed below.

The pre-location is required for mode radius and concentration before Step 2. The general procedure of the initial guess pre-location can be described in two main sub-steps, illustrated in Figure 5.4.2. Firstly, the random values of mode radius and concentration within constraints are generated. They then are used along with pre-computed values for a single particle to calculate bulk optical properties and reflectance signal, I'_{sim}. The resulted signal is, therefore, corresponds to randomly generated parameters of interest. The difference between I'_{sim} and I'_{diff} is then evaluated in the form of relative error δ. If relative error is higher than 15% (expressed in the flowchart as δ_{min}), the process starts over. Otherwise, the value of relative error is recorded along with corresponding mode radius and concentration and the process repeats until at least five combinations of parameters of interest return relative error lower or equal to 15%. If the relative error is not lower than 15%, the generation of random combinations of parameters of interest terminates after 500 iterations. The last step then is to compare the recorded relative error values to select the lowest value, for the initial guess values for parameters of interest.

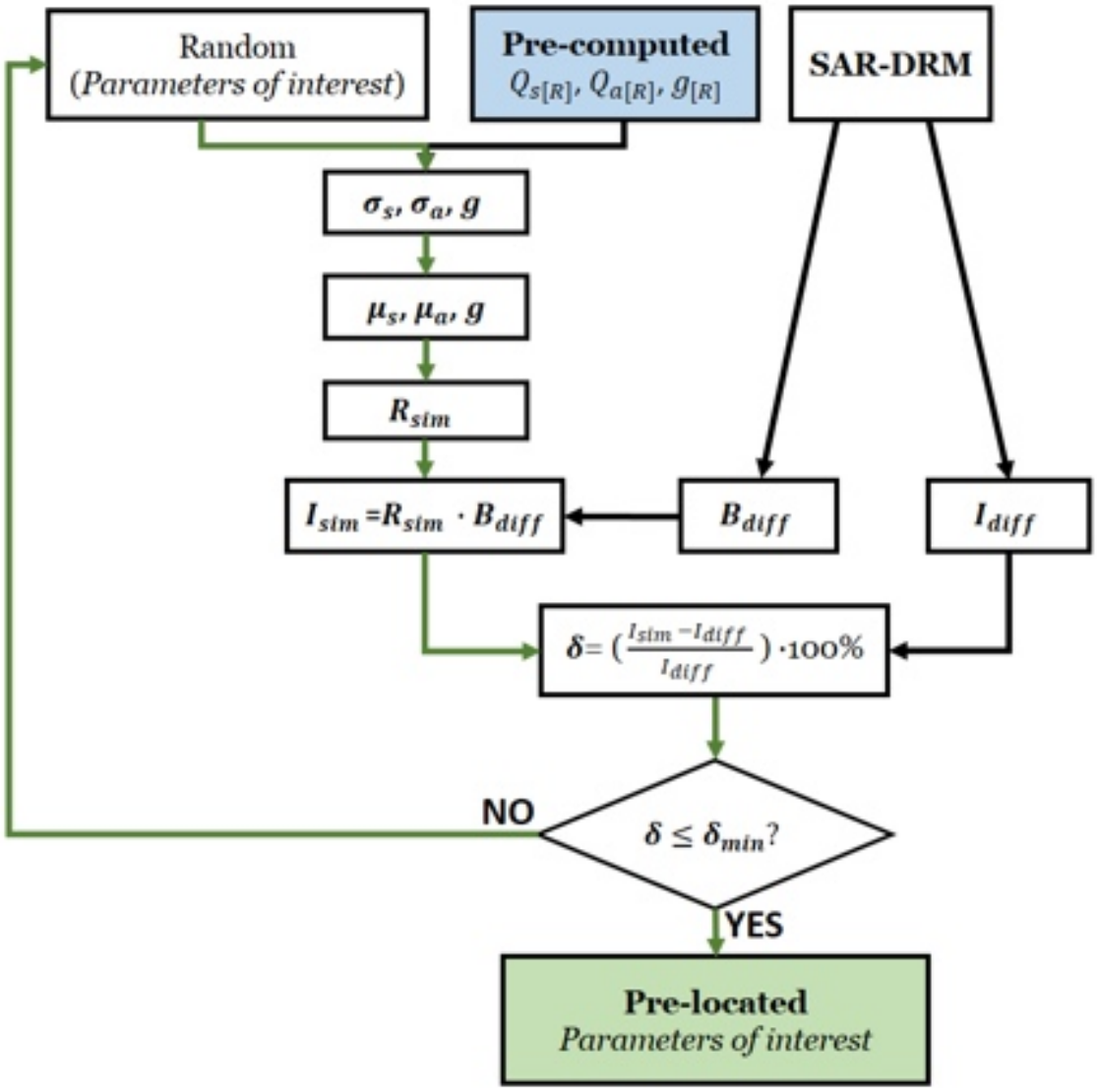

Figure 5.4.2 Flow chart of pre-location of parameters of interest (Step 2).

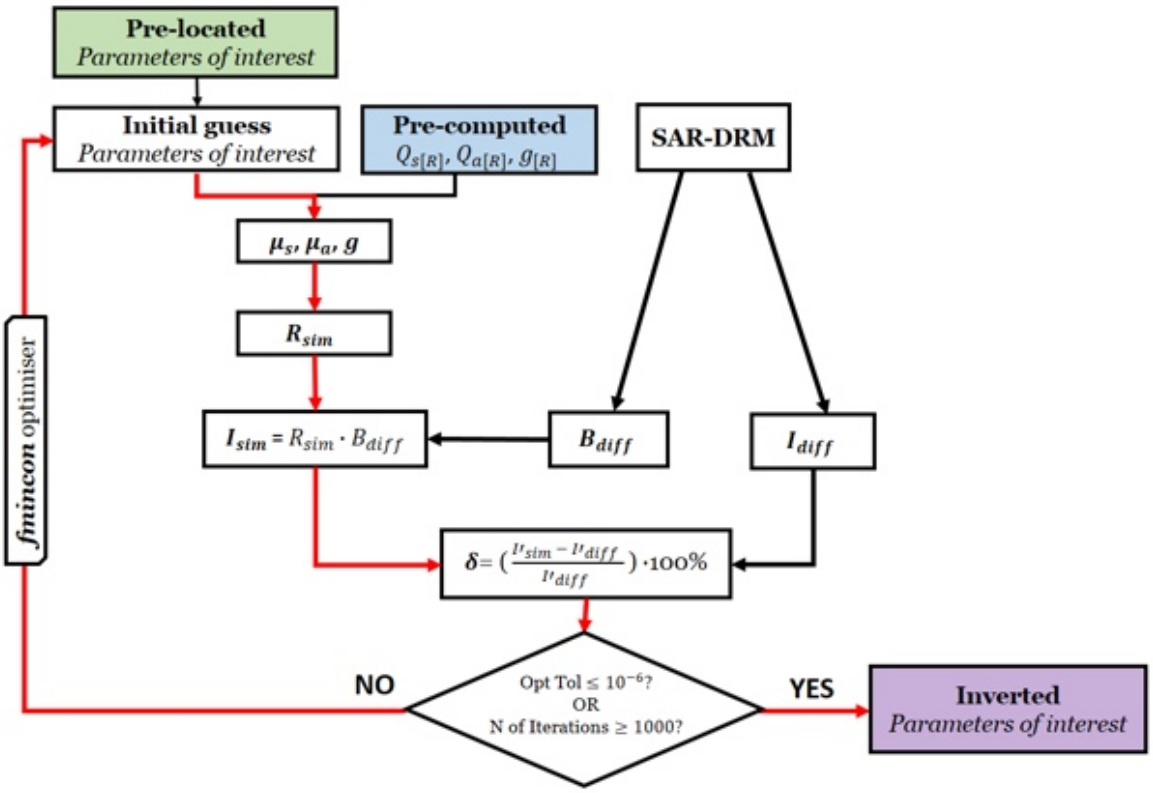

Figure 5.4.3 Flow chart of parameters of interest inversion (Step 3 and 4).

5.4.4 Step 3. Inversion of the parameters of interest for monodisperse system

It is clear that for an objective function with multiple variables there is no alternative but an iterative solution. To reduce the computational cost of the iterative process, various optimisation methods may be used. In this research, Matlab optimisation toolbox was used for solving the function, precisely a non-linear programming solver of constrained multivariable functions, *fmincon*. The algorithm chosen was an interior point method in which the subproblems are solved approximately with sequential quadratic programming (SQP) and trust-region techniques.

A schematic illustration of the general inversion steps can be found in Figure 5.4.3. The overall principle of the inversion algorithm here is similar to a majority of optimisation methods, where the solution of each subproblem is used as a search direction from some initial point to find an improvement, which is then the next subproblem. The iteration is repeated until converged to a constrained local minimum [200]. As a part of the *fmincon* package, the optimisation algorithm returns a minimum value of the objective function as

well as details of algorithm execution. The inversion of the parameters of interest requires several settings and assumptions to be defined to ensure quick and robust estimation of parameters of interest.

The search for the solution during the inversion problem is executed within specified constrains for parameters of interest. Setting the constraints allows to significantly reduce the inversion time. The constraints were set based on the study presented in Chapter 4, therefore the possible solution surface is known from the simulational study. Mode radius was truncated between 25 and 650 nm and concentration between 0.01 and 20 wt%. Apart from search constraints, there is a number of stopping criteria that must be pre-set for *fmincon*. These criteria include several tolerances which, if crossed, stops the iterations of a solver and therefore define the optimisation accuracy. During the inversion, *fmincon* was put through multiple combinations of settings to ensure function repeatable successful conversion and that no contradiction exists between the constraints mentioned above. Based on these results and Matlab optimisation toolbox documentation, lower bound on the size of a step and function tolerance were set to a value of 10^{-6}, whereas a maximum number of iteration was left at the default number of 1000.

The parameters of interest, namely, mode radius and concentration are in different units. As such, the scale is significantly different between the parameters, which would affect the inversion due to uneven weights of contributing parameters. For this project, inversion performance was improved by variables re-scaling. The re-scaling was done with respect to search constraints of each parameter of interest by subtracting the average value between search limits from the parameter of interest and then dividing the result by double variance. In such case, the constrains become minimum and maximum values for the solution search in form of -0.5 and 0.5 respectively for each of the parameters of interest. The *fmincon* then generates the variables within these constraints, which should be converted to the actual units within the optimised function and passed into the forward calculation routine for SRDR. After inversion is complete, the obtained parameters of interest will be returned in the above-mentioned scale, therefore the true values of mode radius and concentration are recovered afterwards for further analysis.

The selected solver *fmincon* is designed to minimise a single value of the objective function, therefore the signal, that is supplied into the minima search shall be modified to suffice this requirement. As was mentioned before, in the current analysis, the signal is averaged across different wavelength. I'_{diff} is supplied by 16 receiving fibres placed

at different S-R distances, organized into four branches. Consequently, the SAR-DRM for single sample consists of four different S-R distances and four different branches. Following the results of the simulational study in Chapter 4, the closest S-R distance is not sensitive to all combinations of the parameters of interest, therefore is eliminated from the analysis. To ensure the compliance of the inversion procedure with diffuse reflectance approximations used for signal simulation, the spectra obtained from the fibres at closest S-R distance were eliminated from the analysis. Therefore, only signals collected at distances 0.6, 0.9 and 1.2 mm were used in the study. This posed a question regarding the implementation of the spectra from different S-R distances in the inversion algorithm in such a way that *fmincon* is supplied with a single value of the objective function for optimisation. The effect of parameters like mode radius and distribution width has a different effect on spectra from different S-R distances, therefore, supplying signals of different S-R distance separately from each other would lead to loss of this effect propagation. For performing analysis on different S-R simultaneously, the I'_{diff} signal from different S-R distances was summarised. Same was done for the simulated signal I'_{sim} in the function passed to *fmincon* where the inversion error was evaluated. The *fmincon* returns scaled parameters of interest that correspond to the lowest inversion error. These parameters were re-scaled back to the actual units, and used in the single run of forward calculation of the optical properties to obtain the corresponding SRDR across different wavelength and S-R distances.

The signal collected at different branches, ideally, should be identical to each other at corresponding S-R distances, however, there is a degree of variation expected due to differences in the individual fibres sensitivities. The signal for different branches will be inverted separately to observe the effect of differences between branches on the estimation of the parameters.

5.4.5 Step 4. Inversion of the parameters of interest for polydisperse system

The Steps 2-3 provide with a solution for a monodisperse system of particles. In the analysis of the system, where only these two parameters (mode radius and concentration) need to know, the inversion may be complete at this point. This project prioritised the inversion of the polydisperse system of particles, therefore the complete inversion algorithm includes Step 4 for expansion of the method to incorporate distribution width

parameter. The general flow of the inversion is similar to the one illustrated in Figure 5.4.3 with the following differences. After the inversion of the monodisperse system, the inverted mode radius and concentration serve as an initial value for the starting point. Since the distribution width was not involved in the inversion yet, the distribution width starting point is set to 0.1.

Expansion of the method in the above-mentioned form is dictated by a few observations made on simulated spectra analysis. First of all, the strongest effect on SAR-DRM was caused by mode radius, concentration and their combination, as suggested in Sections 4.3.2, 4.3.2 and 4.3.3 respectively. The effect of the distribution width is significantly weaker and appears more pronounced in combination with mode radius, whereas in combination with concentration, wide combinations of σ and concentration that result in the same or similar relative error δ (Section 4.3.3). Consequently, pre-location of the probable solution by using Step 2 procedure for three parameters of interest simultaneously may be biased by the stronger effects of mode radius and concentration, that could lead to a misleading outcome, including interference of the distribution width and concentration effect. The latter is especially observed at large values of each parameter of interest. This leads to the conclusion that pre-location of the probable solution should be executed for pairs of parameters of interest, rather than three parameters simultaneously. The solution for the polydisperse system typically situates close to the solution for the monodisperse system, hence, the pre-location of the starting point with a monodisperse assumption can be a reasonable approach.

As the starting point getting pre-located, to optimise the search among five parameters of interest, the pre-defined search constraints are re-assigned in Step 4 to a narrower quadrant. In this case, the solution from Step 3 becomes the pre-located values for Step 4 and together with the new constraints, the values are forming the parameters for the *fmincon* iterative inversion process. The constraints remain relatively broad. For mode radius, the constraints were set ±250nm and for concentration ± 5wt% around the pre-located initial guess. As it is introduced at the later stage of the calculation, distribution width σ was constrained between broader limits, from 0.1 to 1. To monitor if solution found by *fmincon* lie close to the selected constrains, the flag variable was assigned which displays the corresponding message after inversion performance. Overall, Step 4 follows the flow chart in Figure 5.4.3, except that the parameters of interest are expanded, as well as the different constraints set for the parameter.

The flowchart shows the forward calculation steps (red path) that are done iteratively within *fmincon* performance until one of the stopping criteria satisfied. Detailed steps of the full inversion process described as follow:

Step 1: Pre-computation of optical properties of the selected material

1. Optical properties for a single particle

   (a) Define complex refractive index of particles and surrounding medium, material densities, particle size grid, wavelength range;

   (b) Compute optical properties ($Q_{s[R]}$, $Q_{a[R]}$, $g_{s[R]}$) of a single particle in particle size grid for every wavelength in the range;

   (c) Save the result of calculation in .mat format. Repeat from the step 1a if any of the parameters in 1a change.

Step 2-4: Inversion of monodisperse system of particles

1. Pre-location of initial guess for monodisperse parameters of interest (Mode[R] and concentration)

   (a) Select maximum and minimum limitations of Mode[R] and concentration for studied material based on system information and theoretical limitations (Chapter 4)

   (b) Generate random combination of Mode[R] and concentration within the limitations in 1a

   (c) Calculate scattering cross-section (σ_s), absorption cross-section (σ_a) and anisotropy factor (g) for a single particle of generated Mode[R]

   (d) Calculate bulk optical properties in form of scattering coefficient (μ_s) and absorption coefficient (μ_a) for generated concentration

   (e) Calculate diffuse reflectance signal, R_{sim}

   (f) Load SAR-DRM signal in form of signal collected from the sample (I_{diff}) and signal collected from the integrating sphere (B_{diff})

   (g) Re-scale to 1 I_{diff}, B_{diff} and R_{sim}

   (h) Calculate I'_{sim}

(i) Calculate relative error δ for selected wavelength range and S-R distances combination

(j) If the $\delta \leq 15\%$, record the parameter of interest and δ simultaneously updating first and second stopping criteria counter; If the $\delta \geq 15\%$, record the parameter of interest and δ simultaneously updating only second stopping criteria counter; (first: five combinations that return $\delta \leq 15\%$; second: 500 of total iterations)

(k) Repeat the algorithm from step 1b until one of the stopping criteria satisfied

2. Inversion of parameters of interest (Mode[R] and concentration)

(a) Define parameters for *fmincon* solver

i. Set tolerances and steps of the optimisation

ii. Set parameters of interest search constraints based on pre-located initial guess

(b) Re-scale parameters of interest

(c) Perform inversion via *fmincon*, which repeats steps 1c - 1i

(d) Re-scale back the inverted parameters of interest

Step 5-6: Inversion of polydisperse system of particles

1. Inversion of parameters of interest (Mode[R], σ and concentration)

(a) Define parameters for *fmincon* solver

i. Set tolerances and steps of the optimisation

ii. Set parameters of interest search constraints based on the pre-located initial guess

A. Set maximum and minimum limitations of Mode[R] around monodisperse value as ±250nm and concentration ±5 wt%. The distribution width search constraints are identical to the ones in Chapter 4.

B. Normalise the corrected search boundaries

(b) Perform inversion via *fmincon*, which repeats steps 1c - 1i

(c) Re-scale back the inverted parameters of interest

The algorithm, described in this section is used either in full for polydisperse system or only up to Step 3, without the inclusion of the distribution width parameter for the monodisperse system. The inversion of the equivalent spherical radius for CNC study follows the same procedure as those for a monodisperse system, but the concentration is taken directly from the gravimetric analysis rather than pre-located by the search in Step 2. The constraint for the concentration is set to ± 0.01 wt% to allow the *fmincon* only search for minimal error by varying the mode radius.

5.4.6 CONCLUSIONS

In the first section, this chapter provides an overview of the sample sets used for the analysis in current research, their experiment design as well as the reference measurements setups and methodologies. The second section described the inversion algorithm and the associated signal processing changes. Summarising this section, the inversion method described proposes the search for the solution for mono and polydisperse system of colloidal particles. It addresses the current shortcomings of the SAR-DRM signal processing as well as provides an inversion routine which is based on error minimisation between simulated and measured signal. The reliability of the selected constraints and functions is validated in the following Chapter 6 before being applied to the SAR-DRM in the same chapter.

CHAPTER 6

BENCHMARK STUDIES OF SAR-DRM FOR PSD/CONCENTRATION ANALYSIS IN POLYSTYRENE SUSPENSIONS

Previous chapters have explained the concept, that describes the inversion of physical and chemical properties via the combination of physical theory and numerical inversion methods. Chapter 4 summarises the effect of parameters of interest on simulated diffuse reflectance, and Chapter 5 proposes the detailed methodology for inversion of physical and chemical properties, including the spectra pre-processing steps. Therefore, the next step was to perform the inversion itself and evaluate the outcomes.

The following chapter consists of two major sections. The first section validates the SAR-DRM pre-processing routine and inversion algorithm performance. The second section describes the results of the application of the developed algorithm on Sample sets with and without polydispersity, unveiling the quality of the parameters of interest estimation and their interference.

6.1 VALIDATION OF SAR-DRM PROCESSING METHOD

Dataset 1 was used to investigate and validate the signal processing method. This dataset was available from the set of styrene polymerisation reactions and described in details in Section 5.1.1. The spectra were treated through the original and updated signal post-processing routine to assess the improvement from the modifications proposed.

As the first processing step, the spectral signal, collected for polystyrene suspensions, is subtracted by the background spectra. This step reduces the level of noise and clears the spectra profile collected from samples and integrating sphere. This procedure remained unchanged and therefore, will be skipped in the following section. Section 5.3.2 describes the improvement of spectra smoothing and normalisation process to address several problems spotted in spectra processing steps 2 and 3. The results of the proposed steps in Section 5.3.2 will be compared with the results from Section 5.3.2 to assess the improvement.

6.1.1 STEP 2*: IMPROVED SMOOTHING

The second step is smoothing the noise from the SAR-DRM signal that cannot be removed by background subtraction. As discussed in Section 5.3.2, more effective methods, like *proxTV* filter, shall be applied instead of currently employed.

As a confirmation of the proposal, Figure 6.1.1(a) illustrates a typical result of a smoothing UV-vis-short NIR signal via two methods: the original Savitzky-Golay and the proposed *proxTV* filter. As was overviewed in conclusions of Section 5.3.2, both of the methods handle the smoothing of the noise in this wavelength regime in good standards. This concludes that after undertaking the smoothing, the overall profile of the spectra is still maintained yet the apparent noise was significantly reduced.

A similar comparison was made for the signal collected from the NIR spectrometer. This signal originally filtered by Fourier transform-based technique and its performance was compared against *proxTV* filter proposed. Figure 6.1.1(b) illustrates the typical result of a smoothing NIR signal via original FFT and *proxTV*. The signal collected from both sample and integrating sphere contains a significant amount of noise which fluctuates greatly. Due to a specificity of the original filter method, some outliers in the signals cannot be filtered fully and therefore stay in the smoothed signal in the form of a false peak. The proposed method, *proxTV*, performs better, which can be observed in Figure 6.1.1(b). With the application of *proxTV*, less noise has been retained in the smoothed signal, which ultimately would benefit the next steps of the analysis. Considering occasional noise appearance at B_{diff} and consistency in signal processing, *proxTV* method is applied to signals collected from both wavelength ranges.

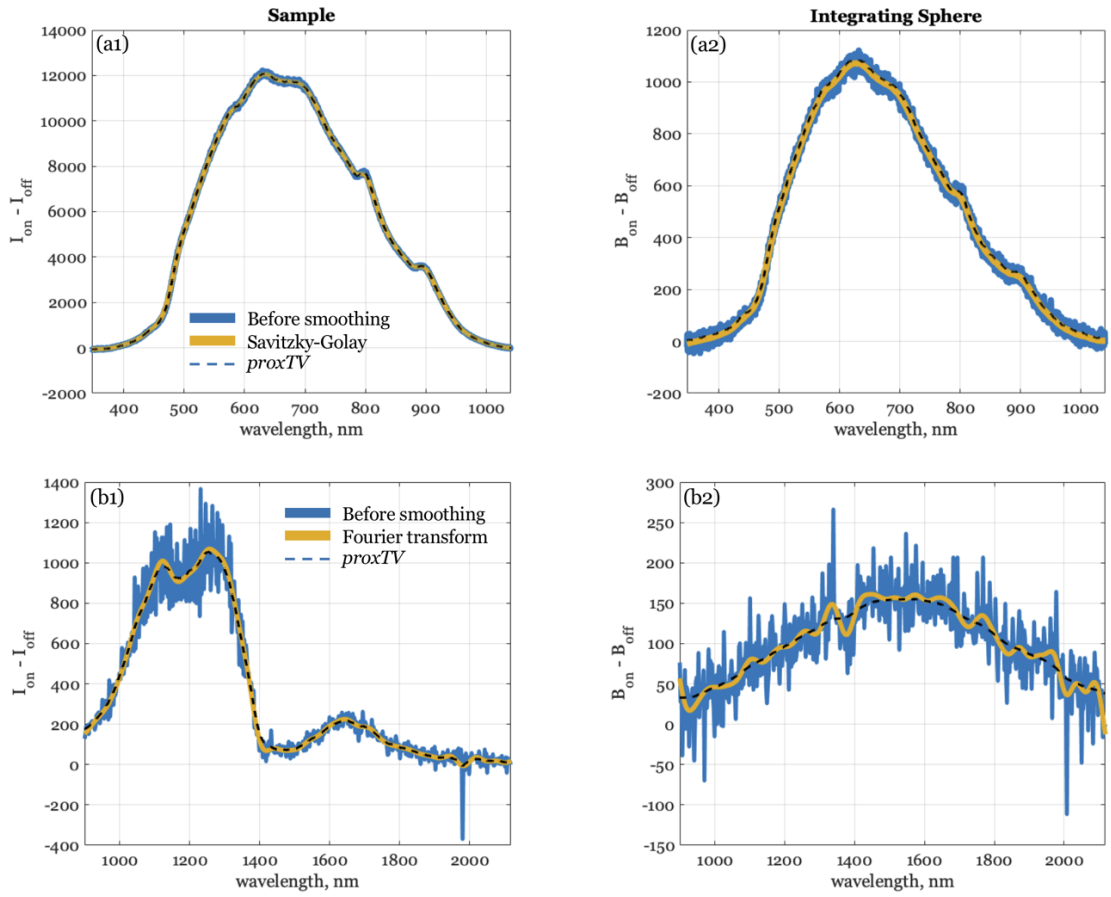

Figure 6.1.1 UV-vis-short NIR(a) and NIR(b) background subtracted signal collected from (1) polystyrene sample, (2) integrating sphere. The figure illustrates the raw signal (semi-transparent line), signal smoothed using Savitzky-Golay (solid line) and signal smoothed with *proxTV* method (dashed line).

6.1.2 STEP 3*: NORMALISING

In this stage, the reflectance signal, I_{diff} is divided by the reference signal from the integrating sphere, B_{diff}. As described before in Section 5.3.2, this approach cannot produce a consistent and stable result at large $S-R$ distance. In this project, the analysis was carried out on UV-vis-short NIR to avoid absorption -related losses of spectral signal, strongly appearing in NIR range. Nevertheless, the signal post-processing optimisation study was carried on both wavelength ranges to find a single processing method and ensure consistency.

To illustrate the issue, Figure 6.1.2 shows examples of problematic diffuse reflectance for both wavelength ranges. One of the most straightforward observations is the fact that the studied issue occurs exclusively at relatively large $S-R$ distances, known for returning low I_{diff} intensity. The values of the latter become comparable with the values returned from reference integrating sphere measurements, B_{diff}, at some wavelengths in both ranges. The variations in the SAR-DRM spectra profile appears at the following normalisation step exclusively at the wavelengths with I_{diff} intensity similar or same to B_{diff}. Breaking down the reasoning behind these occurrences, division of I_{diff} to B_{diff} (Equation 5.3.2) leads to the appearance of the strong spectra peaks at a wavelength as mentioned above that does not typically exhibit material-related properties for measurements of polystyrene suspensions. To avoid such artefacts, I_{diff} signal will be used directly (Figure 6.1.1 (a) and 6.1.1 (b)).

Lastly, the spectra range of I_{diff} was finally reviewed across the wavelength range returned by the spectrometer regarding the signal quality. In the UV-vis-short NIR, used in the analysis further, there are wavelength regions with the fading intensity, making it inapplicable for analysis. The fading spectra are withdrawn from the analysis to truncate the signal between 550 and 950 nm.

To conclude the signal processing validation outcomes, the systematic noise that appeared at both wavelength ranges was reduced, the source of outlier spectra peaks was distinguished and tackled. The following section will shift focus from signal processing to inversion algorithm validation, described in Section 5.4, namely, justification of the objective function choice and robustness test on simulated SAR-DRM.

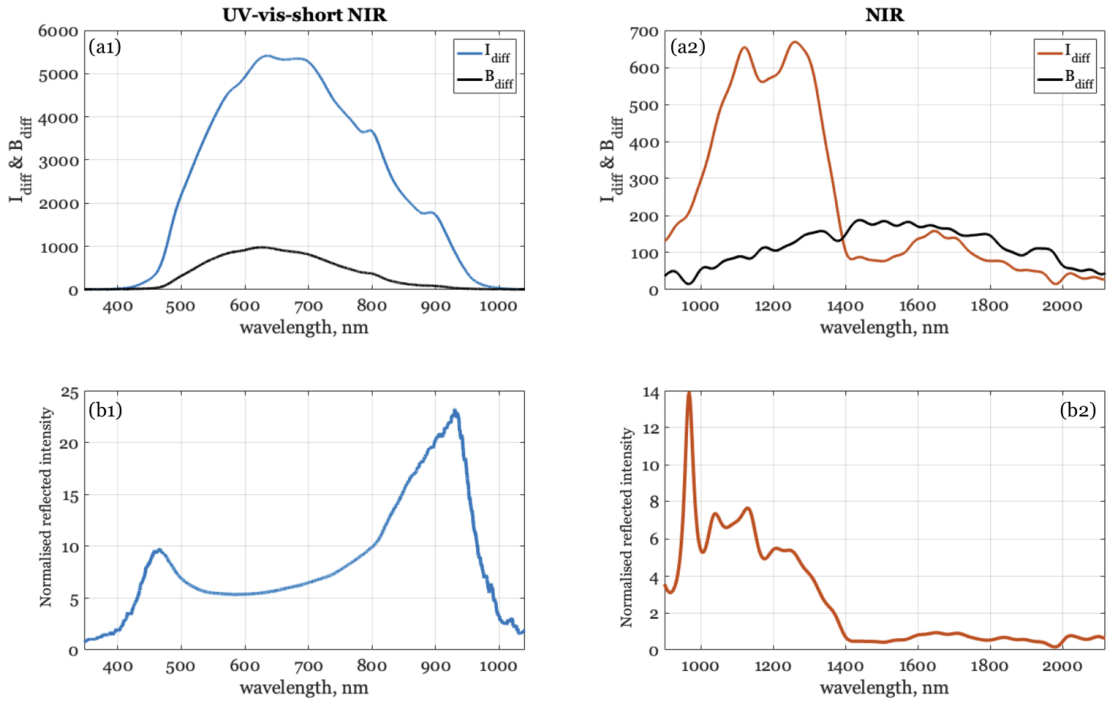

Figure 6.1.2 Background subtracted signal (a) and normalised reflected intensity (b) collected in UV-vis-short NIR (1) and NIR (2) wavelength range.

6.2 Validation of inversion method

The inversion method proposed is a complex numerical tool which was specifically developed to be applied to SAR-DRM inversion. The inversion routine is based on choosing the parameters of interest, using them for simulation of the spectra and systematically comparing the simulated and measured signals, aiming to obtain a good fit between them. To assist the quality of the fit, a mathematical function has been selected. Below, the results of the comparison of the performance of two commonly used objective functions will be shown. The selection process was based on the comparison solution surface of the objective function, precisely, the decay rate and presence or absence of the local minima.

6.2.1 Objective function choice

Section 5.4.1 described two objective functions that can be potentially employed for SAR-DRM inversion, χ^2 and relative error δ. The section below clarifies the choice of the δ by executing a number of experiments on both simulated and measured signal.

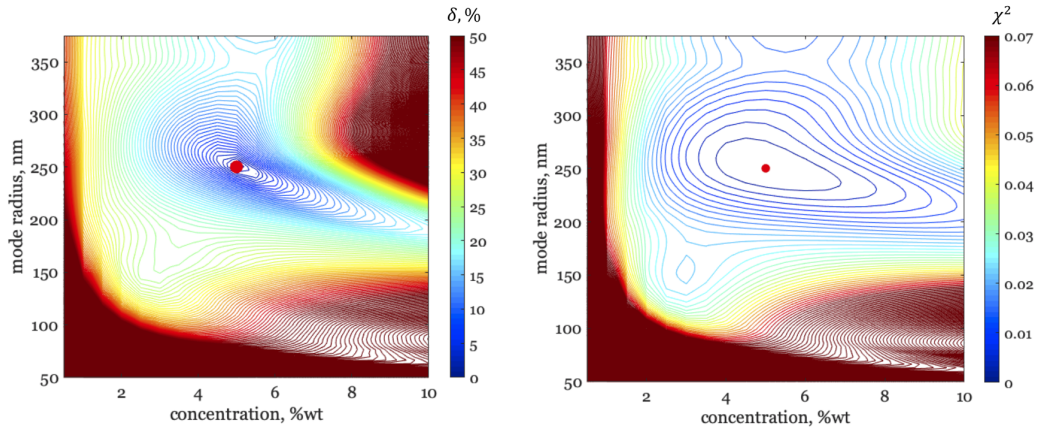

Figure 6.2.1 Response plot of the objective function solutions from (a) δ function and (b) χ^2 function, for simulated signal across mode radii and concentration combinations. The minima of each function is highlighted as a red dot.

Investigation of the objective function performance on simulated signal inversion was performed for two different combinations of parameters of interest: mode radius and concentration and distribution width and concentration. These combinations are identical to ones inverted in each of two stages of the proposed inversion algorithm. To conduct such comparison, a SRDR signal was simulated for a polystyrene suspension with a concentration of 5 %wt, mode radius 250 nm and distribution width 0.25. The first test fixes distribution width to known and illustrates only mode radius and concentration, whereas the second test compares functions performance across distribution width and concentration values.

The first test is based on observation of the solution surface of the objective function across a pair of parameters of interest. The obtained signal was then compared via χ^2 and $\delta, \%$ with signals simulated for a range of mode radii and concentrations. The range limitations were chosen the same as was set in Chapter 4, however since these limits are relatively broad, the result of the solution surface of the objective function, presented in Figure 6.2.1, is truncated.

The surface consists of objective function values corresponding to each combination of parameters. From a comparison of the overall appearance of the solution surfaces, both objective functions exhibit global minima at the actual combination of parameters used for the simulation of the inverted signal. The χ^2 function exhibits a local minima for mode radius 158.3 nm and concentration 3 wt%. Error from δ function for the same

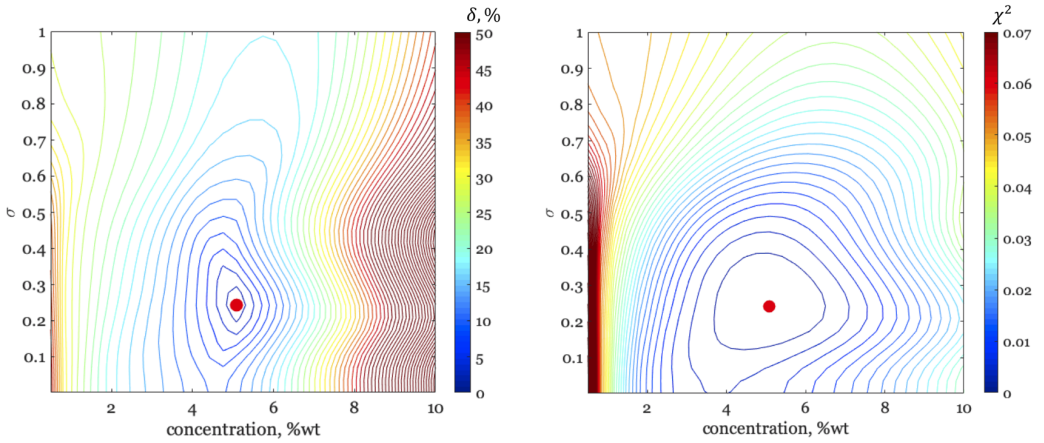

Figure 6.2.2 Response plot of the objective function solutions from (a) δ function and (b) χ^2 function, for simulated signal across σ and concentrations combinations. The minima of each function is highlighted as a red dot.

combination of parameters is smaller compare to neighbouring parameters, however, does not form a local minima.

From the appearance of the solution surface of the objective function, the error for χ^2 decays faster than for δ, which means a faster search for the minima. Minima in δ function are more distinguishable and have a smaller area of similarly small error values around it. Generally, it implies better accuracy of the prediction when δ is employed, however, the conclusion is based on relative observation as the scale of these two functions is different.

The second test was conducted on the combination of concentration and distribution width, resulting in the solution surface in Figure 6.2.2. General observations from this test are similar to what was observed for the combination of mode radius and concentration. Precisely, the surface of solutions for χ^2 develops a shallow area when approaches to the minima, whereas δ function has more distinctive minima. χ^2 does not exhibit any local minima, though, both functions show a steady in error values across concentration values. The steady start at as low as 0.002 σ and continues until ~ 0.1. The change between the neighbour error values is smaller than 10^{-6}, which is the tolerance of the stopping criteria. Presence of such area may be reflected negatively in the quality of the inversion when the solution can be trapped in the area of very low distribution width. This shortcoming can be solved by either reducing the tolerance step, which consequently increases inversion time or truncating the minimum constraints of the distribution width to 0.1. The changes in SRDR from variations at lower values of distribution width appear to be negligible and hence won't affect the quality of the prediction.

To conclude the observations from the above-mentioned section, the δ function exhibits the desirable properties for objective function as its solution surface does not form the local minima and shows well distinguishable minima, free from the shallow surrounding area. The sensitivity of the δ function to distribution width variations below 0.1 is negligible, hence the search constrains can be optimised to 0.1 value as a minimum which indicates the monodisperse system.

6.2.2 VALIDATION OF INVERSION PERFORMANCE

The performance of the inversion algorithm was assessed in two stages. For validation, the method was applied to simulated reflectance signal for various combinations of parameters of interest. This analysis was conducted to test the possibility of the developed method to find global minima. After evaluating the limitations arising from inversion of simulated signal, the inversion algorithm was used to find a fit to sample of the measured signal. Hence, the second stage unveils the visual representation of good, average and poor fit examples.

EVALUATION OF INVERSION ALGORITHM PERFORMANCE ON SIMULATED SPECTRA

In this analysis, a combination of parameters of interest (mode radius, concentration [and] distribution width) was supplied into a forward calculation routine for SRDR signal. Then, the obtained simulated signal was inverted via the proposed inversion algorithm. The validation aim was to illustrate the potential shortcomings that can arise at the second stage of the inversion, where all their parameters of interest are involved in the search, and the most number of degrees of freedom is present in the methodology. A comparison of initial values supplied to the method, and inversion results make a core of the following section.

The analysis below consist of two main goals. The simulated SRDR guarantees the presence of the global minima that correspond to the parameters of interest used in the simulation. Hence, inversion of the simulated dataset testing the robustness of the proposed algorithm. Secondly, the following study justifies the need of δ truncation in the pre-location of the most probable solution (Section 5.4.3).

A set of 125 SRDR spectra was simulated using the forward calculation routine for a range of mode values (5nm – 250nm), distribution width (0.002 – 1) and concentrations (0.05wt% – 20wt%) of hypothetical polystyrene suspensions. This data was passed to the

inversion algorithm, and all three parameters of each sample have been inverted. The study below employed inversion algorithm developed in Chapter 5 with three significant modifications. Because the integrating sphere signal is missing, the inversion was conducted for a simulated diffuse reflectance signal, R_{sim}. Since the following validation will also test the selected stopping criteria for the Step 1 of the pre-location of the most probable solution for a monodisperse system, this part of the algorithm was not performed as described in Chapter 5. Instead of the iterative process, the pre-location was executed via 1000 random combinations of mode radii and concentrations. Apart from these diversions, the rest of the steps were kept the same as described in Section 5.4.4.

Comparison of inverted and actual values can be found in Figure 6.2.3. The figure depicts the objective function values δ presented against variations in the inverted mode radius (Figure 6.2.3 (a)), distribution width (Figure 6.2.3 (b)) and concentration (Figure 6.2.3 (c)). Such representation of the results serves as an illustration of the algorithm's ability to return the values that were used to simulate the signal.

Overall, the majority of the samples were inverted successfully, meaning that inverted value of mode radius, for instance, was either exact to the actual value of supplied mode radius or varied from it by $\pm 3nm$. Inverted distribution width varied within ± 0.01, whereas concentration values varied $\pm 0.007 wt\%$ from actual concentration supplied. The variation between inverted and original result is related to the degree of accuracy, assigned to *fmincon*. Once the optimizer is reaching the minima, the iterations stop once the difference in δ falls below the tolerance criteria, which in this research set to 10^{-6}.

With a closer focus on each parameter inversion, there is a number of parameters of interest combinations that did not lead to convergence. There were samples for which the inverted values did not match the original parameters at a much higher difference. They can be easily spotted in Figure 6.2.3 (a), (b), and (c) in the form of the dots scattered away from the zero levels which stand for a match between actual and inverted values. What can also be noted is that in all those figures, values of δ, returned by inversion algorithm, mostly lie below 10^{-2} and correspond to low variations in the inverted parameters. Respectively, the highest values of δ belong to the samples where inversion has failed to return actual values of parameters of interest. Another evidence of this observation is the number of random combinations that were used to find the optimum starting point. The cases mentioned would require a much larger number of iterations, close to the current limitation of 1000 iterations throughout the starting point search.

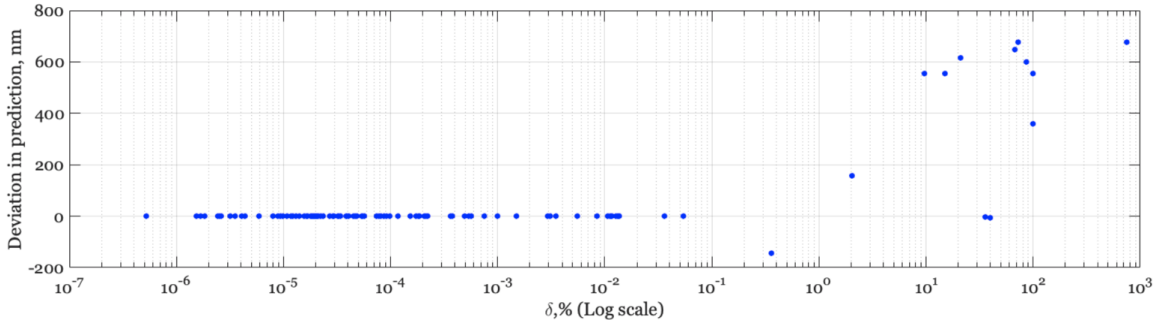

(a) Mode radius

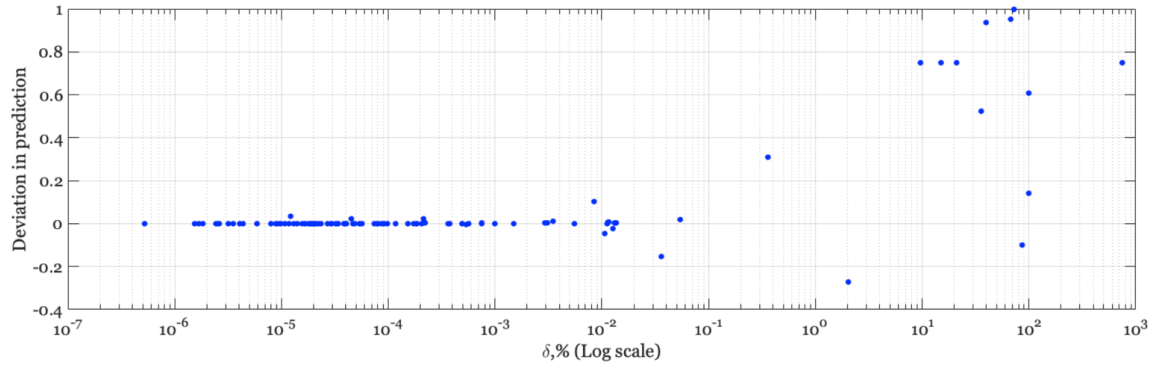

(b) Distribution width

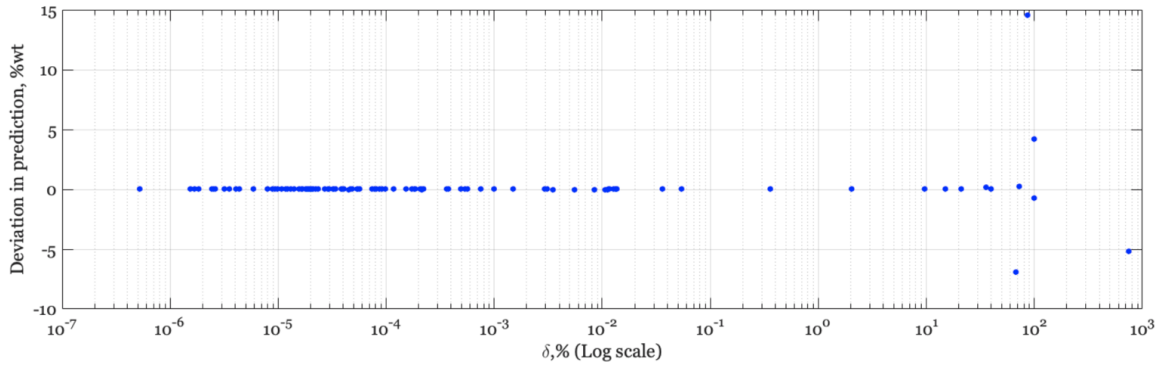

(c) Concentration

Figure 6.2.3 Comparison of the δ values with the actual difference between inverted parameters and original, that were used to simulate the studied signal. (a): mode radius, (b): distribution width, (c): concentration of solids

To monitor this shortcoming, the problematic combinations of parameters of interest were used in the inversion again, however this time, the limitation of iterations to 1000 in the pre-location of the starting point was replaced with looking for a solution lower than previously returned for such system. An additional study showed that if the starting point search continues to find a better solution, then the convergence is achieved and the minima returned is zero.

This raises the question regarding the possibility to ensure the best solution for all potential combinations of parameters of interest. As one of the outcomes from the above study, it can be concluded that starting the optimiser *fmincon* with parameters of interest that correspond to δ below or equal 15% have a high probability of returning the minima of the function, that starting point that corresponds to higher δ. Hence, setting the passing criteria to $\leqslant 15\%$ should reduce the chances of inversion falling into local minima and shorten the time needed for starting point search.

Since, presumably, there is no pre-known information about any of parameters of interest, the only way to give a higher degree of starting point accuracy is to increase the stopping criteria based on a number of random combinations of parameters. The downside of this approach is the consequential increment of total inversion time. Considering a small number of combinations that did not lead to convergence and an ambition to keep the inversion time within 1 hour, the maximum number of iterations in the first part of the inversion algorithm was left limited to 500 combinations. However, most of the other parameters of interest needed much fewer iterations to return $\delta \leqslant 15\%$. To optimise the pre-location of the starting point, the iterative step was implemented that compares each δ returned against $\leqslant 15\%$ threshold. Whenever this condition satisfied more than five times, the pre-location of the starting point is then getting reduced to choosing the minimum between these five options.

The inversion of simulated spectra has shown that the overall performance of the inversion algorithm is satisfying. A majority of the samples were inverted correctly, and those that failed to converge had an insufficient starting point located in the local minima. The observations were used to establish the limitation parameters for polystyrene suspensions inversion to provide a robust and fast method for particle size distribution and concentration inversion. The detailed summary of the established limitations and the overall methodology was explained in Chapter 5.

EVALUATION OF INVERSION ALGORITHM PERFORMANCE ON MEASURED SPECTRA

Investigation of the performance of the developed inversion algorithm on the measured SAR-DRM signal is a much more convoluted task in comparison to a similar study on simulated spectra. The measured signal is affected by multiple experiment parameters, and the pre-knowledge of parameters of interest depends on the reference technique and its accuracy. Generally speaking, the analysis of data sets presented later in the current and followed chapter is dedicated to analysing the performance of the inversion algorithm on measured SAR-DRM, precisely, how well the inversion fit the studied signal and the comparability of the inverted parameters of interest with measured ones. Hence, the following section is aiming to complement the upcoming study by focusing on the small fraction of the inversion analysis, the goodness of the fit in the context of SAR-DRM inversion.

The quality of the fit, by definition, is evaluated by the value of the objective function in such fashion, that the lower the value, the better fit. This analysis aims to illustrate what would be considered as good, average and poor fit quality in the detailed study in the following sections. To do so, I_{diff} signal collected from polystyrene suspensions consist of a Sample set 2, which properties are described in detail in section 5.1.2, was inverted. Figure 6.2.4 shows the comparison of the measured I_{diff} signal against the result of inversion I_{sim}, rescaled to the original scale of the measured signal.

Naturally, the measured signal contains some level of noise, which vary with parameters of interest variations as well as SAR-DRM branches configurations. Hence, the solution provided by the inversion algorithm is not expected to be exactly zero. The top row, coloured green, represents an example of a good fit, that corresponds to low δ. The inverted signal for each $S-R$ distance repeats the corresponding measured signal in an equally good manner.

The average and poor fit represent the signal for shorter S-R significantly better than the one for long S-R distance. The inversion is executed as a simultaneous process for all three $S-R$ distances, and so it was vital to ensure that none of the signals inversions overruled the impact of the other one on the result. One of the preventive measures that were applied to the signal before the inversion was the rescaling of the latest to 1 for each of the $S-R$ distances. Hence, the impact of fading intensity due to increased $S-R$ distances can be obliterated from the discussion. Since the light collected at furthest S-R distance travels longer through the sample, apart from being more diffusely scattered and

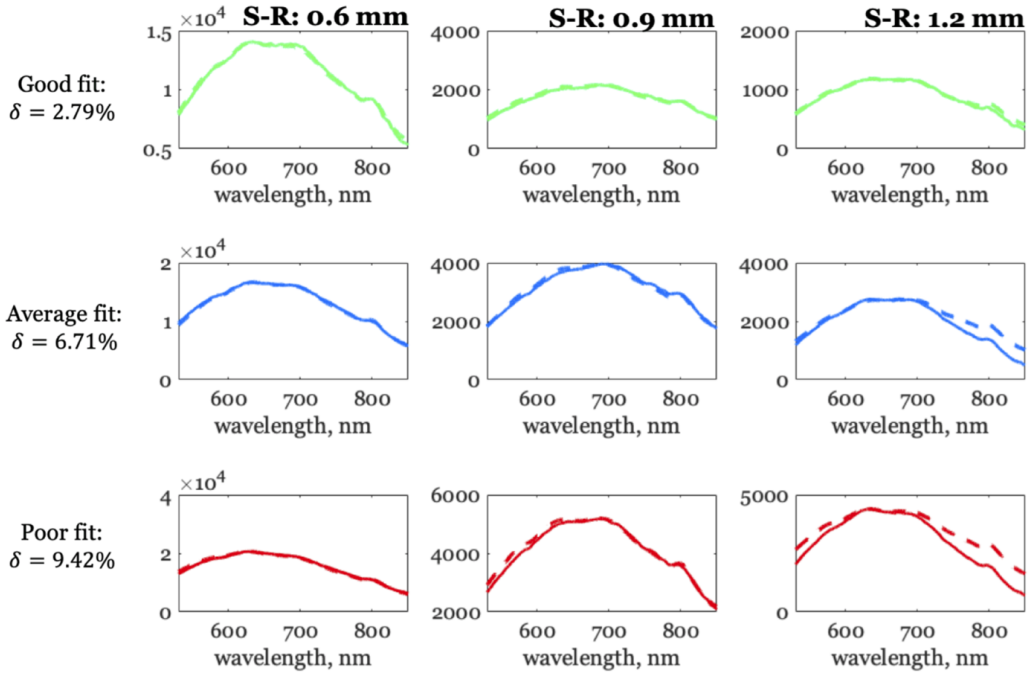

Figure 6.2.4 Examples of SAR-DRM for polystyrene suspensions and corresponding good(green), average(blue) and poor(c) fit.

therefore should be represented by selected theory better, it is also potentially affected by factors not accounted in the current approximation.

6.2.3 Conclusions

This section justified the choice of the objective function, tested the inversion algorithm performance, evaluated the outcomes and set certain limitations to optimise the inversion performance. Clarification of the objective function selection was an essential step to proceed as the results obtained from inversion are judges by the performance of an objective function. The chosen function, δ, has shown a single minima value and straightforward solution surface.

Inversion of the simulated dataset has helped to distinguish the potential shortcomings that might arise from the inversion and eliminate them by introducing the additional stopping criteria. The inversion on the measured diffuse reflectance visualised different δ values in the context of the goodness of the fit. The signal returned from the inversion algorithm repeats the measured reflectance intensity well along all of the wavelengths with some mismatches appearing at longer S-R distances. The study continued with the

application of the method onto polystyrene datasets to analyse the performance of the method.

6.3 SAMPLE SET 1: MONODISPERSE POLYSTYRENE SUSPENSIONS

One of the primary goals of this analysis was testing the effects of each parameter of interest on spectra signal collected by receiving detectors at different distances for vis-short NIR wavelength range. The investigation of potential effects was conducted and presented in Chapter 4, where the simulated spatially resolved signal had a number of distinct changes with the change of each parameter. Those observations implying the possibility of spotting those variations and convert them back to the system's properties via numerical and analytical methods.

Therefore, the goals for the upcoming analysis were:

- To inspect the signal obtained with reference to pre-knowledge of the parameters of interest

- To see how comparable the effects were seen in simulated spectra to the measured signal

- To understand the limitations to the method arising from the measured signal

The inversion algorithm, proposed in Chapter 5, consists of two stages: inversion of the monodisperse system followed by inversion of the polydisperse system. The combination of mode radius and concentration was studied first on sample set 1, consist of monodisperse polystyrene suspensions. To meet the stated goals, the section below presents the following stages of analysis. Initially, the SAR-DRM spectra in the form of I_{diff} were reviewed in the context of pre-known particle radius and concentration of the samples. After a preliminary analysis of the trends, the inversion algorithm was applied to estimate the above-mentioned parameters of interest and clarify the possibility of tracking the properties of the materials back from spatially resolved spectroscopic measurements. This study consist of a comparison of estimated parameters with reference measurements and evaluation of the differences in the prediction in comparison with corresponding objective function values.

6.3.1 FEATURES ANALYSIS OF SAR-DRM SIGNAL

The inversion was preceded by a preliminary examination of the signal collected. As a result of this examination, we expect to classify the effect of different parameters to the measured signal, the difference between them and the degree of each effect.

Spatially resolved spectra were sorted based on physical properties and composition of the suspensions known from the reference measurements. Even though parameters of interest are inverted simultaneously, the analysis is structured to describe each of the effects separately for clarity. The I_{diff} measurements corresponding to different mode radii and concentration of solids were compared between each other.

EFFECT OF MODE RADIUS ON SAR-DRM SPECTRA

The appearance of the particle size effect on I_{diff} was examined first. Figure 6.3.1 shows examples of I_{diff} collected for samples with a similar concentration and different particle size. To illustrate the entire dataset collected from typical measurement, the figure shows I_{diff} collected by different branches of fibred (South, West, North, East) and available S-R distances, although in the current analysis, the latter is truncated to three longest distances.

In comparison to observations from simulated spectra, the effect of particle size does not look as profound, however, it has similar features and exhibits the same behaviour with a variation of sizes overall. There are some features of the signal, that can be confirmed with what was seen in R_{sim} in Chapter 4. For example, the intensity of the signal is decreasing with increment source-to-detector distance. This observation associates with the extinction of the light due to multiple scattering. This observation was discussed in details during the analysis of the forward calculation in Chapter 4. Another observation, confirming the discussion of the simulated signal in similar wavelength range is the moderate decrease of the intensity with an increase of the particle size.

For all the S-R distances, the majority of the size effect appears between 600 and 700 nm wavelength, however, particle size effect appears differently on spectra collected at different distances. At shorter $S-R$, diffuse reflectance signal does not differ between different samples. Still, the trend can be spotted anyway, that the light collected from samples with larger particles has a higher intensity than the light collected from suspensions with particles of smaller sizes. The reverse in the intensity order refers to a larger number of multiple scattering that is happening in the samples with smaller particles in the same

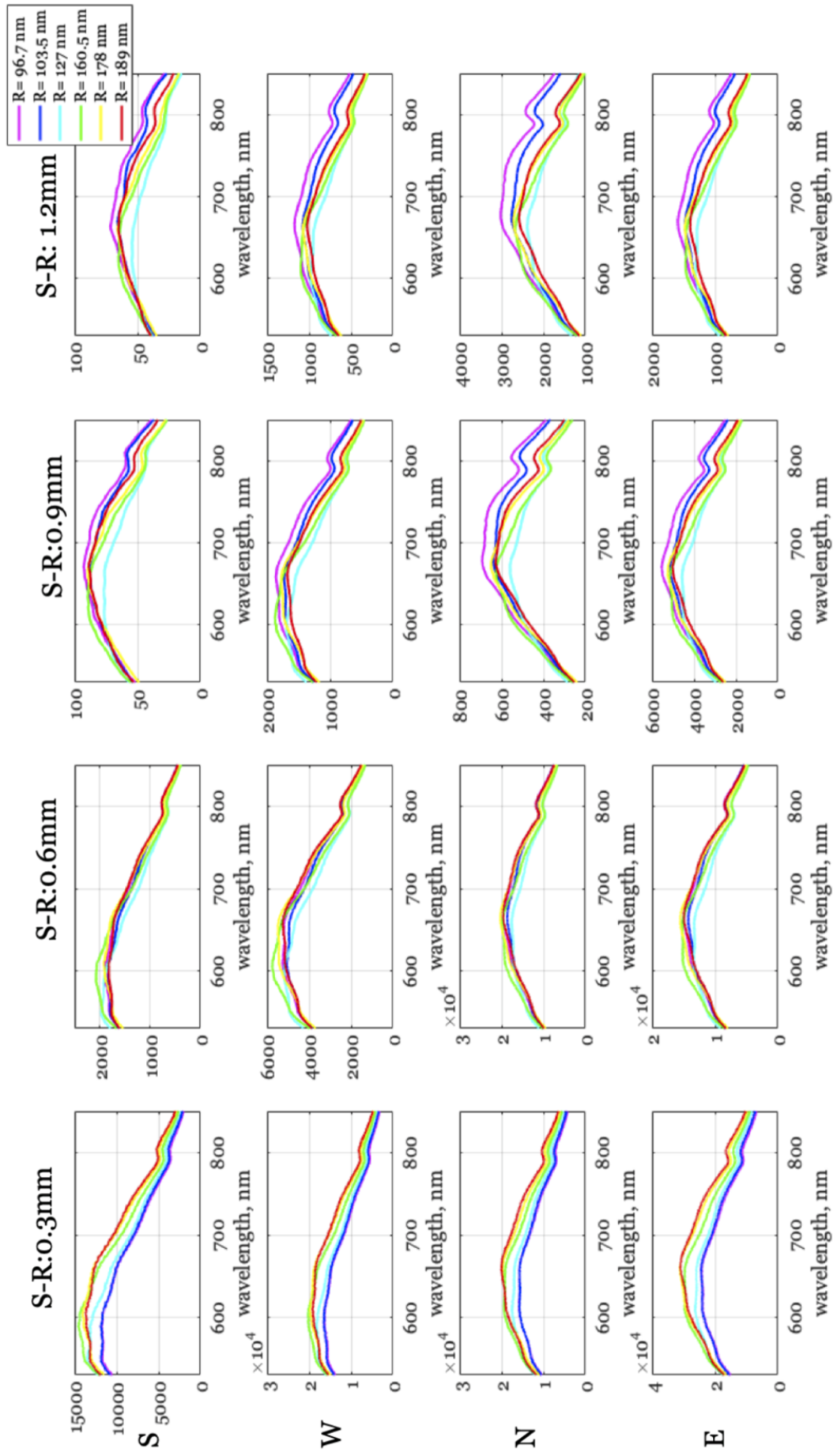

Figure 6.3.1 SAR-DRM collected for polystyrene monodisperse suspensions of concentration ~ 3.75wt%. Colour corresponds to samples with different peak size.

volume of material compared to a number of scattering in the sample of the same volume with particles of large size.

The relative difference in the magnitude between different samples increases with the increase of S-R distance, however, it is mostly located at 700-850 nm wavelength range. There is also a small variability between different samples in the profile formed by spectra over analysed wavelength.

Comparing the signal collected by different branches of SAR-DRM, there is notable variability across them in regards to the signal intensity and appearance across wavelength. The South branch exhibits relatively low-intensity values in comparison with other branches. The signal collected at 1.2 mm has intensity comparable to reference measurements from the integrating sphere. The rest of the branches have similar intensity between each other. There some variations in the signal for each sample itself, for example, the difference in the magnitude, observed at 700-850 nm wavelength range, differs across different branches. Nevertheless, the variations do not appear to change the overall appearance of the spectra observed across different branches.

Effect of concentration on SAR-DRM spectra

A similar comparison was conducted for samples of a different concentration of solids. Figure 6.3.2 shows examples of I_{diff} collected for the polystyrene suspension of the same particle size but five different concentrations. The previous section highlighted the effect of the mode on the spectral signal, therefore the type of effect can be compared with the concentration effect.

The influence of the concentration variation mostly represented as variations in the magnitude between the signals. In contrary to the particle size effect, the difference between concentration can be seen clearly for all S-R distances, including the fibre closest to the source. There is also a slight change in the profile of the spectral signal when compared over different collection distances. However, a majority of the S-R effect appears when analysing specifically samples with 6.1 wt% and 4.78 wt%. The position of the spectra peaks through dilutions does not change, which reflects the same origin of the sample. With an increase in the concentration of solids, the intensity of the collected signal is decreasing. This observation is anticipated and correlates with results of the forward calculation and thoroughly discussed in Chapter 4.

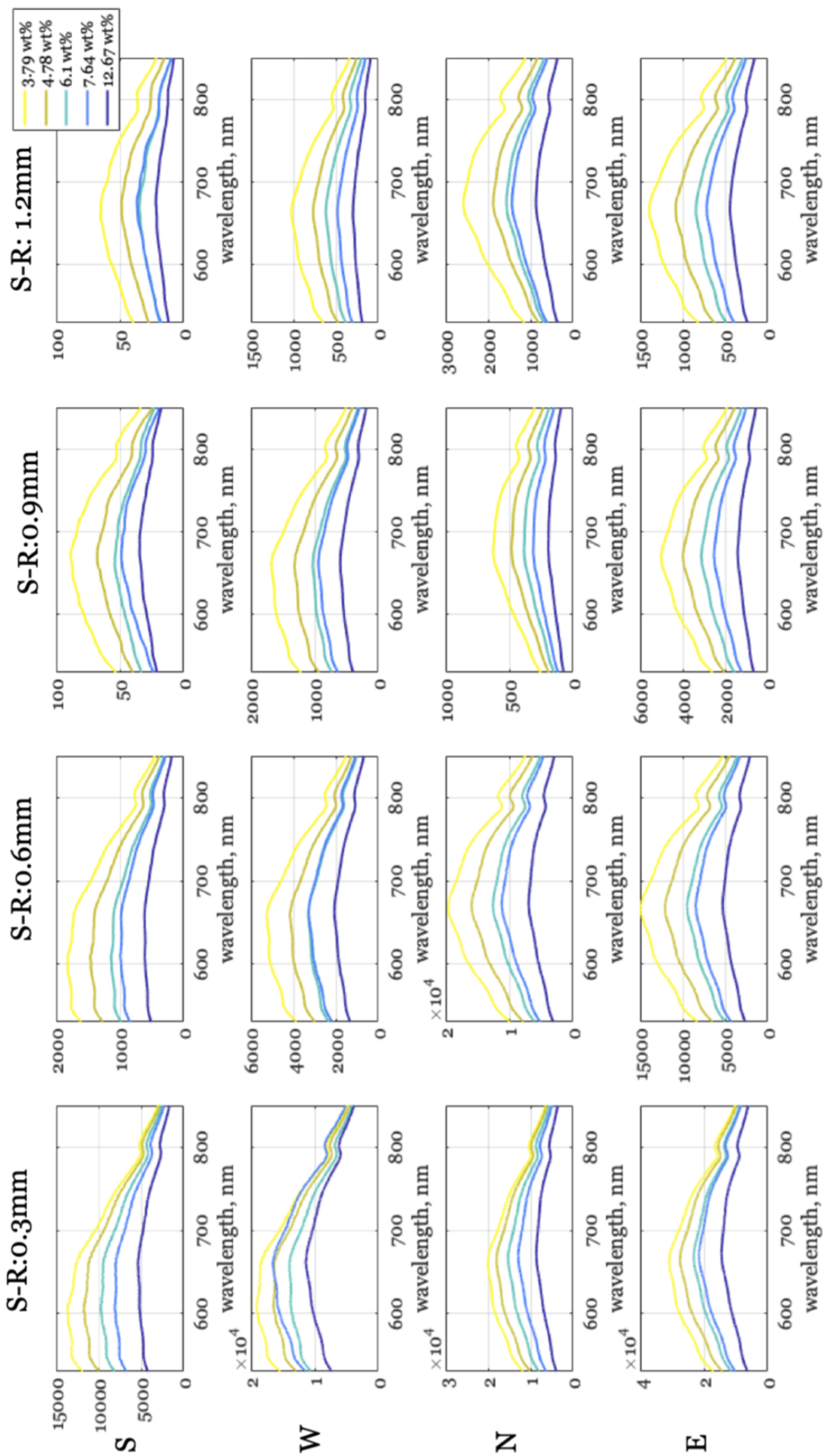

Figure 6.3.2 SAR-DRM collected for monodisperse polystyrene suspensions with mode radius 188.75 nm. Colour corresponds to concentration of solids

Similarly to observations made in the previous section during the particle size effect analysis, there are variations in the signal collected from different SAR-DRM branches. They are mostly appearing in the form of intensity variations and do not affect the appearance of the signal greatly.

The preliminary analysis of the measured signal concluded that the effect of particle size appears differently for particle size and concentration variations. They also confirm the general observations made during the study on the simulated signal. The latter emphasises that forward calculation routine developed accurately describes the measured signal, allowing to pursue the inversion steps to estimate the parameters of interest. As part of the study, the potential effect of intensity variations across branches will be studied as well.

6.3.2 SIGNAL INVERSION

The following sections will highlight the outcomes of inversion, conducted for monodisperse polystyrene suspensions. As followed from the sample set name, the corresponding data set of the measured signal is presumably free from particle size distribution effect. Therefore, with distribution width fixed to monodisperse and particle shape being spherical, the only parameters that suppose to have an effect of spectra are particle radius and concentration of solids.

Following the structure of previous Section 6.3.1, the analysis of the inverted parameters will be presented in two parts, for mode radius and concentration, respectively.

MODE RADIUS ESTIMATION

After executing the inversion algorithm on Dataset 1, the mode radius was estimated and the result of estimation is presented in Figure 6.3.3. The signal from each SAR-DRM fibres branch was inverted separately and therefore, the results are presented for each of them, also in comparison with reference measurements from DLS. The inverted results, presented below have not matched with any of the inversion algorithm searches constrains, therefore, the variations in the predictions shall be considered unaffected by the inversion algorithm parameters.

The variability between measured and estimated mode radii exist across all branches, however, it is especially observable at South branch (Figure 6.3.3(a)). Inversion results from this branch are not systematic and hardly similar to corresponding reference measure-

ments. Inversion of signal from the other three branches returns more consistent results. The Root Mean Square Error (RMSE) between estimated mode radius and measured from DLS is 71.5 nm on average across these three branches. The quality of the fit is also significantly lower at South branch, reaching 8 % against ~ 5% at other branches. Therefore, the following conclusions will be based on an analysis of the remaining three branches. Tables of the inverted and reference mode radius values can be found in Appendix A.1.

There are some of the samples, estimation for which was far from the reference measurement, but the fit returned by the inversion algorithm was quite poor, according to the objective function values. However, it is not a systematic observation as there is a number of samples, estimated mode radius for which did not correspond the reference values, however, the quality of the fit was good. What is systematic is the overall deviation of the estimated results. As depicted in Figure 6.3.3, each branch has a number of samples of various mode radii that have consistent deviation by the value of approximately equal RMSE. After examining the samples manually, it came to attention that they belong to the same original sample, that was diluted to formate the sample set.

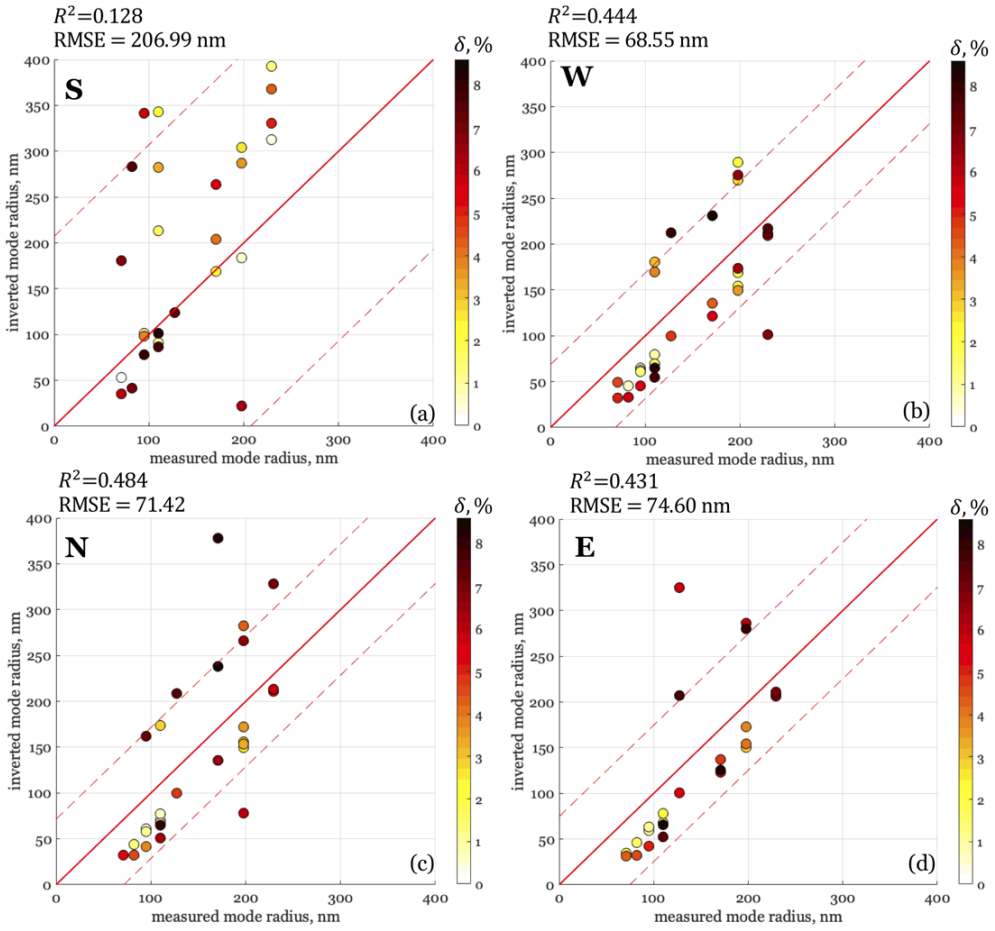

Figure 6.3.3 Comparison of estimated mode particle radius with mode radius from reference measurements (DLS) for different SAR-DRM branches (a-d). Colour corresponds to corresponding to each sample's objective function value δ.

Since the variations of the estimated mode radii from the reference measurement appear across different size values and also do not exhibit correlation with objective function values, another angle for analysis to consider is the appearance of the variations in the estimated mode radii in the context of the actual concentration of each sample. Figure 6.3.4 illustrates the result of the analysis by presenting the variation between estimate and reference mode radius (y-axis) with respect to objective function values (x-axis) for each SAR-DRM branch. It appears that inversion of the samples with a concentration above ~ 8 wt% returns the mode radius within 50 nm difference from the reference measurement. The variation in the estimated particle radius is increasing for samples with the concentration below this value across different branches; however, the number of samples that exhibit suchlike trend is low for the exact trend formation. This occurrence can be

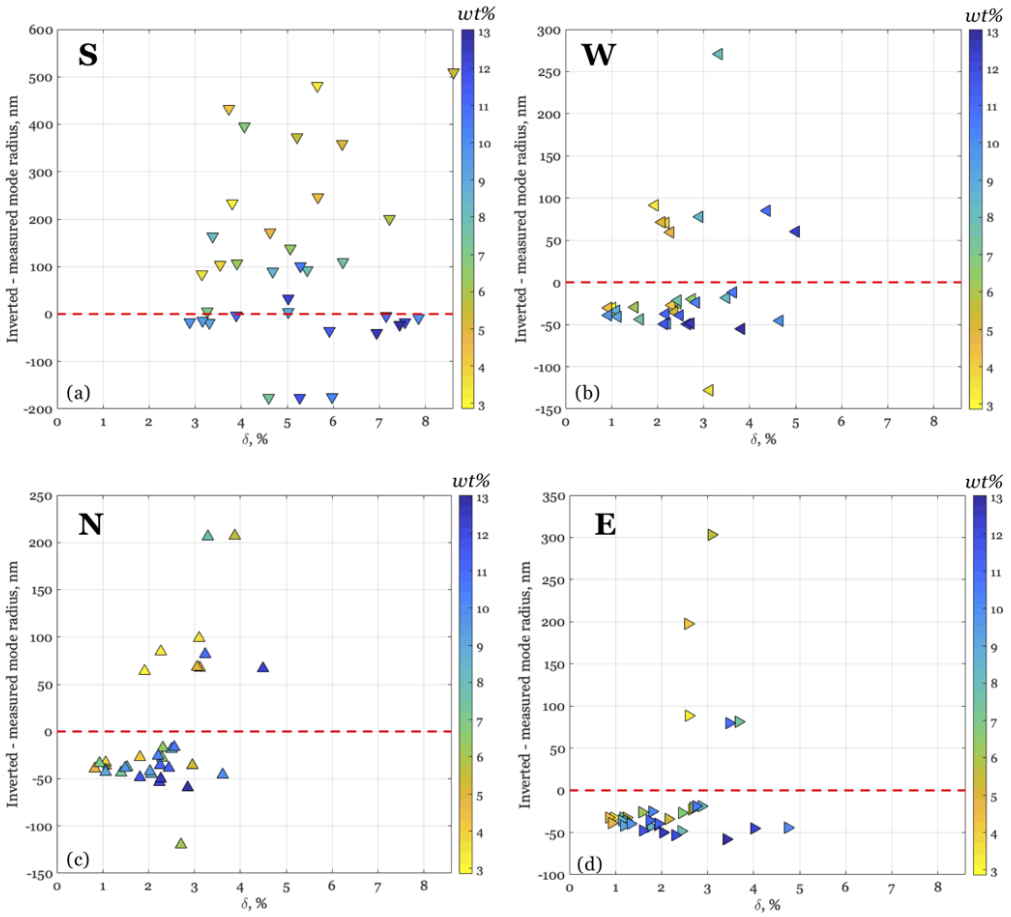

Figure 6.3.4 Actual difference between estimated and measured mode radii in comparison with δ for different SAR-DRM branches (a-d). Colour corresponds to concentration of the samples.

related to many factors. First of all, the reference DLS measurement was collected from the original suspensions that were extremely diluted, whereas inversion algorithm was applied to samples of various concentrations. Therefore, the comparison of the reference measurement with estimated values might reflect the variability of the particle size due to the dilution process.

Estimated mode radius is generally underestimated in comparison with reference measurements. At this stage of the analysis, it is difficult to conclude the reason behind it as it could equally be the effect of concentration inversion, which was performed simultaneously or the accuracy of the DLS measurements.

CONCENTRATION ESTIMATION

The concentration of solids is another parameter of interest that was estimated for Sample set 1. It was inverted simultaneously with mode radius, and therefore, it is vital to not only analyse the estimated concentration in comparison with reference measurements but also evaluate the potential effect of it in the context of estimated mode radius, discussed in the previous section.

The variability of the predicted results is higher from the South branch signal, which is echoing the similar observation made from mode radius inversion. First of all, the quality of prediction is evaluated based on a comparison of values obtained from an inversion with values from gravimetric analysis. Results of the comparison are illustrated in Figure 6.3.5. Some observations follow the trends, observed an estimated mode radius. Concentration estimated from signal collected from the first branch does not correlate with measured concentration as illustrated by R^2 and RMSE. Concentration estimated from the other three branches shows good correlation with measured concentration with average RMSE across different branches being 3.68 wt%. Tables of the inverted and measured concentration can be found in Appendix A.1.

The inverted concentration exhibits similar errors across West, North and East SAR-DRM branches, whereas the North branch is associated with higher variability of the concentration. This observation was already made during the analysis of the mode radius inversion for the same sample set, therefore the following discussion will be generalising observations across the remaining SAR-DRM branches.

The inverted concentration agrees better with the measured values when the latter is below ~ 8 wt%, whereas after exceeding this value, the agreement of the inverted and measured concentration reducing, especially at West and East branches. The variations in the estimated concentration, tailored in a specific concentration range raise the question regarding the possible dependency of these events. As was observed in Chapter 4, the intensity of the SAR-DRM is reducing with the increase of concentration in such range; besides, the SAR-DRM measurements from the closest S-R distance which have the strongest light intensity were excluded from the analysis to benefit all three parameters of interest inversion, which altogether might impact the inversion result. An additional concern may arise from the possibility that the scattering regime at such concentration is different from diffuse, which would contradict with selected theories. The latter will be discussed in more details after analysis on Sample set 2.

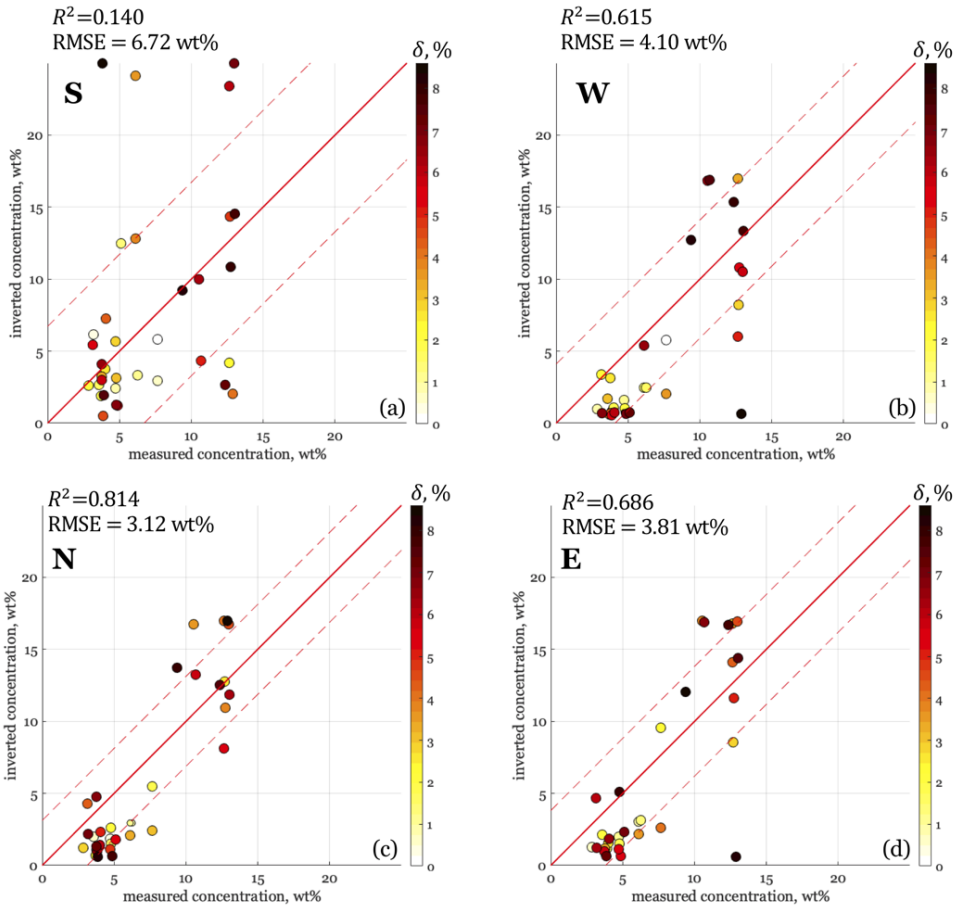

Figure 6.3.5 Comparison of estimated concentration with concentration from reference measurements for different SAR-DRM branches (a-d). Colour corresponds to corresponding to each sample's objective function value δ.

Regarding the possible ways to improve the predicted results, there are a number of samples, inversion of which returned the high inversion error and the concentration parameters, that is drastically different from the measured value, suggesting that the inversion error might indicate the misprediction of the parameters. Some of the samples, however, do not correlate well with reference concentration values and also have large δ value; however, similarly to observations made from mode radius inversion, this is not a regular occurrence. There is, however, the correlation between different regimes concentration of solids and the quality of estimation. As appears in Figure 6.3.5, the inversion of the samples of concentration below ~ 6-8 wt% tends to underestimate the concentration, however, the values are relatively close to the measured ones. In contrast, inversion of the samples with higher concentration has higher variability and estimates

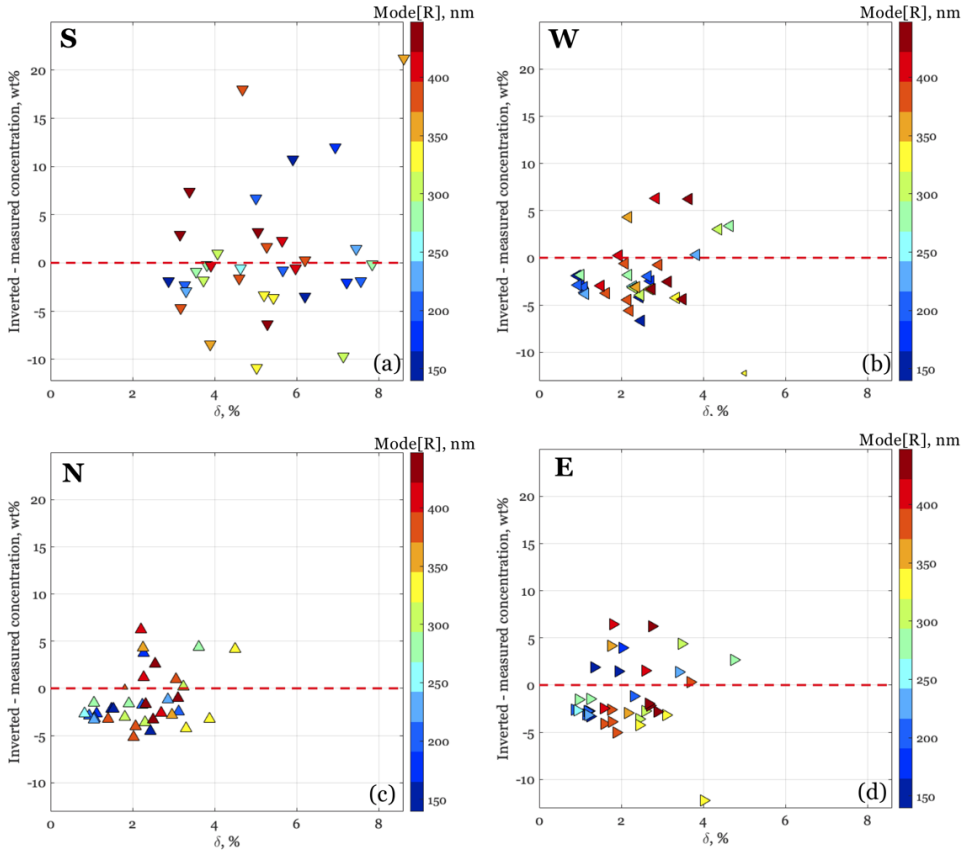

Figure 6.3.6 Actual difference between estimated and measured concentration in comparison with δ for different SAR-DRM branches (a-d). Colour corresponds to samples with different mode radius.

concentration higher as well as lower than the measured values. This observation does not have a straightforward correlation with particle size, as partially confirmed by analysis of the difference between estimated and reference concentration in respect to δ values, shown in Figure 6.3.6. However, the number of samples that exhibit one or another correlation does not allow to draw a straightforward conclusion in this matter, suggesting that there competing for effect between mode radius and concentration, which might be present, does not form a well distinguishable trend, concluding from the current analysis.

Conclusions

Inversion of the Sample set 1 unveiled certain specifics of the SAR-DRM spectra sensitivity to the parameters of interest and the measurement setup.

South branch has the lowest intensity of the sigma among the SAR-DRM branches, which had a negative effect on the estimation of the parameters and led to the variability of the estimated mode radius and concentration. The inverted parameters were associated with high inversion error. The quality of the fit across other branches had a moderate level of variations, which can also be assessed by R^2 and RMSE. From the inversion of both parameters, the North branch has shown results that are closely matching with reference measurements for both parameters.

Considering the observations above, what can be concluded is that there is a distinguishable difference between spectral signals collected for samples of different mode radius and concentration. From the analysis of the branch with lowest error values, the quality of the provided fit is below 5% which is considered as a medium to a good fit and the estimated mode radius and concentration well agree with reference measurements. The interference of these parameters of interest in the estimation of each other does not appear at a significant extension to conclude the exact trend. However, the accuracy of the inverted concentration decreases for samples with a concentration of over ~ 8 wt%, which appears to be a consistent trend across different SAR-DRM branches. The reason behind this phenomena may be associated with the limitation of the diffusion regime of the selected sequence of the SAR-DRM source-to-receiver distances.

6.4 Sample set 2: Polydisperse polystyrene suspensions

The particle size distribution inversion requires the usage of both stages of the developed inversion algorithm. In the following section, the analysis will be presented in two parts. The focus of the first part will be on investigation of number particle size distribution (PSD) effect on SAR-DRM, followed by inversion of the number PSD in the form of the mode radius and distribution width combination. The results are analysed with reference to DLS and Nanosight measurements. The second part discusses the concentration estimation in comparison with reference measurements.

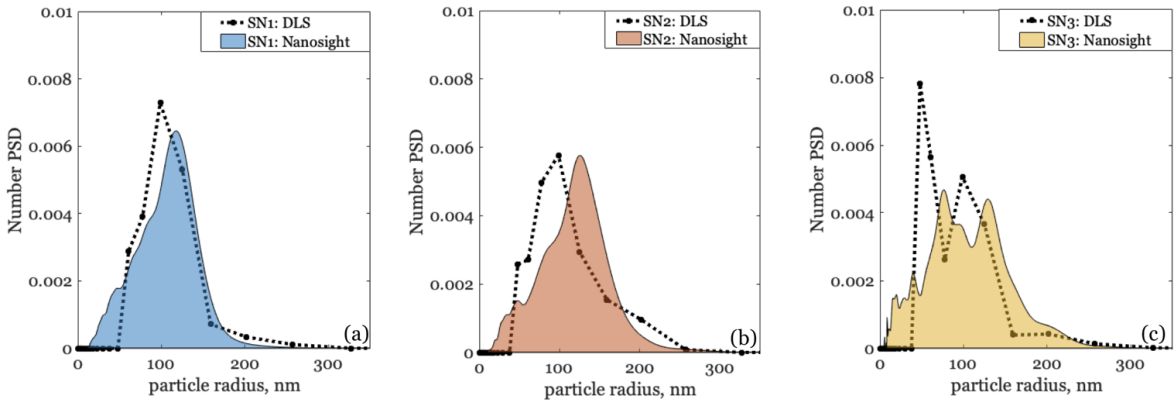

Figure 6.4.1 Reference measurements of number particle size distribution density function obtained from DLS (black dots) and Nanosight (coloured area). Each colour corresponds to different origin sample.

6.4.1 Features analysis of SAR-DRM signal

Sample set 1 consist of monodisperse samples, therefore the analysis of the inversion performance was conducted on Samples set 2. Summarising the description in Chapter 5, the Sample set 2 is based on 3 original polystyrene suspensions, two of which are mixtures of the monodisperse suspensions. The reference number PSD measurements for each of the original samples can be seen in Figure 6.4.1. DLS measurements are generally agreeing with measurements from Nanosight, confirming the presence of three different PSD with different mode radius and distribution width. The relative polydispersity of the samples, when compared the reference measurements for mixtures (SN2 & SN3) against monodisperse sample (SN1), is moderate. This is especially seen comparing Nanosight measurements for SN1 and SN2, which have very similar distribution width. It also should be noted that both reference measurements indicate sample SN3 as multi-modal PSD.

The differences in mixtures were reflected in SAR-DRM, according to Figure 6.4.2. Unlike mode radius or concentration changes, that appear at a similar degree across all S-R distances, the appearance of distribution width changes with an increase of S-R distance. Hence, the signal is presented for all available S-R distances, even though only three longest are used in the analysis. In parallel with the analysis of spectra features for monodisperse suspension in Section 6.3, the SAR-DRM spectra are presented for each branch as well. It should be noted that between a collection of SAR-DRM from Sample set 1 and Sample set 2, the optical probe was replaced, which affected the intensity of the signal, making it slightly higher across all the branches, especially for South branch.

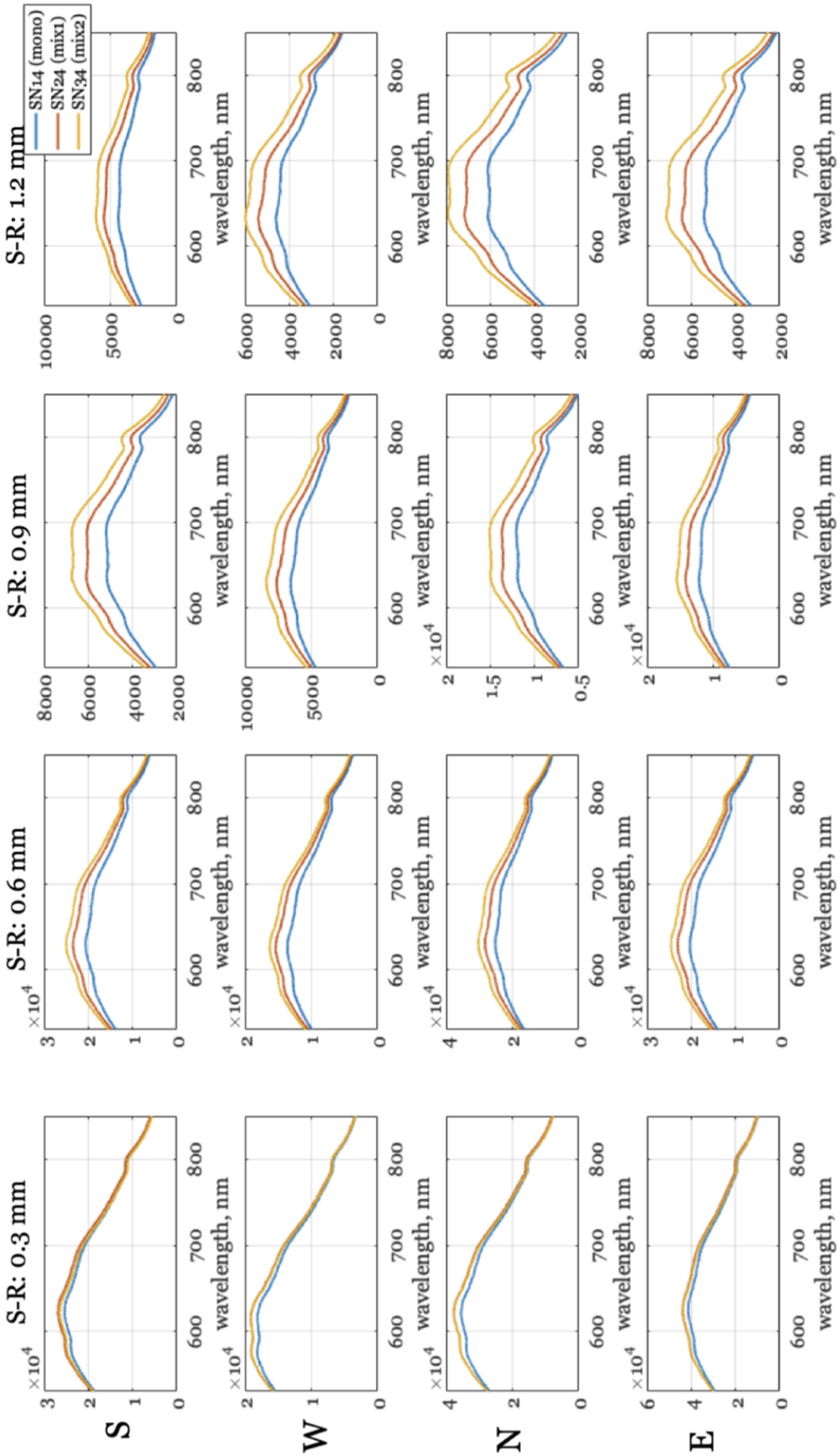

Figure 6.4.2 SAR-DRM collected for polydisperse polystyrene suspensions of concentration ~ $3wt\%$. Colour corresponds to samples with different peak size.

Since, according to reference measurements, the mixtures differ in both distribution width, and mode radii, the nature of the effect on SAR-DRM was identified based on features seen on simulated spectra. The spectra, collected at the closest distance from the source almost does not differ between different samples, the spectra intensity is very similar. With the increase of the S-R distance, the relative magnitude between lines increases, predominantly in the wavelength range 600-750 nm. The concentration of solids affects spectra magnitude, however always in similar proportion across all distances, confirming that the effect seen in the current selection of samples is not associated with concentration changes. Unlike suspensions of different particle sizes, where there was noticeable variability between spectra, the spectral profiles collected from these suspensions are almost identical across different wavelength. It emphasises the fact that these suspensions have a similar predominant particle radius. In the sample set shown in Figure 6.4.2, the magnitude changes along with the overall slope of the spectral profile. Taking into consideration the above mentioned, along with observations made in Chapter 4, it can be concluded that most of the difference between presented samples is caused by variations in distribution width. Changes in the mode radius are also present in the form of the slight spectra profile change, however, the variation is relatively small, which agrees with reference PSD measurements.

The effect of concentration is not presented here as it was illustrated and discussed during the analysis of monodispersed polystyrene suspensions.

6.4.2 SIGNAL INVERSION

As an outcome of the inversion algorithm execution, each sample in the Sample set 2 was provided with the estimated mode radius, distribution width and concentration. The results of the inversion that are obtained at the end of the second stage are analysed below.

PARTICLE SIZE DISTRIBUTION ESTIMATION

Following the discussion of Section 6.3, mode radius and distribution width are inverted for each branch separately. The results on the inversion are organised into Table 6.4.1 for the mode radius and the distribution width inversion from each SAR-DRM branch, compared against the reference DLS measurements. The parameters are visualised in the form of number-based distribution curves in Figure 6.4.3.

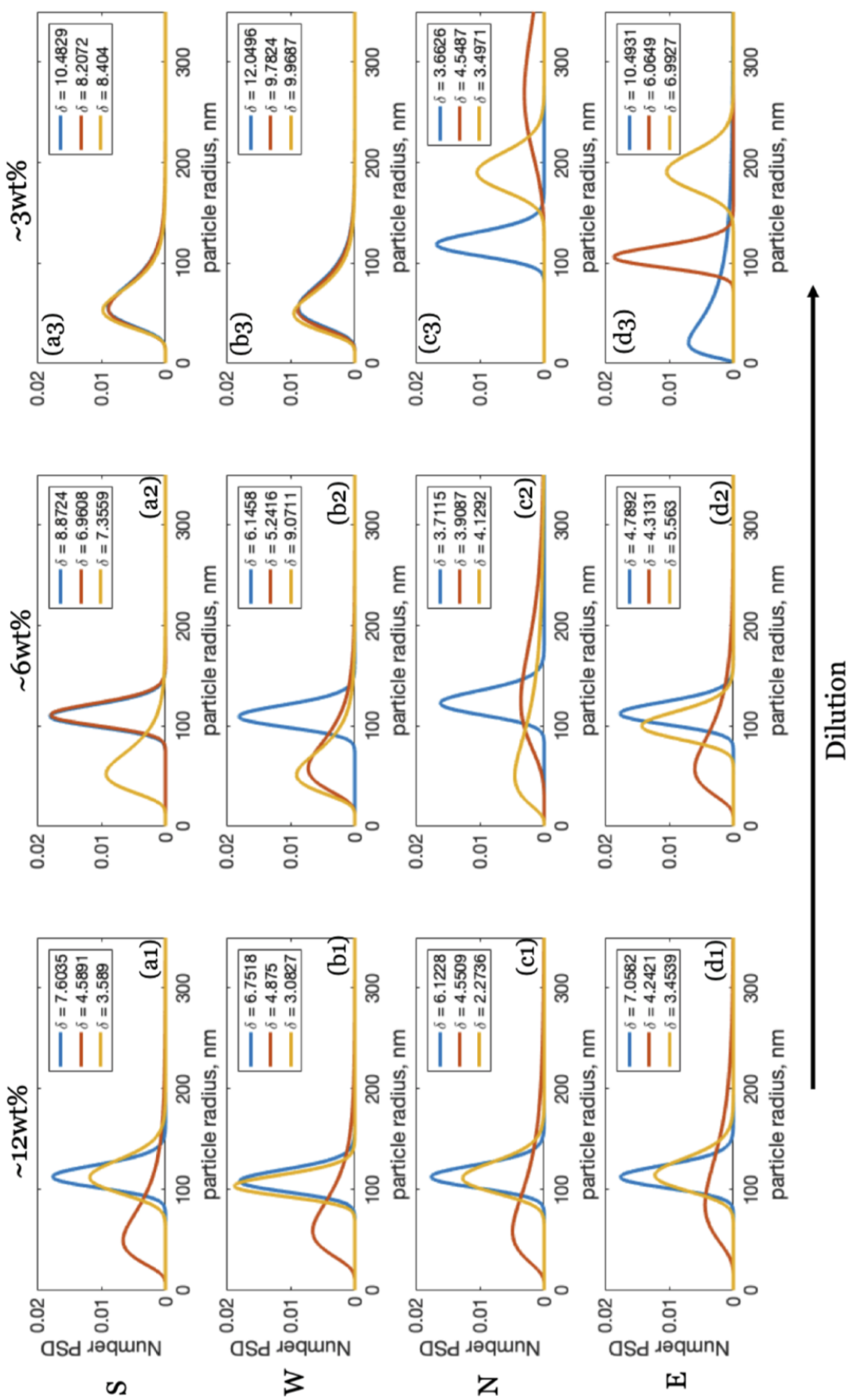

Figure 6.4.3 Number particle size distribution obtained from inversion of SAR-DRM. Each colour corresponds to different origin sample.

The quality of the fit, presented in the legend in Figure 6.4.3, varies from poor to good across different samples. There is no direct correlation of the occurrence of the poorly fitted results, however, a lot of poor quality fits are returned for suspensions of relatively low concentration (Figure 6.4.3 (a3)-(d3)). All δ values returned for Sample set 2 were below 15%, which implies that convergence was reached before these stopping criteria were activated. However, this observation will be additionally analysed in the context of estimated concentration.

Number - based PSD returned for highly concentrated samples indicates that the first sample in the sample set (SN1) is monodisperse the estimated distribution width is 0.1. Out of two remaining samples, which are mixtures, the estimation for SN3 has the broader distribution width and smallest mode radius, whereas SN2 has identical mode radius to monodisperse suspension (SN1), but larger distribution width compares to it. With the reduction of the concentration, the values of estimated parameters change. With some exclusion, the general trend dictates that the distribution width becomes broader with a decrease of concentration, and the mode radius is shifting towards smaller radius values.

At the moment, the result of the inversion exists in the form of four different versions, corresponding to four SAR-DRM branches. Comparing the performance of inversion from each of the branches between each other, the first straightforward observation is that the variability in the estimation of PSD across them differs in much smaller extent compared to what was seen in the analysis of monodispersed polystyrene suspensions, which is a direct effect of a probe replacement and the consequential intensity increase. The variations across different branches are not exceeding 9% of inversion error. Inversion of signal from the North branch is associated with the lowest inversion error across SAR-DRM fibres, however, the difference is relatively low, in comparison with, for example, East branch. Hypothetically, the variations between different branches may be accounted for in respect to a parameter, like δ during the analysis of, for example, averaged parameters of interest after inversion.

The inverted parameters were compared against reference measurements and summarised in the Table 6.4.1. The average variations between inverted and measured mode radius for the whole sample set are similar across different SAR-DRM branches with the same conclusion made for the distribution width variation. Mode radius inverted for the SN1 is estimated close to the reference measurements, which can be related to the fact that this sample is a monodisperse reference sample, a product of the polymerisation reaction.

Table 6.4.1 Table of estimated and measured mode radius(Mode[R]) and distribution width (σ) values for Sample set 2 for all SAR-DRM branches

	South				**West**				**North**				**East**			
	Mode[R], nm		σ		Mode[R], nm		σ		Mode[R], nm		σ		Mode[R], nm		σ	
	Ref.	Inv.	Ref.	Inv.	Ref.	Inv.	Ref.	Inv.	Ref.	Inv.	Ref.	Inv.	Ref.	Inv.	Ref.	Inv.
SN11	106.44	112.94	0.28	0.10	106.44	108.65	0.28	0.10	106.44	112.84	0.28	0.10	106.44	112.74	0.28	0.10
SN12	106.44	109.74	0.28	0.10	106.44	109.45	0.28	0.1	106.44	122.75	0.28	0.10	106.44	112.35	0.28	0.10
SN14	106.44	55.84	0.28	0.37	106.44	55.79	0.28	0.38	106.44	118.56	0.28	0.10	106.44	21.01	0.28	0.91
SN21	101.67	49.96	0.38	0.53	101.67	59.10	0.38	0.46	101.67	58.77	0.38	0.58	101.67	85.31	0.38	0.47
SN22	101.67	111.01	0.38	0.10	101.67	57.84	0.38	0.43	101.67	124.41	0.38	0.41	101.67	57.30	0.38	0.51
SN24	101.67	54.52	0.38	0.38	101.67	53.82	0.38	0.39	101.67	268.41	0.38	0.24	101.67	106.05	0.38	0.10
SN31	84.03	112.27	0.45	0.15	84.03	103.87	0.45	0.1	84.03	111.63	0.45	0.14	84.03	114.48	0.45	0.14
SN32	84.03	52.33	0.45	0.38	84.03	51.46	0.45	0.40	84.03	50.61	0.45	0.68	84.03	100.09	0.45	0.14
SN34	84.03	53.28	0.45	0.36	84.03	49.83	0.45	0.39	84.03	190.15	0.45	0.10	84.03	190.81	0.45	0.10

Table 6.4.2 Table of estimated and measured concentration values for Sample set 2 for all SAR-DRM branches

	South		**West**		**North**		**East**	
	Ref., wt%	Inv., wt%	Ref., wt%	Inv., wt%	Ref., wt%	Inv., wt%	Ref., wt%	Inv., wt%
SN11	12.99	6.92	12.99	5.92	12.99	19.08	12.99	7.40
SN12	6.50	3.08	6.50	3.09	6.50	3.74	6.50	3.53
SN14	3.25	1.75	3.25	1.66	3.25	1.37	3.25	2.91
SN21	12.98	3.57	12.98	3.25	12.98	4.33	12.98	4.28
SN22	6.49	2.34	6.49	2.63	6.49	3.20	6.49	3.08
SN24	3.24	1.54	3.24	1.48	3.24	1.69	3.24	1.28
SN31	11.98	7.69	11.98	3.3	11.98	4.87	11.98	12.96
SN32	6.50	2.31	6.50	2.19	6.50	4.38	6.50	1.93
SN34	3.25	1.64	3.25	1.57	3.25	1.18	3.25	1.16

The highest variability between estimated and measured mode radius exhibited inversion of sample SN3, which is a mixture sample. The variations in the mode radius bear bare no obvious link to the variations in the estimated distribution width. The inversion of the SN1 provided with almost consistent σ of 0.1, which is the lowest limit for this parameter. Although there is a difference between reference and inverted distribution width, which can be estimated roughly as 0.18, this difference may be partially associated with the minimum distribution width values provided by selected DLS measurement.

More detailed statistical analysis between measured and estimated parameters like mode radius and distribution width maybe not entirely illustrative as values of distribution width appear differently depending on mode radius. Due to the fact that even fine variations in one or another parameter may change the PDF appearance, it is more prominent to assist the estimated mode radius and distribution width parameters couple with respect to reference measurements in the form of the number-based PDF. Expansion of the analysis results with distribution width complicates the clarity of the comparison of the results with reference measurements. Ultimately, the results from branches should match as they are collected within the same experiment. Variations in parameters estimated for monodisperse sample (SN1) across different branches are the smallest, whereas mode radius and distribution for mixtures (SN2 & SN3) vary across branches in moderate extent. The δ also vary slightly across different branches, however, this variability can be dictated by differences in the signal returned by each branch. Since the δ did not exceed the stopping criteria at any of the branches and the is no alarming observation made during SAR-DRM features analysis, there is no ground to eliminate any of the branches from the analysis. Therefore, there are two potential routes to address this question, to select a single SAR-DRM branch for the comparison with the reference measurements based on goodness of the fit or to average the estimated PSD across different branches. Since the variability of the δ values in this sample set is large, it is difficult to conclude the reliability of the parameter. Therefore, the averages PSD for the Sample set 2 can be seen in Figure 6.4.4.

Comparison of the estimated PSD with measured confirms the overall good ability of the SAR-DRM inversion to provide with PSD. Most of the number PSD appear in a good agreement with reference measurements from both DLS and Nanosight. The concerns can be raised about two cases. First of all, the relative difference in the size distribution from reference measurements for SN1 and SN2 is quite low, however, the inverted distribution

width for SN2 is largest across the sample set. The reasoning can be, indeed related to the reliability of the reference measurements, especially DLS as it generally not recommended for distribution width analysis. However, in the context of current research, the potential interference of the other parameters with distribution width prediction is at higher importance and will be considered. Inversion provides with mode radius and distribution width similar to reference measurements across different samples and their dilutions. Since mode radius and distribution width vary across SAR-DRM branches, the average across the latter exhibits bi-modality, most notable at the PSD estimated for samples of low concentration (Figure 6.4.4 (a3)-(c3)). This occurrence is difficult to justify a single factor due to various possible influences. First and foremost, the PSD presented in Figure 6.4.4 are average values across different branches, each of which returned fit of different quality, and there was no account on that here. Outside the data processing choices, this might be the effect of the dilution itself, or alternatively, the methodology may contribute to those observations as well. As can be seen from reference PSD, the SN3 may consist of two modes, which could have been spotted by SAR-DRM inversion. On the other hand, the SN1 is a result of the polymerisation reaction and is not expected to have multiple modes, which is confirmed by reference measurements. Summarising the discussion above, the PSD measurements across SAR-DRM are consistent enough, however, the variations in the parameters should be treated carefully before results interpretation.

Concentration estimation

The concentration of solids is inverted simultaneously with mode radius and distribution width. The result of inversion is presented in Figure 6.4.6 and Table 6.4.2 in similar fashion as was previously done in this chapter.

The correlation between the quality of the fit in the form of δ results and the quality of the concentration estimation is counter-intuitive, as can be seen in Figure 6.4.6 . Despite a few outliers, the general trend exhibits that samples provided with good spectra fit have poor correlation with measured concentration and vice versa. Notably, the samples that were mispredicted are underestimated and have the actual concentration above 6 wt%. The latter was also observed at the inversion of monodisperse suspensions. The systematic misprediction of the concentration above a certain value of actual concentration raises concerns regarding the causes of this phenomena. One of the potential causes can be arising from the diffuse approximation requirements. This concern was already voiced

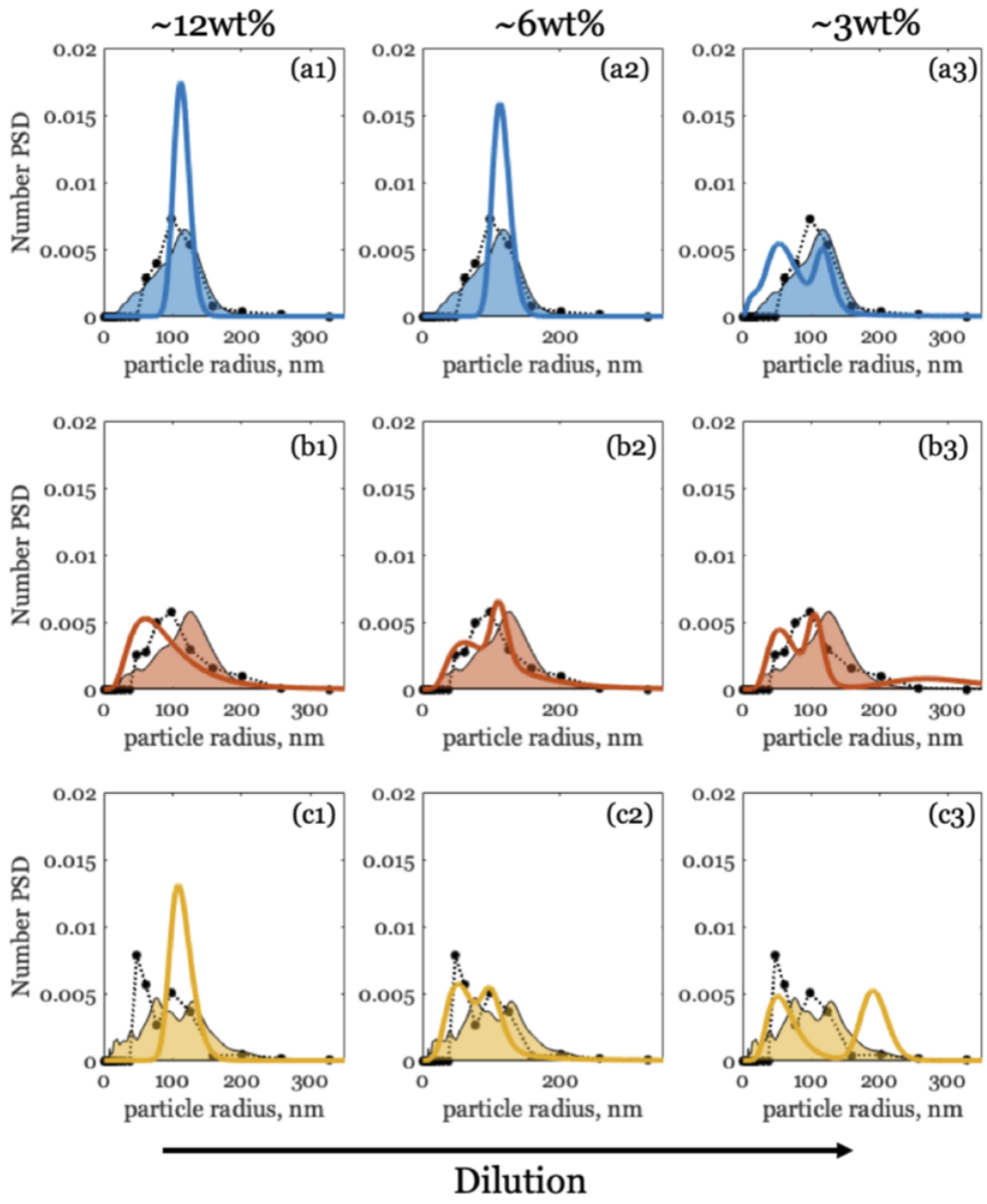

Figure 6.4.4 Number particle size distribution obtained from inversion of SAR-DRM averaged over all branches in comparison with the same particle size distribution from DLS (black dots) and Nanosight (coloured area). Each colour corresponds to a different origin sample.

during the analysis on the simulated signal in Chapter 4 in regards to insufficient transport mean free path at a certain combination of parameters. The analysis of tmfp conducted there concluded that high concentration is associated with short tmfp, therefore every S-R distance of SAR-DRM probe should satisfy the diffuse scattering condition. However, high concentration causing the scattering not nearly as isotropic as required by diffuse approximation. It has a simple physical sense that optical characteristics of a closely packed system of particles will not provide the environment for diffuse scattering and instead start reflecting the light in the more specular way from the layer closer to the collecting probe, whereas isotropic scattering conditions can only be safely met deep within the system.

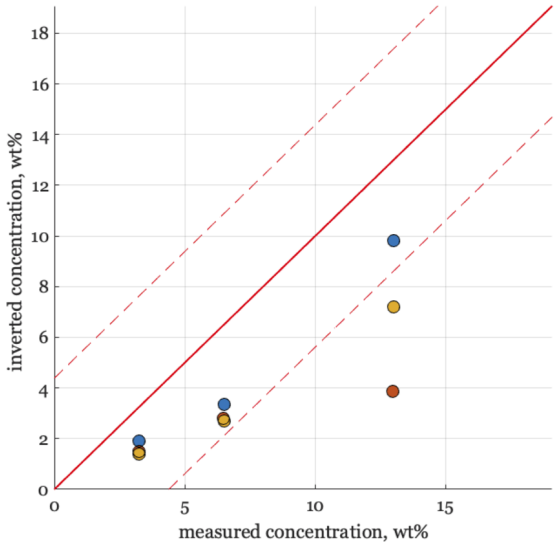

Figure 6.4.5 Comparison of estimated concentration with concentration from reference measurements averaged across West-East SAR-DRM branches. Colour corresponds to the legend.

The variability of estimated results across SAR-DRM branches is very low, which correlates with low variability of other parameters of interest estimation. The lowest accuracy of the estimated concentration is shown by the North branch, according to R^2 value and West branch, according to RMSE, but overall prediction results look similar at remaining branches. To continue the analysis of the parameters of interest in a consistent manner, the estimated concentration was averaged across West, North and East branches and the result presented in Figure 6.4.5, colour-coded accordingly to the sample origin. The general trend of the concentration estimation has not changed with averaging as

expected from the previous observations of the SAR-DRM branches data individually. However, the conclusion can be made that the inversion of the mixtures (SN2 and SN3) deviate the most from the measured concentration, the following analysis focuses of the dependencies between estimated concentration and distribution width, which are parameters associated with the mixtures.

Analysis of this concern was done by examining the potential interference of the parameters of interest prediction for the cases, where one parameter compensate another. Interference of the σ parameters was checked as it has a similar effect on the SAR-DRM as concentration changes. Figure 6.4.7 depicts the actual difference between measured and estimated concentration across corresponding objective functions values. The colour scheme of the Figure corresponds to estimated values of distribution width.

Across all the branches, the samples that have been inverted with high accuracy of concentration are not monodisperse as the result of distribution width estimation. Some of the inverted samples, like SN2, at high concentration, have distribution width estimated higher than the one exhibited on reference measurements. It is the most probable scenario that distribution width is over-compensating the concentration effect, causing misprediction in both by falling into local minima. Avoidance of the situation similar to this in the analysis can be done by providing the concentration information before the SAR-DRM inversion. This would remove a degree of freedom, allowing to minimise the variations in the estimated values of both concentration and distribution width. To keep the concentration estimation intact, another way to approach this matter would be accounting on the degree of misprediction for known material. There is a clear trend in the concentration values misprediction in the form of proportional underestimation of the concentration as the actual concentration increases. Therefore, with an extensive sample set, the trend can be clarified better, and the correction factor can be derived.

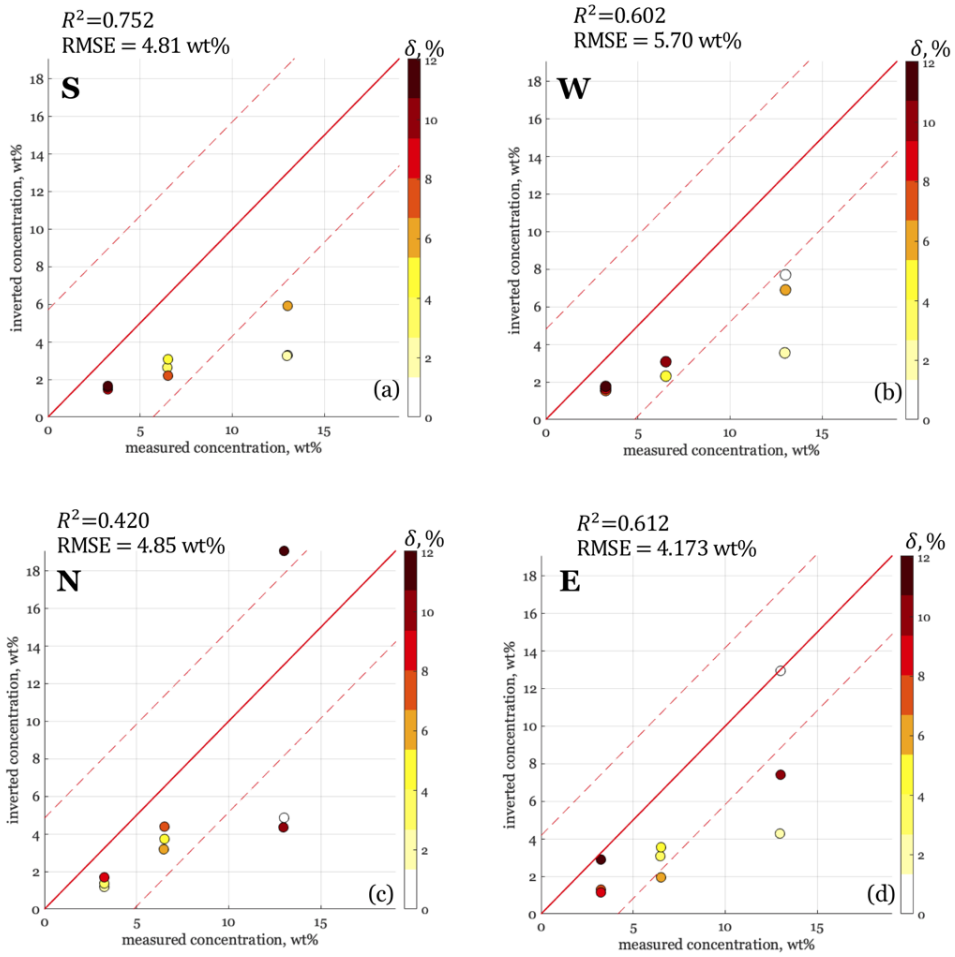

Figure 6.4.6 Comparison of estimated concentration with concentration from reference measurements for different SAR-DRM branches (a-d). Colour corresponds to corresponding to each sample's objective function value δ.

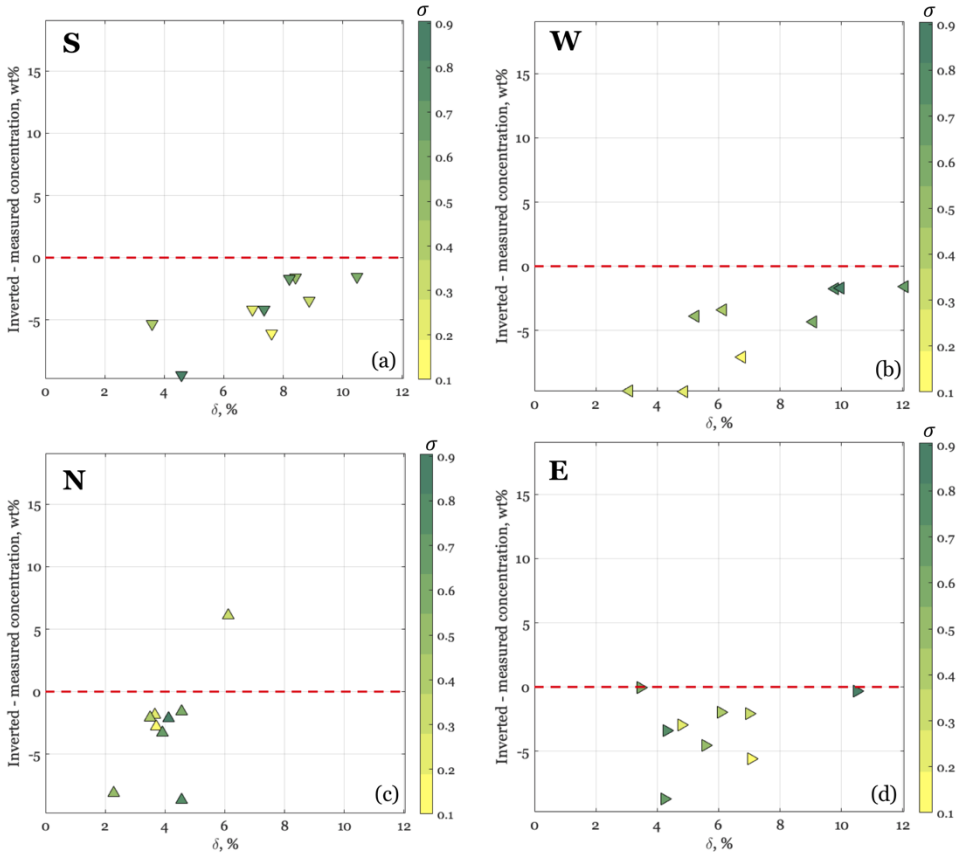

Figure 6.4.7 Actual difference between estimated and measured concentration in comparison with δ for different SAR-DRM branches (a-d). Colour corresponds to estimated σ.

6.5 Conclusions

This chapter has served as a summary of the SAR-DRM inversion routine validation and performance check. Firstly, it brought together the proposed modification in signal pre-processing and confirmed the beneficial effect of the proposed modification in signal filtering and normalisation. The inversion algorithm was validated on simulated spectra, and the results of this study justified the stopping criteria set in methodology.

The major highlight of this is the execution of the inversion algorithm. The algorithm was applied to two separate polystyrene suspensions sample sets. Inversion of the first one tested the ability of the proposed algorithm to provide with particle size and concentration. Most of the variation between estimated and measured parameters concerned the quality of the concentration inversion, and the general misprediction of the latter is associated with highly concentrated suspensions. It can be associated with the limitations of the diffusion theory, which is valid strictly for isotropic scattering scenario, which may not be exactly correct at very high concentrations of the polystyrene suspensions. Another reason may be associated with the elimination of the signal from the closest S-R distance, which may be a carrier of the significant information for the concentration analysis.

The inclusion of the particle size distribution in the inversion is an important step towards the understanding of a degree of information encrypted in the SAR-DRM and the possibility of extracting it. The developed inversion method was applied for a set of polystyrene mixtures of different polydispersity properties, leading to the following conclusions. First of all, inverted physical properties of polystyrene particles (mode radius and distribution width) were compared against reference measurements from DLS and Nanosight. Despite the overall good agreement of the inverted parameters, there is still variability between different samples. Considering the potential reasons for suchlike observation, a conclusion was made that the variation might be caused by dilution, which then would manifest as differences between reference and inverted parameters. Hence, the nature of variations in the predicted results among different concentrations cannot be properly checked. Besides, there is a question of the reliability of the reference measurements from DLS regarding the distribution width parameter.

The results obtained do not indicate the direct link between the overall quality of the inverted results and the presence of the distribution width. However, the introduction of the distribution width parameter to inversion algorithm brings the additional degree of freedom and the consequential issues of overcompensation of one parameter with

another. This shortcoming affects the estimation of the concentration and distribution width as these parameters have a similar effect of SAR-DRM, making it difficult to retrieve the exact one corresponding to each of the parameters. Inversion of the signal from highly concentrated samples ($\sim 12 wt\%$ and $\sim 6 wt\%$) have returned results for the concentration and distribution width.

According to the comparison of the inverted measurements with the reference measurements, the inverted PSD agrees well with the measured ones, from different reference measurement sources. The variability in the mode radius and distribution width estimation appears at some of the samples, especially at lower concentrations. One of the possible reasons contributions to the variations in the possible bi-modality of the PSD of mixtures due to the methodology shortcomings. An alternative way to produce polydisperse polystyrene suspensions could eliminate the degree of methodology effect.

CHAPTER 7

INVERSION APPLICATION FOR COMPLEX ANALYSIS

The previous chapter gave an overview of the particle size distribution and concentration effect on SAR-DRM signal and also the results of followed inversion via the developed algorithm. Inverted simultaneously, the influence of each parameter was studied on simulated SAR-DRM individually. With prior knowledge, the polystyrene suspensions were prepared to allow the study of each specific effect on SAR-DRM spectra. However, only spherical particles are considered in these studies, and the mixtures were prepared based on mixing samples with discrete PSD. This may not truly represent systems such as polymerisation reaction products, where the mode radius varies with reaction parameters, and PSD gradually changes along with the reaction.

In this chapter, polydispersed polystyrene suspensions from emulsion polymerisation reactions are investigated to evaluate the inversion efficiency practically. It also investigates the effect of the non-spherical particles on SAR-DRM, both theoretically and experimentally. The experimental analysis is carried out using crystalline nanocellulose (CNC) of different aspect ratios.

7.1 ANALYSIS OF SAR-DRM OF POLYSTYRENE POLYMERISATION REACTIONS

The study first analyses polystyrene suspensions resulted from polymerisation reactions. The differences between polystyrene suspensions within the sample set can be charac-

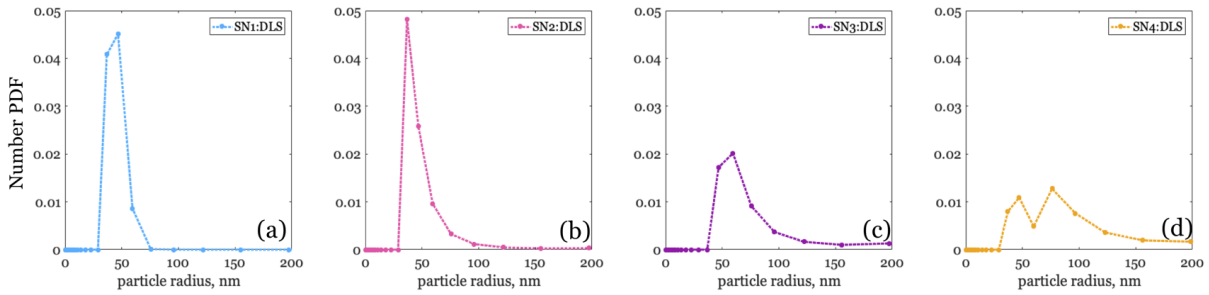

Figure 7.1.1 Reference measurements of number particle size distribution density function obtained from DLS. Each colour corresponds to different origin sample

terised by two main criteria: reaction parameters and the degree of dilution of the reaction product. The exact reaction parameters of the designed experiment were described in Chapter 5. To summarise, the initiator in each of the reactions was supplied into the monomer solution in two parts: gradually with a syringe pump, the other one was added instantly. This resulted in four polystyrene suspensions which will be studied in the section below. The study in this section will overview the SAR-DRM spectra features analysis and describe the results of followed inversion in comparison with reference measurements.

7.1.1 Features analysis of measured SAR-DRM

To begin with, the reference measurements of particles size distribution, executed via DLS, presented in Figure 7.1.1. Sample SR2 has the narrowest distribution width and the finest mode radius, whereas SR4 exhibits the widest distribution width, however, it exhibits bi-modality as DLS measurements have shown two peaks, at 47 and 82.47 nm. Generally, the mode radius varies among samples between 43.32 - 82.47 nm.

From reference measurements, the effects of mode radius and distribution width on SAR-DRM can be envisaged. To examine the differences in the SAR-DRM from different samples, Figure 7.1.2 illustrates the example of I_{diff} for each sample at the concentration set at ~ 9 wt%. Since the closest S-R distance is not used in the following inversion and the example of the spectra collected at the closest S-R distance was already presented in Chapter 6, the result is presented for three S-R distances only. It also presented for different SAR-DRM branches, South, West and North. Spectra signal from some of the fibres in East branch has exhibited a few major inconsistencies with the rest of the measurements, therefore was not used in the analysis.

The signal across the branches is consistent and vary mostly in the intensity values, keeping the trend of intensity reduces with the increase of S-R distance. The signal across different samples has different intensity, where SR1 has the highest, and the SR4 has the lowest. However, this observation is dependant on wavelength and valid between 450-700 nm. At longer wavelength, the intensity of the signal is getting fairly similar to each other. The relative magnitude between the signals increases with an increase of S-R distance. This also affects the signal at 700-850 nm, yet samples SR1, SR2 and SR3 still have similar intensity at selected wavelength range at longest S-R distance. Due to these changes, the signal that corresponds to each different reaction becomes more distinguishable from each other.

At this stage of the analysis, they can be retrieved in the context of the effects that were previously seen in another polystyrene suspensions sample sets. Since the concentration of the samples in this example is similar, the magnitude between different signals increases most probably due to the distribution width effect. This is indirectly confirmed by magnitude changes with an increment of S-R distances, which were linked with distribution width in Chapter 5. The mode radius and distribution width both vary in the sample set, therefore at this stage, the estimation of these parameters from SAR-DRM spectra preliminary analysis is infeasible.

The only correlation with process parameters and the SAR-DRM spectra order is the smallest amount of initiator, supplied by syringe pump corresponds to SR1, which has the highest intensity across SAR-DRM branches and respectively the largest amount of initiator was supplied via syringe pump for SR4, which exhibits the lowest intensity. These observations do not provide sufficient information for conclusions because of the different original recipes used for the reactions. Consequently, the following analysis is focusing on each of the recipes individually, and reactions of each of the recipe referred further as a first and second batch.

7.1.2 SIGNAL INVERSION

Estimation of the parameters of interest was done using the algorithm developed in Chapter 5. The algorithm's goal is to fit a model solution to the measured signal based on minimization of error δ between them, which was performed in Chapter 6. Assessment of particle size distribution parameters inversion (mode radius and distribution width)

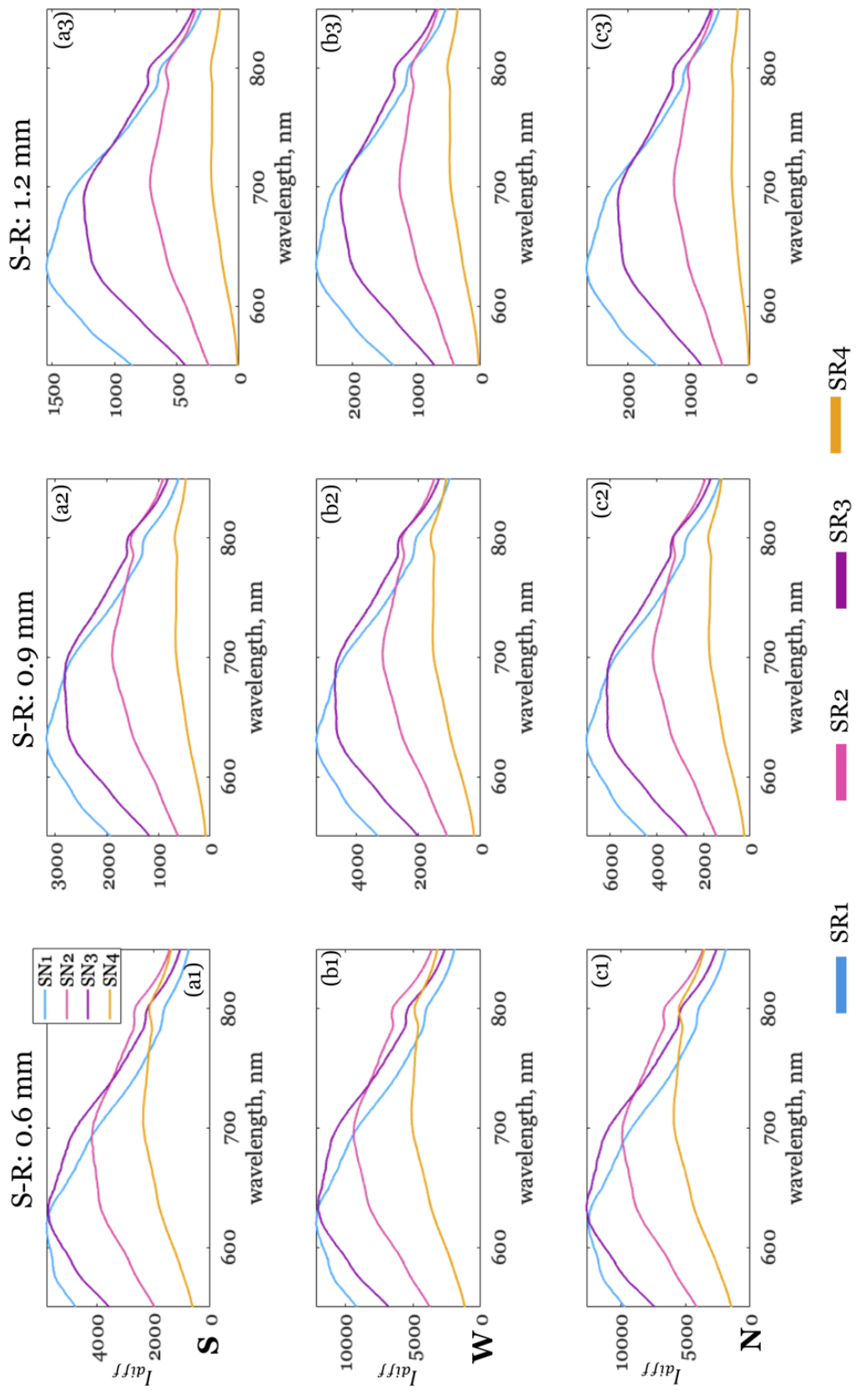

Figure 7.1.2 Reflectance signal I_{diff} presented for samples in Sample set 3 across different SAR-DRM branches (a-c) and different source-to-receiver distances (1-3) . The color scheme indicates the original samples of the sample set

is presented first, followed up by a discussion of the estimated concentration values, inverted simultaneously.

PARTICLE SIZE DISTRIBUTION ESTIMATION

The particle size distribution density functions estimated for all the samples in the sample set can be found in Figure 7.1.3. The variation in estimated density functions among different SAR-DRM branches is present, in a lower degree at higher concentrations than at lower concentrations. The variations are individual from sample to sample; generally, the mode radius of samples remains similar across different branches, whereas distribution width is affected greatly. The variations in the estimated values between SAR-DRM branches were observed before in Chapter 6 and as was discussed there, the possible explanation of it can be the variations in the intensity of the signal from different branches.

The quality of the fit is also individual to each of the sample, however, generally, the inversion error δ across SAR-DRM branches lie between ~ 0.58 - 8.8%, which is considered as an average to the good result of the fit. There are few results of the inversion that converged at δ higher than 13%. These results are occasional at concentrations of 9wt% and higher for SR3 and SR4 and will be discussed in more details in the corresponding section. Overall for studied SAR-DRM branches, inversion error is lower for samples with low concentration.

As an outcome of the fitting process, particle size distribution and concentration were obtained for each suspension and their dilutions. Estimated mode radius is consistent across different dilutions for all samples in the concentration range 15-9wt% with occasional large variations in estimated values, that correspond to large inversion error values, mentioned earlier. Estimated mode radius in concentration range 6-3 wt% increasing compare to previous concentration regime. Among different samples, estimations of mode radius for SR3 and SR4 vary the most across different dilutions. Most likely, the variations in the estimated mode radius are caused by dilution of the samples, since these differences are fine and do not exceed ~ 38 nm for samples SR1-3.

The unspecific to sample observation of the estimated distribution width concludes that for the sample with a concentration equal or above 9 wt%, the estimated distribution width is narrow, with some of the exclusions in sample SR3 inversion, corresponding to high δ. For samples with a concentration lower than 9wt%, the width of the distribution is broad in relation to more concentrated samples.

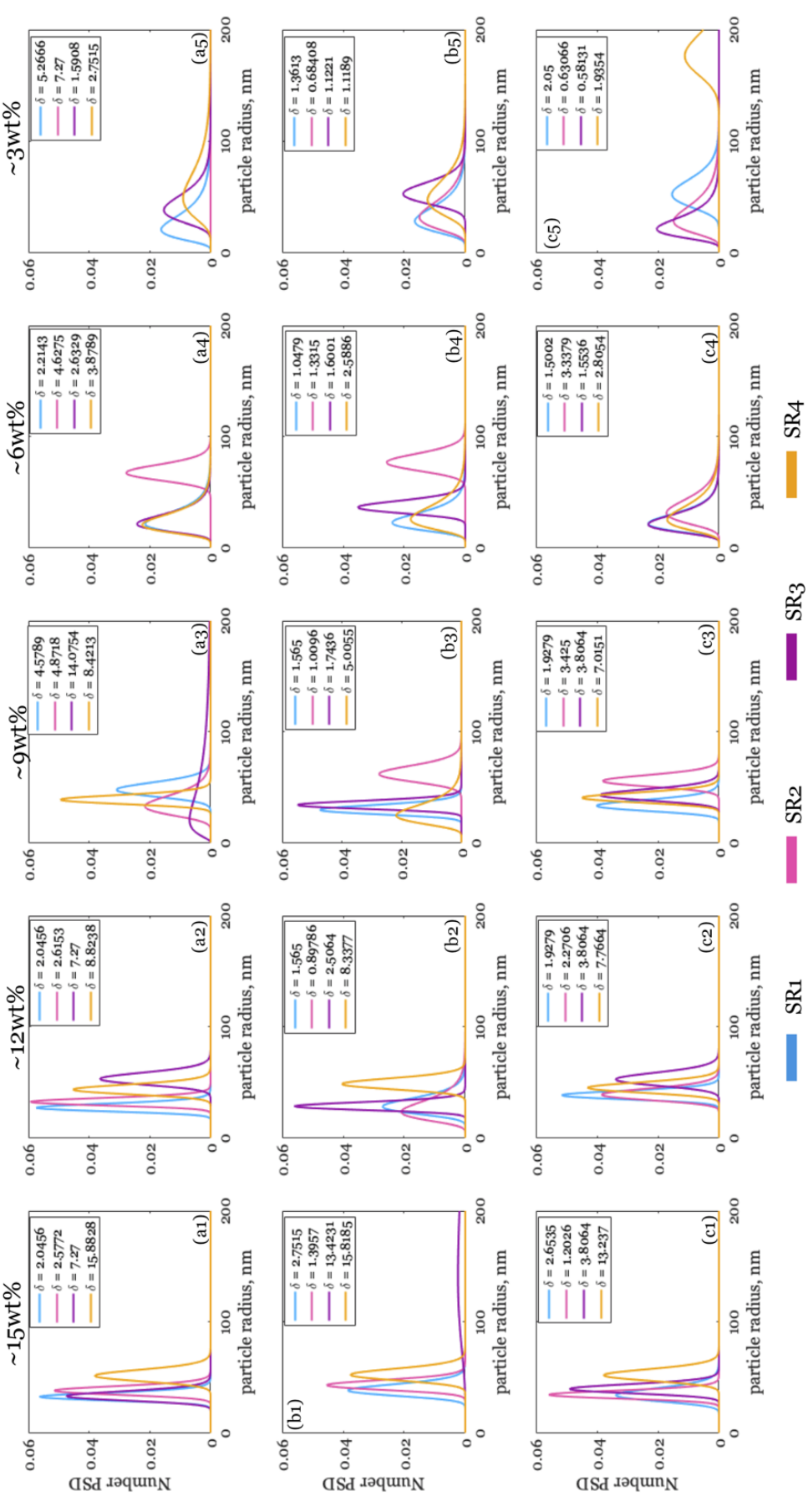

Figure 7.1.3 Number density function inverted for Sample set 3 (colour corresponds to samples in Figure 7.1.2) across different SAR-DRM branches (a-c) and sample dilutions (1-5). Legend shows corresponding inversion error δ.

Across most of the SAR-DRM branches in concentration range 15-9wt%, inversion for SR1 returns smallest mode radius, whereas SR4 has the largest. SR2 exhibits narrow distribution width in a selected concentration range, in some cases narrowest across other samples. Inversion of samples SR3 and SR4 returned average or poor fit in this concentration range. These samples correspond to the two largest amounts of the initiator added via syringe pump and two samples with broadest distribution width, according to reference measurements. Some of the estimated parameters for SR3 and SR4, resulting in δ close or above stopping criteria for solution pre-location. This indicates that for selected samples, the search of the parameters combinations during minima pre-location is complicated in the context of the current method and suggests the difficulty of finding the optimal minima to pass to the inversion algorithm. Since the quality of the fit improves at the lower concentration range (6-3 wt%), the relationship of the quality of the fit with process parameters will be discussed after analysis of the concentration estimation quality as well as particle size distribution estimation quality. The latest was executed similarly to Chapter 6 estimation quality check with the difference of exclusion of the above-mentioned outliers with the poor quality fit. The quality of the particle size distribution estimation is compared against reference DLS measurements in Figure 7.1.4.

Estimated number PSD for sample SR1 has a smaller mode radius and broader distribution width than the reference number PSD from DLS. As was already concluded from Figure 7.1.3, with a decrease of concentration, the distribution width increases, however, due to variability of mode radius and distribution width across different SAR-DRM branches, the distribution width increasing even more at averaged results. Sample SR2 has a better correlation of the estimated and measured mode radius, yet the averaging of PSD density over SAR-DRM branches leads to bi-modality at concentrations 12-6wt%. Notably, the peaks of bi-modal distribution are placed just outside on the measured mode radius value. The most diluted sample, 3wt%, has the broadest distribution width, as was previously documented on SR1.

Inversion of SR3 and SR4 has returned number PSD very different depending on the concentration of the solution. These samples exhibited high variability across SAR-DRM branches which have led to bi-modality at almost every sample. Sample SR3 has mode radius estimated closely to measured value at concentrations 12, 9 and 3wt%; also, distribution width of the sample and its dilutions appears generally lower in comparison with previous samples, which also correlates with reference measurements. Inversion for

Table 7.1.1 Table of estimated and measured mode radius and distribution width values for Sample set 3 for South to North SAR-DRM branches

	South				**West**				**North**			
	Mode[R], nm		σ		Mode[R], nm		σ		Mode[R], nm		σ	
	Ref.	Inv.	Ref.	Inv.	Ref.	Inv.	Ref.	Inv.	Ref.	Inv.	Ref.	Inv.
SR11	43.32	32.88	0.16	0.11	43.32	38.68	0.16	0.13	43.32	34.31	0.16	0.17
SR12	43.32	27.48	0.16	0.13	43.32	28.47	0.16	0.25	43.32	38.70	0.16	0.10
SR13	43.32	47.95	0.16	0.13	43.32	29.98	0.16	0.14	43.32	33.65	0.16	0.15
SR14	43.32	21.74	0.16	0.39	43.32	22.89	0.16	0.34	43.32	21.91	0.16	0.37
SR15	43.32	21.00	0.16	0.51	43.32	28.53	0.16	0.39	43.32	52.50	0.16	0.24
SR21	40.62	38.4	0.12	0.10	40.62	43.31	0.12	0.10	40.62	34.72	0.12	0.10
SR22	40.62	32.75	0.12	0.10	40.62	23.74	0.12	0.37	40.62	39.18	0.12	0.13
SR23	40.62	33.18	0.12	0.23	40.62	62.19	0.12	0.12	40.62	55.92	0.12	0.10
SR24	40.62	67.70	0.12	0.11	40.62	77.00	0.12	0.1	40.62	31.58	0.12	0.35
SR25	40.62	420.66	0.12	0.10	40.62	31.95	0.12	0.39	40.62	28.53	0.12	0.43
SR31	59.09	33.47	0.22	0.12	59.09	141.99	0.22	0.52	59.09	39.93	0.22	0.10
SR32	59.09	53.37	0.22	0.10	59.09	28.74	0.22	0.12	59.09	52.93	0.22	0.11
SR33	59.09	21.12	0.22	0.91	59.09	34.34	0.22	0.11	59.09	43.22	0.22	0.12
SR34	59.09	21.69	0.22	0.36	59.09	36.65	0.22	0.15	59.09	21.35	0.22	0.38
SR35	59.09	38.43	0.22	0.32	59.09	52.96	0.22	0.18	59.09	21.50	0.22	0.42
SR41	82.47	51.77	0.49	0.10	82.47	52.67	0.49	0.10	82.47	52.27	0.49	0.10
SR42	82.47	43.77	0.49	0.10	82.47	48.80	0.49	0.10	82.47	45.46	0.49	0.10
SR43	82.47	39.14	0.49	0.10	82.47	24.98	0.49	0.34	82.47	40.85	0.49	0.11
SR44	82.47	21.00	0.49	0.39	82.47	25.91	0.49	0.4	82.47	25.50	0.49	0.42
SR45	82.47	48.99	0.49	0.41	82.47	47.66	0.49	0.32	82.47	176.45	0.49	0.10

Table 7.1.2 Table of estimated and measured concentration values for Sample set 2 for South to North SAR-DRM branches

	South		**West**		**North**	
	Ref., wt%	Inv., wt%	Ref., wt%	Inv., wt%	Ref., wt%	Inv., wt%
SR11	15.37	8.10	15.37	4.63	15.37	5.36
SR12	12.00	11.58	12.00	5.06	12.00	4.87
SR13	9.00	2.32	9.00	6.93	9.00	5.41
SR14	6.00	2.53	6.00	3.46	6.00	3.10
SR15	3.00	0.50	3.00	0.95	3.00	0.50
SR21	15.16	20.45	15.16	14.80	15.16	24.90
SR22	11.98	24.94	11.98	11.03	11.98	15.14
SR23	8.99	10.50	8.99	4.06	8.99	6.02
SR24	5.99	3.23	5.99	2.14	5.99	5.13
SR25	2.91	1.11	2.91	2.23	2.91	2.10
SR31	14.90	12.13	14.90	24.85	14.9	7.69
SR32	12.00	3.23	12.00	17.39	12.00	3.43
SR33	8.95	13.08	8.95	10.07	8.95	5.47
SR34	5.97	6.07	5.97	6.25	5.97	5.11
SR35	2.98	1.37	2.98	1.37	2.98	2.23
SR41	15.60	24.99	15.60	25.00	15.6	24.99
SR42	12.00	24.61	12.00	22.38	12.00	24.95
SR43	8.99	24.79	8.99	18.65	8.99	24.43
SR44	5.99	14.55	5.99	8.71	5.99	8.15
SR45	2.99	2.55	2.99	2.79	2.99	1.72

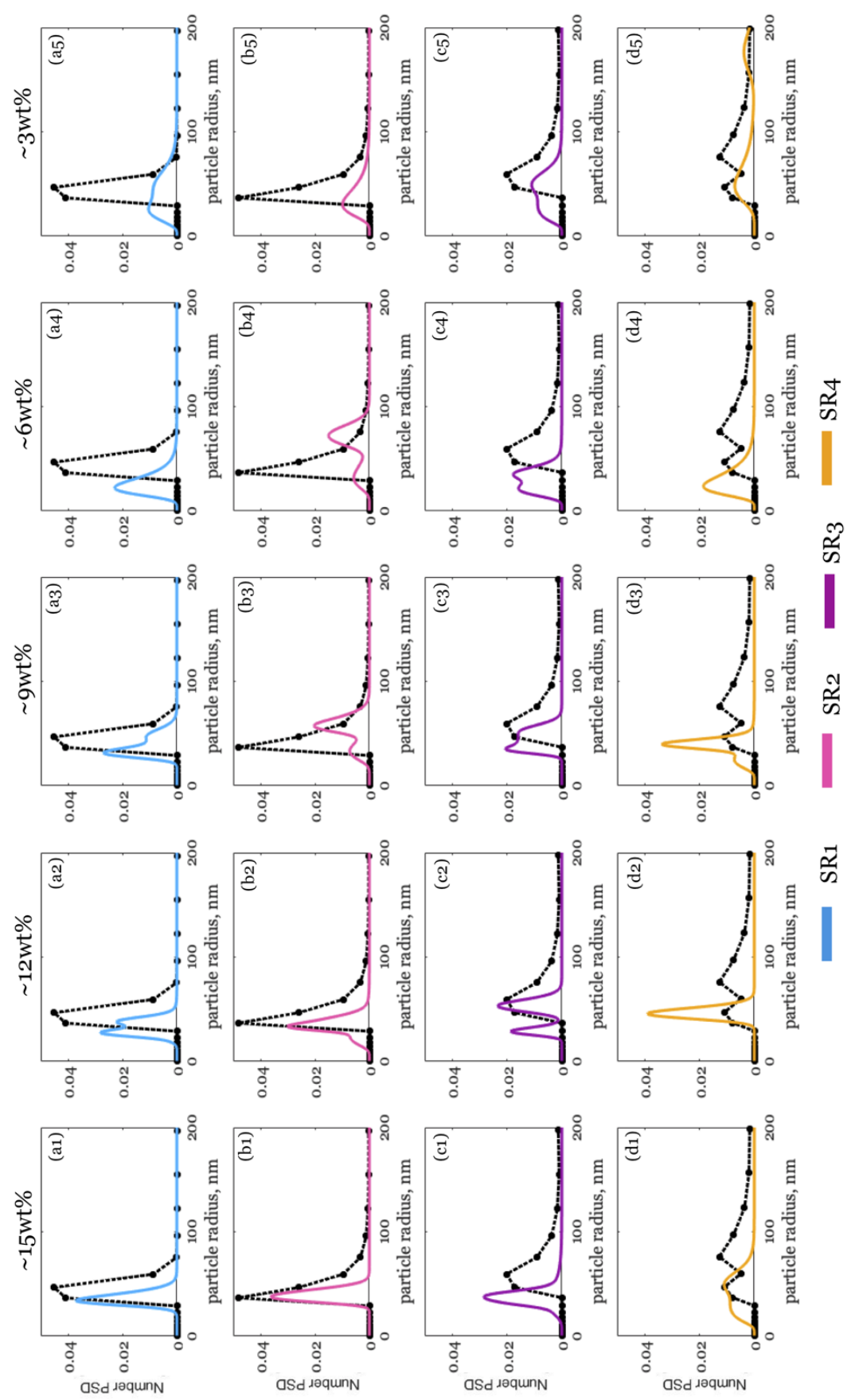

Figure 7.1.4 Number PSD density function estimated as a result of SAR-DRM inversion for the samples in Samples set 3, which consist of different reactions (a-d) and their dilutions (1-5). Colour corresponds to samples in Figure 7.1.2

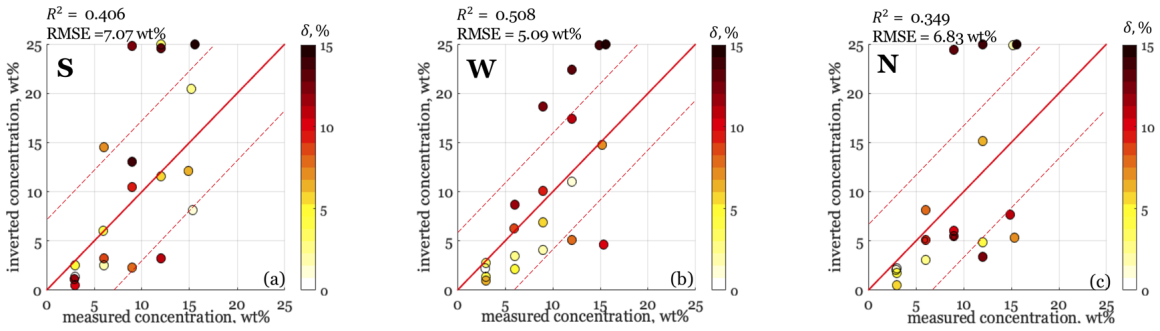

Figure 7.1.5 Estimated concentration for each of the SAR-DRM branches (a-c) in comparison with reference measurements. Colour corresponds to inversion error δ.

Sample SR4 exhibits almost no correlation with reference PSD, showing mainly a single narrow peak in the area of fine particles. Sample SR4 is notable among other samples as one that has the highest inversion error in average over dilutions and branches, which should be accounted as one of the possible fit quality factors. Also, there are other factors to be mentioned that were discussed in Chapter 6. For example, the fact that inversion of SAR-DRM signal was conducted on a variety of concentration in oppose to a DLS provided for highly diluted suspensions, a certain additional degree of variability between reference method results and inverted results is expected. To some extent, the same cause is contributing to the variability of parameters of interest with an increase of dilution. Nevertheless, the discussion will be completed after concentration inversion analysis.

Concentration estimation

Figure 7.1.5 depicts a comparison of estimated concentration with gravimetrically measured in the form of the scatter plot for each of SAR-DRM branches. The prediction of the concentration across different branches which can be followed from the values in Table 7.1.2. The overall quality of the concentration prediction is poor across SAR-DRM branches, as the R^2 values are not exceeding 0.508. The samples that serve as a major source of deviation from the measured concentration have high inversion error δ across the samples and branches. Similarly to observations made during the inversion of the previous sample sets, inversion of the samples with a concentration higher than 6 wt% returns values with high variability from the reference measurements with no specific correlation to δ values apart from the fact that samples with the highest δ were estimated

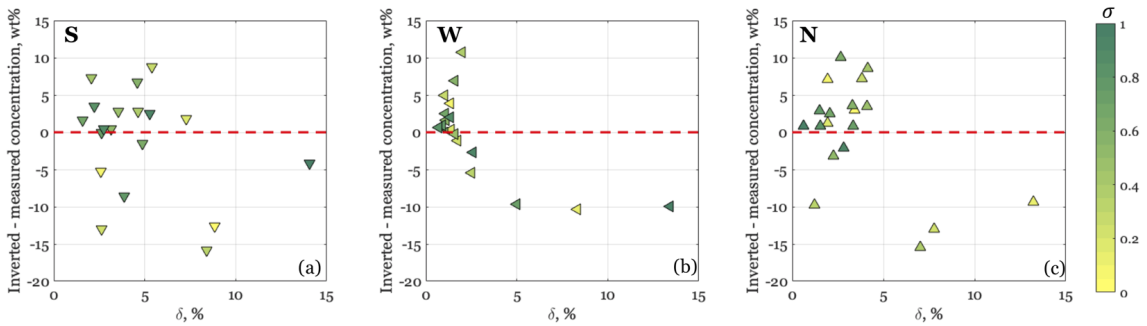

Figure 7.1.6 Actual difference between estimated and measured concentration in comparison with δ for different SAR-DRM branches (a-c). Colour corresponds to estimated distribution width.

with the highest concentration across present branches. Generally, the values were both under and over-estimated in comparison with the measured concentration.

The comparison of relative difference and the concentration can be seen more clearly in Figure 7.1.6. This figure represents the actual difference between estimated and measured concentration, colour coded to estimated corresponding σ values. The general trend, that appears at studied branches suggests, that samples for which broad distribution width was estimated have a smaller difference between estimated and measured concentration, compare to samples with narrow distribution width. This observation contradicts with what was previously observed in Sample set 2 inversions, where concentration mispredictions were associated with the interference of distribution width to the concentration estimation accuracy. As was concluded in Chapter 6, the effect of the concentration and distribution width on spectra in some of the ranges may create an over-compensation effect of one property with another as well as reduce the reliability of relative difference as a single parameter for concentration quality estimation. In the current dataset, however, samples, which have returned poor fit after inversion, exhibited both large difference in the concentration estimation and large distribution width at South and West branches. Such polar observations from different datasets of the same material suggest the great effect of the process parameters on the physical properties of the end product. It is, of course, remain open the concern regarding the reliability of the reference method used for the distribution width estimation.

Following the suggestion in Section 7.1.2 to average the estimated values across SAR-DRM with exclusion to samples of the poor fit, the average of the estimated concentration was executed, and the result is presented in Figure 7.1.7.

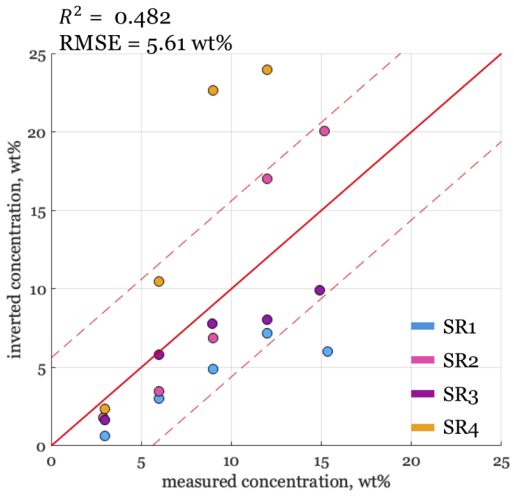

Figure 7.1.7 Estimated concentration averaged over the SAR-DRM branches in comparison with reference measurements. Colour corresponds to the legend.

The trend, depicted in Figure 7.1.7 confirms the dependency between the quality of concentration estimation and the process parameters as it shows it more clearly. However, conduction of the thorough analysis of the inversion results in respect to reaction parameters is a tedious task due to the lack of reliable information regarding the actual properties of the system. From an attempt to analyse the quality of the inversion in respect to each reaction by using values in Table 7.1.1 and 7.1.2 and the average depicted in Figure 7.1.7, it is apparent, that inversion of sample SR4 and its dilutions returns poor fit and as a result of it, the large variations between predicted and measured concentration. Some of the dilutions of sample SR3 have shown a similar pattern. Notably, sample SR1 and its dilutions have low inversion error, however high variability in the estimated concentration. To provide a visual support to the statements, a residual plot Figure 7.1.6 was re-made in the colour-scheme that corresponds to original samples of the sample set Figure A.2.1 and provided in the additional information in Appendix A.2 .

7.1.3 Conclusions

The section above investigated the SAR-DRM inversion method performance on the signal collected from the reaction with complex process parameters. The preceding analysis of the collected signal indicated that the decrease in the initiator ratio leads to an overall decrease of the spectra intensity, which was previously indicated as a decrement of distribution width property. However, according to reference measurements, the changes

in the initiator ratio increased both, mode radius and distribution width in large extent. This observation confirms the original hypothesis that reaction results in different mode radii and distribution width, the cumulative effect of which was not present greatly at previous sample sets.

Summarising the observations for the estimation of the parameters, the reaction parameters correlate with the quality of the estimation. Concluding from Figure 7.1.6, the inversion error is higher for SR3 and SR4 and their dilutions, which are notably samples with the highest amount of initiator added via syringe pump. The estimated PSD for the above-mentioned samples is not uniform across different SAR-DRM branches and concentrations, in comparison with SR1 and SR2. The inversion of the latest returns average of good fit and the results of the inversion are relatively consistents. The correlation with reference measurements follows observations made on Sample set 2 inversion, where the underestimation of the concentration correlates with monodispersity of the sample. Continuing the concentration estimation summary, Figure A.2.1 suggests that concentration inverted for samples with a high ratio of initiator parts (SR4) is greatly mispredicted. These samples have also exhibited large inversion error, which suggests that the solution for the result of such reaction may not exist in the current combination of 3 parameters of interest. Since the reference measurements have shown two peaks of the distribution, there is a possibility that this particular system does have bi-modal size distribution, which was not considered in the inversion algorithm. Therefore, one of the possibilities of providing a better fit for the SAR-DRM is the inclusion of additional parameters into the group of parameters of interest, like multiple mode radius.

On the other hand side, the introduction of such a complex system of parameters to the current method will likely lead to the overfitting of the signal. Therefore this approach should not proceed until there is a reliable parameter for identification of the parameters estimation correctness. At the moment, the solution returned by the inversion algorithm is analysed firstly based on the quality of the fit, and if the quality of the fit is unsatisfactory, the further analysis of the sample might not proceed. For the analysis conducted on current sample set, this approach, however, is not performing as was intended since many samples were provided with a good fit, however, one or a few of the parameters of interest were mispredicted.

7.2 A STUDY OF PARTICLE SHAPE EFFECT ON SAR-DRM

The results of the study presented in this thesis focused heavily on the sensitivity of the SAR-DRM to physical and chemical properties, where physical properties were represented via particle size distribution and chemical were narrowed to the concentration of solids. The inversion algorithm for spherical scatterers was proposed and validated on signal collected from polystyrene, which is highly reflective, nearly perfectly spherical particles. Less reflective materials or the particles of non-spherical shape were out of scope until this point. Kooij *et al* [201] and Lee *et al* [202] have conducted the extensive study on aspect ratio effect on optical properties, however, as many other studies on single particles, they have performed the simulation on fixed target orientation, which conflicts with more realistic approximations to diffuse scattering. To our knowledge, no study to-date evaluates the effect of particle shape on spatially resolved diffuse reflectance, and consequently, no attempt of inverting such properties from the SRDR measurements was reported. Within this study, the attempt was made to step up from the spherical shape of the scatterer to elongated spheroids, expanding current parameters of interest range with the aspect ratio of the particles and setting a sensitivity threshold for the SAR-DRM to particle shape parameters.

This question was investigated within this Chapter in three separate studies. Firstly, the influence of particle aspect ratio (AR) for elongated ellipsoids on SRDR was examined on highly scattering material (polystyrene). This involved calculation of bulk optical properties and diffuse reflectance for polystyrene particle or fixed particle volume, with equivalent radius comparable to radius range, studied in previous chapters. This work serves as a feasibility study, examining the computational nuances and the AR effect appearance on SRDR.

There is, however, no polystyrene system with variable AR available, and so the degree of the effect cannot be further investigated on measured SAR-DRM signal. As an alternative, a system of suspended non-spherical cellulose nanocrystals was proposed as a subject of study. Cellulose nanocrystals suspended in water were chosen due to their high aspect ratio and, at the same time, where the longest dimension would not exceed micron-scale [203]. Absence of dimensions over micron allows refraining directional scattering appearance in the system, which is not supported by diffuse approximation. The material, however, consists of negatively charged colloidal particles that exhibit liquid crystallinity properties at certain concentrations which makes it challenging to account for in the

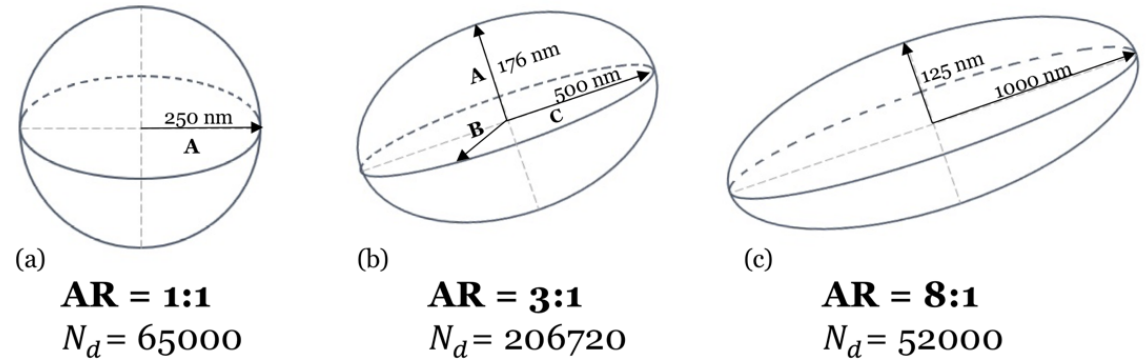

Figure 7.2.1 Polystyrene particles simulated by DDSCAT: (a) sphere, (b) prolate ellipsoid (AR = 3:1), and (c) prolate elliptical (AR = 8:1).

simulation. Hence, this study serves as a preliminary investigation stage of possible aspect ratio tracing in SAR-DRM from the colloidal materials as it does not account on some of the material specifics. The parameters that are included in the study are outlined in Section 7.2.3. To indicate the differences in AR effect caused by material optical properties effect, the CNC system was firstly simulated for same aspect ratios and equivalent radius as the ones used in the polystyrene-based AR study. It was followed up by case study on the commercially available CNC samples, which included forward calculation, features analysis of measured SAR-DRM and its inversion.

7.2.1 Preliminary investigation of the sensitivity of modelled SAR-DRM to the aspect ratio of polystyrene material

The first step of describing light-particle interaction is the calculation of the optical properties of a single particle. This study used the Discrete Dipole Approximation (DDA) method, which has been implemented in the open-source software package *Discrete Dipole SCATtering* (DDSCAT), developed by Draine and Flatau [144]. As described in Chapter 3, the methods are based on the straightforward idea of splitting the scattering body into small spheres of equal size, which is comparable to the size of the radiating dipole. Those dipoles are then placed in the lattice structure to form the desired shape of the particle. In addition to the shape, DDSCAT should be supplied with material properties, such as densities and complex refractive indexes.

The measure of non-sphericity was defined as the ratio between the longest (C) and minor (A and B) semi-axis, the AR for ellipsoid particle. The pre-packaged ellipsoid

geometry, the optical properties of the particle and the medium, and the wavelength range are provided to DDSCAT algorithm. The remaining parameters in the algorithm are kept unchanged.

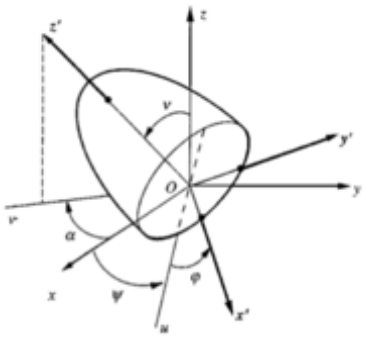

Figure 7.2.2 Specfication of prolate ellipsoid orientation across Euler's angles in cortesian coordinates (half of the ellipsoid displayed) [204]

In the suspension, the particles are randomly oriented within the surrounding medium. The chosen calculation routine uses a systematic sampling of Euler angles, β, θ and ϕ, which schematically depicted in Figure 7.2.2. They can be specified by division at the desired number of sample angles and computing calculation of bulk optical properties. For the preliminary study, the selection of angles sampling was done according to the methodology described in [205]. Hence, the results of the DDSCAT simulations were averaged over 3 samples of each Euler angle, totalling 27 orientations with respect to the polarisation vector of the incident light. The calculations were repeated for 35 wavelengths in the range 550–850 nm. Properties at intermediate wavelengths were estimated using a cubic spline [206].

To examine the impact of the alteration of particle shape on the light scattering behaviour, the simulations were performed for particles of constant volume but different shapes. This work studied prolate ellipsoids, one of the most common geometries, with three different aspect ratios: 1:1 (sphere), 3:1, and 8:1. These aspect ratios were converted into DDSCAT shape inputs with a dipole spacing set to 0.03·A. Figure 7.2.1 illustrates each type of particles studied, the dimensions of their semi-axes (A, B and C), and the number of dipoles N_d used. To keep the volume constant, semi-axes A and B have to decrease along with the increase of the semi-axis C.

The colloidal suspensions were assumed to consist of monodisperse particles with 5 wt% solid loading to ensure that the conditions for diffuse scattering are met. The particle volume fraction remained constant and the aspect ratio of the particles was varied. The material of the suspension are polystyrene and water; the complex refractive indexes are described in Section 4.1.2.

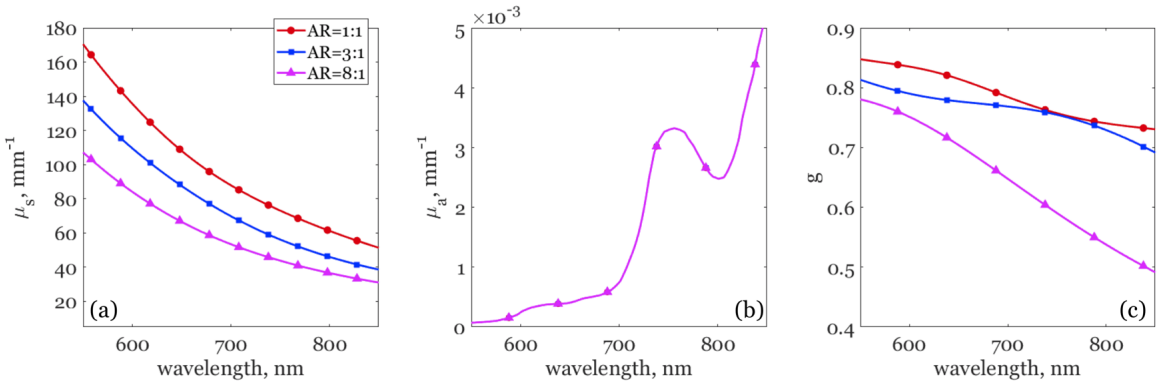

Figure 7.2.3 Bulk optical properties for polystyrene colloid suspensions for different particle aspect ratio: (a) bulk scattering coefficient μ_s, (b) bulk absorption coefficient μ_a and (c) asymmetry parameter, g

BULK OPTICAL PROPERTIES

To gain an understanding of the influence of the aspect ratio to light-particle interactions, the analysis was carried out on the simulated bulk optical properties. Figure 7.2.3 presents the scattering coefficient, asymmetry parameter, and the absorption coefficient for the different AR investigated. The differences in particle shape affect the scattering coefficient and the asymmetry parameter, whereas the absorption coefficient remains unchanged due to the constant volume fraction of both the scatterers and the surrounding medium. The trend of the effects, however, is dependent on the properties investigated.

The scattering coefficient weakens with an increase in aspect ratio. The changes in asymmetry parameter, in contrast, are more specific to the AR. While g for a sphere slowly decreases with increasing wavelengths and shows two distinctive peaks at 650 nm, the same parameter for AR = 3:1 exhibits a single peak at 700 nm, and the magnitude decreases more quickly than for a sphere. Notably, the asymmetry parameter for AR = 8:1 drastically decreases after 650 nm as the wavelength increases, compared to the other two aspect ratios. Overall, changes in AR show large and specific changes in the bulk optical properties that correspond to different particle shapes. The effects on the scattering coefficient are not exclusive to the particle shape, as changes in the particle size have a similar effect on scattering as was studied in Chapter 4. For the case where changes in μ_s are caused by changes in the particle size, the absorption coefficient in the corresponding range is expected to vary simultaneously. Besides, the asymmetry parameter reflects the

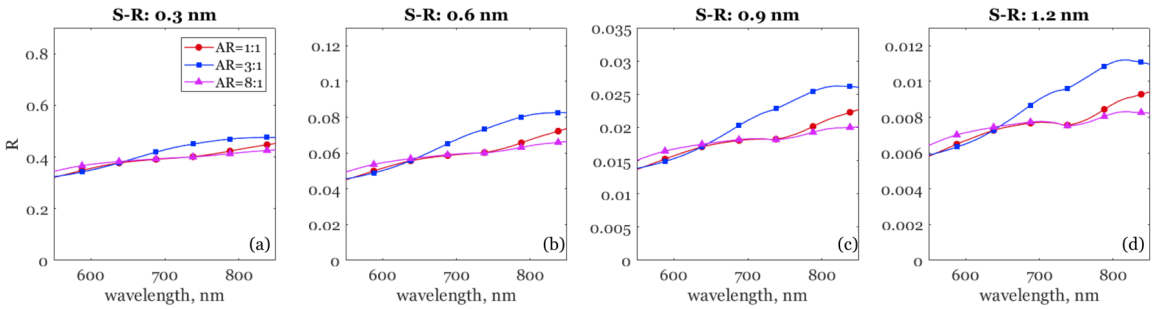

Figure 7.2.4 Spatially resolved diffuse reflectance simulated for various source-to-receiver (S-R) distances from normally emitted light. The symbols correspond to suspensions with particles of different aspect ratio: 1:1 (circles), 3:1 (squares), and 8:1 (triangles). (a)–(d) correspond to S-R distance increase from 0.3 to 1.2 mm with 0.3 mm interval

effect of mode radius and particle AR differently. Therefore, to distinguish between these effects, multiple optical properties should be analysed simultaneously.

The particle shape is also dependent on the wavelength used. The change in the length of particle significantly affects the asymmetry parameter at wavelengths between 700 to 850 nm; however, the effect on the scattering coefficient appears at lower wavelengths, 450–700 nm. The strong wavelength dependence of the optical properties on the particle AR suggests that multiple wavelengths need to be analysed to properly deduce the particle shape.

Spatially resolved diffuse reflectance

In the next step, the optical properties were used to model SRDR spectra. As previously described, the chosen spectroscopic technique emits light at different angles and collects the reflected signal at different S-R distances from the light source, but the fibres at closest S-R distance were eliminated from the analysis. However, this study involves particle AR, the effect of which has not been observed earlier. Therefore, the preliminary analysis of features of simulated and measured diffuse reflectance is conducted using all S-R distances there are. Figure 7.2.4 shows the diffuse reflectance collected at various distances from the light source for each of the samples.

The simulated reflectance is compared using normal emittance for suspensions of particles with different aspect ratio. With a closer look at Figure 7.2.4(a), the overall SAR-DRM differs with the change of the aspect ratio, however, the visual appearance of the effect reduced compare to bulk optical properties observation. The order of the magnitude

for samples has changed and the magnitude between them visibly reduced. As was already observed and discussed in Chapter 4, with an increase of S-R distance, the intensity of the light has reduced. However, signal simulated for longer S-R distance has an increased separation between samples of different AR, clearly showing the effect of aspect ratio at the same wavelength range as observed in g in Figure 7.2.3(b). The relative difference in intensity due to AR continues to increase with the increase of the S-R distance.

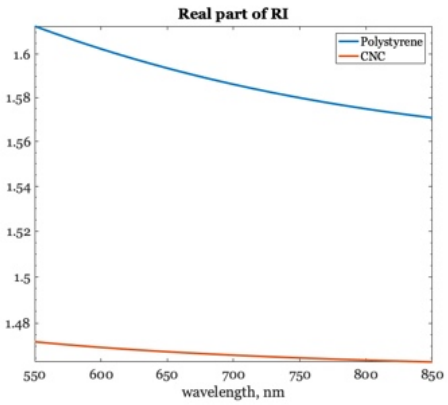

Figure 7.2.5 Real part of refractive index for polystyrene (blue) and cellulose nanocrystalls (orange)

It can be concluded that the difference in particle shape affects the SAR-DRM in the enough extend to consider inverting problem for experimental SAR-DRM spectra (i.e. to estimate the particle aspect ratio from measured spectra). Overall, the difference caused by aspect ratio variations has changes SRDR from the signal corresponding to the equivalent volume sphere, emphasizing the necessity of consideration of aspect ratio parameter when non-sphericity of the particles is present. Yet, the variations in SRDR between 1:1 and 8:1 AR are almost negligible for the selected system of particles for most of the wavelength, which implies the need for AR range expansion to examine the trend.

7.2.2 Preliminary investigation of the sensitivity of modelled SAR-DRM to the aspect ratio of cellulose nanocrystals

The previous section concluded the necessity to expand the AR range to evaluate the exact sensitivity limits of SRDR. However, the feasibility of a comprehensive study on ellipsoidal polystyrene nanoparticles is disputable since the system of such particles is not available on the market. As an alternative material, the cellulose nanocrystals suspensions is considered, however, there is a significant difference in the refractive index of these two materials (Figure 7.2.5) and its density (1.3 [207] - 1.61 g/cm^3 [208] vs 1.05 of polystyrene). These differences may have a significant effect of scattering properties of the material and therefore question the feasibility of the future studies.

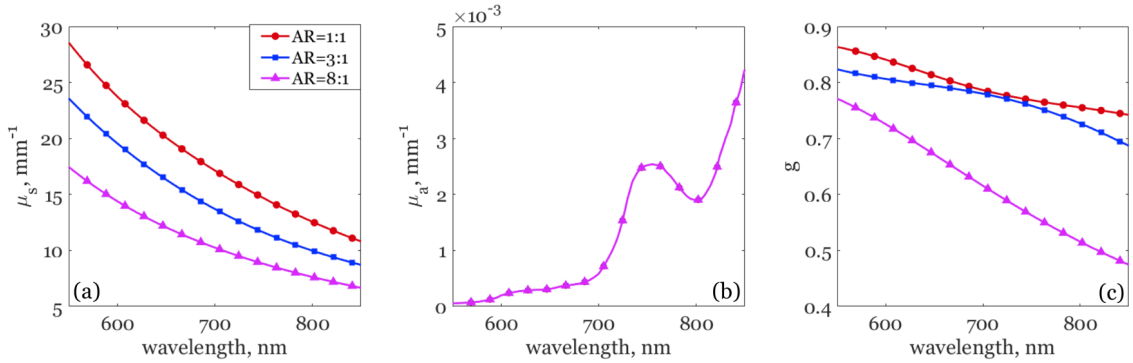

Figure 7.2.6 Bulk optical properties for cellculose nanoparticles suspensions for different particle aspect ratio: (a) bulk scattering coefficient μ_s, (b) bulk absorption coefficient,μ_a and (c) asymmetry parameter, g

To establish a better understanding of the differences caused by material properties, the experiment below was conducted on the simulated SRDR for the three hypothetical suspensions of the CNC in water with density 1.5 g/cm^3 [209]. The AR of the particles in each of them, their dimensions and the concentration on solids were kept identical to ones used the Section 7.2.1.

Bulk optical properties

The bulk optical properties on the CNC system are presented in Figure 7.2.6. Increase of the AR leads to decrease of the bulk scattering coefficient (Figure 7.2.6 (a)) and asymmetry parameter (Figure 7.2.6(c)), whereas bulk absorption remains the same due to constant volume fraction. In comparison with bulk optical properties for polystyrene system of the same particles, the μ_s values are lower for the CNC system, which most likely a result of lower refractive index. Asymmetry parameter does not vary greatly due to its strong dependence on particle dimensions. The impact of the observed differences on SRDR is presented in the following section.

Spatially resolved diffuse reflectance

Spatially resolved reflectance for CNC system is illustrated in Figure 7.2.7. The intensity of the SRDR for the current system at closest S-R distance is similar to the one returned for polystyrene system and it is larger at longer distances. The difference of samples with different AR from the sample of equivalent volume spheres and between each other

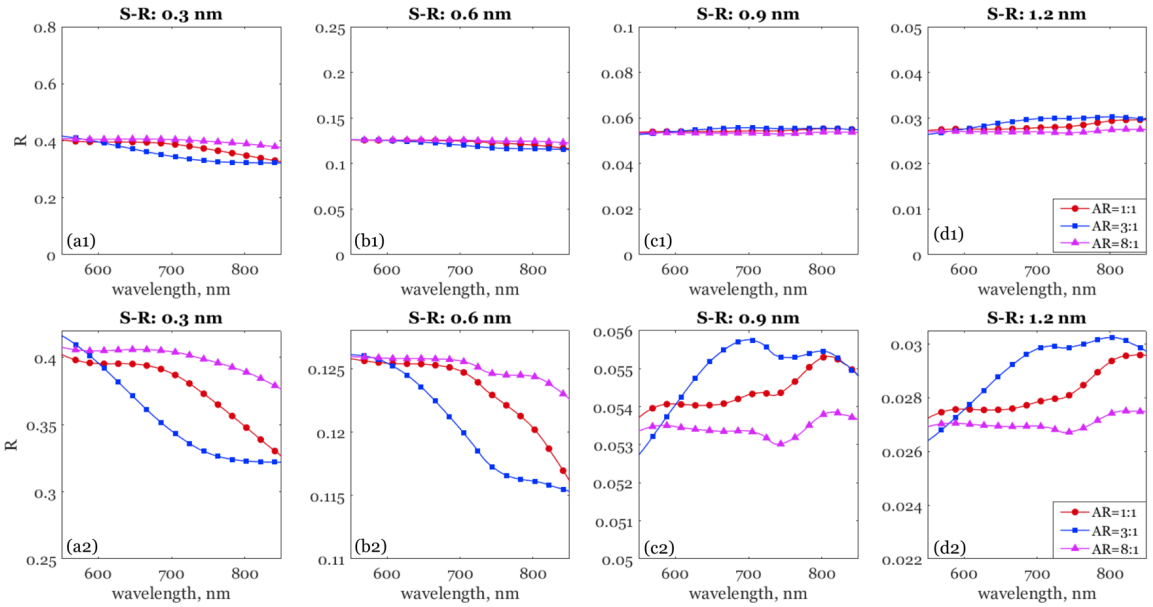

Figure 7.2.7 Spatially resolved diffuse reflectance simulated for cellculose nanoparticles suspensions for various source-to-receiver (S-R) distances from normally emitted light. The symbols correspond to suspensions with particles of different aspect ratio: 1:1 (circles), 3:1 (squares), and 8:1 (triangles). (a)–(d) correspond to S-R distance increase from 0.3 to 1.2 mm and 1-2 illustrate the same R at two different scales.

is distinguishable at every S-R distance. However, the trend of changes caused by AR variations is not unified across different S-R, which is highlighted below.

Aside from the observations made before, for instance, the increase of the intensity with the increase of the S-R, there are a few findings that appeared due to material change. For instance, at longer S-R distances, the order of magnitude for different AR alternates, compare to the closest ones. This can be a result of low bulk optical properties, seen in Figure 7.2.6, which is indirectly confirmed by the changes in the general appearance of the SRDR. The SRDR appearance begins to exhibit features of the absorption coefficient. This phenomena most likely related to the analytical form of the diffuse approximation, that involves parameters like transport mean free path and effective attenuation coefficient. Those parameters are an inverse combination of the bulk optical properties, therefore lower values of it result in an increase of such parameters, consequently affecting the simulated SRDR.

The observations made from a comparison of the effect of AR on SRDR for polystyrene and CNC suspensions not only indicate the specificity of the material effect. Despite lower refractive index values and consequential reduction in the bulk scattering coefficient, the

SRDR has shown more sensitivity to the variations in AR of the CNC material, than to polystyrene. The results from the modelling justify the continuation of the experiment with analysis of available on the market CNC aqueous suspensions. The sequence of the analysis is following the structure used for other sample sets in this thesis. Precisely, it begins with modelling of bulk optical properties and SRDR for CNC of properties of specific samples. It followed by features analysis on measured SAR-DRM, inversion of equivalent sphere and discussion.

In this study, the suspension was assumed to be isotropic (i.e. the particles are randomly oriented), and, therefore, the optical properties were obtained by averaging over a number of particle orientations. However, some of the orientations contribute to the scattering intensity and directionality to a greater extent than others. The number of the successive rotations can vary depending on the shape properties. In order to obtain the most accurate estimate for the optical properties of the suspension, the DDSCAT calculations should be averaged over a sufficient number particle orientations. The further discussion on that question will be provided prior to commercially available CNC suspensions study.

7.2.3 Investigation of the sensitivity of SAR-DRM to the aspect ratio and rotation of commercially available CNC suspensions

The results, presented above conclude the sensitivity of the SRDR to aspect ratio variations for CNC particles of the selected equivalent radius. One of the materials, that exhibits a high aspect ratio of the particles and equivalent radius lies in the nanoscale is cellulose nanocrystal (CNC) suspension. This material, however, has less prominent scattering properties as reflected in its refractive index values. To evaluate the influence of the refractive index difference on SRDR, the modelling study was conducted on ellipsoid cellulose nanocrystals. The section below presents the results of modelling of optical properties, followed up by SRDR and discussion of the degree of sensitivity of the latest to aspect ratio in comparison with similar experiment executed for polystyrene particles.

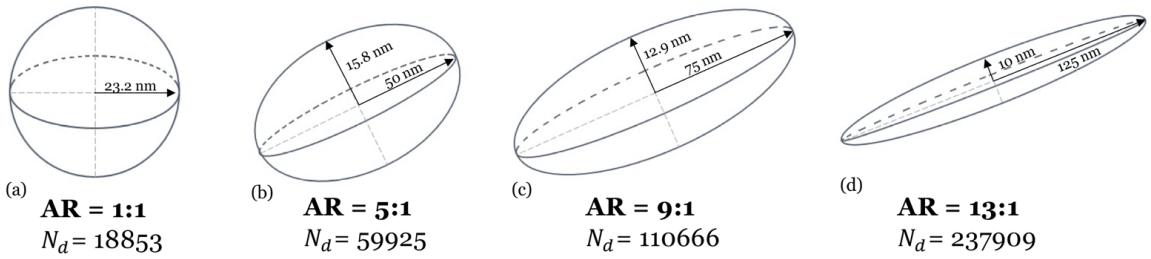

Figure 7.2.8 Schematic illustration of the cellulose prolate ellipsoids used for the analysis of the sensitivity of SAR-DRM to aspect ratio parameter

Parameters of modelled CNC suspensions

To complete the analysis of the aspect ratio effect, the above-mentioned routine was executed for three different aspect ratios: 5:1, 9:1 and 13:1. To concentrate the analysis solely on aspect ratio effect on light scattering, the dimensions were chosen to maintain the constant volume of the particle. The dimensions of the particle were selected to mimic the dimensions reported by the suspension's supplier. The average length of particles in BG Ultra orbits ~100 nm value, so the study below is conducted on dimensions that are significantly smaller than the ones used in the preliminary study in Section 7.2.2.

For a baseline comparison, the simulation output was compared with the one for a sphere of the same volume (AR = 1:1). The dipole spacing was set to a fraction value of shortest semi-axes and can be expressed as 0.03·A. Each type of shape along with the dimensions used and the total number of dipoles(N_d) is schematically illustrated in Figure 7.2.8.

The concentration of the CNC for diffuse reflectance simulation should be chosen carefully. Liquid crystallinity of CNC suspensions results in certain concentrations limitations to proceed with diffusion scattering. Summarising Section 5.1.3, probability of formation of liquid crystals reduces at concentrations as low as 3.5 wt%, which is the concentration chosen for the simulation below.

Rotation average investigation section

The optimal strategy for averaging over Euler angles β, θ and ϕ is an open question depending on particle form. The most straightforward approach to achieve the random orientation of the ellipsoid embedded in the medium is a separation of Euler angles in enough samples that lead to convergence. DDSCAT routine provides the opportunity to

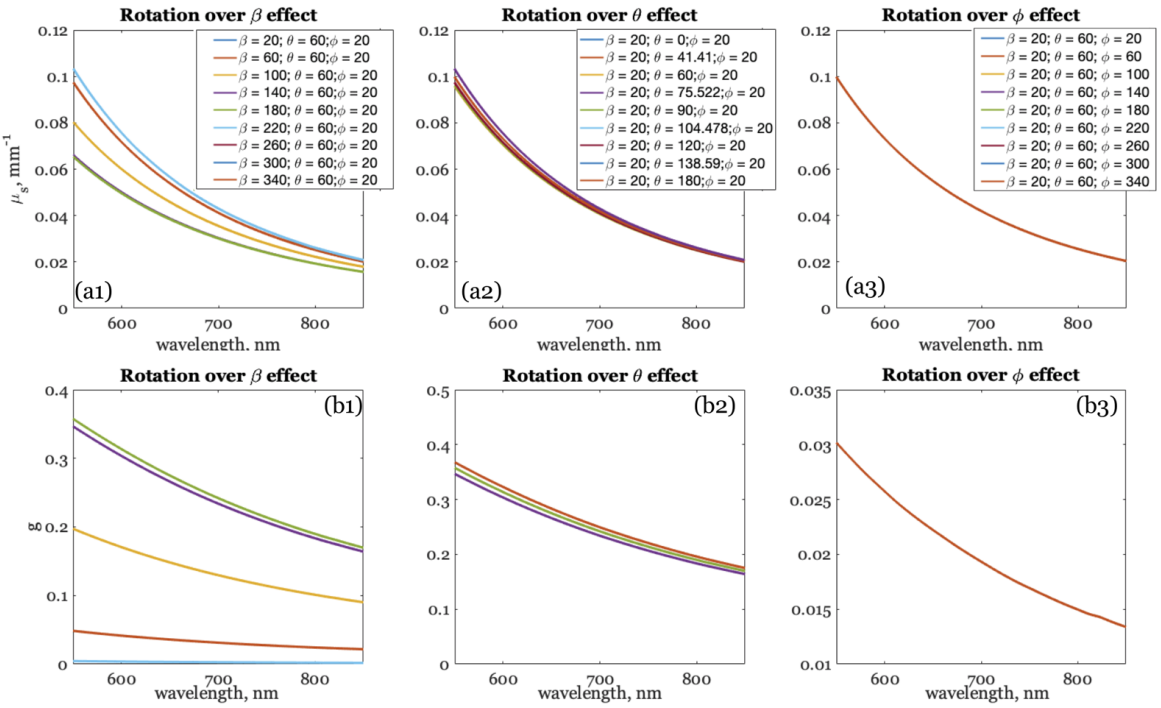

Figure 7.2.9 Bulk scattering coefficient (a) and asymmetry parameter (b) simulated for 5wt% suspension of CNC particles with A=B=10nm and C = 125nm calculated for different angles of rotation

perform the calculation for orientation-averaged ellipsoids efficiently, which was used in the simulations for Sections 7.2.1 and 7.2.2. However, due to computational inefficiency of using all possible rotations, the routine requires a user to manually enter the sampling intervals for Euler angles in the input files. The study in the mentioned sections used the methodology published previously, yet the use of more orientation angles sampling may considerably improve the accuracy of bulk optical properties after averaging over ellipsoid orientations.

As was mentioned already, the averaging over possible orientations would directly affect computational time since it would mean the increment of a number of simulations needed to be performed per sample. Therefore, one of the goals was to way the way of optimizing the orientation-averaging routine. One course of action is accounting on particle symmetries. The prolate ellipsoid, employed in this study, is symmetrical to its longest axis C. The angle of rotation ϕ is aligned with C-axis, hence the sampling over this angle of rotation would result in constant values. The example of rotation of μ_s and g over different angles for the system of CNC particles with AR=8:1 from Section 7.2.2 is illustrated

in Figure 7.2.9. This example confirms that rotation of over ϕ does not impact bulk optical properties. This allows to reduce sampling necessity to angles β and θ, however number of samples or number of orientations (N.O.) has to be defined for a specific experiment.

The experiment of this section is based on CNC particles of various aspect ratios, shown in Figure 7.2.8. The examination of effective rotational selection for CNC system was done by performing a number of forward calculations of bulk optical properties, each of which had a different number of orientation angles sampling, from 1 to 11 for each, β and θ. The end result was averaged and compared against each other to observe the number of combinations that cause convergence to a constant bulk optical properties value. The examination of effective rotational selection for CNC system was done on CNC sample with AR of the ellipsoids 13:1 (Figure 7.2.10(d)) and the concentration of 3 wt%. Increase of a number of orientations improves the accuracy of the bulk optical properties estimation and after meeting 9 angle samples (81 in total) is reaches the constant values. Sampling the orientation angles β and θ into 9 parts was therefore applied to the methodology of the current experiment.

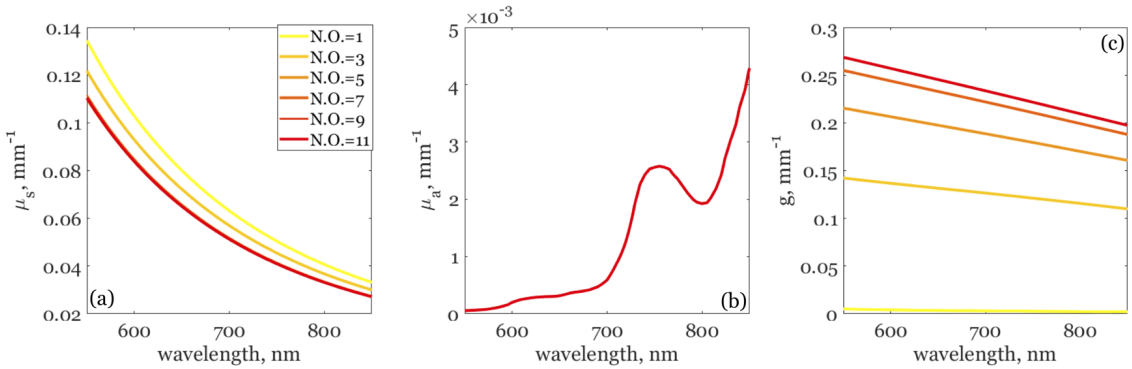

Figure 7.2.10 Bulk optical properties for 3 wt% CNC suspension of needle -like crystals with semi-axes 10 and 250 nm for A and C respectively

Modelled bulk optical properties and spatially resolved diffuse reflectance

The results of the forward calculation are analysed in two parts. Firstly, the bulk optical properties sensitivity to aspect ratio was examined. Bulk optical properties presented are presented in Figure 7.2.11.

Aspect ratio influence can be seen clearly at the asymmetry parameter (Figure 7.2.11 (a)), where the parameter values increase with an increase in the AR across the wavelength range. In bulk scattering coefficient units, the studied effect is not as explicit and

the intensity of it fades with an increase of wavelength number. The bulk absorption coefficient remains constant regardless of AR changes due to the constant volume of the particles present. Inclusion of AR into simulation leads to respective changes in bulk optical properties yet the effect observed does not exhibit features specific enough for AR solely. The effect takes the form of magnitude change however the overall magnitude of the parameters is relatively low which brings difficulty into distinguishing where spherical approximation breaks down.

In comparison with the preliminary study shown in Section 7.2.2, the bulk scattering coefficient and asymmetry parameter have significantly lower values in the current experiment. Since the material properties of the particles in both studies id the same, the observation is most likely the direct result of the dimensions change of the studied particles. The concentration of the current sample set is also lower, which contributes to the magnitude of the bulk scattering coefficient. Another factor that may contribute is the lack of a number of orientations used in the previous study, however, from the observations made in Section 7.2.3, the effect of N.O. is, indeed, appearing strongly on the spectra, however, it is not expected to have an effect at such degree.

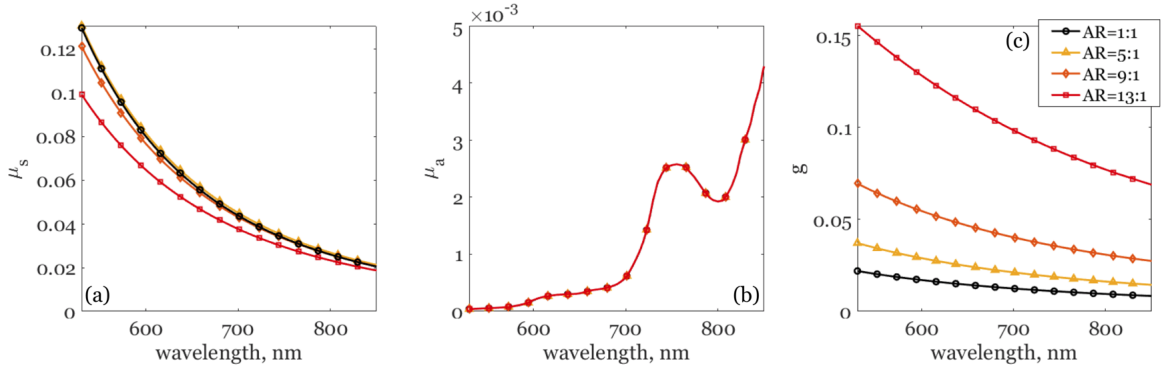

Figure 7.2.11 Bulk optical properties calculated for $3wt\%$ suspensions of cellulose nanocrystals of different aspect ratio

The cumulative effect of optical properties can be observed in Figure 7.2.12 in form of diffuse reflectance. Each of the plots represents the different S-R distance. The overall intensity of the reflectance is relatively low compared to the values observed for polystyrene analysis. Aspect ratio influence on diffuse reflectance becomes distinguishable at relatively high values of AR. Reflectance from the sample of particles with an aspect ratio of 5:1 can be represented by the spherical particle of the same volume. Particles of higher aspect ratio result in signal different from spherical, which in the current scale can be considered

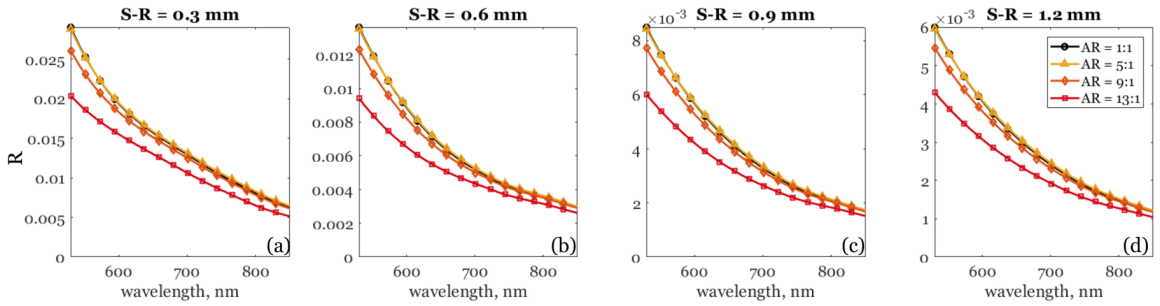

Figure 7.2.12 Spatially resolved diffuse reflectance calculated for $3wt\%$ suspensions of cellulose nanocrystals of different aspect ratio

insignificant. Unlike in previous studies on SAR-DRM, an increase of S-R distance does not influence the reflectance signal, and therefore there is no specific beneficial effect available to study further.

Breaking down the effect of aspect ratio on optical properties, the most sensitive to the effect of was asymmetry parameter. It was discussed before that mixture of various non-spherical particles had affected the scattering coefficient as well as caused pronounced angular features on the asymmetry parameter, especially at high values of size parameter [210]. Analysis of the collected SAR-DRM from the CNC suspensions would indicate the presence of such features as well as overall degree of particle shape effect on measurements and hence following modifications in the current analysis methodology.

The results obtained from modelling SAR-DRM clarified a few important matters. The analysis was conducted on material with different particles dimensions and concentration from the previous sample set. Cellulose nanocrystals are semi-transparent particles that have a refractive index comparable to the refractive index of water. The comparison of the preliminary and current study on CNC suggests that due to above-mentioned specificity of the material, samples with low equivalent radius and concentration of solids do not provide with strong reflectance signal and therefore the studied features, like AR, have less effect on the signal.

Investigation of the measured SAR-DRM sensitivity to aspect ratio variations

For the SAR-DRM signal collection, cellulose nanocrystal suspensions were supplied by Blue Goose Biorefineries Inc. Two samples, BG Natural and BG Ultra, were used in the analysis. The images of the samples themselves are provided in Appendix A.2.

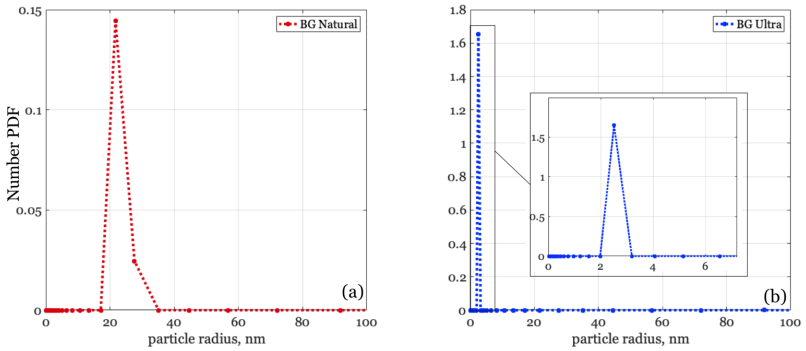

Figure 7.2.13 Reference DLS measurements of number PSD for CNC suspensions: (a) BG Natural and (b)BG Ultra

To summarise, BG Ultra is a slightly hazy solution, close to transparent, whereas BG Natural is cloudy, off-white suspension of CNC (Appendix A.2). The appearance of the samples emphasize the difference in the turbidity and therefore, a difference in the proportion of scattered light. Despite the strong correlation between the concentration of solids and turbidity, this relationship is not unique because equal concentrations of suspended particles do not scatter the same amount of light [211]. Since the material in the same in both of the samples, the major reasons for turbidity differences narrow to the influence of the physical properties of the particles, like size, polydispersity and/or aspect ratio. The SEM images of the example of each of the sample appearance were provided by the supplier and presented in Section 5.1.3, however, these images do not belong to the actual sample that was purchased. To examine one of the parameters, number distribution of the equivalent radii, reference DLS measurements were performed (Figure 7.2.13).

Mode radius returned for BG Natural is 21.7 nm, for BG Ultra it is only 2.51 nm. The low values of them might indicate the values of the shortest axis of the needle-like particles. BG Ultra is a relatively transparent solution of particles with low refractive index, suggesting that DLS measurements of such material embedded in water, which exhibits similar optical properties, are not providing with exact properties of the system.

The particle size distribution of both samples appears to have a single peak, the distribution width of the BG Natural is much wider than the same parameter for BG Ultra. BG Natural, as specified by the supplier, tends to have a higher distribution of the crystal length and therefore equivalent radius distribution. This correlates with sample cloudy off-white appearance.

SAR-DRM FEATURES ANALYSIS Figure 7.2.14 illustrates SAR-DRM collected for two samples at a similar concentration. The spectra presented for all available S-R distance since the parameter of interest was not studied on the SAR-DRM in the previous sections. The BG Natural suspension returns higher intensity signal compare to BG Ultra. The difference in the intensity is valid across S-R distances at a similar degree. With an increase of S-R distance, BG Natural signal changes across wavelength; at shorter S-R distance, the signal has a strong peak at 625 nm, whereas the closer S-R distance is approaching 1.2 mm, the more predominant effect of 575 nm wavelength can be observed. The signal of BG Ultra does not exhibit any notable changes with the variations in S-R. It should be noted for further analysis that the intensity of the measured diffuse reflectance for BG Ultra signal is relatively low and comparable with intensity returned from baseline measurements by integrating sphere.

The significant difference in the intensity of the signals raises the question regarding the source of the effect from the samples. Previously, the similar effect was caused by concentration variations, however, the SAR-DRM presented in Figure 7.2.14 were collected from the samples of similar concentration of solids. Without diminishing the possible influence of fine concentration difference on signal intensity, other parameters tend to influence the signal at stronger extent, like particle size and polydispersity [212]. From the specification sheet of BG Natural, it is known that it consists of both nanocrystals and large agglomerates, that are significantly exceeding micron. In such a regime, the intensity of the reflected light if greatly affected by the size and could cause a significant difference between samples SAR-DRM. The effect of particle size could be combined with more complex physical parameters like particle size distribution and particle shape. Those might have contributed to the differences in samples in such extent that the intensity of the samples differed drastically.

Concluding the observations from the measured and simulated SAR-DRM, due to the low refractive index of the chosen material and constraints to a certain concentration regime, the intensity of the signal is relatively low. The preliminary analysis did not surface any specific features related to the AR effect, the difference between samples appears mostly in the form of magnitude change. Lack of specificity of the effect can potentially affect the inversion outcome, causing the overfitting.

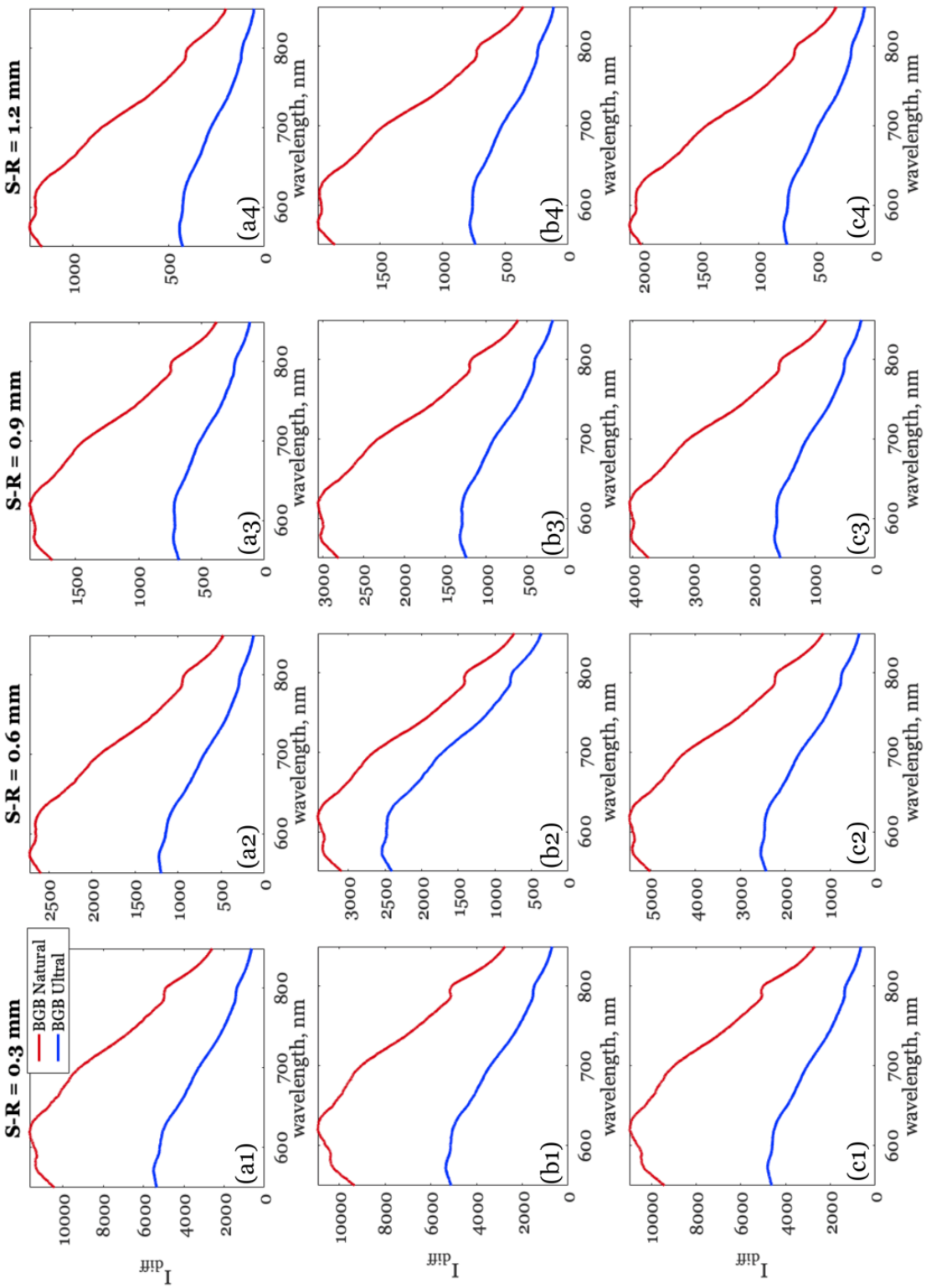

Figure 7.2.14 Spatially resolved reflectance signal collected by different SAR-DRM branches (a-d) for cellulose nanocrystal suspensions samples. Color corresponds to legend.

SIGNAL INVERSION

Since the forward calculation of the bulk optical properties for non-spherical particles was executed via DDSCAT, the inversion algorithm was consequently based on the same method. The routine for the execution of forward calculation and inversion was written in Python 2.7 and provided in Appendix B.

The algorithm flow itself repeats Steps 2- 4 of Mie-based algorithm, highlighted in Chapter 5 with minor modifications. First of all, since the inversion is conduced on equivalent radius only, the need in Step 1 is not justified and therefore, the computation of the single-particle and bulk optical properties is performed iteratively. To enable a single parameter inversion the concentration search was restricted to the gravimetric measurements corresponding to each sample. Methodology-wise, this was executed by setting search constraints to a measured concentration with pm0.01wt% variation. Since DDSCAT takes three variables for the particle size (A, B, C), only A was used in the inversion as the rest of them were set to be equal to A. To validate the performance of the DDSCAT-based inversion routine, Mie-based routine was used in the experiment also. Hence, the modifications mentioned earlier are identical to modifications that were done on Mie-based algorithm.

To clarify the possibility of overfitting, the inversion algorithm was performed in the following sequence. Before considering including the additional particle dimension into the inversion methodology, it was decided to perform inversion for a single parameter, particle radius. To perform the simulation, the inversion was executed the same way as was done for Sample set 1, however, to eliminate the concentration parameter, the concentration limitations were re-adjusted to the measured concentration values. In this case, the inversion is performed for a monodisperse system of spherical particles with no estimation of the concentration.

Performance of the inversion of equivalent radius solely would serve two vital purposes. First of all, the solution obtained with an approximation to spherical particle would serve as an indicator of the need of particle shape parameter for the current samples, without ambiguity caused by concentration or distribution width parameter. Secondly, since the inversion is done using the same algorithm, but with DDSCAT routine instead of Mie for bulk optical properties calculation, this study would also allow to compare the obtained radius with the radius returned by the Mie-based inversion algorithm and hence conduct a validation of the DDSCAT-based inversion.

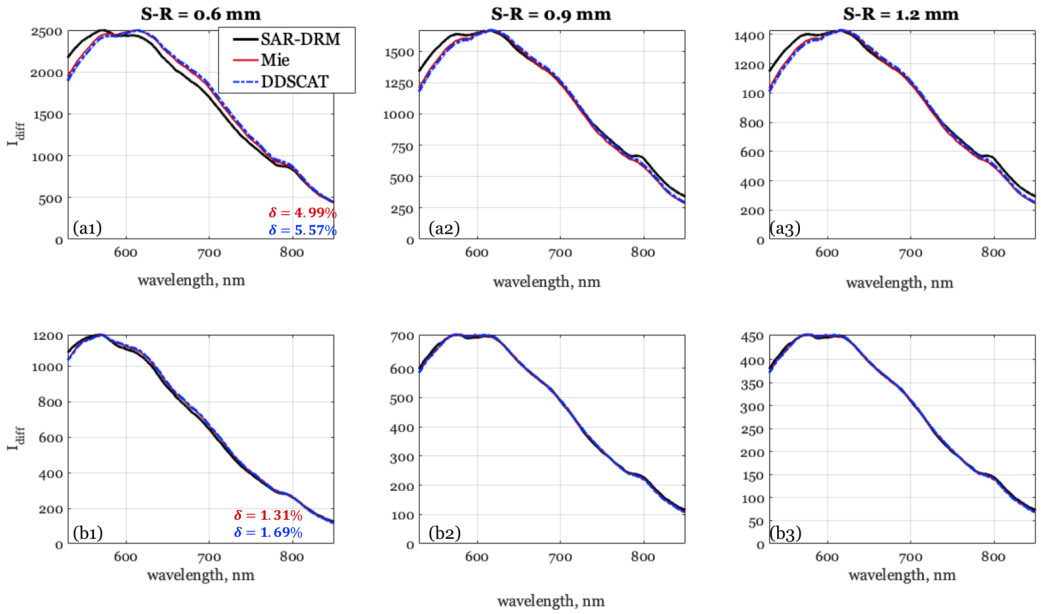

Figure 7.2.15 An example of the re-scaled SAR-DRM signal in comparison with solution SRDR provided by DDSCAT (blue) and Mie(red) based methods for an equivalent sphere. The inversion error δ is presented in bottom left, color-coded for each of the methods.

Therefore, finalising the analysis of the effect of particle shape of CNC on SAR-DRM, the inversion was performed for both available samples. The results below will be examined in the context of quality of the fit, the equivalent sphere radius obtained in comparison with the reference measurement and the computational procedures differences.

EQUIVALENT RADIUS ESTIMATION As a result of the inversion, the best fit was found for BG Ultra and BG Natural via developed DDSCAT and Mie - based algorithms. Figure 7.2.15 illustrates an example of the fit found for each of the originals samples analysed in comparison with SAR-DRM signal for South branch.

From the visual comparison, the produced solutions matching the measured signal well, which is also confirmed by δ values, implying that the correct minima solution for spectra was found. This valid for other samples in the sample set, which can be seen in Table 7.2.1. From the same table, the inverted radius differs from the reference measurements greatly, however, the inverted radius cannot be directly compared with reference DLS measurements mainly due to the fact that DLS returns hydrodynamic radius. By definition, the equivalent sphere radius provided by the SAR-DRM inversion is the radius of a hypothetical sphere that interacts with the light in the colloid suspension in the

Table 7.2.1 Results of the SAR-DRM inversion for CNC suspensions, including mode radius of the equivalent sphere estimated via Mie and DDSCAT based algorithm for South branch

Sample name & conc	δ, %			**Radius, nm**			
	Mie	DDSCAT	Abs. diff.	Mie	DDSCAT	Abs. diff.	Ref. (DLS)
BG Natural, 3.64 wt%	5.70	6.30	0.60	76.75	80.5	3.75	21.7
BG Natural, 1.76 wt%	4.99	5.57	0.58	95.00	99.00	4.00	21.7
BG Ultra, 3.07 wt%	4.02	4.22	0.2	63.42	66.91	3.49	2.51
BG Ultra, 1.56 wt%	1.36	1.68	0.32	68.42	67.37	1.05	2.51
BG Ultra, 1.29 wt%	2.19	2.03	0.16	62.20	60.15	2.05	2.51

same manner as examined CNC. Notably, the inverted diameter is different for each of the samples, therefore the method indicates that the light is scattered differently by particles of different samples. A similar observation was obtained from DLS measurements, which defines the equivalent sphere as the hydrodynamic radius, which is representing a sphere that diffuses at the same rate as studied CNC. The inverted radii have similar values between different method, however with some variations as concentration increases. Inversion of BG Ultra at different concentrations returned the radius values similar across different concentrations. Variations in the inversion outputs for BG Natural are much higher. This sample is known for its polydispersity of sizes and particles dimension ratio, and therefore the variability in equivalent radius estimation might be a result of these properties contributions.

The obtained particle radius confirmed the existence of the equivalent sphere with the possibility of replicating the light scattering behaviour of the analysed CNC. Possibility of providing a good fit to the spectra with an approximation of spherical particle implying that the SAR-DRM for CNC of current dimensions and concentration does not exhibit shape-related effects in the extent sufficient for inversion of the latest.

The simulated SAR-DRM is matching with the solution provided by Mie-based inversion algorithm. The difference in δ values returned by DDA based method in comparison with Mie based method was varying at approximately 2% and can be justified by the difference in the DDA and Mie execution methods. The match between results obtained from Mie -based and DDSCAT -based method indicate that the solution that was found is distinctive since it was obtained by two non-related methods. It indirectly justifies the choice of the function minimisation method for DDSCAT -based inversion as well as

confirms that the randomised search for an optimal starting point in Mie based inversion does not constrain the search for the minima.

Comparing the objective function values returned, overall, the values of the δ corresponding to each fit were relatively low and vary between 6.2 and 1.35 %. The higher values of the objective function are corresponding to an inversion of BG Natural, whereas the solution for BG Natural tends to lay close to measured signal with the low δ difference. The higher values in the results of inversion of BG Natural may be related to other properties of the sample, that were not accounted in this inversion process, like polydispersity, concentration and potentially aspect ratio.

From a comparison of the radius values that were returned by Mie based to DDSCAT method and are shown in Table 7.2.1, the values are close to each other with the difference not exceeding 8 nm. The variations in the estimated radius correlate with the variations in the δ values, meaning that higher variability between objective function results from two different methods is corresponding to high variations in the estimated equivalent sphere radius.

Despite the detectable difference in the equivalent sphere radius between different samples, provided by each of the technique (DLS and inversion), any further derivations from of the Mie radius and hydrodynamic radius to morphology parameters are somewhat problematic. With assumption to a sphere, the Mie radius would not be possible to provide with additional morphology information *a priori*, and for hydrodynamic radius, it has been shown that, despite the possibility to link the length of the particle to the radius value, for high aspect ratio geometries, the contribution of rotational diffusion, not taken into account, can have important effects on the DLS determinations. Hence, alternative approaches like the inclusion of particle length or aspect ratio specifically into the reflectance signal inversion process must be considered closely. According to simulations results for highly scattering material in work mentioned before, variations in aspect ratio may cause a significant influence on SAR-DRM, especially at longer S-R distances. Elaboration of the method further might be considered with the opportunity of studying more scattering material.

The major shortcoming of the developed DDSCAT – method is computational time. Inversion of each sample varies, but stays in 7 to 15 hours window, whereas the Mie-based inversion takes approximately 30 minutes or less. In case of expansion of the method with aspect ratio parameter, this time would have to increase about 81 times due to

orientation averaging needed. Due to time resources needed for the equivalent sphere inversion via DDSCAT, and also because the SAR-DRM spectra from different branches do not vary greatly, the rest of the SAR-DRM branches were not involved into the analysis. For equivalent sphere inversion, Mie theory-based inversion should be applied due to its accuracy and computational speed, however, the developed routine has to be optimised in order to be considered for future application. Potential optimisation routes might parallel processing implementation. Since the DDSCAT routine is an iterative process over a chosen number of wavelength, the parallel calculation could be implemented at this point of the algorithm to replace the sequence calculation.

7.3 CONCLUSIONS

The objectives of this chapter were to analyse the SAR-DRM collected from a sample set from a complex reaction process and with less information available beforehand regarding the parameters of interest compare to previous studies within the project. It included the features analysis of SAR-DRM signal as well as its inversion for polystyrene and cellulose samples.

Inversion results confirmed a number of observations seen in the previous polystyrene sample sets. The Sample set 3 provided a wider concentration range compare to validation study, which allowed to collect more empirical knowledge regarding the inversion quality at higher concentrations. The presence of the samples of higher concentration (>12 wt%) in the sample set allows to extrapolate the previous observations and conclude the concentration of misprediction trend with high values of the actual concentration. Estimation of the parameters of interest does not appear reliable at relatively high values, starting ~ 6 wt%, which agrees from conclusions made after inversion of Sample set 1 and 2. The interference between concentration estimation and polydispersity starts to influence the prediction process greatly at very high concentrations also. At a greater degree of samples dilution, the parameters of interest were similar to each other across different dilutions and agreed better with reference measurements.

The variations in the parameters of interest estimation, despite agreeing with trends observed from the sample sets, might be contaminated with the effect of the process parameters as well. Inversion of the Sample set 3 indicated the differences caused by the polymerisation reaction recipes to the physical properties of the particles. With a decrease

of the initiator ratio, the search for minima returned very high δ values, above stated 15% stopping criteria, indicating the poor quality of the provided fit. Very high inversion error also associated with significant variations in estimated parameters across dilutions implying the possibility of the other parameter influence, that are not currently considered as parameters of interest. Apart from straightforward elimination of the samples that result in the high δ, other indicators of prediction quality might be considered in the future research, for example, the wavelength dependence of the variability of the difference between measured and simulated SAR-DRM can be investigated to identify the kind of the parameter that causes a decrease of the fit quality.

Another parameter that was included in the analysis was the aspect ratio of the particles. Preliminary analysis on simulated SAR-DRM for polystyrene and CNC particles has shown the significant effect of AR on spectra in a degree, sufficient for inversion. Additionally was discovered the beneficial influence of S-R separation on aspect ratio effect appearance. The study was majorly focused further on CNC since this is the material available commercially, however, the particle dimensions are relatively small, and the concentration range that can be used to suffice the diffuse approximation is limited to <3.5wt%. This, along with the particle dimensions, which are generally small, compared to previously studied size range, has a negative effect of the aspect ratio affect appearance, as was concluded from the simulated and measured SRDR. As a result, the spectra can be provided with a good solution for the simple approximation to an equivalent sphere. This means that the solution provided is associated with low inversion error, and therefore, the signal collected for non-spherical CNC can be described by a spherical particle with great accuracy without morphology involved.

In the light of such results, the further analysis of the chosen sample set with additional implementation of the aspect ratio parameter is not necessarily for current material. First of all, the DDA computations take great computing effort, and if spherical approximations can represent the single scattering parameters, computation of scattering parameters can be done more easily by Mie theory. However, the inability to analyze aspect ratio inversion on the CNC suspensions does not automatically imply the overall inability of using SAR-DRM for aspect ratio inversion. Referring back to section 7.2.1, the presence of a strong effect of AR along with some specific changes between light collection settings substantiates the possibility to monitor particle aspect ratio for a highly scattering material experimentally. Since the CNC represent another extreme case of very low reflectance

properties, the SAR-DRM signal for a number of materials of different refractive index should be simulated to evaluate the degree that material has on the appearance of the aspect ratio effect. Also, to invert the desired particle information successfully, one needs to verify that the solution to the inversion is unique.

CHAPTER 8

CONCLUSIONS AND FUTURE WORK

8.1 CONCLUSIONS

The main goal for this project was to develop a physics-based methodology for estimation of parameters, like particle size distribution and concentration, from spatially and angularly resolved diffuse reflectance measurement. The study towards this goal began with the development of the forward calculation routine that consists of two main stages. The first stage aimed to compute the bulk optical properties. To compute bulk optical properties, the resulted routine employed Mie theory for mono and polydisperse system of spherical particles and the Discrete Dipole Approximation for the ellipsoidal particles. These properties apply to a single scattering regime and therefore were expanded in the second stage to cover multiple scattering and provide with spatially resolved diffuse reflectance measurements (SAR-DRM). The second stage in the above-mentioned routine was covered by Farrell's diffuse approximation, which provides with the spatially resolved diffuse reflectance (SRDR). The obtained routine was validated against available literature and was later used in the inversion algorithm to provide with parameters of interests (particle size distribution and concentration).

Before inversion, comprehensive study of the modelled SRDR was conducted to establish limitations that are arising from the methodology itself. Firstly, this method was used to examine the sensitivity of the SRDR to the parameters of interest variations as well as their combinations. As part of this study, mode radius and concentration have each shown a significant effect on SRDR which was specific to the selected parameter of interest. Parameters, like concentration or predominant particle size, were subjects

of studies reported previously, however, the effect of particle size distribution width was not reported at the same extent, making it a primary focus of current research. From the results presented in Chapter 4, the distribution width of lognormal distribution was studied across combinations of parameters of interest. This study concluded that variation in the distribution width above 0.1 and below ~1 has a significant effect on SRDR. The effect appears as a change of magnitude which is similar to the effect of the concentration variation on SRDR. From the point of view of SRDR inversion, this could lead to possible compensation event where over or under-estimation of one of these parameters can lead to decrease in accuracy prediction, causing the possible appearance of the non-unique solutions during the inversion. The possibility of multiple solutions lessens at certain combinations of wavelength and mode radius, due to a strong effect of these parameters. Besides, the effect of distribution width and concentration can be distinguished from each other better when analysed across wavelength in UV-vis- short NIR range, implying the importance of the multi-wavelength analysis to avoid the parameters misprediction.

The relationship between signal collection distances and the appearance of parameters of interest effect on SRDR was studied in the same chapter. The findings have shown that with the increase of S-R distances, the intensity of the signal fades proportionally. However, the effect of the parameters of interest appears more prominently at longer S-R distances due to light travelling deeper into the sample. Further study on the S-R distance unveils that some of the combinations of the parameters of interest result in tmfp longer than closest S-R distance, which hinders the performance of the diffuse approximation for the shortest S-R distance. As the scattering happening further than the shortest S-R, the latter will not be able to depict the scattering events, which would ultimately affect the accuracy of parameters prediction. To comply with the approximation of the diffusion scattering and avoid affecting inversion performance, the SRDR from the closest S-R distance fibres was discarded from the analysis.

To fulfil the main goal, an inversion algorithm was developed, based on fundamental theories for bulk optical properties and diffuse reflectance computation. The spectra signal pre-processing routine involved the improved spectra smoothing methodology as well as needed re-scaling of the SRDR from different S-R distances, eliminating the intensity influence on the inversion result. The inverse method was applied to a number of sample sets to study different combinations of the parameters of interest. Inversion of the monodisperse sample set examined the possibility to provide with mode radius and

concentration. Across the examined size range, estimated mode radius is similar to the values provided by the reference method, resulting RMSE uncertainty ~ 71.5 nm. Notably, the samples, where inverted particle size deviated the most from the reference measurements also returned significant inversion error, δ, allowing to indicate the mispredicted samples based on this parameter. Similar dependence was observed on the inverted concentration values, which confirmed the possibility to link the quality of the parameters inversion with the inversion error when the latter is associated with poor spectra fit (>10%). The indication of the quality of prediction via inversion error at the lower values of δ may be a biased decision, according to the variability in the agreement between reference and inverted values of mode and concentration. Based on results from other sample sets analysis, since the correlation between δ error and the quality of parameters estimation is not exact and exhibited a number of exclusions in studied sample sets, the inversion error solely should not be used for the indication of the parameters quality estimation.

Inversion of the particle size distribution from polydisperse suspensions sample sets provided a result that correlated well with reference measurements of mode radius and distribution width. The particle size distribution parameters were analysed in conjunction with each other as a PDF distribution. Overall results suggest that the inversion method captured the differences in the SAR-DRM associated with distribution width specific for each sample. The inverted PSD parameters and associated δ were consistent across SAR-DRM branches. Generally, the PSD parameters of the samples varied with samples dilution, mostly causing an increase in the distribution width. The probable causes were narrowed to the dilution effect and the competing effect of concentration and distribution width parameters during the inversion. Incorporation of distribution width into the inversion led to interference with concentration estimation, causing the RMSE on averaged across SAR-DRM branches parameters 4.39 wt% and 5.61 wt% for Sample set 2 and 3, respectively. This observation is formalising the conclusions made during the study on simulated SRDR. Significant underestimation of concentration was associated with broad distribution width. It resulted in an average or good quality of the fit, confirming the concerns that were previously made regarding the reliability of the δ error as an exclusive parameter for quality of parameters estimation.

Despite the variations in the accuracy of the concentration estimation across different sample sets, there is a common trend across the sample sets present. The inversion of the concentration indicated the dependency between the quality of the parameter

estimation and the values of the actual concentration. The quality of prediction decreased significantly for samples of concentration above ~ 6 wt%. The reasoning behind this phenomena can be interpreted in the context of exceeding the diffuse scattering regime at a certain concentration level.

The investigation of the aspect ratio effect of prolate ellipsoids on SAR-DRM addressed this question in the context of material properties (refractive index), concentration and the particle dimensions. The case study on the simulated datasets for polystyrene and nanocellulose have concluded that, despite the lower refractive index of the latest, the aspect ratio effect appeared strongly on SRDR. However, the similar study on nanocellulose for the particles of the smaller dimensions and lower concentration has not carried the same degree of aspect ratio effect, which was confirmed by the followed inversion of the equivalent sphere from the SAR-DRM collected for cellulose nanocrystal samples of similar parameters.

Overall, the results of the project indicated that SAR-DRM spectra carry the effect of physical and chemical properties in extent sufficient for retrieving such properties from the observed spectra effects. The developed method for simultaneous estimation of particle size distribution and concentration returned parameters of interest accurately within assigned mode radius, distribution width and concentration constraint. Application of the method outside such constraints has been noted to cause interference of the parameters of interest and hence should be proceeded either with a smaller number of degree of freedom (monodisperse system) or along with reference measurements for results validation.

8.2 Recommendations for Future Work

The conclusions above illustrate the advantage of the developed methodology as well as its limitations. Further study can be considered to include other dimensions of the application of the methods.

Concentration limitation examination Application of the inversion method to the number of sample sets has concluded consistent misprediction of the concentration of solids at the values above 6 wt%. Since this indicates the limitation arising most likely from either diffuse approximation or SAR-DRM configuration, examining this observation may waive the concentration limitation. The proposal is to conduct an inversion on

a monodisperse sample set using all of the S-R distances. For monodisperse systems, transport mean free path is shorter than the shortest S-R distance and the exclusion of the particle size distribution effect on spectra should help to avoid the parameters interference. To understand the concentration limitations of the diffuse approximation, the comparison study between results from diffuse approximation and Monte Carlo simulation can be performed which should indicate if the limitation is arising from the diffuse approximation at all.

THE COMPETING EFFECT BETWEEN DISTRIBUTION WIDTH AND CONCENTRATION The concentration estimation exhibited strong interference from the distribution width parameter as well. Understanding these parameters interference is a complicated task due to the complexity of separation of the effects from the SAR-DRM by non-empirical methods. Consequently, this affects the estimation of the distribution width. Due to the presence of correlation between overestimation of the distribution width and underestimation of the concentration, the further study shall focus on the cumulative effect of these two parameters in more details. The simulated spectra did not exhibit similar shortcomings when inverting combination of these parameters of interest, hence the conducting an experimental study on the large polydisperse samples set could provide sufficient empirical data regarding the parameters interference. The preferable sample set should consist of samples with constant mode radius and range of distribution width parameters, preferable more discrete than in Sample set 2 with mode dilutions degrees. Inverting SAR-DRM from such sample set should clarify the exact concentration - distribution width limitations for polystyrene suspensions. Large sample set can also be used in the data analysis in order to decouple concentration and distribution width effect. Alternatively, improvement of distribution width estimation quality may be achieved by providing the concentration values from reference measurements.

EXPANSION OF METHODOLOGY WITH THE NIR WAVELENGTH RANGE, MEASUREMENT CONFIGURATIONS AND DIFFERENT MATERIALS Some of the capabilities offered by SAR-DRM were not studied in the context of physical and chemical properties of material estimation. Current inversion method averages the spectra signal over wavelength due to the necessity of the single parameter minimisation. Consideration of the wavelength –depended inversion was voiced during this study and is something that can be explored further with more advanced objection function minimisation algorithms. Another direction for the

methodology alteration can focus on the NIR range, the signal-to-noise ratio of which was improved during this research and the spectra were cleared from numerical artefacts. However, the advantages of this improvement were not taken during the current project. Expansion of the algorithm with an additional wavelength range may improve the quality of parameters of interest prediction. It is suggested to validate the method using exclusively the NIR wavelength range first, to gain an understanding of the specificity of using larger wavelength on the polystyrene samples.

Another way to expand the dataset used in the algorithm is to conduct an extensive study on signal collected on oblique incidence light sources. Not only it offers a different reflectance intensity range due to different emittance angles, but also provides with additional S-R distances, larger than the studied here.

The effect of aspect ratio on the SAR-DRM spectra, studied in this project, does not examine the possibilities of the DDSCAT-based inversion algorithm. The material available for the study was not reflective enough in combination with small particle dimensions to exhibit any considerable features of particle shape and also required a degree of dilution to avoid liquid crystal formation, which resulted in the equivalent sphere inversion. Further study can focus on modelling of SAR-DRM for variety of shapes for selected range refractive index values to estimate the minimum value suitable for particle shape estimation. If possible, another material with higher reflective properties shall be studied in this context to validate the modelling results; however, the choice of the material shall consider the diffuse scattering approximation fulfilment.

INVERSION ROUTINE OPTIMISATION TO ENABLE IN-LINE APPLICATION There are directions of the research that were not explored yet might have a significant effect on methodology. One of the straightforward objectives, arising from the obtained results is the optimisation of the algorithm performance to reduce computational time. Achieving the faster inversion time would allow executing the analysis of the processes, like polymerisation reaction.

BIBLIOGRAPHY

[1] US Food, Drug Administration, et al. Process analytical technology (*pat*) initiative. http://www. fda. gov/cder/OPS/PAT. htm, 2004.

[2] Mark L Balboni. Process analytical technology. Pharm. Technol., pages 54–67, 2003.

[3] Zhenguo Gao, Sohrab Rohani, Junbo Gong, and Jingkang Wang. Recent developments in the crystallization process: toward the pharmaceutical industry. Engineering, 3(3):343–353, 2017.

[4] Nils Petitdidier, Anne Koenig, Rémi Gerbelot, Henri Grateau, Sylvain Gioux, and Pierre Jallon. Contact, high-resolution spatial diffuse reflectance imaging system for skin condition diagnosis. Journal of biomedical optics, 23(11):115003, 2018.

[5] Alaa EL Gindy and Ghada M Hadad. Chemometrics in pharmaceutical analysis: an introduction, review, and future perspectives. Journal of AOAC International, 95(3):609–623, 2012.

[6] Alok K Kulshreshtha, Onkar N Singh, and G Michael Wall. Pharmaceutical suspensions: from formulation development to manufacturing. Springer Science & Business Media, 2009.

[7] Anton Paar. The influence of particles on suspension rheology, 2018.

[8] C Logos and QD Nguyen. Effect of particle size on the flow properties of a south australian coal-water slurry. Powder Technology, 88(1):55–58, 1996.

[9] Hua-Gui Yang, Chun-Zhong Li, Hong-Chen Gu, and Tu-Nan Fang. Rheological behavior of titanium dioxide suspensions. Journal of colloid and interface science, 236(1):96–103, 2001.

[10] Zhongwu Zhou, Peter J Scales, and David V Boger. Chemical and physical control of the rheology of concentrated metal oxide suspensions. Chemical Engineering Science, 56(9):2901–2920, 2001.

[11] Dino J Farina. Regulatory aspects of nasal and pulmonary spray drug products. In Handbook of Non-Invasive Drug Delivery Systems, pages 247–290. Elsevier, 2010.

[12] Hamid Reza Baharvandi, Morteza Alebooyeh, Masoud Alizadeh, Mina Saeedi Heydari, Naser Kordani, and Peiman Khaksari. The influences of particle–particle interaction and viscosity of carrier fluid on characteristics of silica and calcium carbonate suspensions-coated twaron® composite. Journal of Experimental Nanoscience, 11(7):550–563, 2016.

[13] Gudrun Birk. Formulation development of a highly concentrated suspension of Cilengitide. PhD thesis, LMU, 2015.

[14] Catherine J Mohr. Medical device with orientable tip for robotically directed laser cutting and biomaterial application. Google Patents, 2015.

[15] Manuela T Raimondi, Shane M Eaton, Michele M Nava, Matteo Laganà, Giulio Cerullo, and Roberto Osellame. Two-photon laser polymerization: from fundamentals to biomedical application in tissue engineering and regenerative medicine. Journal of applied biomaterials & functional materials, 10(1):56–66, 2012.

[16] Peter Vandenabeele, Howell GM Edwards, and Luc Moens. A decade of raman spectroscopy in art and archaeology. Chemical reviews, 107(3):675–686, 2007.

[17] Paula Maria Nogueira Ambrogi, Maria Magdalena Espinola Colmán, and Reinaldo Giudici. Miniemulsion polymerization monitoring using off-line raman spectroscopy and in-line nir spectroscopy. Macromolecular Reaction Engineering, 11(4), 2017.

[18] B. R. Jennings and K Parslow. Particle size measurement: the equivalent spherical diameter. Proceedings of the Royal Society of London. A. Mathematical and Physical Sciences, 419(1856):137–149, 1988.

[19] A. Rawle. Basic of principles of particle-size analysis. Surface coatings international. Part A, Coatings journal, 86(2):58–65, 2003.

[20] Sami Ali. Characterization of powders and porous materials, 2012.

[21] Henk G Merkus. Particle size measurements: fundamentals, practice, quality, volume 17. Springer Science & Business Media, 2009.

[22] Alok K. Kulshreshtha, Onkar N. Singh, and G. Michael Wall. Pharmaceutical suspensions: from formulation development to manufacturing. Springer, 2009.

[23] National Institute of Standards and Technology. Particle size characterization, Sep 2019.

[24] Horiba. Understanding and interpreting particle size distribution calculations.

[25] PHH Araújo. Particle size distribution in heterogeneous polymerization systems. PhD thesis, D. Sc. Thesis, COPPE/Universidade Federal do Rio de Janeiro. Rio de Janeiro . . . , 1999.

[26] JC Ferrari, F Castilhos, PHH Araújo, and C Sayer. Modeling particle size distribution in heterogeneous polymerization systems using multimodal lognormal function. Brazilian Journal of Chemical Engineering, 33(3):469–478, 2016.

[27] Fatemeh Jahanzad. Evolution of particle size distribution in suspension polymerisation reactions. PhD thesis, Loughborough University, 2004.

[28] RK Bajpai, D Ramkrishna, and A Prokop. A coalescence redispersion model for drop-size distributions in an agitated vessel. Chemical Engineering Science, 31(10):913–920, 1976.

[29] Hsiao Tsung Chen and Stanley Middleman. Drop size distribution in agitated liquid-liquid systems. AIChE Journal, 13(5):989–955, 1967.

[30] DE Brown and K Pitt. Effect of impeller geometry on drop break-up in a stirred liquid—liquid contactor. Chemical Engineering Science, 29(2):345–348, 1974.

[31] Sanjeev Kumar, R Kumar, and KS Gandhi. A multi-stage model for drop breakage in stirred vessels. Chemical engineering science, 47(5):971–980, 1992.

[32] AW Pacek, CC Man, and AW Nienow. On the sauter mean diameter and size distributions in turbulent liquid/liquid dispersions in a stirred vessel. Chemical Engineering Science, 53(11):2005–2011, 1998.

[33] Xufei Yang, Jongmin Lee, Douglas E Barker, Xinlei Wang, and Yuanhui Zhang. Comparison of six particle size distribution models on the goodness-of-fit to particulate matter sampled from animal buildings. Journal of the Air & Waste Management Association, 62(6):725–735, 2012.

[34] Paul Kippax. Appraisal of the laser diffraction particle-sizing. Pharmaceutical Technology, 3:88–89, 2005.

[35] SLA Hennart, WJ Wildeboer, P Van Hee, and GMH Meesters. Identification of the grinding mechanisms and their origin in a stirred ball mill using population balances. Chemical Engineering Science, 64(19):4123–4130, 2009.

[36] Anon. Methods for the determination of particle size distribution. guide to microscope and image analysis methods. Technical Report 3406-4, British Standard, 1993.

[37] Terence. Allen. Particle size measurement. Springer, 2013.

[38] Barry A Wills and James Finch. Wills' mineral processing technology: an introduction to the practical aspects of ore treatment and mineral recovery. Butterworth-Heinemann, 2015.

[39] Sagar Aryal. Differences between light microscope and electron microscope. microbiologyinfo.com/differences-between-light-microscope-and-electron-microscope/, 2018.

[40] Renliang Xu. Particle characterization: light scattering methods, volume 13. Springer Science & Business Media, 2001.

[41] Tian Hao. Physics of electrorheological fluids in Electrorheological Fluids: The Non-aqueous Suspensions, volume 22. Elsevier, 2005.

[42] Stephen E Harding and Kornelia Jumel. Light scattering. Current protocols in protein science, 11(1):7–8, 1998.

[43] Peter Hänggi and Fabio Marchesoni. Introduction: 100 years of brownian motion. AIP, 2005.

[44] Anton Paar. The principles of dynamic light scattering. https://wiki.anton-paar.com/en/the-principles-of-dynamic-light-scattering/, 2017.

[45] Jeremy Pencer and F Ross Hallett. Effects of vesicle size and shape on static and dynamic light scattering measurements. Langmuir, 19(18):7488–7497, 2003.

[46] Dynamic Light Scattering (DLS). Particle Technology Lab, 2010.

[47] Jörg Stetefeld, Sean A McKenna, and Trushar R Patel. Dynamic light scattering: a practical guide and applications in biomedical sciences. Biophysical reviews, 8(4):409–427, 2016.

[48] Horiba. Analysis of particle size distribution by dynamic light scattering (dls). https://www.azom.com/article.aspx?ArticleID=16145.

[49] Malvern Panalytical. Achieving high sensitivity at different scattering angles with different optical configurations. https://www.malvernpanalytical.com/en/learn/knowledge-center/technical-notes/TN101104AchievingHighSensitivity.html.

[50] Marie Naiim, Abdelbassit Boualem, Caroline Ferre, Meryem Jabloun, Alain Jalocha, and Philippe Ravier. Multiangle dynamic light scattering for the improvement of multimodal particle size distribution measurements. Soft matter, 11(1):28–32, 2015.

[51] Dennis E Koppel. Analysis of macromolecular polydispersity in intensity correlation spectroscopy: the method of cumulants. The Journal of Chemical Physics, 57(11):4814–4820, 1972.

[52] Stephen W Provencher. A constrained regularization method for inverting data represented by linear algebraic or integral equations. Computer Physics Communications, 27(3):213–227, 1982.

[53] Ian D Morrison, EF Grabowski, and CA Herb. Improved techniques for particle size determination by quasi-elastic light scattering. Langmuir, 1(4):496–501, 1985.

[54] Gary Bryant and John C Thomas. Improved particle size distribution measurements using multiangle dynamic light scattering. Langmuir, 11(7):2480–2485, 1995.

[55] Prof. Kevin J. Wilkinson Group. Nanoparticle tracking analysis (nta).

[56] Vasco Filipe, Andrea Hawe, and Wim Jiskoot. Critical evaluation of nanoparticle tracking analysis (nta) by nanosight for the measurement of nanoparticles and protein aggregates. Pharmaceutical research, 27(5):796–810, 2010.

[57] Particle measurement: Laser diffraction. Sympatec, 2015.

[58] KD Caldwell and HG Barth. Modern methods of particle size analysis. Wiley-Interscience, New York, 1984.

[59] Max Born et al. E. wolf principles of optics. Pergamon Press, 6:188–189, 1980.

[60] Cameil MG Heffels, Daniel Heitzmann, E Dan Hirleman, and Brian Scarlett. The use of azimuthal intensity variations in diffraction patterns for particle shape characterization. Particle & particle systems characterization, 11(3):194–199, 1994.

[61] Zhenhua Ma, Henk G Merkus, Hilda G van der Veen, Melvin Wong, and Brian Scarlett. On-line measurement of particle size and shape using laser diffraction. Particle & Particle Systems Characterization: Measurement and Description of Particle Properties and Behavior in Powders and Other Disperse Systems, 18(5-6):243–247, 2001.

[62] Vladimir Turzhitsky, Le Qiu, Irving Itzkan, Andrei A Novikov, Mikhail S Kotelev, Michael Getmanskiy, Vladimir A Vinokurov, Alexander V Muradov, and Lev T Perelman. Spectroscopy of scattered light for the characterization of micro and nanoscale objects in biology and medicine. Applied spectroscopy, 68(2):133–154, 2014.

[63] Electromagnetic spectrum. Dundee Satellite Receiving Station, 2019.

[64] T Germer, J Zwinkels, and B Tsai. Accurate measurement of optical properties of materials (experimental methods in the physical sciences. Academic Press, 2014.

[65] DF Swinehart. The beer-lambert law. Journal of chemical education, 39(7):333, 1962.

[66] Michael I Mishchenko. Radiative transfer theory: From maxwell's equations to practical applications. In Wave Scattering in Complex Media: From Theory to Applications, pages 366–414. Springer, 2003.

[67] Jeffery S Reynolds, Tamara L Troy, and Eva M Sevick-Muraca. Multipixel techniques for frequency-domain photon migration imaging. Biotechnology progress, 13(5):669–680, 1997.

[68] Huabei Jiang, Joseph Pierce, Jeffrey Kao, and Eva Sevick-Muraca. Measurement of particle-size distribution and volume fraction in concentrated suspensions with photon migration techniques. Applied optics, 36(15):3310–3318, 1997.

[69] Zhenqi Shi and Carl A Anderson. Application of monte carlo simulation-based photon migration for enhanced understanding of near-infrared (nir) diffuse reflectance. part i: Depth of penetration in pharmaceutical materials. Journal of pharmaceutical sciences, 99(5):2399–2412, 2010.

[70] Wouter Saeys, Maria A Velazco-Roa, Suresh N Thennadil, Herman Ramon, and Bart M Nicolaï. Optical properties of apple skin and flesh in the wavelength range from 350 to 2200 nm. Applied optics, 47(7):908–919, 2008.

[71] Ben Aernouts, Eduardo Zamora-Rojas, Robbe Van Beers, Rodrigo Watté, Ling Wang, Mizuki Tsuta, Jeroen Lammertyn, and Wouter Saeys. Supercontinuum laser based optical characterization of intralipid® phantoms in the 500-2250 nm range. Optics express, 21(26):32450–32467, 2013.

[72] Karl-Heinz Koch. Process analytical chemistry. Springer, 1999.

[73] EG Goh, Xiaoxue Xu, and PG McCormick. Effect of particle size on the uv absorbance of zinc oxide nanoparticles. Scripta Materialia, 78:49–52, 2014.

[74] Debashish Acharya, Bidhan Mohanta, Sanjib Deb, and Asoke Kumar Sen. Theoretical prediction of absorbance spectra considering the particle size distribution using mie theory and their comparison with the experimental uv–vis spectra of synthesized nanoparticles. Spectroscopy Letters, 51(3):139–143, 2018.

[75] TC Prathna, N Chandrasekaran, Ashok M Raichur, and Amitava Mukherjee. Biomimetic synthesis of silver nanoparticles by citrus limon (lemon) aqueous extract and theoretical prediction of particle size. Colloids and Surfaces B: Biointerfaces, 82(1):152–159, 2011.

[76] Stefan Tălu, Ram Pratap Yadav, Ashok Kumar Mittal, Amine Achour, Carlos Luna, Mohsen Mardani, Shahram Solaymani, Ali Arman, Fatemeh Hafezi, Azin Ahmadpourian, et al. Application of mie theory and fractal models to determine the optical and surface roughness of ag–cu thin films. Optical and Quantum Electronics, 49(7):256, 2017.

[77] JL Ilari, H Martens, and T Isaksson. Determination of particle size in powders by scatter correction in diffuse near-infrared reflectance. Applied spectroscopy, 42(5):722–728, 1988.

[78] J Doak, RK Gupta, K Manivannan, K Ghosh, and PK Kahol. Effect of particle size distributions on absorbance spectra of gold nanoparticles. Physica E: Low-dimensional Systems and Nanostructures, 42(5):1605–1609, 2010.

[79] Jianhong Wang and F Ross Hallett. Spherical particle size determination by analytical inversion of the uv–visible–nir extinction spectrum. Applied optics, 35(1):193–197, 1996.

[80] Wolfgang Haiss, Nguyen TK Thanh, Jenny Aveyard, and David G Fernig. Determination of size and concentration of gold nanoparticles from uv- vis spectra. Analytical chemistry, 79(11):4215–4221, 2007.

[81] RA Viscarra Rossel, RN McGlynn, and AB McBratney. Determining the composition of mineral-organic mixes using uv–vis–nir diffuse reflectance spectroscopy. Geoderma, 137(1-2):70–82, 2006.

[82] P Frake, CN Luscombe, DR Rudd, I Gill, J Waterhouse, and UA Jayasooriya. Near-infrared mass median particle size determination of lactose monohydrate, evaluating several chemometric approaches. Analyst, 123(10):2043–2046, 1998.

[83] Mohammadreza Khanmohammadi, Hamideh Elmizadeh, and Keyvan Ghasemi. Investigation of size and morphology of chitosan nanoparticles used in drug delivery system employing chemometric technique. Iranian journal of pharmaceutical research: IJPR, 14(3):665, 2015.

[84] Jukka Rantanen, Håkan Wikström, Rebecca Turner, and Lynne S Taylor. Use of in-line near-infrared spectroscopy in combination with chemometrics for improved understanding of pharmaceutical processes. Analytical chemistry, 77(2):556–563, 2005.

[85] Maud Rey-Bayle, Ryad Bendoula, Serge Henrot, Kilani Lamiri, Franck Baco-Antoniali, Noémie Caillol, Alexia Gobrecht, and Jean-Michel Roger. Potential of vis–nir spectroscopy to monitor the silica precipitation reaction. Analytical and bioanalytical chemistry, 409(3):785–796, 2017.

[86] David Lee Black, Mardson Queiroz McQuay, and Michel P Bonin. Laser-based techniques for particle-size measurement: a review of sizing methods and their industrial applications. Progress in energy and combustion science, 22(3):267–306, 1996.

[87] MCB UP Limited. Back scatter optics allow particle size measurement at high concentration. Pigment & Resin Technology, 31(5), 2002.

[88] Michael Kaszuba, Malcolm T Connah, Fraser K McNeil-Watson, and Ulf Nobbmann. Resolving concentrated particle size mixtures using dynamic light scattering. Particle & Particle Systems Characterization, 24(3):159–162, 2007.

[89] PN Segre, W Van Megen, Peter N Pusey, K Schätzel, and W Peters. Two-colour dynamic light scattering. Journal of Modern Optics, 42(9):1929–1952, 1995.

[90] PN Pusey. Suppression of multiple scattering by photon cross-correlation techniques. Current opinion in colloid & interface science, 4(3):177–185, 1999.

[91] F Stieber and W Richtering. Fiber-optic-dynamic-light-scattering and two-color-cross-correlation studies of turbid, concentrated, sterically stabilized polystyrene latex. Langmuir, 11(12):4724–4727, 1995.

[92] John C Thomas and Victoria Dimonie. Fiber optic dynamic light scattering from concentrated dispersions. 3: Particle sizing in concentrates. Applied optics, 29(36):5332–5335, 1990.

[93] FM Horn, W Richtering, J Bergenholtz, N Willenbacher, and NJ Wagner. Hydrodynamic and colloidal interactions in concentrated charge-stabilized polymer dispersions. Journal of colloid and interface science, 225(1):166–178, 2000.

[94] AA Hamidi and J Swithenbank. Treatment of multiple scattering of light in laser diffraction measurement techniques in dense sprays and particle fields. Journal of the Institute of Energy, 59(439):101–105, 1986.

[95] PG Felton, AA Hamidi, and AK Aigal. Measurement of drop size distribution in dense sprays by laser diffraction. In IN: ICLASS-85; Proceedings of the Third International Conference on Liquid Atomisation and Spray Systems, London, England, July 8-10, 1985. Volume 2 (A87-13826 03-34). London, Institute of Energy, 1986, p. IVA/4/1-IVA/4/11. Research supported by the Ministry of Defence, British Council, and SERC., volume 2, 1986.

[96] E Dan Hirleman. Modeling of multiple scattering effects in fraunhofer diffraction particle size analysis. In Optical Particle Sizing. Springer, 1988.

[97] Thomas L Harvill, Jared H Hoog, and Donald J Holve. In-process particle size distribution measurements and control. Particle & particle systems characterization, 12(6):309–313, 1995.

[98] Rui Chen. Novel particle sizing techniques. PhD thesis, University of Nottingham, 2013.

[99] BS ISO. 14887 (2000) sample preparation—dispersing procedures for powders in liquids. International organization for standardization, Geneva, Switzerland, 2000.

[100] BB ISO. 14488 (2007), particulate materials – sampling and sample splitting for the determination of particulate properties. International organization for standardization, Geneva, Switzerland, 2007.

[101] Javier Cardona, Carla Ferreira, John McGinty, Andrew Hamilton, Okpeafoh S Agimelen, Alison Cleary, Robert Atkinson, Craig Michie, Stephen Marshall, Yi-Chieh Chen, et al. Image analysis framework with focus evaluation for in situ characterisation of particle size and shape attributes. Chemical Engineering Science, 191:208–231, 2018.

[102] Martinus de Kanter, Julian Meyer-Kirschner, Jörn Viell, Alexander Mitsos, Michael Kather, Andrij Pich, and Christoph Janzen. Enabling the measurement of particle sizes in stirred colloidal suspensions by embedding dynamic light scattering into an automated probe head. Measurement, 80:92–98, 2016.

[103] Paul Wan Sia Heng, Lai Wah Chan, and Lay Hui Tan. Laser diffraction as a pat tool for spray drying. Pharma Manufacturing, 2009.

[104] Gunnar Kullenberg. Scattering of light by sargasso sea water. In Deep Sea Research and Oceanographic Abstracts, volume 15, pages 423–432, 1968.

[105] Xiao-Sheng Huang, Jinlong Zhang, Wei-Biao Chen, Ting-Lu Zhang, Mingxia He, and Zhishen Liu. New type of scatterometer for measuring the small-angle volume scattering function of seawater and the experiments in the east china sea. In Ocean Optics XII, volume 2258, pages 556–559. International Society for Optics and Photonics, 1994.

[106] John A Boxall, Carolyn A Koh, E Dendy Sloan, Amadeu K Sum, and David T Wu. Measurement and calibration of droplet size distributions in water-in-oil emulsions by particle video microscope and a focused beam reflectance method. Industrial & Engineering Chemistry Research, 49(3):1412–1418, 2009.

[107] AN Saleemi, CD Rielly, and ZK Nagy. Monitoring of the combined cooling and antisolvent crystallisation of mixtures of aminobenzoic acid isomers using atr-uv/vis spectroscopy and fbrm. Chemical engineering science, 77:122–129, 2012.

[108] Elina Hishamuddin and Zaliha Omar. In situ characterisation of palm olein crystallisation behaviour by focused beam reflectance measurement (fbrm). Journal of Oil Palm Research, 28(1):44–51, 2016.

[109] Huayu Li, Martha A Grover, Yoshiaki Kawajiri, and Ronald W Rousseau. Development of an empirical method relating crystal size distributions and fbrm measurements. Chemical Engineering Science, 89:142–151, 2013.

[110] Ajinkya V Pandit and Vivek V Ranade. Chord length distribution to particle size distribution. AIChE Journal, 62(12):4215–4228, 2016.

[111] M Li, D Wilkinson, and Kumar Patchigolla. Comparison of particle size distributions measured using different techniques. Particulate Science and Technology, 23(3):265–284, 2005.

[112] Vijay Kumar, Michael K Taylor, Amit Mehrotra, and William C Stagner. Real-time particle size analysis using focused beam reflectance measurement as a process analytical technology tool for a continuous granulation–drying–milling process. Aaps Pharmscitech, 14(2):523–530, 2013.

[113] Katherine A Bakeev. Process analytical technology: spectroscopic tools and implementation strategies for the chemical and pharmaceutical industries. John Wiley & Sons, 2010.

[114] Mettler Toledo. Advancing beyond turbidity: Selecting appropriate technology for monitoring and control of complex particle and droplet systems.

[115] Michael L Myrick, Michael N Simcock, Megan Baranowski, Heather Brooke, Stephen L Morgan, and Jessica N McCutcheon. The kubelka-munk diffuse reflectance formula revisited. Applied Spectroscopy Reviews, 46(2):140–165, 2011.

[116] Diffuse reflectance - theory and applications. Pike Technologies, https://www.piketech.com/files/pdfs/PIKE_Diffuse-Reflectance-Theory-Applications.pdf, 2015.

[117] Peter Naglič, Franjo Pernuš, Boštjan Likar, and Miran Bürmen. Limitations of the commonly used simplified laterally uniform optical fiber probe-tissue interface in monte carlo simulations of diffuse reflectance. Biomedical optics express, 6(10):3973–3988, 2015.

[118] Rodrigo Watté, Nghia Nguyen Do Trong, Ben Aernouts, Chyngyz Erkinbaev, Josse De Baerdemaeker, Bart Nicolaï, and Wouter Saeys. Metamodeling approach for efficient estimation of optical properties of turbid media from spatially resolved diffuse reflectance measurements. Optics express, 21(26), 2013.

[119] Shao-Pow Lin, Lihong Wang, Steven L Jacques, and Frank K Tittel. Measurement of tissue optical properties by the use of oblique-incidence optical fiber reflectometry. Applied optics, 36(1):136–143, 1997.

[120] Yi-Chieh Chen, David Foo, Nicolau Dehanov, and Suresh N Thennadil. Spatially and angularly resolved spectroscopy for in-situ estimation of concentration and particle size in colloidal suspensions. Analytical and bioanalytical chemistry, 409(30):6975–6988, 2017.

[121] Alwin Kienle, Lothar Lilge, Michael S Patterson, Raimund Hibst, Rudolf Steiner, and Brian C Wilson. Spatially resolved absolute diffuse reflectance measurements for noninvasive determination of the optical scattering and absorption coefficients of biological tissue. Applied optics, 35(13):2304–2314, 1996.

[122] RMP Doornbos, Roland Lang, MC Aalders, FW Cross, and HJCM Sterenborg. The determination of in vivo human tissue optical properties and absolute chromophore concentrations using spatially resolved steady-state diffuse reflectance spectroscopy. Physics in Medicine & Biology, 44(4):967, 1999.

[123] VV Tuchin. Tissue optics: Light scattering methods and instruments for medical diagnosis (spie tutorial texts in optical engineering vol. tt38, 2000); pk gupta," tissue optics.

[124] Dizem Arifler, Calum E MacAulay, Michelle Follen, and Rebecca R Richards-Kortum. Spatially resolved reflectance spectroscopy for diagnosis of cervical precancer: Monte carlo modeling and comparison to clinical measurements. Journal of Biomedical Optics, 11(6):064027, 2006.

[125] Jianwei Qin and Renfu Lu. Measurement of the optical properties of fruits and vegetables using spatially resolved hyperspectral diffuse reflectance imaging technique. Postharvest Biology and Technology, 49(3):355–365, 2008.

[126] Jian-Xu Wang, Li-Feng Fan, Hai-Hua Wang, Peng-Fei Zhao, Hao Li, Zhong-Yi Wang, and Lan Huang. Determination of the moisture content of fresh meat using visible and near-infrared spatially resolved reflectance spectroscopy. Biosystems Engineering, 162:40–56, 2017.

[127] Ryad Bendoula, Arnaud Ducanchez, Ana Herrero-Langreo, Pablo Guerrero-Castro, Jean-Michel Roger, and Alexia Gobrecht. Effect of the architecture of fiber-optic probes designed for soluble solid content prediction in intact sugar beet slices. Sensors, 19(13):2995, 2019.

[128] Manuela Zude. Optical monitoring of fresh and processed agricultural crops. CRC press, 2008.

[129] Peter Naglič, Franjo Pernuš, Boštjan Likar, and Miran Bürmen. Estimation of optical properties by spatially resolved reflectance spectroscopy in the subdiffusive regime. Journal of biomedical optics, 21(9):095003, 2016.

[130] Otto Scheibelhofer, Patrick R Wahl, Boris Larchevêque, Fabien Chauchard, and Johannes G Khinast. Spatially resolved spectral powder analysis: experiments and modeling. Applied spectroscopy, 72(4):521–534, 2018.

[131] Craig F Bohren and Donald R Huffman. Absorption and scattering of light by small particles. John Wiley & Sons, 2008.

[132] M Lodomez, M Pirotton, B Dewals, P Archambeau, and S Erpicum. Sustainable hydraulics in the era of global change. In Proc., 4th IAHR Europe Congress. Boca Raton, FL: CRC Press, 2016.

[133] John Tyndall. On the blue color of the sky, the polarization of skylight, and polarization of light by cloudy matter generally. Journal of the Franklin Institute, 88(1):34–40, 1869.

[134] Lord Rayleigh. Xlii. on the scattering of light by a cloud of similar small particles of any shape and oriented at random. The London, Edinburgh, and Dublin Philosophical Magazine and Journal of Science, 36(209):373–381, 1918.

[135] G. Mie. Beiträge zur optik trüber medien, speziell kolloidaler metallösungen. Annalen der physik, 330(3)(377-445), 1908.

[136] M Faubel. The "fraunhofer theory"of rotational inelastic scattering of he on small molecules. The Journal of chemical physics, 81(12):5559–5569, 1984.

[137] Lord Rayleigh. Xli. the dispersal of light by a dielectric cylinder. The London, Edinburgh, and Dublin Philosophical Magazine and Journal of Science, 36(215):365–376, 1918.

[138] BS ISO. 13320-1: 1999 particle size analysis-laser diffraction methods. part 1: General principles. British Standards Institution, London, 1999.

[139] Petr Chỳlek and Venkatachalam Ramaswamy. Lower and upper bounds on extinction cross sections of arbitrarily shaped strongly absorbing or strongly reflecting nonspherical particles. Applied optics, 21(23):4339–4344, 1982.

[140] Shoji Asano and Giichi Yamamoto. Light scattering by a spheroidal particle. Applied optics, 14(1):29–49, 1975.

[141] B Sinha and R MacPhie. Electromagnetic scattering from prolate spheroids for axial incidence. IEEE Transactions on Antennas and Propagation, 23(5):676–679, 1975.

[142] T Onaka. Light scattering by spheroidal grains. Annals of the Tokyo Astronomical Observatory, 18(1–54), 1980.

[143] Wenbo Sun, Norman G Loeb, and Bing Lin. Light scattering by an infinite circular cylinder immersed in an absorbing medium. Applied optics, 44(12):2338–2342, 2005.

[144] Bruce T Draine and Piotr J Flatau. User guide for the discrete dipole approximation code ddscat 7.3. arXiv preprint arXiv: 1305.6497, 2003.

[145] Peter Barber and Cavour Yeh. Scattering of electromagnetic waves by arbitrarily shaped dielectric bodies. Applied Optics, 14(12):2864–2872, 1975.

[146] Peter C Waterman. Symmetry, unitarity, and geometry in electromagnetic scattering. Physical review D, 3(4):825, 1971.

[147] Maxim Yurkin and Michael Kahnert. Light scattering by a cube: Accuracy limits of the discrete dipole approximation and the t-matrix method. Journal of Quantitative Spectroscopy and Radiative Transfer, 123:176–183, 2013.

[148] D Langbein. Van der waals attraction between macroscopic bodies. The Journal of Adhesion, 1(4):237–245, 1972.

[149] Edward M Purcell and Carlton R Pennypacker. Scattering and absorption of light by nonspherical dielectric grains. The Astrophysical Journal, 186(705–714), 1973.

[150] Romolo Savo, Romain Pierrat, Ulysse Najar, Rémi Carminati, Stefan Rotter, and Sylvain Gigan. Mean path length invariance in multiple light scattering. arXiv preprint arXiv:1703.07114, 2017.

[151] Michael I Mishchenko and Ping Yang. Far-field lorenz–mie scattering in an absorbing host medium: theoretical formalism and fortran program. Journal of Quantitative Spectroscopy and Radiative Transfer, 205:241–252, 2018.

[152] BC Wilson and MS Patterson. The physics of photodynamic therapy. Physics in Medicine & Biology, 31(4):327–360, 1986.

[153] Kuo-Nan Liou. An introduction to atmospheric radiation, volume 84. Elsevier, 2002.

[154] Subrahmanyan Chandrasekhar. Radiative transfer. Courier Corporation, 2013.

[155] Scott A Prahl. The adding-doubling method. In Optical-thermal response of laser-irradiated tissue, pages 101–129. Springer, 1995.

[156] Valeriĭ Viktorovich Tuchin and V Tuchin. Tissue optics: light scattering methods and instruments for medical diagnosis. SPIE press Bellingham, 2007.

[157] Maria Alejandra Velazco Roa. Estimation of optical constants of particles in suspension from multiple-scattered light. PhD thesis, Newcastle University, 2007.

[158] Suresh N Thennadil and Yi-Chieh Chen. Measurement apparatus and method. Google Patents, Oct 2014.

[159] Y Marechal, JL Coulomb, G Meunier, and G Touzot. Use of the diffuse approximation method for electromagnetic field computation. IEEE transactions on magnetics, 30(5):3558–3561, 1994.

[160] Rolf H Bremmer, Martin JC van Gemert, Dirk J Faber, Ton G van Leeuwen, and Maurice C Aalders. Diffuse reflectance relations based on diffusion dipole theory for large absorption and reduced scattering. Journal of Biomedical Optics, 18(8), 2013.

[161] Larry Reynolds, C Johnson, and Akira Ishimaru. Diffuse reflectance from a finite blood medium: applications to the modeling of fiber optic catheters. Applied optics, 15(9):2059–2067, 1976.

[162] RAJ Groenhuis, Hedzer A Ferwerda, and JJ Ten Bosch. Scattering and absorption of turbid materials determined from reflection measurements. 1: Theory. Applied optics, 22(16):2456–2462, 1983.

[163] Thomas J. Farrell, Michael S. Patterson, and Brian Wilson. A diffusion theory model of spatially resolved, steady state diffuse reflectance for the noninvasive determination of tissue optical properties invivo. Medical physics, 19:879–888, 1992.

[164] Guillermo Marquez and Lihong V Wang. White light oblique incidence reflectometer for measuring absorption and reduced scattering spectra of tissue-like turbid media. Optics Express, 1(13):454–460, 1997.

[165] Ricky Hennessy, Will Goth, Manu Sharma, Mia K Markey, and James W Tunnell. Effect of probe geometry and optical properties on the sampling depth for diffuse reflectance spectroscopy. Journal of Biomedical Optics, 19(10):107002, 2014.

[166] A. Kienle, L. Lilge, M. S. Patterson, R. Hibst, R. Steiner, and B. C. Wilson. Spatially resolved absolute diffuse reflectance measurements for noninvasive determination of the optical scattering and absorption coefficients of biological tissue. Applied optics, pages 2304–2314, 1996.

[167] Kung-Bin Sung, Kuang-Wei Shih, Fang-Wei Hsu, Hong-Po Hsieh, Min-Jie Chuang, Yi-Hsien Hsiao, Yu-Hui Su, and Gen-Hao Tien. Accurate extraction of optical properties and top layer thickness of two-layered mucosal tissue phantoms from spatially resolved reflectance spectra. Journal of Biomedical Optics, 19(7):77002, 2014.

[168] Robert T Jacobsen, Milton Kerker, and Egon Matijevic. Aerosol studies by light scattering. v. preparation and particle-size distribution of aerosols consisting of particles exhibiting high optical absorption. The Journal of Physical Chemistry, 71(3):514–520, 1967.

[169] Michael Quinten. Optical Properties of Nanoparticle Systems: Mie and beyond. John Wiley & Sons, 2011.

[170] Michael I Mishchenko. Electromagnetic scattering by particles and particle groups: an introduction. Cambridge: Cambridge University Press., Cambridge, 2014.

[171] Ben Aernouts, Rodrigo Watté, Robbe Van Beers, Filip Delport, Martine Merchiers, Jan De Block, Jeroen Lammertyn, and Wouter Saeys. Flexible tool for simulating the bulk optical properties of polydisperse spherical particles in an absorbing host: experimental validation. Optics express, 22(17):20223–20238, 2014.

[172] Annelies Postelmans, Ben Aernouts, and Wouter Saeys. Estimation of particle size distributions from bulk scattering spectra: sensitivity to distribution type and spectral noise. Optics express, 26(12):15015–15038, 2018.

[173] WA De Rooij and CCAH Van der Stap. Expansion of mie scattering matrices in generalized spherical functions. Astronomy and Astrophysics, 131:237–248, 1984.

[174] Thermo Scientific. Particle technology product catalog and technical reference guide, 2014.

[175] MEWFWAS Kerker, E Matijević, WF Espenscheid, WA Farone, and S Kitani. Aerosol studies by light scattering. i. particle size distribution by polarization ratio method. Journal of Colloid Science, 19(3):213–222, 1964.

[176] M Quinn Brewster. Thermal radiative transfer and properties. John Wiley & Sons, 1992.

[177] Michael F Modest. Radiative Heat Transfer 2nd Ed. Academic Press, 2013.

[178] Sigma-Aldrich. Polystyrene | sigma-aldrich, Polystyrene | Sigma-Aldrich 2018.

[179] George M Hale and Marvin R Querry. Optical constants of water in the 200-nm to 200-μm wavelength region. Applied optics, 12(3):555–563, 1973.

[180] Nina Sultanova, S Kasarova, and Ivan Nikolov. Dispersion proper ties of optical polymers. Acta Physica Polonica-Series A General Physics, 116(4):585, 2009.

[181] Michael I Mishchenko, Janna M Dlugach, Edgard G Yanovitskij, and Nadia T Zakharova. Bidirectional reflectance of flat, optically thick particulate layers: an efficient radiative transfer solution and applications to snow and soil surfaces. Journal of Quantitative Spectroscopy and Radiative Transfer, 63(2-6):409–432, 1999.

[182] Christian Mätzler. Matlab functions for mie scattering and absorption. IAP Res. Rep, 8(1):1–9, 2002.

[183] Suresh N Thennadil and Yi-Chieh Chen. Alternative measurement configurations for extracting bulk optical properties using an integrating sphere setup. Applied spectroscopy, 71(2):224–237, 2017.

[184] YJ Kaufman, A Gitelson, A Karnieli, E Ganor, RS Fraser, T Nakajima, S Mattoo, and BN Holben. Size distribution and scattering phase function of aerosol particles retrieved from sky brightness measurements. Journal of Geophysical Research: Atmospheres, 99(D5):10341–10356, 1994.

[185] J Varva. Influence of polydispersity on mie scattering from colloid dispersions. Chem. zvesti, 29(6):777–782, 1975.

[186] David Sinclair and Victor K La Mer. Light scattering as a measure of particle size in aerosols. the production of monodisperse aerosols. Chemical reviews, 44(2):245–267, 1949.

[187] Tami C Bond, Gazala Habib, and Robert W Bergstrom. Limitations in the enhancement of visible light absorption due to mixing state. Journal of Geophysical Research: Atmospheres, 111(D20), 2006.

[188] McGarragh Greg. Lmie: Optical properties computational routine, 2017.

[189] Michael I Mishchenko and Ping Yang. Far-field lorenz–mie scattering in an absorbing host medium: theoretical formalism and fortran program. Journal of Quantitative Spectroscopy and Radiative Transfer, 205:241–252, 2018.

[190] M. Meinke, G. Müller, J. Helfmann, and M. Friebel. Optical properties of platelets and blood plasma and their influence on the optical behavior of whole blood in the visible to near infrared wavelength range. Journal of biomedical optics, 12(1), 2007.

[191] Shao-Pow Lin, Lihong Wang, Steven L Jacques, and Frank K Tittel. Measurement of tissue optical properties by the use of oblique-incidence optical fiber reflectometry. Applied optics, 36:136–143, 1997.

[192] Ashwini Sood. Particle size distribution control in emulsion polymerization. Journal of Applied Polymer Science, 92:2884–2902, 2004.

[193] Cellulose nanocrystal characterisation. Blue Goose Refineries, 2017.

[194] Tiffany Abitbol and Emily D Cranston. Chiral nematic self-assembly of cellulose nanocrystals in suspensions and solid films. In HANDBOOK OF GREEN MATERIALS: 3 Self-and direct-assembling of bionanomaterials, pages 37–56. World Scientific, 2014.

[195] Konrad W Klockars, Blaise L Tardy, Maryam Borghei, Anurodh Tripathi, Luiz G Greca, and Orlando J Rojas. Effect of anisotropy of cellulose nanocrystal suspensions on stratification, domain structure formation, and structural colors. Biomacromolecules, 19(7):2931–2943, 2018.

[196] James F Snyder, Joshua Steele, Hong Dong, Joshua A Orlicki, Richard S Reiner, and Alan W Rudie. Optical properties of nanocellulose dispersions in water, dimethylformamide and poly(methyl methacrylate). Technical Report ARL-TR-6691, Army Research Laboratory, 2013.

[197] Labsphere. Integrating sphere theory and applications, 2017.

[198] Suvrit Sra Barbero Alvaro. Modular proximal optimization for multidimensional total-variation regularization. arXiv preprint, 1305.6497:1411.0589, 2014.

[199] Alexander V Terekhov, Yakov B Pesin, Xun Niu, Mark L Latash, and Vladimir M Zatsiorsky. An analytical approach to the problem of inverse optimization with additive objective functions: an application to human prehension. Journal of mathematical biology, 61(3):423–453, 2010.

[200] Richard H. Byrd, Mary E. Hribar, and Jorge Nocedal. An interior point algorithm for large-scale nonlinear programming. Society for Industrial and Applied Mathematics, 9:877–900, 1999.

[201] E Stefan Kooij and Bene Poelsema. Shape and size effects in the optical properties of metallic nanorods. Physical Chemistry Chemical Physics, 8(28):3349–3357, 2006.

[202] Kyeong-Seok Lee and Mostafa A El-Sayed. Dependence of the enhanced optical scattering efficiency relative to that of absorption for gold metal nanorods on aspect ratio, size, end-cap shape, and medium refractive index. The Journal of Physical Chemistry B, 109(43):20331–20338, 2005.

[203] Stephanie Beck-Candanedo, Maren Roman, and Derek G Gray. Effect of reaction conditions on the properties and behavior of wood cellulose nanocrystal suspensions. Biomacromolecules, 6(2):1048–1054, 2005.

[204] Paul Mazeron and Stéphane Muller. Light scattering by ellipsoids in a physical optics approximation. Applied optics, 35(19):3726–3735, 1996.

[205] Katia E Peceros, Xiaoda Xu, Shaun R Bulcock, and Michael B Cortie. Dipole- dipole plasmon interactions in gold-on-polystyrene composites. The Journal of Physical Chemistry B, 109(46):21516–21520, 2005.

[206] Eric Jones, Travis Oliphant, Pearu Peterson, et al. SciPy: Open source scientific tools for Python, 2001–.

[207] VA Barbash, OV Yaschenko, and OM Shniruk. Preparation and properties of nanocellulose from organosolv straw pulp. Nanoscale research letters, 12(1):241, 2017.

[208] Rainer Jonas and Luiz F Farah. Production and application of microbial cellulose. Polymer degradation and stability, 59(1-3):101–106, 1998.

[209] Hyung-Joo Lee, Heon-Seok Lee, Junwon Seo, Yong-Hak Kang, Woosuk Kim, and Thomas H-K Kang. State-of-the-art of cellulose nanocrystals and optimal method for their dispersion for construction-related applications. Applied Sciences, 9(3):426, 2019.

[210] Min-Jeong Kim. Single scattering parameters of randomly oriented snow particles at microwave frequencies. Journal of Geophysical Research: Atmospheres, 111, 2006.

[211] D Pavanelli and A Pagliarani. Sw—soil and water: Monitoring water flow, turbidity and suspended sediment load, from an apennine catchment basin, italy. Biosystems engineering, 83(4):463–468, 2002.

[212] Meng Yao, Jun Nan, and Ting Chen. Effect of particle size distribution on turbidity under various water quality levels during flocculation processes. Desalination, 354:116–124, 2014.

APPENDIX A

APPENDIX A. ADDITIONAL TABLES AND FIGURES

A.1 ADDITIONAL TABLES FOR CHAPTER 6

Table A.1.1 Table of estimated and measured mode radius values for Sample set 1 for all SAR-DRM branches

	South		**West**		**North**		**East**	
	Ref., nm	Inv., nm	Ref., nm	Inv., nm	Ref., nm	Inv., nm	Ref., nm	Inv., nm
2	82.09	41.80	82.09	33.00	82.09	32.17	82.09	32.17
3	110.10	86.69	110.10	54.67	110.10	50.51	110.10	52.17
4	198.03	22.51	198.03	173.86	198.03	172.19	198.03	173.02
5	229.33	330.16	229.33	217.20	229.33	213.03	229.33	210.53
6	171.00	168.67	171.00	133.85	171.00	135.52	171.00	135.52
7	70.89	35.71	70.89	32.17	70.89	32.17	70.89	31.34
8	95.07	77.84	95.07	45.51	95.07	41.34	95.07	42.17
9	110.10	101.22	110.10	64.68	110.10	64.68	110.10	65.51
10	127.50	123.53	127.50	212.19	127.50	208.86	127.50	207.19
11	198.03	22.06	198.03	148.85	198.03	149.69	198.03	150.52
12	171.00	203.53	171.00	231.36	171.00	238.03	171.00	125.52
13	70.89	53.20	70.89	32.17	70.89	32.17	70.89	31.34
14	198.03	183.73	198.03	149.69	198.03	155.52	198.03	153.85
15	110.10	91.29	110.10	69.68	110.10	67.18	110.10	68.01
16	229.33	392.63	229.33	211.36	229.33	210.53	229.33	210.53
17	95.07	98.64	95.07	61.34	95.07	58.01	95.07	59.67
18	198.03	287.29	198.03	275.54	198.03	153.02	198.03	155.52
19	198.03	304.14	198.03	168.86	198.03	78.01	198.03	172.19
20	229.33	368.12	229.33	209.69	229.33	212.19	229.33	208.86
21	70.89	180.55	70.89	49.67	70.89	33.00	70.89	34.67
22	95.07	101.25	95.07	62.17	95.07	61.34	95.07	63.01
23	110.10	213.58	110.10	180.52	110.10	77.18	110.10	78.01
24	127.50	523.69	127.50	99.68	127.50	99.68	127.50	100.51
25	198.03	21.93	198.03	153.85	198.03	154.69	198.03	279.70
26	171.00	263.52	171.00	441.39	171.00	377.22	171.00	123.02
27	82.09	283.13	82.09	45.51	82.09	43.84	82.09	46.34
28	198.03	678.91	198.03	289.71	198.03	282.20	198.03	286.37
29	229.33	312.75	229.33	101.35	229.33	328.04	229.33	206.36
30	110.10	282.16	110.10	169.69	110.10	70.51	110.10	71.34
31	171.00	681.00	171.00	135.52	171.00	135.52	171.00	137.18
32	95.07	341.28	95.07	64.68	95.07	162.19	95.07	63.01
33	110.10	342.92	110.10	79.68	110.10	173.86	110.10	78.01
34	127.50	559.55	127.50	100.51	127.50	100.51	127.50	324.71
35	198.03	556.36	198.03	269.70	198.03	266.37	198.03	154.69

Table A.1.2 Table of estimated and measured concentration values for Sample set 1 for all SAR-DRM branches

	South		**West**		**North**		**East**	
	Ref., wt%	Inv., wt%	Ref., wt%	Inv., wt%	Ref., wt%	Inv., wt%	Ref., wt%	Inv., wt%
2	12.97	24.96	12.97	10.52	12.97	16.72	12.97	16.94
3	13.04	14.53	13.04	13.35	13.04	11.86	13.04	14.40
4	10.54	9.97	10.54	16.84	10.54	16.76	10.54	16.97
5	10.68	4.34	10.68	16.90	10.68	13.24	10.68	16.89
6	12.63	4.19	12.63	16.95	12.63	16.97	12.63	16.78
7	12.66	23.38	12.66	5.99	12.66	8.10	12.66	14.11
8	12.75	10.86	12.75	10.82	12.75	10.97	12.75	11.60
9	9.37	9.20	9.37	12.73	9.37	13.74	9.37	12.03
10	12.36	2.65	12.36	15.35	12.36	12.53	12.36	16.70
11	12.67	14.33	12.67	8.20	12.67	12.75	12.67	8.55
12	12.87	2.02	12.87	0.64	12.87	17.00	12.87	0.62
13	7.68	5.81	7.68	5.79	7.68	5.46	7.68	9.57
14	7.64	2.93	7.64	2.04	7.64	2.44	7.64	2.61
15	6.26	3.31	6.26	2.45	6.26	2.94	6.26	3.12
16	5.13	12.50	5.13	0.74	5.13	1.81	5.13	2.30
17	6.12	12.81	6.12	2.45	6.12	2.94	6.12	3.03
18	6.10	24.11	6.10	5.38	6.10	2.07	6.10	2.17
19	4.03	3.76	4.03	1.08	4.03	1.43	4.03	1.57
20	4.03	7.26	4.03	0.73	4.03	2.33	4.03	1.83
21	4.79	1.28	4.79	0.65	4.79	2.60	4.79	1.50
22	4.74	2.44	4.74	1.62	4.74	1.86	4.74	2.00
23	3.57	2.64	3.57	1.72	3.57	2.00	3.57	2.11
24	4.70	5.70	4.70	0.72	4.70	1.11	4.70	1.10
25	4.78	3.15	4.78	1.03	4.78	1.52	4.78	5.10
26	4.87	1.21	4.87	0.63	4.87	0.66	4.87	0.65
27	3.93	1.93	3.93	1.00	3.93	1.24	3.93	1.19
28	3.14	5.45	3.14	3.38	3.14	4.30	3.14	4.69
29	3.21	6.15	3.21	0.69	3.21	2.17	3.21	1.23
30	3.78	3.24	3.78	0.73	3.78	1.07	3.78	1.13
31	3.80	25.00	3.80	0.71	3.80	0.98	3.80	0.81
32	3.78	2.98	3.78	0.88	3.78	1.32	3.78	1.15
33	2.85	2.63	2.85	0.99	2.85	1.21	2.85	1.29
34	3.73	1.89	3.73	0.58	3.73	0.67	3.73	0.98
35	3.79	4.08	3.79	3.16	3.79	4.78	3.79	1.19

A.2 Additional figures for Chapter 7

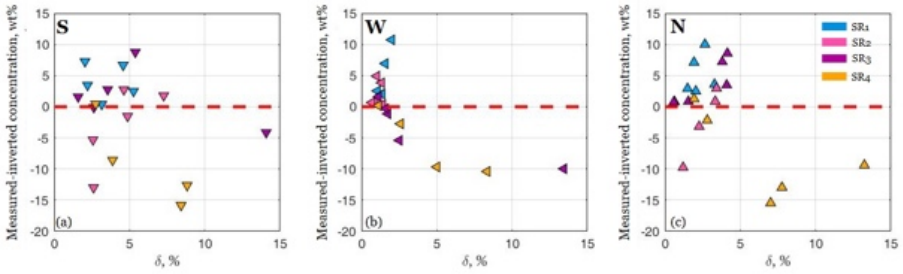

Figure A.2.1 Actual difference between estimated and measured concentration in comparison with δ for different SAR-DRM branches (a-c). Colour corresponds to original samples on the sample set.

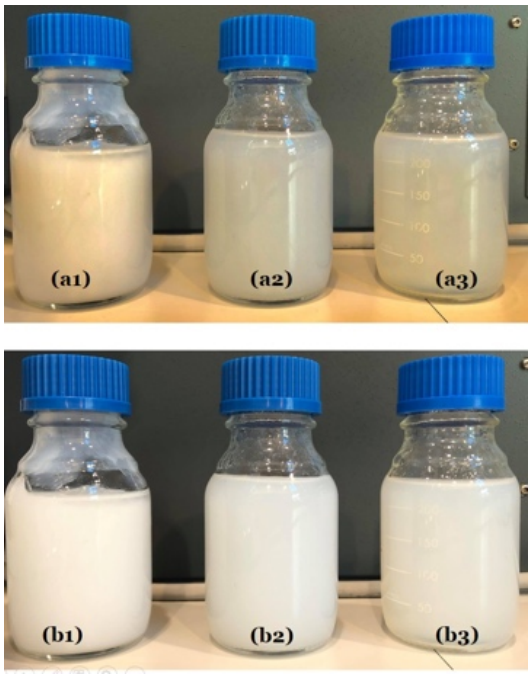

Figure A.2.2 Cellulose nanocrystalline suspensions dilutions (1-3) for (a) BG Ultra, (b) BG Natural.

APPENDIX B

COMPUTATIONAL CODES

B.1 MATLAB CODE FOR MIE -BASED BULK OPTICAL PROPERTIES CALCULATION ROUTINE FOR POLYDISPERSE SYSTEM OF PARTICLES: FORWARD CALCULATION

B.1.1 MAIN FILE

```
%Calculation for scattering and absorption coefficient by
    polydisperse system of particles by using Mie theory.
%Code based on routine from Matzler(2002), which was modified by
    Maria A. Velazco (2006);
clear all; close all; tic
%% Pre-saved sample set parameters
% Param file inputs:
% mode_diam:  mode diameter in nm.
% conc: concentration of solids in wt%.
% sigma_log: distribution width for lognormal distribution
load param.mat
%% Particle size grid
    ..................................................
Dmin = 1; Dmax = 20000;
D = [Dmin:2:Dmax];
%Download refractive indexes for each WL
load refwater.txt
load RI_CLS_interp.txt
den = 1.05;     % particle density g/cm3
den_w = 0.997; % water density g/cm3
%Download refractive indexes for each WL
```

```
lambda1 = refwater(:,1);lambda2 = RI_CLS_interp(:,1);
% Match wavelength of refractive data
w = [lambda2(end):-1:lambda2(1)]'; [lambda,IA, IB1] = intersect(w,
    lambda1);[lambda,IA, IB2] = intersect(w,lambda2);
%Calculate volume fraction
rho_tot = conc * den + (1-conc)*den_w;
phi0 = conc.*rho_tot/den;
phi(:,1)  = phi0 ;
phi(:,2)  = 1-phi0;
phi1  = 1-phi0;

nwater = refwater(IB1,2);            kwater = (refwater(IB1,3));
npsty  = RI_CLS_interp(IB2,2);       kpsty  = (RI_CLS_interp(IB2,3));
n = [npsty nwater]; k = [kpsty kwater];

%Running the Mie script over wavelength range - Loop through the conc
    .
for j = 1:length(conc)
    for i = 1 : length(lambda)
    [scattering, extinction, absorption,scatt_albedo,asymmetry_p,
        scat_prime,df] = Mie_lognormal_function(nwater(i),npsty(i),
        kpsty(i),kwater(i), mode_diam(j), sigma_log(j), lambda(i),
        den, size_range,conc(j),den_w, phi1(j));
    [mew_a_mono,mew_s_mono,g_mono] = calc_optical_props_mono(phi(j,:)
        ,lambda(i),n(i,:),k(i,:),mode_diam(j));
    data.mew_s_mono(i,1) = mew_s_mono;
    data.mew_a_mono(i,1) = mew_a_mono;
    data.g_mono(i,1) = g_mono;
    data.mew_s(i,j) = scattering;
    data.mew_e(i,j) = extinction';
    data.mew_a(i,j) = absorption';
    data.g(i,j) = asymmetry_p';
    data.mew_s_p(i,j) = scat_prime';
    data.scatt_albedo(i,j) = scatt_albedo';
    data.distrib = df';
    data.xrange = size_range';
    data.lambda      = lambda;
    data.diam_mean(:,j) = (mode_diam);
    data.signa_log(:,j) = sigma_log;
    data.conc(:,j) = conc';
    end
end
toc
```

B.1.2 ASSOCIATED FUNCTIONS

```
function [scattering, extinction, absorption,scatt_albedo,asymmetry_p
    , scat_prime,df,x_range, mew_a] = Mie_lognormal_function(nwater,
    npsty,kpsty,kwater, mode_diam, gsd, lambda, den, x_range,conc,
    den_w,phi1)
%The function below computes cross-sections and asymmetry parameters
    for values in the x_range, then integrate over lognormal PSD
%% Set-up the lognormal distribution
Mie_result = [];
asym = [];
x_in_mm = 0.5.*x_range.*10^-6;
med_dia1 = log(0.5.*mode_diam.*10^-6);
df = monomodal_logedit(med_dia1, gsd,x_in_mm);
%% Calculate the efficiencies (Matzler's Mie code):
for i=1:max(size(x_range))
    m = complex(npsty,kpsty)/nwater;
    k    = 2*pi./lambda.*nwater;
    k = k';
    x_coef    = k.*(0.5.*x_range(i));
    result = Mie(m, x_coef);
    eff = result(1:3);
    % add results to the list
    Mie_result = [Mie_result; eff];
    asym = [asym; result(5)];
end
extinction_q = Mie_result(:,1)';
scattering_q = Mie_result(:,2)';
absorbtion_q = Mie_result(:,3)';
%% Account on polydispersity.............
D_int = ((4.*pi.*x_in_mm.^3)./3).*df;
VoP= trapz(x_in_mm,D_int);
num_of_p_per_v = (den_w./(den_w+ den/conc - den))./VoP;

funct_extinction = (extinction_q.*(pi.*x_in_mm.^2)).*df;
cof1 = trapz(x_in_mm,funct_extinction);
Q_extinction = cof1.*num_of_p_per_v;

funct_scattering = (scattering_q.*(pi.*x_in_mm.^2)).*df;
cof1 = trapz(x_in_mm,funct_scattering);
Q_scattering = cof1.*num_of_p_per_v;

funct_absorbtion = (absorbtion_q.*(pi.*x_in_mm.^2)).*df;
cof1 = trapz(x_in_mm,funct_absorbtion);
```

```
Q_absorbtion = cof1.*num_of_p_per_v;

%Calculate abs for water.............
mew_a(:,1) = (4*pi*kwater./(lambda*1.0e-6)) * phi1;
mew_a(:,2) = Q_absorbtion;

%Average asymmetry parameter.........
x_areas = pi.*(x_in_mm.^2);
scats = scattering_q .* x_areas.*num_of_p_per_v.*df;
top = trapz(x_range,(asym .* scats'));
bottom = trapz(x_range,scats);
asymmetry_p = top/bottom;

% Structure outputs
extinction = Q_extinction;
scattering = Q_scattering;
absorption = sum(mew_a);

scat_prime = scattering*(1-asymmetry_p);
scatt_albedo = scattering./extinction;
return
```

```
function [F_temp,F_check] = monomodal_log_function(mode_temp,
    sigma1_temp,diam_range)
% The function returns lognormal distribution of the defined mode
    radius
mean_temp = exp(mode_temp +sigma1_temp^2); %converts mode to mean
F_temp = (1./(diam_range.*sigma1_temp.*sqrt(2*pi))).*exp((-(log(
    diam_range) - log(mean_temp)).^2)./(2*(sigma1_temp.^2)));
F_check = F_temp;
return
```

B.2 MATLAB CODE FOR SPATIALLY RESOLVED DIFFUSE REFLECTANCE: FORWARD CALCULATION

B.2.1 MAIN FILE

```
clear all
close all
% Forward code for Diffuse Approximation based on :
% Source : White light oblique incidence reflectometer for measuring
    absorption and reduced scattering spectra of tissue like turbid
    media

% Written by : Sarra Tiernan 10/12/2013

load param.mat
wave= Sim.wave;
g    = Sim.g;
mus = Sim.mu_s;
mua = Sim.mu_a;

%% ... Define oblique incident light angle....
 tran_angle = 0;
% tran_angle=pi()/4; %angle associated to 45 degrees
% tran_angle=pi()/6; %angle associared to 30 degrees

%% Set source-receiver distances (in mm)
rho_d= [0.3 0.6 0.9 1.2];
n = 1; %Relative refractive index of tissue-air interface. (n=1 for
    matched boundary.)

% Define optical parameter
musp   = mus.*(1-g);          % Reduced scattering coefficient (musp =
     mu_s')
mutr   = musp+mua;            % Total interaction coefficient

% Define diffuse approximation parameter
D = 1./(3.*(mua+musp));        % Diffusion constant
%*0.35 had been removed from the mua term as it has been deemed
    unnessesary as the probe is immersed in the sample

mueff =(mua./D).^0.5;  % Effective attenuation coefficient
a_tr=musp./(mua+musp); %albedo term( which has been added in for the
    equatioj to be able to
```

```
%used in areas where the scattering effect does not completely dominate the
%eqaution

% Account for internal reflection
rd = -1.4399.*n.^-2+0.7099.*n.^-1+0.6681+0.0639.*n; % Eqn. (9) (=1 for matched boundary)
A  = (1+rd)./(1-rd); % Eqn.(8) = the internal reflection at boundary:
zb = 2.*A.*D;        % Extrapolated boundary
z  = 0;              % Depth position of collecting fibre

% Calculate reflectance at diff. distances using Diffuse Approximation
for i = 1 : size(Sim.radius)
    for d = 1 : length(rho_d)
        for j = 1 : length(a_tr)
            R_rho(j) = gaussLagQuad(@DA_Ext_Angular, 128, 1, rho_d(d), z, zb(j,i), a_tr(j,i), mutr(j,i), mueff(j,i), tran_angle);
        end
        Ref(:,d) = R_rho;

    end
    DA_Ext_Angle45.Ref_d1(:,i) = Ref(:,1);
    DA_Ext_Angle45.Ref_d2(:,i) = Ref(:,2);
    DA_Ext_Angle45.Ref_d3(:,i) = Ref(:,3);
    DA_Ext_Angle45.Ref_d4(:,i) = Ref(:,4);
end

figure; plot (wave,DA_Ext_Angle45.Ref_d1);
            title(' reflectance from distance 0.3mm');
            xlabel('\bf Wavelength / nm');
            ylabel('\bf Reflectance');


figure; plot (wave,DA_Ext_Angle45.Ref_d2);
            title(' reflectance from distance 0.6mm');
            xlabel('wavelength /nm');
            ylabel('reflectance');


figure; plot (wave,DA_Ext_Angle45.Ref_d3);
            title(' reflectance from distance 0.9mm');
```

```
71              xlabel('wavelength /nm');
72              ylabel('reflectance');
73
74
75  figure; plot (wave,DA_Ext_Angle45.Ref_d4);
76              title(' reflectance from distance 1.2mm');
77              xlabel('wavelength /nm');
78              ylabel('reflectance');
```

B.2.2 ASSOCIATED FUNCTIONS

```
1   function f = function_DA_Ext_Angular.(y, rho, z, zb, a_tr, mutr,
        mueff, tran_angle)
2   % Calculate reflectance at diff. distances using Eqn. (11),(13)&(18)
3   % Written by : Sarra Tiernan 10/12/2013
4
5   % Source : A diffusion theory model of spatially resolved, steady-
        state diffuse
6   %          reflectance for the noninvasive determination of tissue
        optical
7   %          properties in vivo
8   %          T. J. Farrell and M. S. Patterson
9   %          Medical Physics, Vol. 19, No. 4, page 879-888 (1992)
10  %
11  % Input :
12  % y     - (=mutr*z0) in Eqn. (18) to satisfy the expression form for
        using gaussLagQuad wtype = 1
13  % rho   - Source-Detector fibre core-to-core distance (in mm)
14  % z     - Depth position of collecting fibre
15  % zb    - Extrapolated boundary
16  % a_tr  - Transport albedo (= musp./mutr);
17  % mutr  - Total interaction coefficient
18  % mueff - Effective attenuation coefficient (=(3*mua*mutr).^0.5)
19  % tran_angle - Oblique incident angle.
20
21  delta_x= y./mutr.*sin(tran_angle);
22  delta_z= y./mutr.*cos(tran_angle);
23  r_value=rho-delta_x;
24
25  r1=sqrt((delta_z).^2+r_value.^2);          % Eqn. (11)
26  r2=sqrt((z+delta_z+2*zb).^2+r_value.^2); % Eqn. (13)
27
28  % Calculate Eqn. (19) in part to reduce chance of errors
29  Term0 = a_tr./4/pi();
```

```
Term1 = (delta_z).*mueff.*exp(-mueff.*r1)./(r1.^2);
Term2 = (delta_z).*(exp(-mueff*r1)./(r1.^3));
Term3 = (z+(delta_z)+2*zb).*(mueff.*exp(-mueff*r2)./r2.^2);
Term4 = (z+(delta_z)+2*zb).*exp(-mueff*r2)./(r2.^3);

f=(Term0.*Term1)+(Term0.*Term2)+(Term0.*Term3)+(Term0.*Term4);
```

B.3 MATLAB CODE FOR INVERSION ALGORITHM

B.3.1 MAIN FILE

```
clear all; close all; clc; tic
%The following script performs the inversion of the SAR-DRM spectra by providing the spectra solution, that corresponds to global minima between measured and simulated spectra.
% Written by: D. Stoliaskaia, 2019

%.....MAIN OUTPUTS.............
%Fdelta_mono: inversion error from Step 1 (monodisperse)
%Coeff_after_opt_Step1_rescaled: estimated mode radius and concentration
%Fdelta_poly: inversion error from Step 2 (polydisperse)
%Coeff_after_opt_Step2_rescaled: estimated mode radius, distribution width and concentration

%% Pre-saved sample set parameters (from param.mat)
% SAMPLENAMES: 1xn numerical vector of sample names. In the current research, the sample name is represented by a number that consists of the original sample name and its dilution degree (e.g SN14 corresponds to Sample 1 diluted 4 times from the original concentration).
% EXPERIMENT_NAME: corresponds to the raw data folder indicator.
load paramEXP17.mat
%% Inversion parameters
material = 'PS';          % type of material used in the method: CNC (cellulose nanocrystals) and PS (polystyrene)
%% SAR-DRM parameters
branches_list = [1,2,3,4];% Fibres branches: S(1);, W(2); N(3); E(4);
WL = 'UV';                % type of spectrometer: UV or NIR
ANGLE = '00';             % emmitance angle: 00, 30, 45
distan = '2to4';          % which S-R distances used in the inversion: 1to4 or 2to4.
type_of_wavegrid = 'SARDRM';% wavelength grid either linear (LIN) of supplied from the spectrometer (SARDRM)
%% Input spectra\Output save parameters
DIRNAME_SARDRM_LOAD = '/Users/dariastoliarskaia/Dropbox/PhD/data_example/IO3_postpross/proxTV/proxTV_results_ExpAug17_upd/';
savetofolder_name = '/Users/dariastoliarskaia/Dropbox/PhD/inverted_results/RESULTS_EXP17/';
```

```
26 nameoffilebegin = 'INV_FINAL_RUN_UNIFY_EXP17_branch'; % Begining of
       the output filename/custom !! must end with "_branch" as it
       indicates the SAR-DRM branch used
27 %% Begin the parameters estimation
       .....

28 for branch = branches_list   %loop over SAR-DRM branches
29     for SAMPLE = 1:length(SAMPLENAMES) %loop over selected samples
30         %% Loading/pre-computing the OP from the Mie theory
31         [S2,A2,asym,D,lambda,den_w,den_part, kwater,coef_1,coef_2] =
               tech_function_load_pre_computed_BOP(WL, material,
               type_of_wavegrid);
32         %% Loading the SAR-DRM data for inversion
33         [SAMPLES] = tech_function_SARDRM_load(ANGLE,WL,
               DIRNAME_SARDRM_LOAD,coef_1,coef_2,SAMPLENAMES(SAMPLE),
               EXPERIMENT_FOLDER_NAME,branch);
34         %% Step 1: Randomiser & inversion of mode diameter and conc
35         % Constrains for Step 1
36         mode_in_nm_min1 = 50; mode_in_nm_max1 = 1300; conc_min =
               0.005; conc_max = 0.25; sigma = 0.1; %fixed for now while
                searching for mode and sigma
37         % Run the minima pre-location
38         [F_randomiser,mode_rand_list,conc_rand_list,count_rand_total,
               Coeff_after_prelocation_Step1,F_pre_location] =
               run_pre_location_start_point(sigma,lambda,D,den_w,
               den_part,S2,asym,A2,ANGLE, SAMPLES, distan,
               mode_in_nm_min1,mode_in_nm_max1,conc_min,conc_max,kwater)
               ;
39         % Run the inversion
40         [mode_in_mm_minscaled,mode_in_mm_maxscaled,conc_min_scaled,
               conc_max_scaled] = rescale_constraints_step_1(
               mode_in_nm_min1,mode_in_nm_max1,conc_min,conc_max);
41         [Coeff_after_opt_Step_mono,Coeff_after_opt_Step1_rescaled,
               Fdelta_mono] = run_inversion_fmincon_step1mono(
               Coeff_after_prelocation_Step1,sigma,lambda,D,den_w,
               den_part,S2,asym,A2,ANGLE, SAMPLES, distan,
               mode_in_nm_min1,mode_in_nm_max1,conc_min,conc_max, kwater
               ,mode_in_mm_minscaled,mode_in_mm_maxscaled,
               conc_min_scaled,conc_max_scaled);
42         %% Step 2: Re-assigment of the constrains
43         sigma_min = 0.1;
44         sigma_max = 1;
```

```
45          [mode_in_nm_min2scaled,mode_in_nm_max2scaled,mode_in_nm_min2,
                mode_in_nm_max2,conc_min2scaled,conc_max2scaled,conc_min2
                ,conc_max2,sigma_start_point,sigma_min_scaled,
                sigma_max_scaled,Coeff_after_prelocation_Step1_rescaled]
                = redefine_constrains_step2_wide(
                Coeff_after_opt_Step1_rescaled,mode_in_nm_max1,
                mode_in_nm_min1,conc_min,conc_max, sigma, sigma_min,
                sigma_max);
46          % Run the inversion of mode diameter/conc/distribution width
47          [Coeff_after_opt_Step2,Coeff_after_opt_Step2_rescaled,
                Fdelta_poly] = run_inversion_fmincon_step2poly(
                Coeff_after_prelocation_Step1_rescaled,lambda,D,den_w,
                den_part,S2,asym,A2,ANGLE, SAMPLES, distan,
                mode_in_nm_min2,mode_in_nm_max2,conc_min2,conc_max2,
                sigma_min, sigma_max, kwater,mode_in_nm_min2scaled,
                mode_in_nm_max2scaled,conc_min2scaled,conc_max2scaled,
                sigma_start_point,sigma_min_scaled,sigma_max_scaled);
48          % Remarks
49          toc
50          elapsedTime = (toc/60);
51          disp(['Inversion for Sample ', num2str(SAMPLENAMES(SAMPLE)),'
                 is finished in ',num2str(elapsedTime), ' with delta = '
                , num2str(Fdelta_poly)]);
52          nameoffile = [savetofolder_name,nameoffilebegin,num2str(
                branch),'_Idiff_SN',num2str(SAMPLENAMES(SAMPLE)),'_',
                ANGLE,'_',distan,WL,'_',num2str(count_rand_total)];
53          save([nameoffile,'.mat'])
54      end
55  end
```

B.3.2 Associated functions

Functions for pre-computing the OP and loading SAR-DRM

```
1   function [S2,A2,asym,D,lambda_exp,den_w,den_part, kwater,coef_1,
        coef_2] = tech_function_load_pre_computed_BOP(WL, material,
        type_of_wavegrid)
2   %The function below:
3   %- checking if the optical properties for a single spherical particle
        of selected material were already pre-computed;
4   %- in not, initiates the calculation of the optical properties and
        saves the corresponding .mat file.
5   %- loading wavelength range
6   % OUTPUTS:
```

```
% Preamble: n = length of size range; m = length of wavelength range;
% S2: n x m matrix of scattering efficiency;
% A2: n x m matrix of absorption efficiency;
% asym: n x m matrix of asymmetry parameter;
% den_part,den_w: density of the material and medium
% kwater: imaginary part of RI water;
%% Particle size grid
    ..................................................
SEP = '/';
Dmin = 1; Dmax = 15000;
D = [Dmin:2:Dmax];
if strcmp(type_of_wavegrid, 'SARDRM')
    [lambda_exp,coef_1,coef_2] = loader_WL(type_of_wavegrid,WL);  %
       wavelength loader from the spectrometer; coef_1,coef_2 -
       first and last wavelength
elseif strcmp(type_of_wavegrid, 'LIN')
    lambda_exp = [400:1:1850];
    coef_1 = lambda_exp(1);
    coef_2 = lambda_exp(end);
end
% Download refractive index for material/medium
load (['sub_f_INV',SEP,'refwater.txt'])
den_w = 0.997;                          % water density    g/cm3
if (strcmp(material, 'CNC'))
    load (['sub_f_INV',SEP,'RI_CLS_interp.txt']);
    den_part = 1.5;                          % particle density g/cm3
    Ref_ind_material = RI_CLS_interp; % RI of the material
elseif (strcmp(material, 'PS'))
    load (['sub_f_INV',SEP,'Ref_PS.txt']);
    den_part = 1.05;                           % particle density g/cm3
    Ref_ind_material = Ref_PS;          % RI of the material
end

% Match RI and the wavelength range
lambda2 = [Ref_ind_material(1,1):0.01:Ref_ind_material(end,1)];
lambda1 = [refwater(1,1):0.01:refwater(end,1)];

Ref_ind_material_interp = interp1(Ref_ind_material(:,1),
    Ref_ind_material(:,[1:3]),lambda2,'spline');
refwater_interp = interp1(refwater(:,1), refwater(:,[1:3]),lambda1,'
    spline');

[B, ix] = ismember(round((100.*lambda_exp)),round((100.*lambda1)));
```

```
45 [B, iy] = ismember(round((100.*lambda_exp)),round((100.*lambda2)));
46 [lambda_exp1,IA, IB1] = intersect(lambda_exp,lambda1);
47 [lambda_exp1,IA, IB2] = intersect(lambda_exp,lambda2);
48 % Find refractive index - ! text files "Ref_PS" and "Refwater" have
       to be in the folder to make sure we have a correct list of RI
49 nwater = refwater_interp(ix,2);    kwater = (refwater_interp(ix,3));
50 npsty  = Ref_ind_material_interp(iy,2);       kpsty  = (
       Ref_ind_material_interp(iy,3));
51 %% Optical properties for a spherical particles
52 CHECKNAME = ['OP_for_',WL,'_', material,'_',num2str(length(lambda_exp
       )),'.mat'];
53 if exist(CHECKNAME, 'file') == 2
54     load(CHECKNAME)
55 else
56 [S2,A2,asym] = scatt_cross_s_no_conc(D, nwater, npsty, kpsty,
       lambda_exp);%calling Thennadil et. al. code
57 save(CHECKNAME, 'S2','A2','asym');
58 end
```

```
1 function [lambda_exp,coef_1,coef_2] = loader_WL(type_of_wavegrid,WL)
2 if (strcmp(type_of_wavegrid, 'SARDRM'))
3     if (strcmp(WL, 'UV'))
4         load('waveUV.mat')
5         coef_1 = 871; coef_2 = 2519;
6         lambda_exp1 = waveUV(coef_1:coef_2,:);
7         lambda_exp = lambda_exp1(1:2:end,1);
8     elseif (strcmp(WL, 'NIR'))
9         load('waveNIR.mat')
10        coef_1 = 126; coef_2 = 398;
11        lambda_exp1 = waveNIR(coef_1:coef_2,1);
12        lambda_exp = lambda_exp1(1:2:end,1);
13    end
14 elseif (strcmp(type_of_wavegrid, 'LIN'))
15        lambda_exp = [400:1:1850]';
16 end
17
18 end
```

```
1 function  [SAMPLES] = tech_function_SARDRM_load(ANGLE,WL,
       DIRNAME_SARDRM_LOAD,coef_1,coef_2,SAMPLENAME,
       EXPERIMENT_FOLDER_NAME,branch)
2 %The function below:
3 % - loads corresponding to the sample Idiff and Bdiff after smoothing
       ;
```

```
% - re-scales both;
%% Data loading
if ((strcmp(ANGLE, '00'))&&(strcmp(WL, 'UV')) || ((strcmp(ANGLE, '00'
    ))&&(strcmp(WL, 'NIR'))|| ((strcmp(ANGLE, '30'))&&(strcmp(WL, 'UV
    '))))))
    filenameProxTV = [DIRNAME_SARDRM_LOAD,'proxTV_for_SN_',num2str(
        SAMPLENAME),'_',WL,'_R1_',ANGLE,'_exp_',num2str(
        EXPERIMENT_FOLDER_NAME),'.txt'];
    proxTV_data_R1 = dlmread(filenameProxTV);
    filenameProxTV = [DIRNAME_SARDRM_LOAD,'proxTV_for_SN_',num2str(
        SAMPLENAME),'_',WL,'_R2_',ANGLE,'_exp_',num2str(
        EXPERIMENT_FOLDER_NAME),'.txt'];
    proxTV_data_R2 = dlmread(filenameProxTV);
    filenameProxTV = [DIRNAME_SARDRM_LOAD,'proxTV_for_SN_',num2str(
        SAMPLENAME),'_',WL,'_R3_',ANGLE,'_exp_',num2str(
        EXPERIMENT_FOLDER_NAME),'.txt'];
    proxTV_data_R3 = dlmread(filenameProxTV);
    filenameProxTV = [DIRNAME_SARDRM_LOAD,'proxTV_for_SN_',num2str(
        SAMPLENAME),'_',WL,'_R4_',ANGLE,'_exp_',num2str(
        EXPERIMENT_FOLDER_NAME),'.txt'];
    proxTV_data_R4 = dlmread(filenameProxTV);

    SAMPLE_R1I = proxTV_data_R1([coef_1:coef_2],[1:4]);
    SAMPLE_R2I = proxTV_data_R2([coef_1:coef_2],[1:4]);
    SAMPLE_R3I = proxTV_data_R3([coef_1:coef_2],[1:4]);
    SAMPLE_R4I = proxTV_data_R4([coef_1:coef_2],[1:4]);

    SAMPLE_R1B = proxTV_data_R1([coef_1:coef_2],[5:end]);
    SAMPLE_R2B = proxTV_data_R2([coef_1:coef_2],[5:end]);
    SAMPLE_R3B = proxTV_data_R3([coef_1:coef_2],[5:end]);
    SAMPLE_R4B = proxTV_data_R4([coef_1:coef_2],[5:end]);
end
%% Data re-scaling
    tempSAMPLE_R1_I  = mean((SAMPLE_R1I(1:2:end,[branch])),2);
    tempSAMPLE_R2_I  = mean((SAMPLE_R2I(1:2:end,[branch])),2);
    tempSAMPLE_R3_I  = mean((SAMPLE_R3I(1:2:end,[branch])),2);
    tempSAMPLE_R4_I  = mean((SAMPLE_R4I(1:2:end,[branch])),2);

    SAMPLES.SAMPLE_R1_I  = tempSAMPLE_R1_I./max(tempSAMPLE_R1_I(:));
    SAMPLES.SAMPLE_R2_I  = tempSAMPLE_R2_I./max(tempSAMPLE_R2_I(:));
    SAMPLES.SAMPLE_R3_I  = tempSAMPLE_R3_I./max(tempSAMPLE_R3_I(:));
    SAMPLES.SAMPLE_R4_I  = tempSAMPLE_R4_I./max(tempSAMPLE_R4_I(:));

```

```
    SAMPLES.SAMPLE_R1_B   = mean((SAMPLE_R1B(1:2:end,[branch])),2);
    SAMPLES.SAMPLE_R2_B   = mean((SAMPLE_R2B(1:2:end,[branch])),2);
    SAMPLES.SAMPLE_R3_B   = mean((SAMPLE_R3B(1:2:end,[branch])),2);
    SAMPLES.SAMPLE_R4_B   = mean((SAMPLE_R4B(1:2:end,[branch])),2);


    SAMPLES.SAMPLE_R1_I_for_scale   = tempSAMPLE_R1_I;
    SAMPLES.SAMPLE_R2_I_for_scale   = tempSAMPLE_R2_I;
    SAMPLES.SAMPLE_R3_I_for_scale   = tempSAMPLE_R3_I;
    SAMPLES.SAMPLE_R4_I_for_scale   = tempSAMPLE_R4_I;

end
```

FUNCTIONS FOR STEP 1 OF INVERSION ROUTINE

```
function [F_randomiser,mode_rand_list,conc_rand_list,count_rand_total
    ,Coeff_after_prelocation_Step1,F_pre_location] =
    run_pre_location_start_point(sigma,lambda,D,den_w,den_part,S2,
    asym,A2,ANGLE, SAMPLES, distan,mode_in_nm_min1,mode_in_nm_max1,
    conc_min,conc_max,kwater)
%The function below:
%calls generator of random mode radius and concentration;
%computes BOP and SRDR for the corresponding combination of
    parameters;
%Measures goodness of the fit with delta;
%Iterates until 5 combinations with delta >15% found or after 500
    iterations;
num_of_low_delta_rand = 0;
count_rand_total = 0;   %record of how many iterations needed

while (num_of_low_delta_rand < 5)&&(500 > count_rand_total)
    count_rand_total = count_rand_total+1;
    [mode_rand,conc_rand] = return_rand_values_for_2var(
        mode_in_nm_min1,mode_in_nm_max1,conc_min,conc_max);
    mode_rand_list_all(count_rand_total,:) = mode_rand;
    conc_rand_list_all(count_rand_total,:) = conc_rand;
    Coeff_from_rand(count_rand_total,:) = [mode_rand,conc_rand];
    F_randomiser_iter = error_calculation_step1mono(Coeff_from_rand(
        count_rand_total,:),sigma,lambda,D,den_w,den_part,S2,asym,A2,
        ANGLE, SAMPLES, distan,mode_in_nm_min1,mode_in_nm_max1,
        conc_min,conc_max,kwater);
    F_randomiser_all(count_rand_total,:) = F_randomiser_iter;
    if F_randomiser_iter <= 15
        num_of_low_delta_rand= num_of_low_delta_rand+1;
```

```
            F_randomiser(num_of_low_delta_rand,:) = F_randomiser_iter;
            mode_rand_list(num_of_low_delta_rand,:) = mode_rand;
            conc_rand_list(num_of_low_delta_rand,:) = conc_rand;

        end
    end
    if size(F_randomiser,1)<5
        F_randomiser = F_randomiser_all;
        mode_rand_list = mode_rand_list_all;
        conc_rand_list = conc_rand_list_all;
    end
        [val,idx] = min(F_randomiser(:));
        F_pre_location = val;
        [index, col] = find(F_randomiser==val);
        mode1_tempscales = mode_rand_list(index,1);
        conc1_tempscales = conc_rand_list(index,1);
        Coeff_after_prelocation_Step1 = [mode1_tempscales,
            conc1_tempscales];
```

```
function [mode_rand,conc_rand] = return_rand_values_for_2var(
    mode_in_mm_min1,mode_in_mm_max1, conc_min, conc_max)

mode_in_mm_min1scaled = round(((mode_in_mm_min1 - mean(
    mode_in_mm_min1:0.01:mode_in_mm_max1))./(mode_in_mm_max1-
    mode_in_mm_min1)).*100);
mode_in_mm_max1scaled = round(((mode_in_mm_max1 - mean(
    mode_in_mm_min1:0.01:mode_in_mm_max1))./(mode_in_mm_max1-
    mode_in_mm_min1)).*100);

conc_min1scaled = round(((conc_min - mean(conc_min:0.001:conc_max))
    ./(conc_max-conc_min)).*100);
conc_max1scaled = round(((conc_max - mean(conc_min:0.001:conc_max))
    ./(conc_max-conc_min)).*100);

mode_rand = randi([mode_in_mm_min1scaled mode_in_mm_max1scaled],1,1)
    ./100;
conc_rand = (randi([conc_min1scaled conc_max1scaled],1,1))./100;

end
```

```
%
    ..........................................................................
```

```
function [Coeff_after_opt_Step1,Coeff_after_opt_Step1_rescaled,
    F_randomiser_iter_Step1] = run_inversion_fmincon_step1mono(
    Coeff_after_prelocation_Step1,sigma,lambda,D,den_w,den_part,S2,
    asym,A2,ANGLE, SAMPLES, distan,mode_in_nm_min1,mode_in_nm_max1,
    conc_min,conc_max,kwater,mode_in_nm_min1scaled,
    mode_in_nm_max1scaled,conc_min_scaled,conc_max_scaled)
%The function below:
% - runs the fmincon optimiser
A = [];
b = [];
Aeq = [];
beq = [];
TolF = 10^-6;

opt = optimoptions(@fmincon,'Algorithm','interior-point','TolFun',
    TolF, 'TolX',10^-6,'MaxFunEvals',1e6,'display','final-detailed');
lb = [mode_in_nm_min1scaled,conc_min_scaled]'; % min boundaries for
    the search
ub = [mode_in_nm_max1scaled,conc_max_scaled]'; % max boundaries for
    the search

h = @(x)error_calculation_step1mono(x,sigma,lambda,D,den_w,den_part,
    S2,asym,A2,ANGLE, SAMPLES, distan,mode_in_nm_min1,mode_in_nm_max1
    ,conc_min,conc_max,kwater);
x = fmincon(h,Coeff_after_prelocation_Step1,A,b,Aeq,beq,lb,ub,[],opt)
    ;
mean_temp = x(1);
conc_temp = x(2);
Coeff_after_opt_Step1 = [mean_temp,conc_temp];
F_randomiser_iter_Step1 = error_calculation_step1mono(
    Coeff_after_opt_Step1,sigma,lambda,D,den_w,den_part,S2,asym,A2,
    ANGLE, SAMPLES, distan,mode_in_nm_min1,mode_in_nm_max1,conc_min,
    conc_max,kwater);

mode_inverted_mono = Coeff_after_opt_Step1(1)*(mode_in_nm_max1-
    mode_in_nm_min1) + mean(mode_in_nm_min1:0.0001:mode_in_nm_max1);
conc_inverted_mono = Coeff_after_opt_Step1(2)*(conc_max-conc_min) +
    mean(conc_min:0.0001:conc_max);

Coeff_after_opt_Step1_rescaled = [mode_inverted_mono,
    conc_inverted_mono];
```

```
function F = error_calculation_step1mono(x,sigma,lambda,D,den_w,den,
    S2,asym,A2,ANGLE, SAMPLES, distan,mode_in_nm_min1,mode_in_nm_max1
    ,conc_min,conc_max,kwater)
%The function below: [used in both, fmincon and following computation
     of the found solution]
%-computes BOP and SAR-DRM
%-re-scales the resulted SAR-DRM
%-computes I_sim
%-evaluates delta

mode1_tempscales = x(1);
conc_tempscales = x(2);
% Scale back to the actual units
mode_temp = mode1_tempscales*(mode_in_nm_max1-mode_in_nm_min1) + mean
    (mode_in_nm_min1:0.0001:mode_in_nm_max1);
conc_temp = conc_tempscales*(conc_max-conc_min) + mean(conc_min
    :0.0001:conc_max);
% Compute BOP and SARDRM
[TempPSD] = monomodal_log_function(log(mode_temp), sigma,D);
[mew_s,asym_par,scat_prime,mew_a] =calculate_scattering_coeff_3var(
    conc_temp,lambda, TempPSD,D,den_w,den,S2,asym,A2,kwater);
[DA_Ext_Angle45] = DA_Forward_ANG(mew_s,asym_par,mew_a,lambda, ANGLE)
    ;

if (strcmp(ANGLE, '00'))
    %Re-scaling
    SAMPLE_R1_TEMP_SC = (DA_Ext_Angle45.Ref_d1);
    SAMPLE_R2_TEMP_SC = (DA_Ext_Angle45.Ref_d2);
    SAMPLE_R3_TEMP_SC = (DA_Ext_Angle45.Ref_d3);
    SAMPLE_R4_TEMP_SC = (DA_Ext_Angle45.Ref_d4);

    tempSAMPLE_R1_TEMP = SAMPLE_R1_TEMP_SC.*SAMPLES.SAMPLE_R1_B;
    tempSAMPLE_R2_TEMP = SAMPLE_R2_TEMP_SC.*SAMPLES.SAMPLE_R2_B;
    tempSAMPLE_R3_TEMP = SAMPLE_R3_TEMP_SC.*SAMPLES.SAMPLE_R3_B;
    tempSAMPLE_R4_TEMP = SAMPLE_R4_TEMP_SC.*SAMPLES.SAMPLE_R4_B;

    SAMPLE_R1_TEMP  = tempSAMPLE_R1_TEMP./max(tempSAMPLE_R1_TEMP(:));
    SAMPLE_R2_TEMP  = tempSAMPLE_R2_TEMP./max(tempSAMPLE_R2_TEMP(:));
    SAMPLE_R3_TEMP  = tempSAMPLE_R3_TEMP./max(tempSAMPLE_R3_TEMP(:));
    SAMPLE_R4_TEMP  = tempSAMPLE_R4_TEMP./max(tempSAMPLE_R4_TEMP(:));

    F_ersq(1) = abs(sum((SAMPLES.SAMPLE_R1_I - SAMPLE_R1_TEMP).*100./
        SAMPLES.SAMPLE_R1_I)./length(lambda));
```

```
36      F_ersq(2) = abs(sum((SAMPLES.SAMPLE_R2_I - SAMPLE_R2_TEMP).*100./
            SAMPLES.SAMPLE_R2_I)./length(lambda));
37      F_ersq(3) = abs(sum((SAMPLES.SAMPLE_R3_I - SAMPLE_R3_TEMP).*100./
            SAMPLES.SAMPLE_R3_I)./length(lambda));
38      F_ersq(4) = abs(sum((SAMPLES.SAMPLE_R4_I - SAMPLE_R4_TEMP).*100./
            SAMPLES.SAMPLE_R4_I)./length(lambda));
39      if (strcmp(distan, '1to4'))
40          F_ersq(5) = sum(F_ersq(1)+F_ersq(2)+F_ersq(3)+F_ersq(4))/4;
41          F = F_ersq(5);
42      elseif (strcmp(distan, '2to4'))
43          F_ersq(5) = sum(F_ersq(2)+F_ersq(3)+F_ersq(4))/3;
44          F = F_ersq(5);
45      end
46  elseif (strcmp(ANGLE, '30')&&strcmp(distan, '2to4')) || (strcmp(ANGLE
        , '45')&&strcmp(distan, '2to4'))
47      SAMPLE_R1_TEMP_SC = (DA_Ext_Angle45.Ref_d1);
48      SAMPLE_R2_TEMP_SC = (DA_Ext_Angle45.Ref_d2);
49      SAMPLE_R3_TEMP_SC = (DA_Ext_Angle45.Ref_d3);
50      SAMPLE_R4_TEMP_SC = (DA_Ext_Angle45.Ref_d4);
51
52      tempSAMPLE_R1_TEMP = SAMPLE_R1_TEMP_SC.*SAMPLES.SAMPLE_R1_B;
53      tempSAMPLE_R2_TEMP = SAMPLE_R2_TEMP_SC.*SAMPLES.SAMPLE_R2_B;
54      tempSAMPLE_R3_TEMP = SAMPLE_R3_TEMP_SC.*SAMPLES.SAMPLE_R3_B;
55      tempSAMPLE_R4_TEMP = SAMPLE_R4_TEMP_SC.*SAMPLES.SAMPLE_R4_B;
56
57      SAMPLE_R1_TEMP  = tempSAMPLE_R1_TEMP./max(tempSAMPLE_R1_TEMP(:));
58      SAMPLE_R2_TEMP  = tempSAMPLE_R2_TEMP./max(tempSAMPLE_R2_TEMP(:));
59      SAMPLE_R3_TEMP  = tempSAMPLE_R3_TEMP./max(tempSAMPLE_R3_TEMP(:));
60      SAMPLE_R4_TEMP  = tempSAMPLE_R4_TEMP./max(tempSAMPLE_R4_TEMP(:));
61
62      F_ersq(1) = sum((SAMPLES.SAMPLE_R1_I - SAMPLE_R1_TEMP)./SAMPLES.
            SAMPLE_R1_I)./length(lambda);
63      F_ersq(2) = sum((SAMPLES.SAMPLE_R2_I - SAMPLE_R2_TEMP)./SAMPLES.
            SAMPLE_R2_I)./length(lambda);
64      F_ersq(3) = sum((SAMPLES.SAMPLE_R3_I - SAMPLE_R3_TEMP)./SAMPLES.
            SAMPLE_R3_I)./length(lambda);
65      F_ersq(4) = sum((SAMPLES.SAMPLE_R4_I - SAMPLE_R4_TEMP)./SAMPLES.
            SAMPLE_R4_I)./length(lambda);
66      if (strcmp(distan, '1to4'))
67          F_ersq(5) = sum(F_ersq(1)+F_ersq(2)+F_ersq(3)+F_ersq(4));
68          F = F_ersq(5);
69      elseif (strcmp(distan, '2to4'))
70          F_ersq(5) = sum(F_ersq(2)+F_ersq(3)+F_ersq(4))/4;
```

```
71          F = F_ersq(5);
72      elseif (strcmp(distan, '1to8'))
73          F_ersq(5) = sum(F_ersq(2)+F_ersq(3)+F_ersq(4))/3;
74          F = F_ersq(5);
75      end
76  end
77  end
```

FUNCTIONS FOR STEP 2 OF INVERSION ROUTINE

```
1  %
       ....................................................................

2  function [mode_in_nm_min2scaled,mode_in_nm_max2scaled,mode_in_nm_min2
       ,mode_in_nm_max2,conc_min2scaled,conc_max2scaled,conc_min2,
       conc_max2,sigma_start_point,sigma_min_scaled,sigma_max_scaled,
       Coeff_after_prelocation_Step1_rescaled] =
       redefine_constrains_step2_wide(Coeff_after_opt_Step1_rescaled,
       mode_in_nm_max1,mode_in_nm_min1,conc_min,conc_max, sigma,
       sigma_min, sigma_max)
3
4
5  %The function below:
6  %- re-adjust the search constraints for mode diameter and
       concentration
7  result_mode2 = Coeff_after_opt_Step1_rescaled(1);
8  result_conc2 = Coeff_after_opt_Step1_rescaled(2);
9
10 mode_in_nm_min2 = result_mode2-500;
11 if (mode_in_nm_min2 <50)
12     mode_in_nm_min2 = 50;
13 else
14 end
15
16 mode_in_nm_max2 = result_mode2+500;
17 if (mode_in_nm_max2 >1300)
18     mode_in_nm_max2 = 1300;
19 else
20 end
21
22
23
24 conc_min2 = result_conc2-0.05;
25 if (conc_min2 <0.005)
```

```
26      conc_min2 = 0.005;
27  else
28  end
29
30  conc_max2 = result_conc2+0.05;
31  if (conc_max2 >0.25)
32      conc_max2 = 0.25;
33  else
34  end
35
36
37  sigma_start_point = (sigma - mean(sigma_min:0.0001:sigma_max))./(
        sigma_max-sigma_min);
38  sigma_min_scaled = (sigma_min - mean(sigma_min:0.0001:sigma_max))./(
        sigma_max-sigma_min);
39  sigma_max_scaled = (sigma_max - mean(sigma_min:0.0001:sigma_max))./(
        sigma_max-sigma_min);
40
41  mode_starting_point2 = (result_mode2 - mean(mode_in_nm_min1:0.0001:
        mode_in_nm_max1))./(mode_in_nm_max1-mode_in_nm_min1);
42  mode_in_nm_min2scaled = (mode_in_nm_min2 - mean(mode_in_nm_min1
        :0.0001:mode_in_nm_max1))./(mode_in_nm_max1-mode_in_nm_min1);
43  mode_in_nm_max2scaled = (mode_in_nm_max2 - mean(mode_in_nm_min1
        :0.0001:mode_in_nm_max1))./(mode_in_nm_max1-mode_in_nm_min1);
44
45  conc_starting_point2 = (result_conc2 - mean(conc_min:0.0001:conc_max)
        )./(conc_max-conc_min);
46  conc_min2scaled = (conc_min2 - mean(conc_min:0.0001:conc_max))./(
        conc_max-conc_min);
47  conc_max2scaled = (conc_max2 - mean(conc_min:0.0001:conc_max))./(
        conc_max-conc_min);
48
49  Coeff_after_prelocation_Step1_rescaled = [mode_starting_point2,
        conc_starting_point2];
50
51  return
```

```
1   function [Coeff_after_opt_Step2,Coeff_after_opt_Step2_rescaled,
        Fdelta_poly] = run_inversion_fmincon_step2poly(
        Coeff_after_opt_Step1,lambda,D,den_w,den,S2,asym,A2,ANGLE,
        SAMPLES, distan, mode_in_nm_min,mode_in_nm_max,conc_min,conc_max,
        sigma_min, sigma_max, kwater,mode_in_nm_min2scaled,
        mode_in_nm_max2scaled,conc_min2scaled,conc_max2scaled,
        sigma_start_point,sigma_min_scaled,sigma_max_scaled)
```

```
%The function below:
% - runs the fmincon optimiser
A = [];
b = [];
Aeq = [];
beq = [];
TolF = 10^-6;

opt = optimoptions(@fmincon,'Algorithm','interior-point','TolFun',
    TolF, 'TolX',10^-6,'MaxFunEvals',1e6,'display','final-detailed');
lb = [mode_in_nm_min2scaled,sigma_min_scaled,conc_min2scaled]';
ub = [mode_in_nm_max2scaled,sigma_max_scaled,conc_max2scaled]';

Coeff_for_Step2 = [Coeff_after_opt_Step1(1),sigma_start_point,
    Coeff_after_opt_Step1(2)];
h2nd = @(x2)error_calculation_step2poly(x2,lambda,D,den_w,den,S2,asym
    ,A2,ANGLE, SAMPLES, distan, mode_in_nm_min,mode_in_nm_max,
    conc_min,conc_max,sigma_min, sigma_max, kwater);
x2 = fmincon(h2nd,Coeff_for_Step2,A,b,Aeq,beq,lb,ub,[],opt);
mean_temp = x2(1);
sigma_temp = x2(2);
conc_temp = x2(3);
Coeff_after_opt_Step2 = [mean_temp,sigma_temp,conc_temp];
Fdelta_poly = error_calculation_step2poly(Coeff_after_opt_Step2,
    lambda,D,den_w,den,S2,asym,A2,ANGLE, SAMPLES, distan,
    mode_in_nm_min,mode_in_nm_max,conc_min,conc_max,sigma_min,
    sigma_max, kwater);


mode_inverted_poly = Coeff_after_opt_Step2(1)*(mode_in_nm_max-
    mode_in_nm_min) + mean(mode_in_nm_min:0.0001:mode_in_nm_max);
sigma_inverted_poly = Coeff_after_opt_Step2(2)*(sigma_max-sigma_min)
    + mean(sigma_min:0.0001:sigma_max);
conc_inverted_poly = Coeff_after_opt_Step2(3)*(conc_max-conc_min) +
    mean(conc_min:0.0001:conc_max);

Coeff_after_opt_Step2_rescaled = [mode_inverted_poly,
    sigma_inverted_poly,conc_inverted_poly];
```

```
function F = error_calculation_step2poly(x2,lambda,D,den_w,den,S2,
    asym,A2,ANGLE, SAMPLES, distan, mode_in_nm_min1,mode_in_nm_max1,
    conc_min,conc_max,sigma_min, sigma_max, kwater)
%The function below: [used in both, fmincon and following computation
     of the found solution]
```

```
%-computes BOP and SAR-DRM
%-re-scales the resulted SAR-DRM
%-computes I_sim
%-evaluates delta
mode2_tempscales = x2(1);
sigma_tempscales = x2(2);
conc2_tempscales = x2(3);
% Scale back to the actual units
mode_temp = mode2_tempscales*(mode_in_nm_max1-mode_in_nm_min1) + mean
    (mode_in_nm_min1:0.0001:mode_in_nm_max1);
sigma_temp = sigma_tempscales*(sigma_max-sigma_min) + mean(sigma_min
    :0.0001:sigma_max);
conc_temp = conc2_tempscales*(conc_max-conc_min) + mean(conc_min
    :0.0001:conc_max);
% Compute BOP and SARDRM
[TempPSD] = monomodal_log_function(log(mode_temp), sigma_temp,D);
[mew_s,asym_par,scat_prime,mew_a] =calculate_scattering_coeff_3var(
    conc_temp,lambda, TempPSD,D,den_w,den,S2,asym,A2,kwater);
[DA_Ext_Angle45] = DA_Forward_ANG(mew_s,asym_par,mew_a,lambda, ANGLE)
    ;

if (strcmp(ANGLE, '00'))
    %Re-scaling
    SAMPLE_R1_TEMP_SC = (DA_Ext_Angle45.Ref_d1);
    SAMPLE_R2_TEMP_SC = (DA_Ext_Angle45.Ref_d2);
    SAMPLE_R3_TEMP_SC = (DA_Ext_Angle45.Ref_d3);
    SAMPLE_R4_TEMP_SC = (DA_Ext_Angle45.Ref_d4);

    tempSAMPLE_R1_TEMP = SAMPLE_R1_TEMP_SC.*SAMPLES.SAMPLE_R1_B;
    tempSAMPLE_R2_TEMP = SAMPLE_R2_TEMP_SC.*SAMPLES.SAMPLE_R2_B;
    tempSAMPLE_R3_TEMP = SAMPLE_R3_TEMP_SC.*SAMPLES.SAMPLE_R3_B;
    tempSAMPLE_R4_TEMP = SAMPLE_R4_TEMP_SC.*SAMPLES.SAMPLE_R4_B;

    SAMPLE_R1_TEMP  = tempSAMPLE_R1_TEMP./max(tempSAMPLE_R1_TEMP(:));
    SAMPLE_R2_TEMP  = tempSAMPLE_R2_TEMP./max(tempSAMPLE_R2_TEMP(:));
    SAMPLE_R3_TEMP  = tempSAMPLE_R3_TEMP./max(tempSAMPLE_R3_TEMP(:));
    SAMPLE_R4_TEMP  = tempSAMPLE_R4_TEMP./max(tempSAMPLE_R4_TEMP(:));

    F_ersq(1) = abs(sum((SAMPLES.SAMPLE_R1_I - SAMPLE_R1_TEMP).*100./
        SAMPLES.SAMPLE_R1_I)./length(lambda));
    F_ersq(2) = abs(sum((SAMPLES.SAMPLE_R2_I - SAMPLE_R2_TEMP).*100./
        SAMPLES.SAMPLE_R2_I)./length(lambda));
```

```
38      F_ersq(3) = abs(sum((SAMPLES.SAMPLE_R3_I - SAMPLE_R3_TEMP).*100./
            SAMPLES.SAMPLE_R3_I)./length(lambda));
39      F_ersq(4) = abs(sum((SAMPLES.SAMPLE_R4_I - SAMPLE_R4_TEMP).*100./
            SAMPLES.SAMPLE_R4_I)./length(lambda));
40
41      if (strcmp(distan, '1to4'))
42          F_ersq(5) = sum(F_ersq(1)+F_ersq(2)+F_ersq(3)+F_ersq(4));
43          F = F_ersq(5)./4;
44      elseif (strcmp(distan, '2to4'))
45          F_ersq(5) = sum(F_ersq(2)+F_ersq(3)+F_ersq(4));
46          F = F_ersq(5)./3;
47      end
48  elseif (strcmp(ANGLE, '30')&&strcmp(distan, '2to4')) || (strcmp(ANGLE
        , '45')&&strcmp(distan, '2to4'))
49      SAMPLE_R1_TEMP_SC = (DA_Ext_Angle45.Ref_d1);
50      SAMPLE_R2_TEMP_SC = (DA_Ext_Angle45.Ref_d2);
51      SAMPLE_R3_TEMP_SC = (DA_Ext_Angle45.Ref_d3);
52      SAMPLE_R4_TEMP_SC = (DA_Ext_Angle45.Ref_d4);
53
54      tempSAMPLE_R1_TEMP = SAMPLE_R1_TEMP_SC.*SAMPLE.SAMPLE_R1_B;
55      tempSAMPLE_R2_TEMP = SAMPLE_R2_TEMP_SC.*SAMPLE.SAMPLE_R2_B;
56      tempSAMPLE_R3_TEMP = SAMPLE_R3_TEMP_SC.*SAMPLE.SAMPLE_R3_B;
57      tempSAMPLE_R4_TEMP = SAMPLE_R4_TEMP_SC.*SAMPLE.SAMPLE_R4_B;
58
59      SAMPLE_R1_TEMP  = tempSAMPLE_R1_TEMP./max(tempSAMPLE_R1_TEMP(:));
60      SAMPLE_R2_TEMP  = tempSAMPLE_R2_TEMP./max(tempSAMPLE_R2_TEMP(:));
61      SAMPLE_R3_TEMP  = tempSAMPLE_R3_TEMP./max(tempSAMPLE_R3_TEMP(:));
62      SAMPLE_R4_TEMP  = tempSAMPLE_R4_TEMP./max(tempSAMPLE_R4_TEMP(:));
63
64      F_ersq(1) = sum(((SAMPLE.SAMPLE_R1_I - SAMPLE_R1_TEMP)./length(
            lambda)).^2);
65      F_ersq(2) = sum(((SAMPLE.SAMPLE_R2_I - SAMPLE_R2_TEMP)./length(
            lambda)).^2);
66      F_ersq(3) = sum(((SAMPLE.SAMPLE_R3_I - SAMPLE_R3_TEMP)./length(
            lambda)).^2);
67      F_ersq(4) = sum(((SAMPLE.SAMPLE_R4_I - SAMPLE_R4_TEMP)./length(
            lambda)).^2);
68      if (strcmp(distan, '1to4'))
69          F_ersq(5) = sum(F_ersq(1)+F_ersq(2)+F_ersq(3)+F_ersq(4));
70          F = F_ersq(5);
71      elseif (strcmp(distan, '2to4'))
72          F_ersq(5) = sum(F_ersq(2)+F_ersq(3)+F_ersq(4));
73          F = F_ersq(5);
```

```
74      elseif (strcmp(distan, '1to8'))
75          F_ersq(5) = sum(F_ersq(2)+F_ersq(3)+F_ersq(4));
76          F = F_ersq(5);
77      end
78  end
79  end
```

B.4 PYTHON CODE FOR FORWARD CALCULATION OF BULK OPTICAL PROPERTIES

B.4.1 MAIN FILE

```
import sys
import math
import pprint
import numpy as np

#The following code is creating the input file for DDSCAT routine and then processes the multiple output .txt file to create a summary of the bulk optical properties.
#Written by D. Stoliarskaia (2018)



####...Enter input parameters here:

def create_C_range(): # Create the range of C-axis of the ellipsoidal particles to run the simulation the loop. If not needed, should be spaced between the same values, microns
        C_size = []
        R_list = []
        NUMSIZE_A = 1
        R_size = np.linspace(0.175, 0.175,num=NUMSIZE_A)
        NUMSIZE_C = 1
        CR_size = np.linspace(0.5, 0.5,num=NUMSIZE_C)
        C_size_index = CR_size
        for R_1 in R_size:
                for C_1 in CR_size:
                        C_size.append(C_1)
                        R_list.append(R_1)
        return C_size,R_list,C_size_index,R_size
def create_AB_range(C_size,R_list, R_size):# Create the range of A and B axis of the ellipsoidal particles (equal to each other), microns
        A_size = []
        B_size = []

        NUMSIZE_A = len(R_size)
        for i in R_size:
                for j in range(5):
```

```
33                              A_size.append(i)
34                              B_size.append(i)
35          return A_size,B_size
36
37 peak_radius = 0.10
38 stddev = 0.1
39
40 target_type = 'ELLIPSOID' # specify type of the particle for DDSCAT
41 folder_type = 'CNC_FORWARD_ORIENT_THESIS_CNC_AR2_ANG_6/'
42
43 #Wavelength range set up, microns
44 WL_first = 0.3965
45 WL_last = 0.6417
46 WL_HOWMANY = 35
47
48 concentration = 0.05
49 statistics = 'poly'
50
51 #
    ..........................................................................
52 den_particles = 1.5
53 den_fluid = 0.997
54 #
    ..........................................................................
55
56 #...Enter datapath
57 datapath_im_water = '/home/njb15196/Desktop/PhD_2nd_code/DDSCAT/'
58 location_base ='/home/njb15196/Desktop/PhD_2nd_code/DDSCAT/
    examples_exp/'
59
60 #
    ..........................................................................
61 #
62 C_size,R_list,C_size_index,R_size= create_C_range()
63 A_size,B_size = create_AB_range(C_size,R_list,R_size)
64
65 # First command - create the ddscat.par and run the simulation
66 # Second command - compile the result from multiple text files
67 import RUN_DDSCAT_abc_k_CNC
68 import RUN_TO_ANALYSE_DDSCAT_range_of_abs_k_CNC
```

B.4.2 ASSOCIATED FUNCTIONS

```
1
2  import os
3  import numpy as np
4  import math
5  import stat
6  import subprocess
7  from shutil import copyfile
8  from shutil import copy2
9
10
11 def create_directory(C_size,target_type, folder_type,location_base):
12         uv = 1
13         preflod = os.path.join(location_base+folder_type)
14         if not os.path.exists(preflod):
15                 os.mkdir(preflod)
16         index = range(0, len(C_size))
17         for i in index:
18                 C_exp = C_size[i]
19                 C_exp_r = round(C_exp,3)
20                 target_name = target_type+'_'+str(C_exp_r)+'_ar_'+str
                       (i)
21                 filename = os.path.join(location_base+folder_type,
                       target_name)
22                 if not os.path.exists(filename):
23                         os.mkdir(filename)
24         return uv
25 def create_file_ddscat(A_size,B_size,C_size,target_type,WL_first,
       WL_last,WL_HOWMANY,folder_type,location_base):
26         index = range(0, len(C_size))
27         for i in index:
28                 A = A_size[i]
29                 B = B_size[i]
30                 C = C_size[i]
31
32                 dipole_space = A*0.04
33                 C_exp_r = round(C,3)
34                 target_name = target_type+'_'+str(C_exp_r)+'_ar_'+str
                       (i)
35                 filename = (location_base+folder_type+target_name+'/
                       ddscat.par')
36
37                 SHAPR1 = int(round(A/dipole_space))
```

```
38 SHAPR2 = int(round(B/dipole_space))
39 SHAPR3 = int(round(C/dipole_space))
40
41 alloc1 = int(float(SHAPR1)+50)
42 alloc2 = int(float(SHAPR2)+50)
43 alloc3 = int(float(SHAPR3)+50)
44
45 def calculate_volume(target_type, A,B,C):
46     if 'ELLIPSOID' in target_type:
47             volume = 1.3333*math.pi*A*B*C
48     if 'CONELLIPS' in target_type:
49             volume = 1.3333*math.pi*A*B*C
50     if 'ONIONSHEL' in target_type:
51             volume = 1.3333*math.pi*B*B*B
52     if 'CYLINDER1' in target_type:
53                 volume = math.pi*(A**2)*C
54     if 'RCTGLPRSM' in target_type:
55                 volume = A*B*C
56     return volume
57 volume = calculate_volume(target_type, A,B,C)
58 pre_radius = (3*volume)/(4*math.pi)
59 radius_first = round((pre_radius**(0.333333)),4)
60 radius_last = radius_first
61 radius_HOWMANY = 1
62 textbody1 = "' ========== Parameter file for v7.3
   ==================='\n'**** Preliminaries ****'\n
   'NOTORQ' = CMDTRQ*6 (DOTORQ, NOTORQ) -- either do
    or skip torque calculations\n'PBCGS2' = CMDSOL*6
    (PBCGS2, PBCGST, GPBICG, QMRCCG, PETRKP) -- CCG
   method\n'GPFAFT' = CMETHD*6 (GPFAFT, FFTMKL) --
   FFT method\n'GKDLDR' = CALPHA*6 (GKDLDR, LATTDR,
   FLTRCD) -- DDA method\n'NOTBIN' = CBINFLAG (
   NOTBIN, ORIBIN, ALLBIN) -- binary output?"
63 textbody2 = "'**** Initial Memory Allocation ****'"
64 textbody3 = (str(alloc1)+' '+str(alloc2) +' '+str(
   alloc3) +' '+'= dimensioning allowance for target
    generation')
65 textbody4 = "'**** Target Geometry and Composition
   ****'"
66 textbody5 = (target_type +' = CSHAPE*9 shape
   directive')
67 textbody6 = (str(SHAPR1) +' '+str(SHAPR2) +' '+ str(
   SHAPR3) +' '+'= shape parameters 1 - 3')
```

```
68 textbody7 = """1          = NCOMP = number of
       dielectric materials\n'../../diel/RI_CLS6.txt' =
       refractive index\n'**** Additional Nearfield
       calculation? ****'\n0 = NRFLD (=0 to skip
       nearfield calc., =1 to calculate nearfield E)\n
       '0.0 0.0 0.0 0.0 0.0 0.0 (fract. extens. of calc.
        vol. in -x,+x,-y,+y,-z,+z)\n**** Error Tolerance
        ****\n1.00e-4 = TOL = MAX ALLOWED (NORM OF |G>=
       AC|E>-ACA|X>)/(NORM OF AC|E>)\n'**** Maximum
       number of iterations ****'\n700      = MXITER \n
       '**** Integration limiter for PBC calculations
       ****'\n1.00e-2 = GAMMA (1e-2 is normal, 3e-3 for
       greater accuracy)\n'**** Angular resolution for
       calculation of <cos>, etc. ****'\n0.5 = ETASCA (
       number of angles is proportional to [(3+x)/ETASCA
       ]^2 )\n'**** Wavelengths (micron) ****'"""
69 textbody8 = (str(WL_first)+' '+str(WL_last)+' '+str(
       WL_HOWMANY)+' '+"'LIN' = wavelengths (1st,last,
       howmany,how=LIN,INV,LOG,TAB)")
70 textbody9 = "'**** Refractive index of ambient medium
        ****'\n1.0000 = NAMBIENT\n'**** Effective Radii
       (micron) **** '"
71 textbody10 = (str(radius_first)+' '+str(radius_last)+
       ' '+str(radius_HOWMANY)+' '+"'LIN' = eff. radii
       (1st,last,howmany,how=LIN,INV,LOG,TAB)")
72 textbody11 = "'**** Define Incident Polarizations
       ****'\n(0,0) (1.,0.) (0.,0.) = Polarization state
        e01 (k along x axis)\n2 = IORTH  (=1 to do only
       pol. state e01; =2 to also do orth. pol. state)\n
       '**** Specify which output files to write ****' \
       n1 = IWRKSC (=0 to suppress, =1 to write sca file
        for each target orient.\n'**** Specify Target
       Rotations ****'\n0    360  9 = BETAMI, BETAMX,
       NBETA  (beta=rotation around a1)\n0    180  9  =
       THETMI, THETMX, NTHETA (theta=angle between a1
       and k) \n 0    360  1  = PHIMIN, PHIMAX, NPHI (
       phi=rotation angle of a1 around k) \n '****
       Specify first IWAV, IRAD, IORI (normally 0 0 0)
       ****' \n 0   0   0    = first IWAV, first IRAD,
       first IORI (0 0 0 to begin fresh)\n'**** Select
       Elements of S_ij Matrix to Print ****' \n 9     =
        NSMELTS = number of elements of S_ij to print (
       not more than 9)\n11 12 21 22 31 33 44 34 43   =
```

```
                    indices ij of elements to print \n '**** Specify
                    Scattered Directions ****'\n'LFRAME' = CMDFRM (
                    LFRAME, TFRAME for Lab Frame or Target Frame)\n1
                    = NPLANES = number of scattering planes \n 0.  0.
                     180. 1 = phi, theta_min, theta_max (deg) for
                    plane A''"
73
74                  with open(filename, 'w') as file:
75                      file.write(textbody1+'\n'+textbody2+'\n'+textbody3
                            +'\n'+textbody4+'\n'+textbody5+'\n'+textbody6+
                            '\n'+textbody7+'\n'+textbody8+'\n'+textbody9+'
                            \n'+textbody10+'\n'+textbody11)
76
77  def move_ddscat(C_size,location_base,target_type,folder_type):
78          index = range(0, len(C_size))
79          for i in index:
80                  C_exp = C_size[i]
81                  C_exp_r = round(C_exp,3)
82                  target_name = target_type+'_'+str(C_exp_r)+'_ar_'+str
                        (i)
83                  filename1 = os.path.join(location_base+folder_type+
                        target_name)
84                  ddscatname = '/home/njb15196/Desktop/PhD_2nd_code/
                        DDSCAT/examples_exp/ALL_EXP/ELLIPSOID/ddscat'
85                  copy2(ddscatname, filename1)
86                  st = os.stat(filename1)
87                  os.chmod(filename1, st.st_mode | stat.S_IEXEC)
88
89  def move_python(C_size,location_base,target_type,folder_type):
90          index = range(0, len(C_size))
91          for i in index:
92                  C_exp = C_size[i]
93                  C_exp_r = round(C_exp,3)
94                  target_name = target_type+'_'+str(C_exp_r)+'_ar_'+str
                        (i)
95                  filename3 = os.path.join(location_base,folder_type,
                        target_name,'functions_ddscat_ind_run_CNC.py')
96                  name_of_input = os.path.join(location_base,
                        folder_type,target_name,'ddscat.par')
97                  ddscat_runner_name = '/home/njb15196/Desktop/
                        PhD_2nd_code/python_code/DDSCAT_post_pros/
                        functions_ddscat_ind_run_CNC.py'
98                  copy2(ddscat_runner_name, filename3)
```

```
99                  filename2 = os.path.join(location_base,target_name,'
                        ddscat')
100                 execfile(filename3)

1   #The function below:
2   #reads the txt files generated during DDSCAT run
3   #extracts the optical properties, rotation angles values, wavelength
4   #calculates bulk optical properties
5   #compiles the output file for all wavelength and rotation angles
6
7   import csv
8   import string
9   import os
10  import math
11  import scipy.integrate as integrate
12  import linecache
13  from pylab import *
14  from matplotlib.pyplot import *
15  from matplotlib import pyplot as plt
16  import matplotlib.pyplot as plt
17  from scipy.interpolate import interp1d
18  import numpy as np
19  from scipy.stats import lognorm
20  import numpy as np
21  import pprint
22  import pylab as pl
23
24  pp = pprint.PrettyPrinter(depth=6)
25  def read_the_data_for_RI(datapath_im_water):
26      water_RI_data = []
27      with open(os.path.join(datapath_im_water,'RI_part_WATER_FR.txt'),
            'r') as f:
28          collection_of_lines = []
29          for line in f:
30              collection_of_lines.append([ float(x) for x in line.split
                    ()])
31              water_RI_imaglist = [ x[2] for x in collection_of_lines]
32              wave_wl = [ x[0] for x in collection_of_lines]
33              del water_RI_imaglist[-1]
34              del wave_wl[-1]
35          w_expand = np.linspace(0.3965, 0.6417, 825)
36          g_ext = interp1d(wave_wl, water_RI_imaglist, kind='quadratic'
                )
37          water_RI_imag = g_ext(w_expand)
```

```
38          return water_RI_imag
39
40  def count_amount_of_folders(location_base,C_size, target_type,
        water_RI_imag,concentration,den_particles,den_fluid,folder_type):
41      radius_list = []
42      index = range(0, len(C_size))
43      for i in index:
44          C_exp = C_size[i]
45          C_str = round(C_exp,3)
46          folder_name = target_type+'_'+str(C_str)+'_ar_'+str(i)
47          with open(os.path.join(location_base,folder_type,folder_name,
                'ddscat.par'), 'r') as f:
48              lines = f.readlines()
49              for line in lines:
50                  if line== lines[26]: #extract number of files in
                        folder [respectively to num of WL]
51                      raw_line = line.split()
52                      num_of_datafiles = int(raw_line[2])
53                  elif line== lines[30]:
54                          raw_line = line.split()
55                          radius_1 =float(raw_line[0])
56                          radius_2 = float(raw_line[1])
57                          num_of_sizes = float(raw_line[2])
58                          radius = np.linspace(radius_1, radius_2,
                                num_of_sizes)
59                          radius_list.append(float(radius))
60                  elif line== lines[37]:
61                          raw_line = line.split()
62                          num_of_betha = float(raw_line[2]) #k
                                parameter
63                  elif line== lines[38]:
64                          raw_line = line.split()
65                          num_of_theta = float(raw_line[2]) #k
                                parameter
66                  elif line== lines[39]:
67                          raw_line = line.split()
68                          num_of_psy =  float(raw_line[2]) #k parameter
69                          num_of_k = num_of_psy*num_of_theta*
                                num_of_betha
70                          print num_of_psy
71                          print num_of_theta
72                          print num_of_betha
```

```
73                          create_list_of_datafiles(num_of_datafiles,
                                num_of_sizes,num_of_k,radius,folder_name,
                                location_base,water_RI_imag,concentration
                                ,den_particles,den_fluid,C_str,
                                folder_type)
74      return radius_list
75
76
77  def create_list_of_datafiles(num_of_datafiles,num_of_sizes,num_of_k,
        radius,folder_name,location_base,water_RI_imag,concentration,
        den_particles,den_fluid,C_str,folder_type):
78      list_of_files = []
79      print num_of_k
80      for k in range(int(num_of_k)):
81          for r in range(int(num_of_sizes)):
82              for i in range(int(num_of_datafiles)):
83                  file = ("w"+str(i).zfill(3)+"r"+str(r).zfill(3)+"k"+
                        str(k).zfill(3)+".sca")
84                  list_of_files.append(file)
85      #pp.pprint(list_of_files)
86      read_the_data(list_of_files,radius,location_base,folder_name,
            water_RI_imag,concentration,den_particles,den_fluid,C_str,
            folder_type)
87
88
89  def read_the_data(list_of_files,radius,location_base,folder_name,
        water_RI_imag,concentration,den_particles,den_fluid,C_str,
        folder_type):
90      collection_of_lines = []
91      data_w = []
92      k_name_list = []
93      for current_file in list_of_files:
94          with open(os.path.join(location_base,folder_type,folder_name,
                current_file), 'r') as f:
95              n = 3
96              k_name_d = [current_file[i:i+n] for i in range(0,len(
                    current_file),n)]
97              k_name = k_name_d[3]
98              lines = f.readlines()
99              wave_for_lib = (lines[16]).split(' ')
100             wave = float(wave_for_lib[8])
101             rad_for_lib = (lines[15]).split(' ')
102             radii = float(rad_for_lib[8])
```

```
103             Q_for_lib = str(lines[39]).split()
104             Qs = float(Q_for_lib[3])
105             Qa = float(Q_for_lib[2])
106             Qe = float(Q_for_lib[1])
107             G = float(Q_for_lib[4])
108             line_from_file = radii, wave, Qs, Qa, Qe, G, k_name
109             collection_of_lines.append(line_from_file)
110             data_w.append(wave)
111             k_name_list.append(k_name)
112     interpolate_data_DDSCAT(collection_of_lines,radius,water_RI_imag,
            concentration,den_particles,den_fluid,location_base,
            folder_name,C_str,folder_type,k_name_list)
113
114 def interpolate_data_DDSCAT(collection_of_lines,radius,water_RI_imag,
    concentration,den_particles,den_fluid,location_base,folder_name,
    C_str,folder_type,k_name_list):
115     for Lib_Q in radius:
116         for Lib_k in k_name_list:
117             names = []
118             data_Qs = []
119             data_Qs_ext = []
120             data_Qa = []
121             data_Qa_ext = []
122             data_g = []
123             data_g_ext = []
124             phi1 = []
125             data_w = []
126
127             data_w_ext = np.linspace(0.3965, 0.6417, 825)
128             for line in collection_of_lines:
129                 if Lib_Q in line:
130                     if Lib_k in line:
131                         Qs = line[2]
132                         Qa = line[3]
133                         g = line[5]
134                         w = line[1]
135                         data_Qs.append(Qs)
136                         data_Qa.append(Qa)
137                         data_g.append(g)
138                         data_w.append(w)
139             Qs_ext = interp1d(data_w, data_Qs, kind='cubic')
140             Qa_ext = interp1d(data_w, data_Qa, kind='cubic')
141             g_ext = interp1d(data_w, data_g, kind='cubic')
```

```
142
143             data_Qs_ext = Qs_ext(data_w_ext)
144             data_Qa_ext = Qa_ext(data_w_ext)
145             data_g_ext = g_ext(data_w_ext)
146             degr1 = 10**(-3)
147             degr = ((math.pi)*((Lib_Q*degr1)**2))
148
149             rho_tot = concentration * den_particles + (1-
                    concentration)*den_fluid
150             phi_p = concentration*rho_tot/den_particles
151             phi_w = 1-phi_p
152             Vp    = (1.3333)*(math.pi)*((Lib_Q*degr1)**3)
153             rhop = phi_p/(Vp)
154
155
156             sigma_s = data_Qs_ext*degr
157             sigma_a = data_Qa_ext*degr
158             data_w_not_norm = np.linspace(0.5302,0.8501,825)
159             sigma_water = ((4*(math.pi)*(array(water_RI_imag)))/((
                    data_w_not_norm*10**(-3)))*phi_w)
160
161             mew_s = sigma_s*rhop
162             mewa = sigma_a*rhop
163             mew_a = mewa+sigma_water
164
165             fn1 = os.path.join(location_base,folder_type,folder_name,
                    'DDSCAT_eff_'+str(C_str)+'_k_'+str(Lib_k)+'.txt')
166             f = open(fn1,'w')
167             for a1, b1, c1, d1 in zip(data_w_ext, data_Qs_ext,
                    data_Qa_ext, data_g_ext):
168                 f.write(str(a1)+'\t'+str(b1)+'\t'+str(c1)+'\t'+str(d1
                        )+'\n')
169             f.close()
170
171             fn2 = os.path.join(location_base,folder_type,folder_name,
                    'DDSCAT_OP_'+str(C_str)+'_k_'+str(Lib_k)+'.txt')
172             f2 = open(fn2,'w')
173             for a, b, c, d in zip(data_w_ext, mew_s, mew_a,
                    data_g_ext):
174                 f2.write(str(a)+'\t'+str(b)+'\t'+str(c)+'\t'+str(d)+'
                        \n')
175             f2.close()
176
```

```
177 def read_the_data_DDSCAT(location_base, target_type, C_size,
    folder_type):
178     data_w_ext = np.linspace(0.3965, 0.6417, 825)
179     indxtmp = int(len(data_w_ext))-1
180     waves = np.linspace(0,indxtmp, num = 825)
181     Qus_size_range = []
182     Qua_size_range = []
183     g_size_range = []
184 
185     Mus_size_range = []
186     Mua_size_range = []
187     collection_of_lines = []
188     for wave in waves:
189         i = int(wave)
190         for Cs in C_size:
191             C_str = round(Cs,3)
192             folder_name = target_type+'_'+str(C_str)
193             with open(os.path.join(location_base,folder_type,
                    folder_name,'DDSCAT_eff_'+str(C_str)+'_k_'+str(Lib_k)
                    +'.txt'), 'r') as f:
194                 lines = f.readlines()
195                 Qus_size_range_unit = lines[i].split()[1]
196                 Qua_size_range_unit = lines[i].split()[2]
197                 g_size_range_unit = lines[i].split()[3]
198 
199                 Qus_size_range.append(Qus_size_range_unit)
200                 Qua_size_range.append(Qua_size_range_unit)
201                 g_size_range.append(g_size_range_unit)
202     return Qus_size_range,Qua_size_range,g_size_range,data_w_ext
203 
204 def read_the_data_DDSCAT_OP(location_base, target_type, C_size,
    folder_type):
205     data_w_ext = np.linspace(0.3965, 0.6417, 825)
206     indxtmp = int(len(data_w_ext))-1
207     waves = np.linspace(0,indxtmp, num = 825)
208     g_size_range = []
209 
210     Mus_size_range = []
211     Mua_size_range = []
212     collection_of_lines = []
213     for wave in waves:
214         i = int(wave)
215         index = range(0, len(C_size))
```

```
216         for i in index:
217             C_exp = C_size[i]
218             C_str = round(C_exp,3)
219             folder_name = target_type+'_'+str(C_str)+'_ar_'+str(i)
220             with open(os.path.join(location_base,folder_type,
                    folder_name,'DDSCAT_OP_'+str(C_str)+'_k_'+str(Lib_k)+
                    '.txt'), 'r') as f:
221                 lines = f.readlines()
222                 Mus_size_range_unit = lines[i].split()[1]
223                 Mua_size_range_unit = lines[i].split()[2]
224                 g_size_range_unit = lines[i].split()[3]
225 
226                 Mus_size_range.append(Mus_size_range_unit)
227                 Mua_size_range.append(Mua_size_range_unit)
228                 g_size_range.append(g_size_range_unit)
229     return Mus_size_range,Mua_size_range,g_size_range,data_w_ext
230 
231 def integrate_over_sizes(Qus_size_range,Qua_size_range,g_size_range,
        peak_radius,stddev,radius_list,data_w_ext, concentration,
        den_particles,den_fluid,folder_type):
232     mew_s_int = []
233     mew_a_int = []
234     g_int = []
235     degr1 = 10**(-3)
236 
237     radius_list_interp = radius_list
238     numind = len(Qus_size_range)/len(radius_list_interp)
239     split_index = np.linspace(len(radius_list_interp), len(
            Qus_size_range), numind)
240     radius_list_arr = np.asarray(radius_list_interp)
241 
242     indxtmp = int(len(split_index))-1
243     wavelen = np.linspace(0,indxtmp, num = 825)
244 
245     for wave in wavelen:
246         i = int(wave)
247 
248 
249         ind_last = int(split_index[i])
250         ind_first = int(ind_last - (int(len(radius_list))))
251 
252         int_lim_low = float(radius_list[0])
253         int_lim_high = float(radius_list[1])
```

```
254         #....Interpolation of
255         Qus_size_range_unit = Qus_size_range[ind_first:ind_last]
256         Qua_size_range_unit = Qua_size_range[ind_first:ind_last]
257         g_size_range_unit = g_size_range[ind_first:ind_last]
258
259         Qs_interp_unit = interp1d(radius_list, Qus_size_range_unit,
                kind='cubic')
260         Qa_interp_unit = interp1d(radius_list, Qua_size_range_unit,
                kind='cubic')
261         g_interp_unit = interp1d(radius_list, g_size_range_unit, kind
                ='cubic')
262
263         Qs_interp = Qs_interp_unit(radius_list_interp)
264         Qa_interp = Qa_interp_unit(radius_list_interp)
265         g_interp = g_interp_unit(radius_list_interp)
266
267         diam_list = [x * 2 * degrl for x in radius_list_interp]
268         distr = (1 / (stddev*radius_list_arr*sqrt(2*math.pi))) * exp
                (-(((np.log(radius_list_arr)-np.log(peak_radius))**2)/(2*
                stddev**2)))
269         D_int2 = integrand(diam_list, distr,int_lim_high,int_lim_low)
270         D_aft_int = integrate.trapz(D_int2, dx = int_lim_high-
                int_lim_low)
271         Numpuv = (6*concentration*den_fluid)/(math.pi*(den_fluid*
                concentration+(den_particles*(1-concentration)))*
                D_aft_int)
272
273         rad_list = [(x* degrl) ** 2  for x in radius_list_interp]
274         mid_cross_scat =  (array(map(float,(Qs_interp))))*math.pi*
                array(rad_list)*array(distr)
275         cross_scat = integrate.trapz(mid_cross_scat, dx =
                int_lim_high-int_lim_low)
276         mew_s_int_unit = cross_scat*Numpuv
277         mew_s_int.append(mew_s_int_unit)
278
279         mid_cross_abs =  (array(map(float,(Qa_interp))))*math.pi*
                array(rad_list)*array(distr)
280         cross_abs = integrate.trapz(mid_cross_abs, dx = int_lim_high-
                int_lim_low)
281         mew_a_int_unit = cross_abs*Numpuv
282         mew_a_int.append(mew_a_int_unit)
283
```

```
284             mid_cross_g =  (array(map(float,(Qs_interp))))*math.pi*array(
                    rad_list)*array(distr)
285             mid_cross_gg = array(mid_cross_g)*(array(map(float,(
                    g_size_range_unit))))
286             topeq = integrate.trapz(mid_cross_gg, dx = int_lim_high-
                    int_lim_low)
287             bottomeq = integrate.trapz(mid_cross_g, dx = int_lim_high-
                    int_lim_low)
288             g_int_unit = topeq/bottomeq
289             g_int.append(g_int_unit)
290
291     return mew_s_int,mew_a_int,g_int
292
293
294 def integrand(diam_list, distr,int_lim_high,int_lim_low):
295     D_int = (list(map(lambda x:pow(x,3),diam_list)))*distr
296     D_int2 = np.ndarray.tolist(D_int)
297     return D_int2
298
299 def save_csv(mew_s_int,mew_a_int,g_int,folder_type,location_base,
        data_w_ext):
300     fn2 = os.path.join(location_base,folder_type,'DDSCAT_POLY_OP.txt'
            )
301     f2 = open(fn2,'w')
302     for a, b, c, d in zip(data_w_ext, mew_s_int,mew_a_int,g_int):
303         f2.write(str(a)+'\t'+str(b)+'\t'+str(c)+'\t'+str(d)+'\n')
304     f2.close
```